

AD-A056 767

COLUMBIA RADIATION LAB NEW YORK

F/G 7/4

RESEARCH INVESTIGATION DIRECTED TOWARD EXTENDING THE USEFUL RAN--ETC(U)

MAR 78 W HAPPER

DAA629-77-C-0019

NL

UNCLASSIFIED

1 OF 4
AD
A056 767



COLUMBIA RADIATION LABORATORY ✓

RESEARCH INVESTIGATION DIRECTED TOWARD
EXTENDING THE USEFUL RANGE OF THE
ELECTROMAGNETIC SPECTRUM

Progress Report No. 28

April 1, 1977 through March 31, 1978

Contract DAAG29-77-C-0019 ✓

(Continuation of Contract DAAB07-74-C-0341)

Object of the research:

Basic and applied research in the fields of quantum electronics, electromagnetic propagation and solid state electronics.

The research reported in this document was made possible through support extended the Columbia Radiation Laboratory, Columbia University, by the Joint Services Electronics Program (U.S. Army Electronics Command and U.S. Army Research Office, Office of Naval Research, and the Air Force Office of Scientific Research) under Contract DAAG29-77-C-0019.

Submitted by: W. Happer, Director

Coordinated by: P. A. Pohlman, Administrative Assistant

COLUMBIA UNIVERSITY

Division of Government-Aided Research

New York, New York 10027

March 31, 1978

Approved for public release; distribution unlimited.

78 07 21 055

The research reported in this document was made possible through support extended the Columbia Radiation Laboratory, Columbia University, by the Joint Services Electronics Program (U. S. Army Electronics Command and U. S. Army Research Office, Office of Naval Research, and the Air Force Office of Scientific Research) under Contract DAAG29-77-C-0019.

Portions of this work were also supported by:

Air Force Office of Scientific Research

Grant AFOSR-74-2685

Army Research Office

Grant DAAG29-77-G-0015

National Science Foundation

Grant NSF-ENG 75-09325

Grant NSF-ENG 75-18074

Grant NSF-ENG 76-16424

Grant NSF-CHE 76-04118

Grant NSF-ENG 76-15063

Grant NSF-DMR 77-05995

ALFOSR	
SEARCHED	INDEXED
SERIALIZED	FILED
JUN 19 1977	
FBI - NEW YORK	
DISPATCHED	
SPECIAL	
A	

The support of these agencies is acknowledged in footnotes in the text.

Unclassified

SECURITY CLASSIFICATION OF THIS PAGE (When Data Entered)

REPORT DOCUMENTATION PAGE		READ INSTRUCTIONS BEFORE COMPLETING FORM
1. REPORT NUMBER Progress Report No. 28	2. GOVT ACCESSION NO.	3. RECIPIENT'S CATALOG NUMBER 9
4. TITLE (and Subtitle) RESEARCH INVESTIGATION DIRECTED TOWARD EXTENDING THE USEFUL RANGE OF THE ELEC- TROMAGNETIC SPECTRUM.		5. TYPE OF REPORT & PERIOD COVERED Interim progress rept. no. 28 1 Apr 77-31 March 78
7. AUTHOR(s) William Happer		6. CONTRACT OR GRANT NUMBER(s) DAAG29-77-C-0019 VDAAG-29-77-G-0015
9. PERFORMING ORGANIZATION NAME AND ADDRESS Columbia Radiation Laboratory Columbia University New York, New York 10027		10. PROGRAM ELEMENT, PROJECT, TASK AREA & WORK UNIT NUMBERS 1L161102BH57-03
11. CONTROLLING OFFICE NAME AND ADDRESS Department of the Army U. S. Army Research Office Research Triangle Park, NC 27709		12. REPORT DATE 31 March 1978
14. MONITORING AGENCY NAME & ADDRESS (if different from Controlling Office) 12347 P.		13. NUMBER OF PAGES 334
		15. SECURITY CLASS. (of this report) Unclassified
		15a. DECLASSIFICATION/DOWNGRADING SCHEDULE
16. DISTRIBUTION STATEMENT (of this Report) Approved for public release; Distribution unlimited.		
17. DISTRIBUTION STATEMENT (of the abstract entered in Block 20, if different from Report)		
18. SUPPLEMENTARY NOTES Portions of this work were supported by the Air Force Office of Scientific Research, the Army Research Office, and the National Science Foundation.		
19. KEY WORDS (Continue on reverse side if necessary and identify by block number) Methyl fluoride Oxygen Carbonyl fluoride Rare gases continued on page vi		
20. ABSTRACT (Continue on reverse side if necessary and identify by block number) A method has been developed which provides a complete description of the energy and population distributions in a laser pumped, metastable polyatomic molecule. Different temperatures are required for each mode and for the translational/rotational degrees of freedom. Good agreement between calculated and measured distributions has been found for CH ₃ F. Vibrational		

DD FORM 1 JAN 73 1473

EDITION OF 1 NOV 65 IS OBSOLETE

Unclassified

SECURITY CLASSIFICATION OF THIS PAGE (When Data Entered)

088 600

16

Block 20 continued - Abstract

energy for this system tends to accumulate preferentially in the ν_3 C-F stretch vibrational mode. As a result, extremely large population inversions are predicted for CH_3F when optically pumped by a CO_2 laser. These results are expected to apply to many polyatomic molecules.

Energy transfer cross sections have been measured for methyl fluoride/rare gas collision events. For the first time in a polyatomic molecule larger than 3 atoms, individual kinetic rate constants for specific intermode energy exchange processes have been obtained. The general qualitative features which describe the variation of rate constants with rare gas atoms are predicted by simple theoretical considerations, but quantitative agreement is seriously lacking.

Intermode collisional energy exchange events coupling the ν_2 , ν_6 , and $\nu_{3,5}$ modes of fluorophosgene (COF_2) have been studied in detail. Approximately 500 gas kinetic collisions are required to transfer population from ν_2 to ν_6 while only 180 collisions are necessary for ν_6 to $\nu_{3,5}$ transfer. The direct coupling between ν_2 and $\nu_{3,5}$ has been found to be weak (> 1500 collisions). The transfer of energy into the translational and rotational degrees of freedom has been found to be noticeably slower than intermode collisional energy exchange.

Energy transfer processes which collisionally couple the vibrational modes of CH_3Cl have been investigated. On the time scale of a laser pulse width, at high pressures of CF_3Cl , significant energy transfer takes place. No evidence for locking of energy into a single mode has been found for this molecule.

The CO_2 laser driven decomposition of perfluorocyclobutanone has been studied. Time resolved infrared fluorescence from product molecules has been observed, and product yields have been measured. The present experimental evidence suggests that at least some of the products are formed coincident with the laser pulse suggesting multiphoton decomposition of the parent perfluorocyclobutanone.

Photon echo modulation effects in $\text{Pr}^{3+}:\text{LaF}_3$ are analyzed in terms of a combined interaction of the nuclear quadrupole interaction and the second order hyperfine interaction. Using the interaction parameters obtained elsewhere, the theoretical echo behavior fits the experimental data successfully. The sign of the electric field gradient at the Pr site inferred from our data is negative.

We have made the first observations in Na vapor of three new types of echoes: excited-state photon echoes, tri-level echoes, and two-photon echoes. The excited-state photon echo extends the photon echo effect to transitions between states

which are both thermally unpopulated. The tri-level echo is a totally new effect peculiar to multilevel (three levels or more) systems. The two-photon echo is the sum-frequency analogue of the Raman (difference-frequency) echo. We have used these new effects to study foreign-gas collisional relaxation of atomic Na S-P and S-D superposition states.

A new diagnostic technique for flames has been developed. The flame is seeded with a small amount of sodium salt and the sodium atoms in the flame are spin polarized by optical pumping. The spin relaxation rates vary substantially across the spatial extent of the flame.

Time resolved studies of NO₂ fluorescence in the visible region of the spectrum have been undertaken to gain a better understanding of the anomalous radiative lifetimes of this important product of combustion in air.

Studies of spin exchange between spin polarized sodium atoms and odd isotopes of xenon and krypton have been undertaken. The sodium atoms are highly polarized by optically pumping with a dye laser.

Good agreement has been found between recent calculations of emission and absorption profiles of alkali-noble gas excimers and experimental measurements from this laboratory.

Experimental evidence has been obtained for the existence of potassium polyxenide exciplexes of the form KXe_n n = 1,2,3,4. These exciplexes radiate strongly in the green region of the spectrum.

The narrow absorption bands of Cs₂ molecules near 700 nm have been identified for the first time as transitions at very large internuclear separations, possibly from the repulsive ³Σ_u ground state.

Pulsed dye laser excitation of alkali vapors has been shown to lead to nearly complete photoionization of the alkali atoms. The local electric fields from the resulting plasma lead to stimulated emission of highly forbidden atomic transitions.

A heterodyne correlation radiometer is considered for the sensitive detection of radiating species. A sample of the species to be detected is physically made a part of the laboratory receiver, and serves as a frequency-domain template with which the remote radiation is correlated, after heterodyne detection. Requirements for local oscillator stability and tunability are less stringent than in the conventional heterodyne system and the use of a multiline local oscillator may be advantageous.

A simple threshold detector is derived for a wide class of binary decision problems involving the likelihood-ratio detection of a signal embedded in noise. A comparison of the sum of N independent observations with a unique threshold comprises an optimum detector, if a weak condition on the noise is satisfied, independent of the signal.

The optimal design of a heterodyne laser radar system requires that the coherence properties of the signal be properly taken into account. Performance is optimum when the degeneracy parameter of the scattered signal light is unity.

It is shown that, for an arbitrary discrete process embedded in independent additive discrete noise, the classical binary detection problem using a likelihood-ratio test reduces to a simple comparison of the number of events with a single threshold. Only a weak condition on the noise distribution is required. Our results are appropriate for the analysis of photocounting optical communications and photocounting radar systems.

Expressions are obtained for the mean and variance of the number of events in a fixed sampling time for a nonparalyzable dead-time counter. The input process is assumed to be Poisson with a rate that is a known function of time. Experiments performed with triangularly and sinusoidally modulated laser radiation provide results that are in accord with the theory.

We report a series of optical experiments that verify the full theoretical photocounting distributions obtained by Diamant and Teich for triangularly and sinusoidally modulated laser radiation. Another series of experiments validates the non-paralyzable-dead-time-modified versions of these formulas obtained by Cantor and Teich. A new expression is obtained for the paralyzable-dead-time-modified counting distribution for a modulated source.

The detection of a fluctuating signal in the presence of noise is considered for a doubly-stochastic Poisson counting system that is subject to fixed nonparalyzable detector dead time. The probability of error and channel capacity are examined. A maximum-likelihood estimate of the mean signal level is obtained for a simple image detection system with a dead-time-perturbed counting array.

Photocounting distributions have been calculated for an exponentially decaying pulse of light with a uniformly distributed starting time for the sampling interval. The results are of interest in spontaneous emission and radioactive decay experiments.

Block 20 continued - Abstract

Experimental studies have been made of Si MOS devices with ultra-thin (10-50 Å) oxide layers fabricated by low-temperature (700°C) dry oxidation. Electrical and optical properties of these devices reveal that photocurrent suppression occurs for oxides ≥ 20 Å in thickness, and that these effects can be removed by appropriate reverse bias. New modes of quantum detection are suggested by these devices and one such mode, a low-voltage photomultiplication, is demonstrated for a Au-SiO₂-n type Si structure.

The physical mechanisms of the breakdown of carrier confinement are considered using both the thermionic-emission and diffusion models. It is shown that, for most practical AlGaAs/GaAs DH lasers, the diffusion current is responsible for carrier leakage. The thermionic-emission of minority carriers is important when the confinement barrier or the mobility is very large. The theory presented here is also applicable to structures other than the AlGaAs/GaAs laser.

Majority and minority carrier transport in small geometry (2 µm diameter) Pt-GaAs Schottky barriers have been characterized experimentally. Transistor measurements on a matrix of these diodes, lying within approximately a minority carrier diffusion length of one another, indicates that majority-carrier thermionic emission current dominates for large forward bias (≥ 0.4 V). At smaller bias recombination in the space-charge region is most important. The minority carrier injection ratio decreases from 10^{-2} to 10^{-5} over the measurable range of voltage 0.5 to 1.0V. The implications for submillimeter detection and mixing using these devices are discussed.

Block 19 continued - Key Words

Vibrational relaxation
V-V energy transfer
Metastable state
Vibrational temperatures
Perfluorocyclobutanone
Infrared photochemistry
Trifluorochloromethane
Steady-state
Population inversion
Pseudo quadrupole interaction
Enhanced nuclear Zeeman effect
PENDOR
Excited-state photon echo
Tri-level echo
Two-photon echo
Raman echo
Collisional relaxation
Flames
Sodium
Spin polarization
NO₂
Fluorescence lifetimes
Noble gas spin polarization
Optical pumping
Excimers
Potassium polyxenide exciplexes
Cs₂ absorption spectrum
Laser induced plasmas
Plasma induced forbidden lines
Heterodyne correlation radiometry
Photon counting
Nonlinear heterodyne detection
Infrared sensing
Optical communications
Optical radar
Likelihood-ratio detection
Dead-time effects
Image detection
Channel capacity
Schottky barriers
Quantum detectors
Optical communications
MOS devices
Heterojunctions
Injection lasers
Carrier confinement
Thermionic emission
Diffusion
Micron devices
Classical detectors
Submillimeter radiation detectors

TABLE OF CONTENTS

PUBLICATIONS AND REPORTS	x
------------------------------------	---

FACTUAL DATA, CONCLUSIONS, AND PROGRAMS FOR THE NEXT INTERVAL

I. RELAXATION AND ENERGY TRANSFER	1
A. Chemical Reactions and Energy Transfer	1
1. Vibrational population and energy distributions of laser pumped metastable polyatomic molecules	1
2. Steady state population inversions in laser pumped polyatomic molecules	20
3. Some energy transfer parameters for laser driven chemical reactions in CF_3Cl	24
B. Laser Studies of Intermode Energy Transfer Events in Small Molecules	37
1. Intermode energy flow in CH_3F induced by rare gas collisions	37
2. Collision controlled vibrational energy exchange in COF_2 : Equilibration of the ν_2 , ν_6 , and $\nu_{3,5}$ modes	46
3. Intermode energy transfer in COF_2 induced by rare gases	56
C. Optical Pumping of Flames	67
D. Time Resolved Spectroscopy of NO_2	79
E. Nuclear Spin Polarization of Xe by Optical Pumping	85
F. Relaxation and Excitation Transfer of Optically Excited States in Solids	90
G. Dynamics of Laser Initiated Chemical Reactions in Low Pressure Gases with Mode Specific Excitation (CO_2 Laser Decomposition of Perfluorocyclobutanone)	103

II.	GENERATION AND CONTROL OF RADIATION	112
A.	Spontaneous and Induced Coherent Radiation Generation and Control in Atomic Vapors	112
B.	Alkali-Noble-Gas Diatomic Excimers	144
C.	Visible Emission Bands from KXe_n Polyatomic Exciplexes	155
D.	Absorption Studies of Cs_2 and Rb_2 Molecular Bands in the Visible and Near Visible	168
E.	Photoionization and Stimulated Emission in Alkali-Noble-Gas Vapors	177
III.	QUANTUM DETECTION AND SENSING OF RADIATION	194
A.	Nonlinear Heterodyne Detection and Sensing in the Infrared and Optical Regions of the Spectrum	194
1.	Heterodyne correlation radiometry	194
2.	Simple threshold detection of a continuous signal in noise with multiple independent observations	205
3.	Heterodyne detection of rough targets in the infrared and optical	213
B.	Photon Counting Detection for Communications, Radar, and Imaging	214
1.	Optimum photon detection with a simple counting processor	214
2.	Effects of rate variation on the counting statistics of dead-time-modified Poisson processes	220
3.	Observation of dead-time-modified photocounting distributions for modulated laser radiation	228
4.	Information, error, and imaging in dead-time-perturbed doubly-stochastic Poisson counting systems	238
5.	Photocounting distributions for exponentially decaying sources	256

IV. PHYSICAL EFFECTS OF ELECTRONIC MATERIALS	257
A. Carrier Transport Across Semiconductor Interfaces	257
1. MIS-Schottky barrier quantum detectors . .	257
2. Carrier transport across heterojunction interfaces	279
3. Schottky barrier classical detectors for submillimeter radiation	295
B. Thermodynamics of Laser Snow-Photochemical Cooling	315
PERSONNEL	325
JSEP REPORTS DISTRIBUTION LIST	327

PUBLICATIONS AND REPORTS

Publications

- Kent H. Casleton and George W. Flynn, "Laser Excited Infrared Fluorescence in COF_2 : Equilibration and Relaxation of the C=O and C-F Stretching Modes," J. Chem. Phys. 67, 3133 (1977).
- H. C. Card, "Photovoltaic Properties of MIS-Schottky Barriers," Solid-State Elect. 20, 971 (1977).
- H. C. Card and F. F. Fang, "Spectral Response of Photocurrents in the MOS and the Dependence on Gate and Substrate Bias," J. Appl. Phys. 48, 2481 (1977).
- H. C. Card, E. S. Yang, and P. Panayotatos, "Peaked Schottky Barrier Solar Cells by Al-Si Metallurgical Reaction," Appl. Phys. Lett. 30, 643 (1977).
- H. C. Card and E. S. Yang, "Electronic Processes at Grain Boundaries in Polycrystalline Semiconductors under Optical Illumination," IEEE Trans. on Electron Devices, ED-24, 397 (1977).
- P. Panayotatos, H. C. Card and E. S. Yang, "The Effects of Illumination on the Depletion-Region Recombination Currents in Schottky-Barrier Solar Cells," IEEE Proceedings (Lett.) 65, 1213 (1977).
- K. K. Ng and H. C. Card, "Photocurrent Suppression and Interface State Recombination in MIS-Schottky Barriers," IEEE-IEDM Digest of Technical Papers, 57 (1977).
- G. W. Flynn, "Laser Fluorescence and Thermal Lensing Studies of Intermode Energy Transfer and Chemical Reactivity in Small Polyatomic Molecules," A.C. Symposium on State-to-State Chemistry, Am. Chem. Soc. Meeting, New Orleans, La., March 1977, ACS Symposium Series, P. R. Brooks and E. F. Hayes, Editors, 1977.
- S. Lemont¹ and G. W. Flynn, "Vibrational State Analysis of Electronic to Vibrational Energy Transfer Processes," An. Rev. of Phys. 28, 261 (1977).

¹ Present Address: Naval Research Laboratory, Washington, D.C.

- A. C. Tam² and W. Happer, "Plasma Production in a Cs Vapor by a Weak CW Laser Beam at 6010 Å," Opt. Comm. 21, 403 (1977).
- A. C. Tam and W. Happer, "Oscillating Laser-Production of Particulates in a Cs/D₂ Vapor," Chem. Phys. Lett. 49, 320 (1977).
- W. Happer and A. C. Tam, "Effect of Rapid Spin Exchange on the Magnetic-Resonance Spectrum of Alkali Vapors," Phys. Rev. A 16, 1877 (1977).
- G. Moe³ and W. Happer, "Conservation of Angular Momentum for Light Propagating in a Transparent Anisotropic Medium," J. Phys. B 10, 1191 (1977).
- T. Mossberg, A. Flusberg, R. Kachru, and S. R. Hartmann, "Tri-Level Echoes," Phys. Rev. Lett. 39, 1523 (1977).
- Eknoyan, S. M. Sze and E. S. Yang, "Microwave BARITT Diodes with Retarding Field-an Investigation," Solid-State Electronics 20, 285 (1977).
- Eknoyan, E. S. Yang and S. M. Sze, "Multilayered Ion Implanted BARITT Diodes with Improved Efficiency," Solid-State Electronics 20, 291 (1977).
- M. C. Teich, "Nonlinear Heterodyne Detection," Topics in App. Phys., edited by R. J. Keyes 19, 229 (1977).
- M. C. Teich, Editor, Proc. NSF Grantee-User Meeting, Opt. Comm. Systems, 1977.
- M. E. Breton, M. C. Teich and L. Martin, "Intensity Fluctuations Produced by Multimode Lasers in Combination with Dielectric Beam-splitters," Beh. Res. Meth. Instr. 9, 324 (1977).
- Malvin Carl Teich, Paul R. Prucnal, and Giovanni Vannucci, "Optimum Photon Detection with a Simple Counting Processor," Opt. Lett. 1, 208 (1977).
- S. Meth⁴ and S. R. Hartmann, "Photon Echo Modulation in Ruby," Opt. Comm. 24, 100 (1978).

² Present Address: Bell Laboratories, Murray Hill, New Jersey.

³ Present Address: Riverside Research Institute, New York, New York.

⁴ Present Address: Inco. Incorporated, McLean, Virginia.

- S. M. Curry,⁵ W. Happer, A. C. Tam, and T. Yabuzaki,⁶ "Spin Polarization in Flames by Optical Pumping," Phys. Rev. Lett. 40, 67 (1978).
- R. S. Sheorey, R. C. Slater,⁷ and G. W. Flynn, "Overtone Fluorescence as a Probe of Intermode Energy Flow in Laser Pumped Molecules," J. Chem. Phys. 68, 1058 (1978).
- A. Flusberg, T. Mossberg, and S. R. Hartmann, "Excited-State Photon-Echo Relaxation in Na Vapor," Opt. Comm. 24, 207 (1978).
- R. Gupta, "Hyperfine Structures in the Excited States of Alkali-Metal Atoms," North-Holland Publishing Co. Hyperfine Interactions 4, 79 (1978).
- R. Gupta, W. Happer, J. Wagner, and E. Wennmyr, "Absorption Studies of Cs₂ and Rb₂ Molecular Bands in the Visible and Near Visible," J. Chem. Phys. 68, 799 (1978).
- M. C. Teich, "Heterodyne Correlation Radiometry," Opt. Eng. 17, 170 (1978).
- G. Vannucci and M. C. Teich, "Effects of Rate Variation of the Counting Statistics of Dead-Time-Modified Poisson Processes," Opt. Comm. 25, (1978), in press.
- E. S. Yang, "Fundamentals of Semiconductor Devices," McGraw-Hill Book Co., New York, 1978.
- T. Yabuzaki, A. C. Tam, M. Hou, W. Happer, and S. M. Curry, "Preferential Excitation Transfer in Cs*(6D_{3/2})-Cs(6S_{1/2}) Collisions," Opt. Comm. 24, 305 (1978).

⁵ On leave from the University of Texas at Dallas, Richardson, Texas.

⁶ On leave from the Ionosphere Research Laboratory, Kyoto University, Kyoto, Japan.

⁷ Present Address: Avco Everett Research Laboratories, Everett, Massachusetts.

Papers by CRL Staff Members Presented at Scientific Meetings

- H. C. Card, "Physics of MIS-Schottky Barrier Solar Cells," Device Research Conference, Cornell University, Ithaca, New York, June 27-29, 1977.
- H. C. Card and K. K. Ng, "Photocurrent Suppression and Interface State Recombination in MIS-Schottky Barriers," IEEE International Electron Devices Meeting, Washington, D.C., December, 1977.
- H. C. Card, "Physics and Applications of MOS Devices with Ultra-Thin (Tunnelable) Oxides," JSEP Topical Review on Semiconductor I.C.'s, Devices and Materials, Stanford University, August 3-4, 1977.
- K. H. Casleton, "Vibrational Relaxation of the C=O and C-F Stretching Modes in Carbonyl Fluoride," Gordon Conference on Molecular Energy Transfer, Brewster Academy, Wolfeboro, New Hampshire, July 13, 1977.
- S. M. Curry, "Infrared CW Laser Excitation and Particulate Formation in Cs and Rb Vapor," San Francisco Meeting of the American Physical Society, San Francisco, California, January 25, 1978.
- G. W. Flynn, "Lasers, Energy Transfer, and Vibrational Photochemistry," Illinois Institute of Technology, Symposium on "Lasers in Chemical Dynamics," May 19, 1977.
- G. W. Flynn, "Progress in Vibrational Energy Transfer," Symposium in Honor of E. Bright Wilson, Georgia Institute of Technology, Atlanta, Georgia, May 25, 1977.
- G. W. Flynn, "Mode-to-Mode Energy Transfer: The Vibrational Overhauser Effect," Workshop on Laser Chemistry, Battelle Institute Northwest, Seattle, Washington, August 23, 1977.
- G. W. Flynn, "Intermode Vibrational Energy Transfer in Small Molecules," Symposium on Energy Transfer in Atoms and Molecules, American Physical Society Meeting, Knoxville, Tennessee, December 5, 1977.
- W. Happer, "États Atomique et Moléculaires Couplés à un Continuum; Atomes et Molécules Hautement Excités," Colloque Internationale du CNRS, France, June 13-17, 1977.
- W. Happer, "Long Range Interactions between CW Self-Focused Laser Beams in an Atomic Vapor," Third International Conference on Laser Spectroscopy, Jackson Hole, Wyoming, July 4-8, 1977.

- S. R. Hartmann, "The Multiphoton Coherent Hanle Effect," Fourth Rochester Conference on Coherence and Quantum Optics, Rochester, New York, June 8-10, 1977.
- S. R. Hartmann, "Superradiance and the Laser," DOD Conference on New Laser Concepts, Durham, North Carolina, September, 1977.
- J. K. McVey, "Energy Transfer in CF_3Cl ," Gordon Research Conference on Molecular Energy Transfer, Brewster Academy, Wolfeboro, New Hampshire, July 13, 1977.
- J. K. McVey, "Vibrational Relaxation Processes in CF_3Cl at Low Pressures," American Chemical Society Conference, Anaheim, California, March 15, 1978.
- G. Moe and W. Happer, "Three and Four-wave Mixing and Photoionization in Cs Vapor," 1978 Annual Meeting of the American Physical Society, San Francisco, California, January 23, 1978; Bull. Am. Phys. Soc. 23, 33 (1978).
- T. Mossberg, "Two-Photon Echoes in Na Vapor," 1978 Annual Meeting of the American Physical Society, San Francisco, California, January 23, 1978; Bull. Am. Phys. Soc. 23, 33 (1978).
- I. Shamah, "Translation and Vibration Energy Distributions in Metastable Laser Pumped Polyatomic Molecules," Poster Session at Gordon Research Conference on Molecular Energy Transfer, Brewster Academy, Wolfeboro, New Hampshire, July 13, 1977.
- A. C. Tam, "Long Range Interaction Between Laser Beams in an Atomic Vapor," Gordon Research Conference (Atomic Physics) Brewster Academy, Wolfeboro, New Hampshire, July 4-8, 1977.
- A. C. Tam, "Plasma Production in Cs Vapor by a Weak CW Laser Beam at 6010 Å," Gordon Research Conference (Nonlinear Effects and Lasers), Holderness School, New Hampshire, August 15-19, 1977.
- M. C. Teich, "Information and Error in Photon Counting Optical Communications and Radar Systems," Topical Conference on Informational Aspects of Decision and Control, Joint Services Electronics Program, Harvard University, Cambridge, Massachusetts, May 5, 1977.
- M. C. Teich, "Photon Counting and Energy Detection: The Experiment of Hecht, Schlaer, and Pirenne Revisited," Annual Meeting of the Society for Neuroscience, Anaheim, California, November 7, 1977.

Lectures

- H. C. Card, "Schottky Barrier Optoelectronics," Research Seminar, RCA Labs. David Sarnoff Res. Ctr., Princeton, N. J., May 26, 1977.
- H. C. Card, "Schottky Barriers," Electrical Engineering Seminar, University of Manitoba, January 10, 1978.
- K. H. Casleton, "Studies of Mode to Mode Vibrational Energy Transfer and Laser Induced Chemistry," Seminar, Ford Motor Company Research Laboratory, Dearborn, Michigan, September 28, 1977; Seminar, Oak Ridge National Laboratory, Oak Ridge, Tennessee, November 2, 1977.
- S. M. Curry, "Excitation Transfer Reactions in Laser-Excited Cesium Vapor," Seminar, University of Connecticut, Storrs, Connecticut, March 6, 1978.
- S. M. Curry, "Laser-Induced Plasma Formation in Cesium Vapor: An Atomic Chain Reaction," Colloquium, University of Arkansas, Fayetteville, Arkansas, March 24, 1978.
- A. Flusberg, "Multi-level Echoes in Na Vapor," Seminar, NRL, Washington, D. C., November 3, 1977.
- A. Flusberg, "Coherent Atomic Transients and Multi-level Echoes," Colloquium, Hebrew University, Jerusalem, Israel, January 3, 1978.
- A. Flusberg, "Tri-level Echoes," Seminar, Ben Gurion University of the Negeo, Beersheva, Israel, January 5, 1978.
- A. Flusberg, "Tri-level Echoes: A New Coherent Transient Effect," Seminar, IBM Research Corp., San Jose, California, February 23, 1978.
- G. W. Flynn, "Mode-to-Mode Energy Transfer in Small Polyatomic Molecules," Allied Chemical Company, Morristown, New Jersey, June 6, 1977; Livermore Laboratories, Livermore, California, August 18, 1977; University of Rochester, Rochester, New York, September 21, 1977; Rice University, Houston, Texas, October 7, 1977; Ohio State University, Columbus, Ohio, October 20, 1977; Argonne National Laboratory, Argonne, Illinois, October 21, 1977; University of Iowa, December 1, 1977.
- G. W. Flynn, "Energy Transfer and Chemical Reactivity in Small Molecules," University of North Carolina, Raleigh, North

- Carolina, January 30, 1978; Amherst College, Amherst, Massachusetts, March 3, 1978; University of Toronto, Toronto, Canada, March 15, 1978; University of Waterloo, Waterloo, Canada, March 16, 1978.
- W. Happer, "Laser Snow," Wesleyan University, Middletown, Connecticut, April 7, 1977; Harvard University, Cambridge, Massachusetts, May 23, 1977.
- W. Happer, "Highly Excited Alkali-Noble Gas Excimers," Meudon Observatory, Paris, France, June 10, 1977.
- W. Happer, "Long Range Interactions Between cw Self-Focused Laser Beams in an Atomic Vapor," University of Rochester, Rochester, New York, November 8, 1977; Thomas J. Watson IBM Research Center, Yorktown Heights, New York, November 17, 1977.
- S. R. Hartmann, "Tri-Level Echoes in Atomic Vapors," Seminar, Massachusetts Institute of Technology, Cambridge, Massachusetts, March 2, 1978.
- S. R. Hartmann, "Superradiance," Colloquium, University of Maryland, College Park, Maryland, 1977.
- J. K. McVey, "Energy Transfer and Chemistry in IR-Excited Polyatomics," Seminar, Princeton University, Princeton, New Jersey, March 1, 1978.
- T. Mossberg, "Excited State Echoes," Seminar, Naval Research Laboratory, Washington, D.C., October 17, 1977.
- I. Shamah, "Vibrationally Excited States Produced by the Relaxation of Laser Pumped Polyatomic Molecules," Oral Dissertation Seminar, Columbia University, New York, New York, November 16, 1977.
- A. C. Tam, "Forces Between Laser Beams," Seminar, Columbia Radiation Laboratory, New York, New York, June, 1977; Colloquium, Columbia University, New York, New York, November, 1977; Seminar, New York University, New York, New York, December, 1977.
- A. C. Tam, "Display-Magnetometers and Spectrometers," Seminar, Massachusetts Institute of Technology, Cambridge, Massachusetts, October, 1977; Seminar, University of Massachusetts, Amherst, Massachusetts, November, 1977.
- M. C. Teich, "Photon Counting in the Presence of Dead Time," Seminar, New York University, New York, New York, December 19, 1977.

- M. C. Teich, "Imaging, Error, and Information Transmission in Photocounting Optical Radar and Communications Systems," Seminar, Riverside Research Institute, New York, New York, March 8, 1978.
- E. S. Yang, "Carrier Confinement in Double Heterostructure Injection Lasers," Seminar, Phillips Research Laboratories, Briarcliff Manor, New York, March 2, 1978.

Resonance Seminars

Meetings are held periodically at Columbia University, New York, New York, during the academic year and are open to all members of the Physics Department. Guest speakers are invited to discuss work in the general area of the research in the Columbia Radiation Laboratory.

Avigdor Ronn, Brooklyn College, "Laser-Induced Particulate Formation," April 15, 1977.

Andrew Tam, Columbia University, "Bouncing Laser Beams," April 22, 1977.

Jean F. Delpech, Université Paris, "Isotopic Effects in the Rotational Relaxation of Helium Molecules," May 9, 1977.

C. T. Lee, Princeton University, "Transition from Incoherence to Coherence in Superradiance," June 2, 1977.

H. C. Card, Columbia University, "Physics and Applications of MOS Devices with Ultra-Thin (Tunnelable) Oxides," June 8, 1977.

N. Takeuchi, National Institute for Environmental Studies, Japan, "Remote Measurement of Atmospheric Pollution by Lidar Echoes," June 13, 1977.

Robert Krotkov, University of Massachusetts, "Coherent Excitation of Atomic Hydrogen," September 23, 1977.

Bruce D. McCombe, Naval Research Laboratory, "Far Infrared Magnetoabsorption Studies of Space Charge Layers in Silicon Mosfets," October 14, 1977.

Thomas Mossberg, Columbia University, "Excited State Photon Echoes," October 28, 1977.

Eli Yablonovitch, Harvard University, "Multiphoton Induced Chemical Reactions," November 4, 1977.

Allen Flusberg, Columbia University, "Multi-State Echoes,"
November 11, 1977.

Thomas Johnson, West Point, "High Power UV Gas Lasers,"
December 2, 1977.

George W. Flynn, Columbia University, "Vibrational Energy
Transfer and Chemical Reactivity in Small Molecules,"
December 9, 1977.

Kenneth Spears, Northwestern University, "Picosecond Probes
of Hydrogen Bonding and Molecular Rotation," January 19,
1978.

Mark Havey, University of New Hampshire, "Luminescence Studies
of Matrix Isolated Sodium Atoms," January 27, 1978.

Terry A. Miller, Bell Laboratories, "Laser Spectroscopy of
Atoms, Free Radicals and Molecular Ions," February 24,
1978.

H. Craig Casey, Jr., Bell Laboratories, "Components for
Optical Fiber Communication Systems," March 3, 1978.

Michael S. Lubell, Yale University, "What Can Polarized
Electrons Teach Us? Forty-Five Years of Collision
Theory Dispelled," March 31, 1978.

I. RELAXATION AND ENERGY TRANSFER

A. CHEMICAL REACTIONS AND ENERGY TRANSFER

1. Vibrational Population and Energy Distributions of Laser Pumped Metastable Polyatomic Molecules*

(I. Shamah, G. W. Flynn)

Introduction:

Infrared laser devices provide a convenient means for exciting single vibrational states of molecules. Under collision free conditions the excitation placed in the vibrational level will remain trapped for long periods of time because of the low probability of spontaneous emission. Typical radiative lifetimes in the infrared range from 1-100 msec. At a pressure of 1 torr a molecule at room temperature undergoes approximately 10^4 - 10^6 gas kinetic collisions in this time. The lifetimes of most vibrational levels are thus limited by collisions in a bulk gas. In many polyatomic molecules vibrational relaxation occurs in two distinct stages. Initially, vibration-to-vibration (V-V) energy transfer processes redistribute excitation between vibrational modes until all or part of the vibrational manifold reaches a steady state with a well defined population distribution. In the second stage vibration to translation/rotation (V-T/R) relaxation processes re-equilibrate the vibrational manifold with the translational and rotational degrees of freedom. The steady state

vibrational population distribution, which results from the initial V-V relaxation, is generally nonuniform, highly selective, and significantly different from Boltzmann-like expectations.⁽¹⁾⁻⁽⁸⁾ The presence of this metastable energy and population distribution is of intrinsic interest in the study of molecular relaxation processes, laser initiated chemical reactions, and optically pumped molecular laser systems.

At the present time there is no prescription for obtaining the vibrational steady state energy and population distributions for a polyatomic gas, initially equilibrated at an ambient temperature T , which absorbs a fixed energy per molecule E_{in} from a pulsed laser. The vibrational energy distribution at steady state is not a simple function of E_{in} and T because the collision processes which lead to intermode equilibration usually require the exchange of energy between the vibrational and translational/rotational degrees of freedom. Instead a nonuniform multi-temperature distribution is required to fully define the energy distribution. Indeed the multiple temperature effects, which are a consequence of this energy exchange, are sensitive functions of the energy transfer mechanism. A knowledge of this mechanism is required before the vibrational steady state energy and population distributions can be calculated from E_{in} and T . Fortunately, due to a variety of improved experimental techniques, the intermode energy transfer mechanisms or paths can now be deduced for at least a few small molecules.⁽¹⁾⁽²⁾⁽⁹⁾⁽¹⁰⁾

We have developed a multi-temperature model to completely

characterize the vibrational steady state of a polyatomic molecule. This analysis emphasizes the effects on the steady state thermodynamics due to the large intermode nonresonances and treats the vibrational modes as simple harmonic oscillators. This particular model is especially useful in characterizing the population distribution of any vibrationally pumped molecule whose V-V equilibration processes are much faster than its overall (V-T/R) relaxation. Such a description is presented for laser pumped CH_3F , a molecule whose vibrational energy transfer path has been well studied.

Discussion:

A molecule which has been vibrationally excited by a laser and allowed to internally equilibrate its modes cannot be described by a single temperature until the vibrational degrees of freedom have come into equilibrium with the translational/rotational degrees of freedom (characteristic time scale τ_{VT}). Nevertheless, any state in the molecule with vibrational quantum numbers $v_1, v_2, \dots, v_\ell \equiv \{v_j\}$ can be described by a temperature $T_{\{v_j\}}$ where

$$N_{\{v_j\}} = N_0 g_{\{v_j\}} \exp[-E_{\{v_j\}}/kT_{\{v_j\}}] . \quad (1)$$

$N_{\{v_j\}}$, $g_{\{v_j\}}$, and $E_{\{v_j\}}$ are respectively the population, degeneracy and energy of state $\{v_j\}$. N_0 is the population of the ground vibrational state and k is Boltzmann's constant. Although in principle each vibrational state of a metastable system is

described by a different $T_{\{v_j\}}$, the states within a given mode of frequency v_j will all have the same mode temperature T_j in the harmonic oscillator limit. (11) (12) In general for ℓ modes any temperature $T_{\{v_j\}}$ will be given by

$$\frac{\sum_{j=1}^{\ell} v_j v_j}{T_{\{v_j\}}} = \sum_{j=1}^{\ell} v_j \left(\frac{v_j}{T_j} \right) . \quad (2)$$

Equation (2) illustrates that the vibrational temperature of any level at vibrational steady state is a linear combination of the mode temperatures T_j , and the task of describing vibrational metastable states is reduced to the problem of finding only a small number (ℓ) of mode temperatures.

The mode vibrational temperatures T_j are also not independent. The populations and hence temperatures of the different modes are controlled by steady state equilibrium constants which are sensitive to the energy transfer mechanism. Suppose that two modes are coupled through any two states in their respective manifolds by a process such as

$$M(v_i^C v_i) + M \rightleftharpoons M(v_j^C v_j) + M + \Delta E = v_i^C \epsilon_i - v_j^C \epsilon_j , \quad (3)$$

where v_i^C and v_j^C are the quantum numbers for the states between which intermode energy transfer occurs. The effective equation linking the fundamental levels v_i and v_j , can easily be shown to be (13)

$$v_i^C M(v_i) \rightleftharpoons v_j^C M(v_j) + (v_i^C - v_j^C) M(0) + \Delta E = v_i^C \epsilon_i - v_j^C \epsilon_j, \quad (4)$$

where $M(0)$ is a ground state molecule. Equation (4) merely reflects the fact that v_i^C quanta of type v_i are required to produce v_j^C quanta of type v_j with a translational/rotational energy change of ΔE . The equilibrium constant for (4) then becomes^{(3) (5) (11) (12) (14)}

$$K_{eq} = \frac{N_O (v_i^C - v_j^C) N_j^{v_j^C}}{N_i^{v_i^C}} = \frac{g_j^{v_j^C}}{g_i^{v_i^C}} e^{(v_i^C \epsilon_i - v_j^C \epsilon_j)/kT'}. \quad (5)$$

where T' is the steady-state translational temperature. Inserting the vibrational temperature definitions for the N_i (Eq. 1) gives

$$T_i = [\epsilon_i T_j / (f_{ji} \epsilon_j T' + (\epsilon_i - f_{ji} \epsilon_j) T_j)] T', \quad (6)$$

where $f_{ji} = v_j^C / v_i^C$.

Equation (6) illustrates that the details of the vibrational energy transfer pathway will affect the steady state temperature distribution. The temperature of the various modes will differ at vibrational steady state in a manner determined by the mode energy gaps, "adjusted" to include the path factor f_{ji} . If the energy transfer process (3) is endothermic going from mode i to mode j , $f_{ji} \epsilon_j > \epsilon_i$ and T_i will blow up when T_j reaches the limiting value

$$T_j = [f_{ji} \epsilon_j / (f_{ji} \epsilon_j - \epsilon_i)] T'. \quad (7)$$

The proportionality constant relating T_j to T' is now a function of the "adjusted" energy $f_{ji}\epsilon_j$ instead of just ϵ_j . On the other hand, if the energy transfer process (3) is exothermic, $f_{ji}\epsilon_j < \epsilon_i$, T_i will reach a limiting value while T_j blows up. Therefore, the sign of the energy gap in the intermode crossover step will indicate which temperature will be the highest. Endothermic energy gaps favor the reactant mode and exothermic energy gaps favor the product mode. The mode with the lowest frequency may not necessarily be the hottest; however after adjusting the energies to include path factors the mode with the lowest adjusted energy will be the hottest. In general for any given level of excitation different vibrational temperature distributions can be expected for different pathways. Since the source of the multiple temperature effect is the presence of the energy differences in the crossover steps (3), if these processes were completely resonant, all the vibrational degrees of freedom will be at one excited temperature. However, because most pathways are non-resonant, a few vibrational modes will show enhanced vibrational excitation. The choice and extent of enhancement is critically dependent on the energy transfer path.

Once the complete energy transfer pathway is known, all temperatures can be directly given as a function of T' and a single reference vibrational temperature T_i . For convenience, the reference mode is generally taken to be the mode pumped by the laser, though the choice is arbitrary. T_i and T' can be related to measurable initial conditions by employing additional

constraint equations. The first constraint used is the conservation of excited molecules (or vibrational quanta). This conservation condition actually keeps track of the pumped molecules as they traverse the energy transfer path to establish a steady state condition. A convenient way of expressing the condition can be shown⁽¹³⁾ to be given by the fraction of molecules pumped, f_p , which is equivalent to the number of photons absorbed per molecule.

$$f_p = (E_{in}/\epsilon_i) = \sum_j (\overline{\Delta E_j^{vib}}/f_{ji}\epsilon_j) . \quad (8)$$

E_{in} is the energy absorbed per molecule and ϵ_i is the photon energy. Equation (8) states that the laser energy absorbed by ν_i is redistributed among all the vibrational modes in a manner weighted by the adjusted mode energy, $f_{ji}\epsilon_j$, which is in turn controlled by the particular energy transfer path. Hence a relation between the vibrational temperatures and an easily measurable quantity has been derived.

A second constraint equation can be obtained by keeping a careful accounting of the translational/rotational energy throughout the V-V equilibration. Whenever molecules undergo V-V processes which exchange unequal amounts of vibrational energy, the vibrational nonresonance must be made up by the translational/rotational degrees of freedom. Thus translational/rotational energy changes may occur during V-V energy transfer resulting in a steady state gas which is translationally cold or hot relative to the ambient temperature. The general equation which sums up

the total translational/rotational energy changes per molecule occurring during V-V equilibration can be shown⁽¹³⁾ to reduce to

$$\Delta \bar{E}^{T/R} = \sum_j \left(\frac{\epsilon_i}{f_{ji} \epsilon_j} - 1 \right) \Delta \bar{E}_j^{\text{vib}} \quad (9)$$

As in the particle summation the total translational/rotational energy change (9) is a sum of individual mode contributions adjusted for the energy transfer path, and therefore the overall translational/rotational energy change will depend on the magnitude and sign of the translational/rotational energy change of each of the intermode crossover steps (4).

Under most experimental conditions the translational and rotational degrees of freedom can be considered to reach their equipartition limit. Therefore, Eq. (9) can be rewritten as

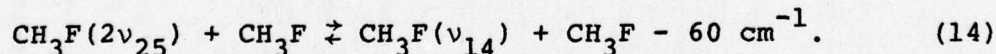
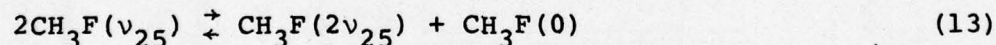
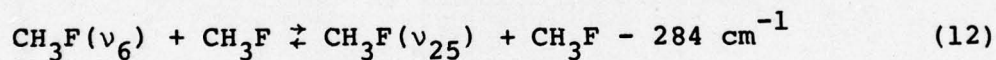
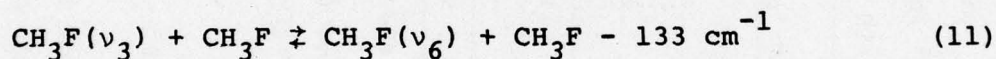
$$3Nk(T' - T) = N \sum_j \left(f_{ij} \frac{\epsilon_i}{\epsilon_j} - 1 \right) \Delta \bar{E}_j^{\text{vib}} \quad (10)$$

another equation relating the internal temperatures to T' and T . The temperature relations (6) allow all the vibrational temperatures to be calculated in terms of two free temperatures T_i and T' , while the constraint equations (8) and (10) restrict the remaining two free temperatures by fixing them to the specific initial conditions. Thus knowledge of the energy transfer pathway permits the determination of all the internal molecular temperatures and consequently the steady state thermodynamic quantities as a function of the input energy and ambient temperature.

Results:

Some vibrational steady state thermodynamic quantities are calculated below for laser pumped CH_3F . CH_3F has 6 vibrational modes, however, accidental degeneracies allow both mode pairs ν_2, ν_5 and ν_1, ν_4 to be treated as triply degenerate single levels ν_{25} and ν_{14} . This reduces the number of modes to four ($\ell=4$). The energy (ϵ_j) and the degree of degeneracy (g_j) for each of the four resultant fundamentals are given in Table I. Laser studies of vibrational relaxation⁽¹⁵⁾⁻⁽²²⁾ have shown that a reasonable V-V energy transfer pathway coupling the fundamental states of CH_3F following laser excitation of the ν_3 fundamental state is as follows

Path 1



A set of five molecular temperatures can easily be found as a function of laser input energy and ambient temperature. These temperatures are plotted in Figure 1 for absorbed laser energies

TABLE I

Stoichiometric Coefficients (f_{ij}) (a) and Adjusted Mode Frequencies ($\epsilon_{ij}^{\text{ADJ}} = \epsilon_j/f_{ij}$) (b) for CH_3F Undergoing Various Relaxation Pathways (c) and Mode Excitations

mode d_j	(d)	A PUMPING ν_3						B PUMPING ν_6		C PUMPING ν_{14}		
		PATH 1		PATH 1A		PATH 2		PATH 3		PATH 1		PATH 1A
		$f_{3,j}$	ϵ_j^{ADJ}	$f_{3,j}$	ϵ_j^{ADJ}	$f_{3,j}$	ϵ_j^{ADJ}	$f_{3,j}$	ϵ_j^{ADJ}	$f_{6,j}$	ϵ_j^{ADJ}	$f_{14,j}$
ν_3	1	1049	1	1049	1	1049	1	1049	1	1049	1/2	2098
ν_6	2	1182	1	1182	1	1182	1	1182	1	1182	1/2	2364
$\nu_{25}^{(e)}$	3	1466	1	1466	1	1466	1	1466	1	1466	1/2	2932
$\nu_{14}^{(e)}$	3	2992	2	1496	3	997	3	997	3	1496	1	2992

(a) f_{ij} is the number of molecules from the pumped level ν_i ($\nu=1$) required to produce one molecule in the level ν_j ($\nu=1$).

(b) The lower the ϵ_j^{ADJ} the hotter the mode (see Table II).

(c) The following outline summarizes the processes for the various pathways. A single arrow (-) represents a linear process (Eq. 19); a double arrow (\Rightarrow) represents a nonlinear process (Eq. 2).

PATH 1: $\nu_3 \rightarrow \nu_6 \rightarrow \nu_{25} \Rightarrow 2\nu_{25} \rightarrow \nu_{14}$

PATH 2: $\nu_3 \rightarrow \nu_6, \nu_3 \Rightarrow 2\nu_3 \rightarrow \nu_{25}, 2\nu_3 \Rightarrow 3\nu_3 \rightarrow \nu_{14}$

PATH 3: $\nu_3 \rightarrow \nu_6, \nu_3 \Rightarrow 2\nu_3 \rightarrow \nu_{14}$

$2\nu_{25} \Rightarrow \nu_{25}$

(d) d_j is the degree of degeneracy of mode j .

(e) ν_{25} and ν_{14} represent the accidentally degenerate mode pairs ν_2, ν_5 and ν_1, ν_4 respectively.

Figure 1:

Calculated curves for the mode vibrational temperatures (T_j) and translational/rotational temperature (T') of CH_3F at vibration-vibration steady state as a function of absorbed laser energy. Level ν_3 ($v=1$) is pumped and relaxation occurs according to pathway 1 (Eqs. (11) - (14)). The vibrational modes are treated as harmonic oscillators and the translational/rotational energy is taken to be $3kT'$ (equipartition limit) with a variable temperature T' . Vibration-translation/rotation relaxation has been neglected. T_{25} and T_{14} are the vibrational temperatures of the accidentally degenerate mode pairs ν_2, ν_5 and ν_1, ν_4 respectively.

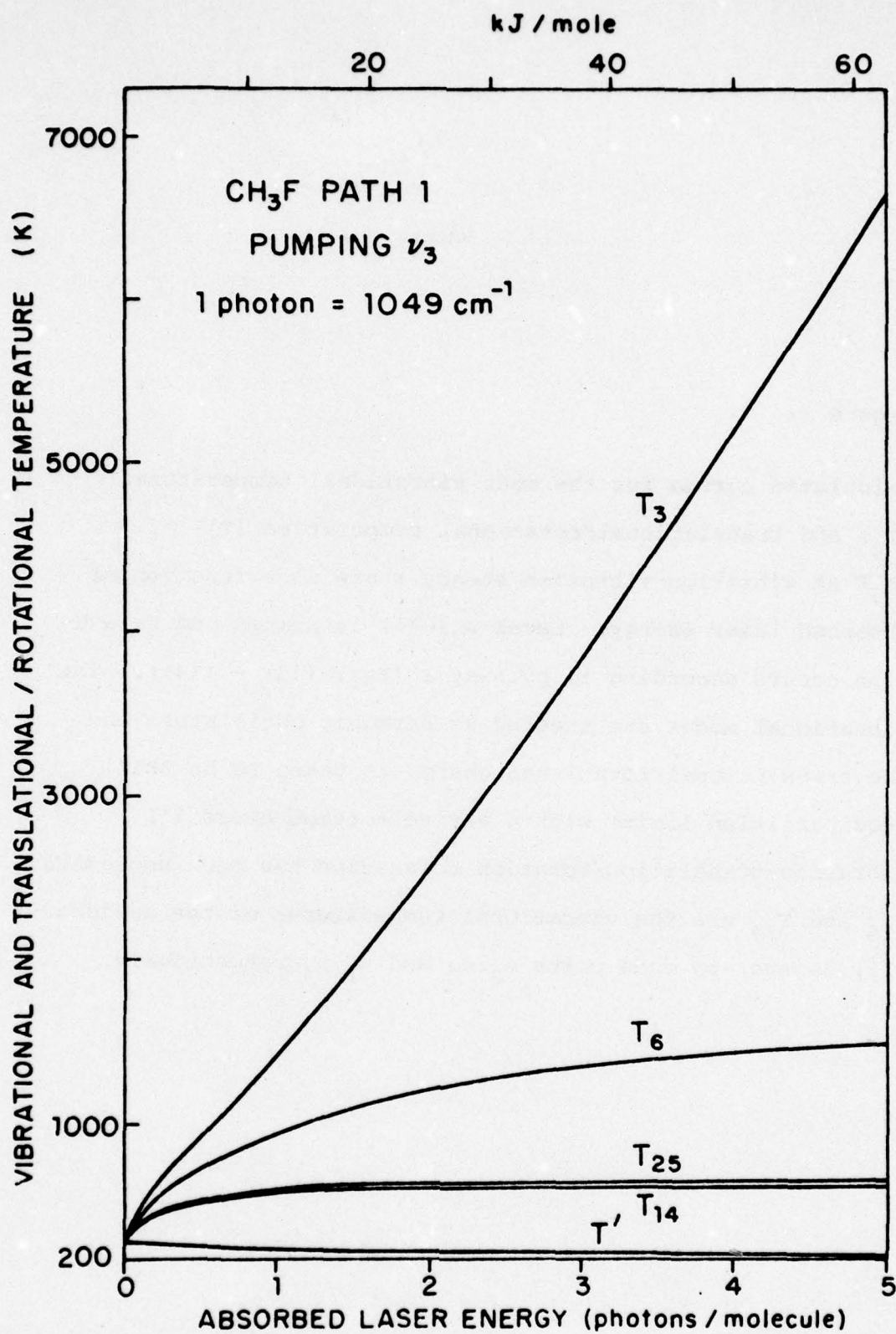


Figure 1

ranging from 0-5 photons absorbed per molecule (each laser photon = 1049 cm^{-1}). The values for the temperatures at an excitation of 2.5 photons per molecule are also listed in row A of Table II. Under ambient conditions where no energy has been added, all the temperatures are at the same ambient value $T = 300^\circ\text{K}$. As the added energy increases the temperatures separate and increase at different rates related to the magnitude of the intermode energy gaps occurring in the crossover reactions (11), (12) and (14). The ordering of the temperatures follows the inverse order of the adjusted energies listed in Table I. T_3 is hottest since ν_3 has the lowest adjusted energy resulting from its endothermic coupling to the remaining modes. Although path 1 retains the actual energy ordering after the adjustment, the energy gap between ν_{25} and ν_{14} is greatly reduced so that their adjusted energies are nearly equal (Table I, sec. A, path 1). Therefore T_{25} and T_{14} remain close to each other in all excitation regimes. The translational/rotational temperature T' falls monotonically with increasing excitation since pumping the lowest adjusted mode guarantees an overall endothermic equilibration pathway. Therefore this path predicts that CH_3F will cool translationally/rotationally during V-V equilibration when pumped at ν_3 . The limiting vibrational temperatures for the higher adjusted modes (ν_{25} , ν_{14} , ν_6) vary linearly with T' , Eq. (7), thus the endothermicity of this path and pumping conditions (decreasing T') facilitate the achievement of the asymptotic limit for T_{14} , T_{25} , and T_6 as seen in Figure 1. The lowest adjusted mode temperature T_3 increases

TABLE II

Mode Vibrational Temperatures (T_j) and Translational/Rotational Temperature (T') in CH_3F for Various Relaxation Pathways (a) and Initial Conditions: Excitation Level (f_p) (b), Excitation Mode (ν_i) and Ambient Temperature (T)

PATH (a)	ν_i	f_p (b)	T	T'	T_3	T_6	T_{25}	T_{14}	REMARKS (c)
A 1	ν_3	2.5	300	226	3182	1286	673	648	cooling
B 1A	ν_3	2.5	300	276	1570	1027	672	2075	$f_p < 1.5$ cooling, $f_p > 1.5$ heating
C 2	ν_3	2.5	300	551	966	891	1431	1005	heating
D 3	ν_3	2.5	300	333	1180	918	1449	1358	$f_p < 0.1$ cooling, $f_p > 0.1$ heating
E 1	ν_6	2.5	300	333	2583	1468	884	856	heating
F 1	ν_6	2.2	300	328	2322	1378	850	823	heating
G 1	ν_{14}	2.5	300	890	2828	2272	1747	1714	heating
H 1	ν_{14}	0.9	300	540	1541	1275	1009	992	heating
I 1A	ν_{14}	2.5	300	209	2267	1076	597	4626	cooling
J 1A	ν_{14}	0.9	300	230	1584	953	593	2277	cooling
K 1	ν_3	2.5	250	192	3407	1183	592	569	cooling
L 1	ν_3	2.5	200	159	3662	1053	504	483	cooling

(a) For the details of the designated paths see Table I, note (c).

(b) f_p is the number of ν_i photons absorbed per molecule.

(c) Translational/Rotational cooling or heating is indicated.

rapidly in this excitation regime since additional input energy remains in the ν_3 mode after T_{14} , T_{25} , and T_6 have reached their limiting values. Thus laser pumping of ν_3 under high excitation conditions sustains the large initial enhancement in ν_3 even at vibrational steady state where the input energy has been partitioned among the modes according to energy transfer path 1. Within the V-V time scale, therefore, these conditions predict a vibrational energy locking into a single vibrational mode. The experimental temperature values are remarkably similar to the distribution of Figure 1 showing relatively little excitation in ν_{14} with about 40-50% of the total energy in ν_3 .⁽²²⁾ In particular at an excitation of about 1.7 photons/molecule a vibrational temperature of 2000°K was observed for the ν_3 mode in excellent agreement with the calculated temperature of ν_3 predicted by path 1 (see Fig. 1). Therefore, all experimental evidence indicates that path 1 is the dominant vibrational energy transfer mechanism for laser pumped CH_3F and that the C-F stretching vibration can be enormously enhanced over the remaining vibrational motions of CH_3F . Relaxation experiments have also shown that the overall V-T/R rate is about three orders of magnitude slower than the V-V equilibration rate,⁽²⁾ further suggesting the possibility of laser induced fluorine extraction or replacement reactions.

As pointed out by Teare and coworkers⁽¹¹⁾ the ultimate temperature attainable by the hot mode in a multiple temperature distribution is limited in a real molecule. Under conditions of high level excitation new collisional and noncollisional relaxation

channels may open up which are unavailable to the relaxing molecules at lower input energies. Such channels will serve to reduce the localization of vibrational energy in any one mode and promote a more thermal distribution of energy. However, the present model emphasizes the effects of the intermode energy gaps under conditions of moderate excitation (up to 5 photons per molecule for CH_3F). Within its limitations the model can provide an approximate description which will indicate the temperature distribution given the pathway and initial conditions. For the case of laser pumped CH_3F the agreement with experiment has been highly satisfactory at least for input energies up to 2.5 photons per molecule.⁽²²⁾ Conversely, vibrational temperature measurements can serve as a probe to monitor vibrational relaxation mechanisms in all excitation regimes. At low excitation such measurements identify the energy transfer path among the low lying vibrational states. Measurements of the relative vibrational temperatures as a function of input energy can indicate at what excitation level the low energy pathway description becomes inadequate as new excitation and relaxation channels open up.

Conclusions:

1) A formalism has been developed for describing the steady state vibrational energy and population distributions of laser pumped polyatomic gases. The formalism, valid on a time scale where collisional intermode energy transfer is fast while vibration-translation/rotation transfer is slow, assumes that a pulsed laser pumps a fundamental vibrational state.

2) The vibrational state population distribution is found to be a sensitive function of the intermode vibrational energy transfer mechanism or pathway. Thus measurements of steady state populations can conversely be used to determine energy transfer mechanisms.

3) The steady state differs significantly from that predicted for a Boltzmann distribution with equivalent total energy.

a) Localization of energy in one vibrational mode can occur, a condition which depends strictly on the energy transfer path. The mode which exhibits the enhanced excitation need not be the one with the lowest vibrational frequency.

b) Energy saturation (a condition in which the energy of a mode does not increase with increasing pump power) can arise for some modes, placing an upper limit on the total energy which can reside in these modes at steady state.

4) The steady state distribution is also dependent on the identity of the vibrational level initially pumped.

a) To obtain maximum energy enhancement of a nonsaturating mode, it should be pumped directly.

b) Weaker enhancement or localization in the nonsaturating mode will occur if a saturating mode is pumped. The vibrational enhancement of a saturating mode is not improved much if it is directly pumped.

5) Large steady state population inversions between vibrational modes can occur with minimal laser pump energy.

6) The formalism has been used to describe the energy distribution of laser pumped CH_3F . The agreement between the calculated and observed steady state distributions is excellent.

7) Because of the sensitivity of the distribution to the energy transfer pathway, experimental measurements of vibrational populations can serve as a diagnostic tool to probe for changes in the energy transfer mechanism as a function of laser pump power. This may prove to be a sensitive probe for collision free energy transfer channels.

8) The formalism used employs the harmonic oscillator approximation and hence emphasizes the effects of vibrational relaxation on the steady state caused by the intermode energy gaps. The time scale for validity of this model is one long compared to intermode vibrational energy exchange, but short compared to overall vibration-translation/rotation relaxation.

* This work was also supported by the National Science Foundation under Grant NSF-CHE76-04118.

- (1) P. Hess and C. B. Moore, J. Chem. Phys. 65, 2339 (1976).
- (2) E. Weitz and G. W. Flynn, Ann. Rev. Phys. Chem. 25, 275 (1974).
- (3) W. D. Breshears and L. S. Blair, J. Chem. Phys. 59, 5824 (1973); W. D. Breshears, Chem. Phys. Lett. 20, 429 (1973).
- (4) R. K. Huddleston and E. Weitz, J. Chem. Phys. 66, 1740 (1977).
- (5) D. R. Siebert and G. W. Flynn, J. Chem. Phys. 62, 1212 (1975).
- (6) I. Procaccia and R. D. Levine, J. Chem. Phys. 63, 4261 (1975); R. D. Levine and A. Ben-Shaul in Chemical and Biochemical Applications of Lasers, edited by C. B. Moore (Academic Press, New York, 1977) in press.
- (7) I. Shamah and G. W. Flynn, J. Am. Chem. Soc. 99, 3191 (1977).

- (8) S. Mukamel and J. Ross, J. Chem. Phys. 66, 5235 (1977).
- (9) D. I. Rosen and T. A. Cool, J. Chem. Phys. 62, 466 (1975);
K. Hui and T. A. Cool, J. Chem. Phys. 65, 3536 (1976).
- (10) K. Casleton and G. W. Flynn, J. Chem. Phys. 67, 0000 (1977);
K. Casleton and G. W. Flynn, "Rates and Mechanisms for
Intermode Energy Transfer in COF₂", (work in progress).
- (11) J. D. Teare, Seventh AGARD Colloquim, Oslo, 1966; J. D. Teare,
Semi-Annual Program Progress Report Re-entry Physics (REP)
Program, Avco Everett Research Laboratory, 1966; J. D. Teare,
R. L. Taylor, and R. L. Von Rosenberg jun., Nature 255, 240
(1970).
- (12) C. E. Treanor, J. W. Rich and R. G. Rehm, J. Chem. Phys. 48,
1798 (1968).
- (13) I. Shamah, Ph.D. Thesis, Department of Chemistry, Columbia
University, New York, NY, 1978. This reference is also
available from University Microfilms, Ann Arbor, MI.
- (14) A. W. Overhauser, Phys. Rev. 92, 411 (1953).
- (15) F. R. Grabiner, D. R. Siebert, and G. W. Flynn, Chem. Phys.
Lett. 17, 189 (1972).
- (16) I. Shamah and G. W. Flynn, "Laser Catalyzed Translational to
Vibrational Energy Conversion in CH₃F-O₂ Mixtures", J. Chem.
Phys. (submitted for publication).
- (17) E. Weitz and G. W. Flynn, J. Chem. Phys. 58, 2781 (1973).
- (18) F. R. Grabiner, G. W. Flynn, and A. M. Ronn, J. Chem. Phys.
59, 2330 (1973).
- (19) J. M. Preses, Ph.D. Thesis, Department of Chemistry, Columbia
University, New York, NY, 1975. This reference is available
from University Microfilms, Ann Arbor, MI.
- (20) J. Preses, G. W. Flynn, and E. Weitz, "Laser Fluorescence
Study of Vibrational Energy Equilibration in CH₃F:O₂ Mixtures:
Impurity Molecules as Probes of Mode to Mode Energy Flow
Pathways", (submitted for publication).
- (21) R. S. Sheory, R. C. Slater, and G. W. Flynn, "Overtone
Fluorescence as a Probe of Intermode Energy Flow in Laser
Pumped Molecules", J. Chem. Phys. (submitted for publication).
- (22) R. E. McNair, B. J. Feldman, M. S. Feld and G. W. Flynn,
Chem. Phys. Lett. 48, 241 (1977).

2. Steady State Population Inversions in Laser Pumped Polyatomic Molecules*

(I. Shamah, G. W. Flynn)

Introduction:

The vibrational relaxation of a laser pumped gas following a restricted energy transfer mechanism has been shown to lead to a non-Boltzmann, selective, metastable equilibrium.⁽¹⁾⁽²⁾ Here two further aspects of this unusual relaxation and steady state will be explored. Considering molecules whose vibrational modes behave as harmonic oscillators each mode will be at its own characteristic steady state temperature. The population of every level within the mode manifold will be fixed by the mode temperature. Some modes will be at a relatively high steady state temperature reflecting a large population enhancement of the mode's constituent levels. Therefore, upper levels of a hot mode may be inverted with respect to lower levels of a colder mode. Here the exact conditions for a population inversion at vibrational steady state are discussed. Excitation thresholds for the inversions for a given energy transfer mechanism are described. Effects of a varying ambient temperature and an explanation of state population maxima at V-V equilibrium are also provided. Such calculations are illustrated for a transition of CH_3F pumped at ν_3 .

Discussion:

Figure 1 shows the temperature distribution as a function of excitation for CH_3F undergoing path 1 (Eqs. (11) - (14)). The vibrational temperature of ν_3 was found to be enhanced relative to the remaining modes and the enhancement grew rapidly with

excitation. Since all the levels within the ν_3 manifold are at the same temperature, inversions may be expected between overtones in ν_3 and lower states in a colder mode. As an illustration, consider the states $2\nu_3$ and ν_2 . At a Boltzmann equilibrium at 300°K $N_{\nu_2}/N_{2\nu_3} = 21.0$ with a total population between the levels of 0.09% of the total molecules. Using the temperature of Figure 1 the steady population of $2\nu_3$ and ν_2 were calculated and are plotted in Fig. 2 as a function of excitation. The onset of inversion occurs at an excitation of 315 cm^{-1} (0.3 photons) per molecule with a ν_3 temperature of 716°K. Since path 1 produces translational/rotational cooling when CH_3F is pumped at ν_3 , the path temperature T' is reduced to 283°K at the threshold excitation. The inversion grows continuously with excitation since ν_2 reaches a maximum much earlier than $2\nu_3$ and decreases with excitation more rapidly than $2\nu_3$. In particular, $N_{2\nu_3}/N_{\nu_2} = 8.05$, and $N_{2\nu_3} + N_{\nu_2} = 7.78\%$ of the total number of molecules, at an excitation of 2.22 photons per molecules where $2\nu_3$ has its maximum population. CH_3F has been observed experimentally to absorb about 2.5 photons/molecule. (1)

Not every state in a hot mode can be inverted with respect to a lower state in a colder mode. Vibrational state populations are not simply increasing functions of the excitation. The populations are limited in number as can be seen by Fig. 2. Therefore, other features must control the possibility for steady state inversions.

Conclusions:

The multiple temperature distribution resulting from vibrational relaxation leads to a selective, non-Boltzmann population

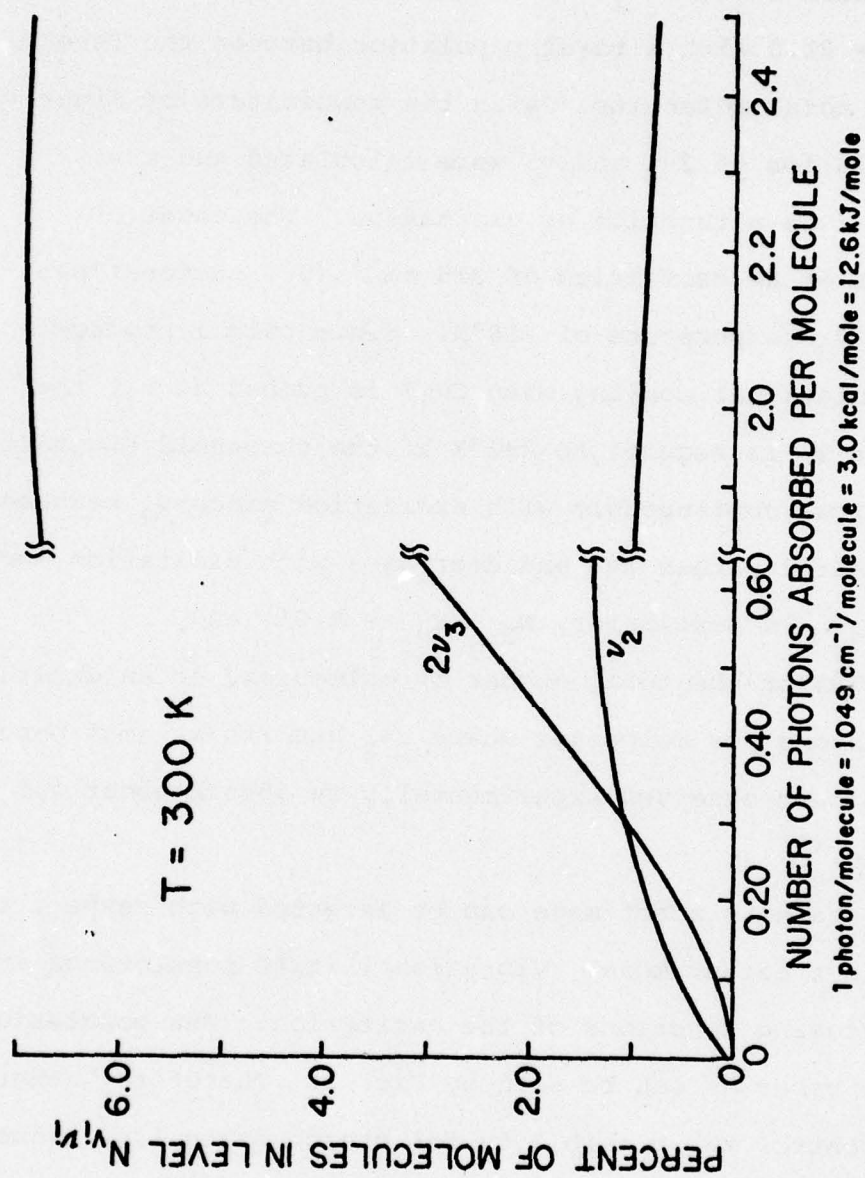


Figure 2:

Percent of molecules calculated to be in levels $2v_3$ and v_2 in CH_3F at vibrational steady state as a function of absorbed laser energy. The calculations were based on the temperature distribution of Fig. 1 which assumed an ambient temperature of 300°K .

distribution at steady state, creating the possibility for population inversions.

- a) Upper states in a hot mode will be inverted with respect to lower states in a colder mode.
- b) Excitation thresholds for inversions may be calculated given the energy transfer processes linking the two states and the translational/rotational temperature T' . The threshold is a monotonically increasing function of T' and consequently the ambient temperature. In particular if both states are of equal degeneracy the threshold varies linearly with T' .
- c) Steady state population calculations show that the $2\nu_3$ level in CH_3F will invert with respect to the ν_2 level with a threshold for inversion of 0.3 photons absorbed per molecule at an ambient temperature of 300°K . The inversion reaches a $2\nu_3$ to ν_2 ratio of about 8, with 8% of the total molecules residing in these two levels, at 2.22 photons absorbed per molecule. The threshold is reduced to 0.09 photons absorbed per molecule at 200°K ambient temperature.

* This work was also supported by the National Science Foundation under Grant NSF-CHE76-04118.

- (1) R. E. McNair, B. J. Feldman, M. S. Feld and G. W. Flynn, Chem. Phys. Lett. 48, 241 (1977).
- (2) I. Shamah, Ph.D. Thesis, Department of Chemistry, Columbia University, New York, NY, 1978. This reference is available from University Microfilms, Ann Arbor, MI.

3. Some Energy Transfer Parameters for Laser Driven Chemical Reactions in CF_3Cl^*

(J. K. McVey, G. W. Flynn)

Introduction:

Recent interest in the infrared induced chemistry of halogenated hydrocarbons dates from preliminary reports of Grunwald.⁽¹⁾ Following absorption of many photons by molecules such as CF_3Cl and CCl_3F the observed chemistry is found to be efficient and reactions similar to those encountered in simple bulk heating experiments are observed. Many additional studies have probed the reactivity of other freon molecules in both the collisional and collisionless region. At sample pressures of less than 10^{-3} torr, molecular beam studies have shown that the laser driven reaction process favored is generally that of the lowest energy channel,⁽²⁾ that preferred in thermal reactions. This regime is amenable to detailed examination and several groups have considered the deposition of excess energy, following the unimolecular reaction, into the vibrational, rotational and translational modes of the products.⁽³⁾ Of central concern is the process by which energy flows between the many vibrational levels that exist in the ground electronic states at excitation levels approaching the energy of bond dissociation. One early interpretation⁽¹⁾⁽⁴⁾ of the results involving IR photon excited CF_3Cl and CCl_3F suggested that energy was being retained in the pumped C-F vibrational manifold for times longer than that required for bond cleavage. In the absence of any direct measurements of rates of vibration-to-vibration (V-V) and vibration to rotation/translation (V-T/R) collision induced

energy transfer several theories were proposed. It is therefore important that we consider the case of IR laser induced chemistry in the collisional regime (2 to 60 torr sample pressures) and address the question of timescales of excitation, energy transfer, and reactivity in freons.

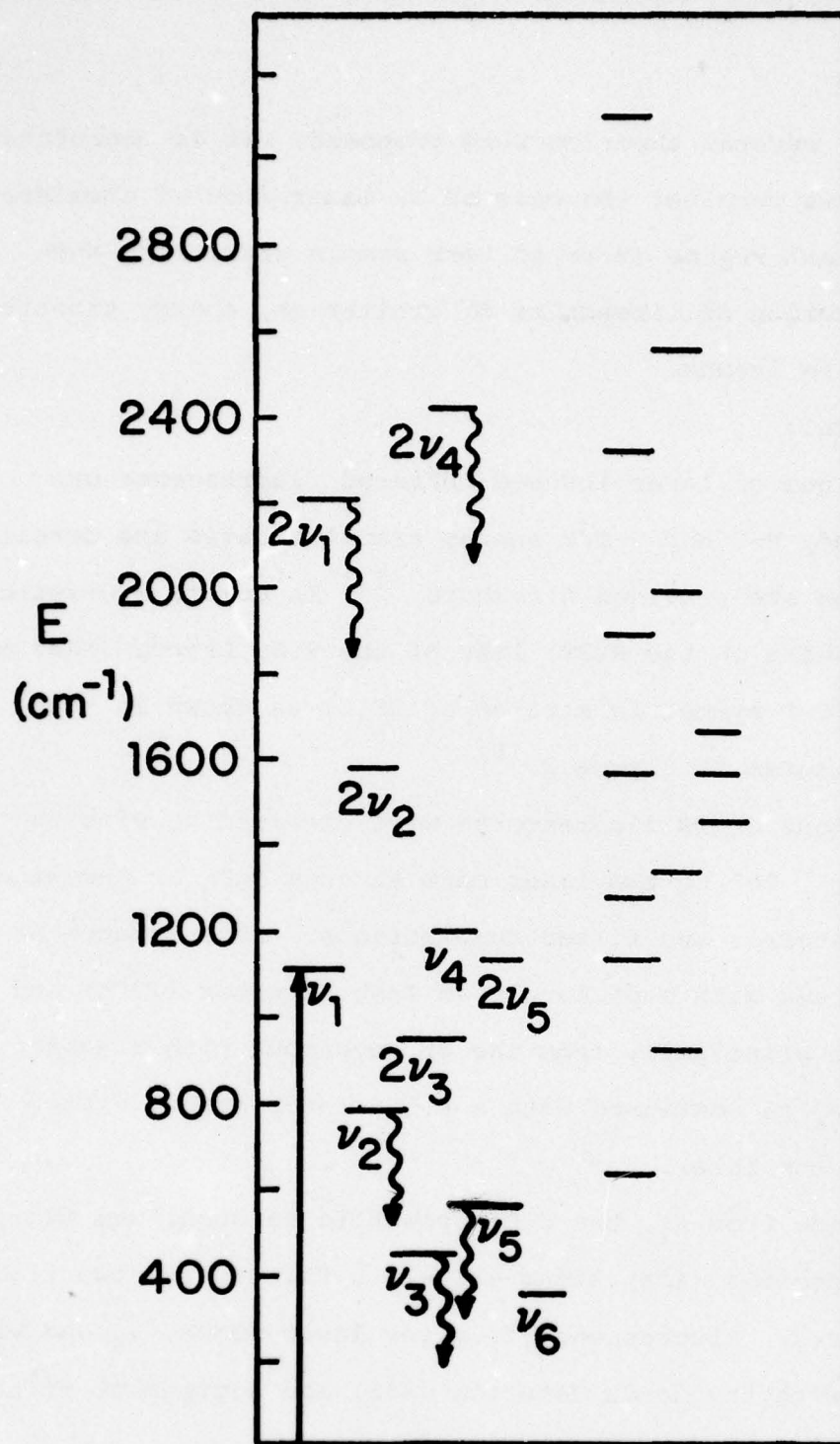
Experimental:

The technique of laser induced infrared fluorescence was employed to study V-V and V-T/R energy transfer rates and details of the apparatus are provided elsewhere.⁽⁵⁾ In brief, a Q-switched CO₂ laser operating on the R(28) line of the 9.6 μ branch (1083 cm⁻¹) excites the ν_1 C-F symmetric stretch of CF₃Cl as shown in the energy level diagram in Figure 3.⁽⁶⁾

Three regions of IR fluorescence were examined by viewing the emission at 90° to the laser beam through MgF₂ or KBr windows with several detector and filter combinations. Fluorescence at 4.5 μ was observed with a photovoltaic InSb detector (77°K) and was found to be principally from the 2 ν_1 overtone with a small component of 2 ν_4 as confirmed with a 4.5 μ interference filter which excludes the later.

Fluorescence from ν_2 , the C-Cl symmetric stretch, was examined with a Ge:Cu detector (4°K) using a 10-14 μ filter with two 11.3 μ long pass filters. Fluorescence from the lower modes, ν_5 and ν_3 , was monitored with the Ge:Cu detector (4°K) and a group of filters giving a 14 to 22 μ bandpass.

Thermal lensing studies were performed to explore the path of the V-V processes and measure overall V-V and V-T/R relaxation



CF_3Cl

Figure 3

rates. The apparatus is described elsewhere⁽⁷⁾ and basically measures the magnitude and rate at which vibrational energy is degraded collisionally to translational energy by measuring small changes in the index of refraction of the gas.

Results:

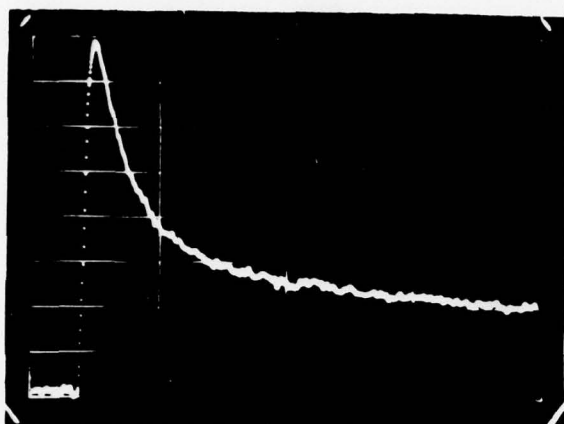
In Figure 4 fluorescence emission from ν_2 is shown following excitation of ν_1 . It is immediately apparent that even at lower pressures (3 torr) of CF_3Cl , the filling process is rapid as shown in the risetime of $\sim 1 \mu\text{sec}$. Collisional quenching studies as a function of CF_3Cl pressure (self-quenching) and other quenchers (Ar, Kr) were performed to extract V-V and V-T/R relaxation rates from the fluorescence decay curves. Plots of \ln (Intensity) versus time were constructed and the slopes provide rates at a given sample pressure. Stern-Vollmer plots of rate vs pressure provide the desired rate constants, in units of $\text{msec}^{-1} \text{ torr}^{-1}$.

Figure 5 illustrates how the heavier rare gas collision partners can be employed to preferentially quench various relaxation pathways. What appears to be a single exponential decay in Figure 5 with 2 torr CF_3Cl 'breaks' into a fast and slow component with the addition of 35 torr of krypton. Values of the rate constants for collisional quenching of $2\nu_1$, $2\nu_4$ levels, the ν_2 level, and the ν_3 , ν_5 levels are presented in Table III. Thermal lensing studies provide direct measurements of V-T/R rates. In Figure 6 thermal lensing signals of CF_3Cl are displayed and values are also given in Table III.

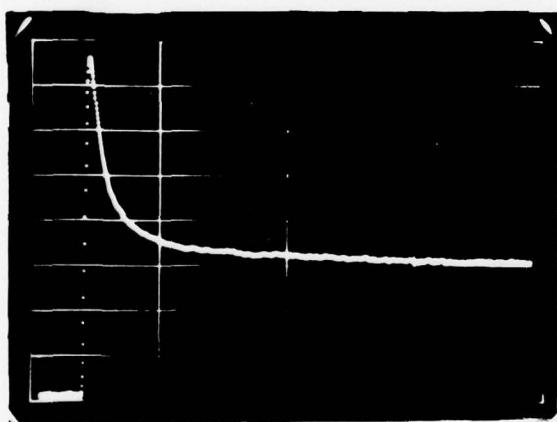
IR FLUORESCENCE CF_3Cl

102.4 μsec full scale

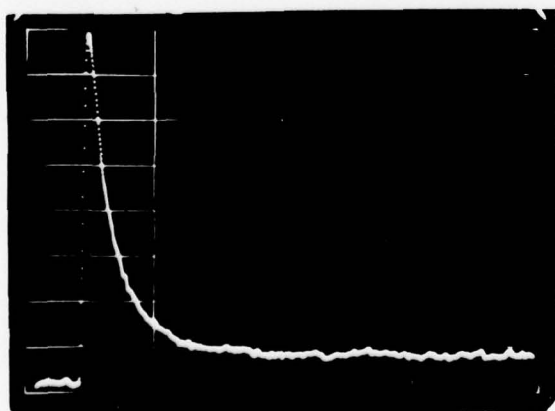
ν_2



3.082 t CF_3Cl



15.09 t CF_3Cl



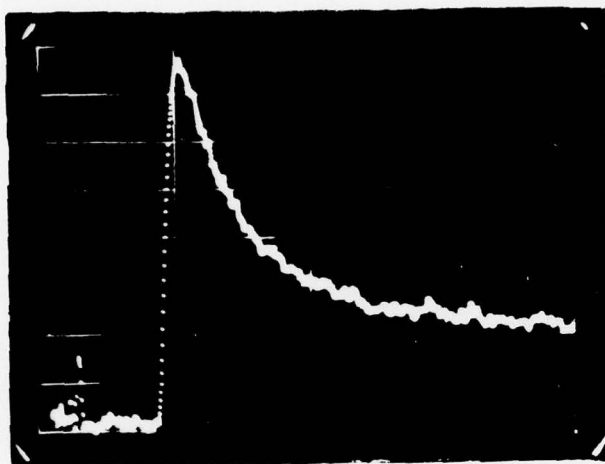
3.082 t CF_3Cl
+ 49.18 t ARGON

Figure 4

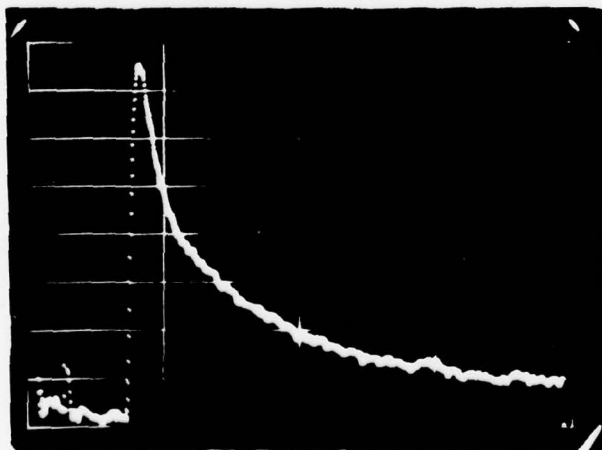
IR FLUORESCENCE CF_3Cl

102.4 μsec full scale

ν_2



2.002 torr CF_3Cl



2.002 \dagger CF_3Cl
+ 35.168 \dagger KRYPTON

Figure 5

Table III

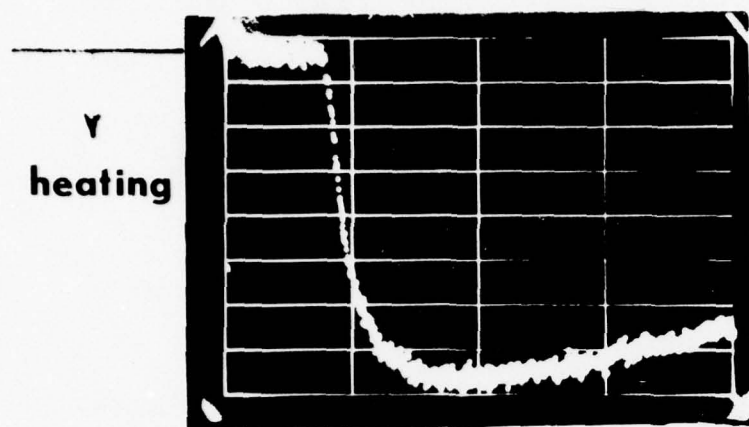
CF₃Cl COLLISIONAL QUENCHING
RATE CONSTANTS
(msec⁻¹ torr⁻¹)

	Self- Quenching	Argon Quenching	Krypton Quenching
$2\nu_1, 2\nu_4$	60 ± 10 7.5 ± 2.5* (rise>350)	11.3 ± 1.5 2.3 ± 0.3	
ν_2	65 ± 10 15 ± 1.5 =5 (rise=350)	22 ± 5 5.4 ± 0.5	7.5 ± 2.0 = 0
ν_3, ν_5	45 ± 10 12 ± 4 (rise=90 ± 20)		
Thermal Lensing	6.0 ± 2	2.0 ± 0.5	

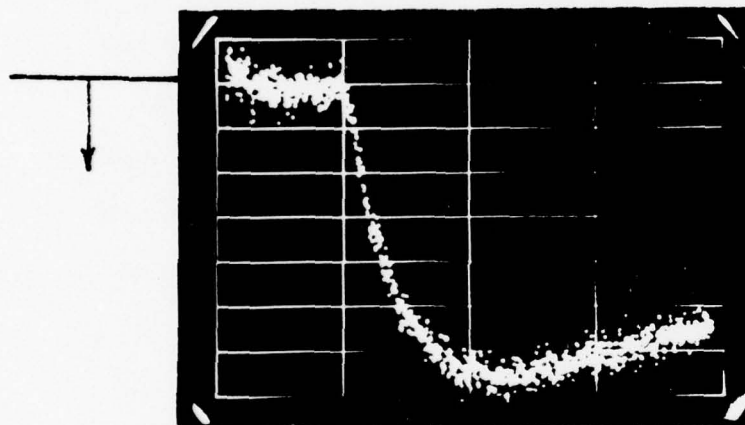
* probable sum of two exponentials as indicated by intercept data in argon quenching experiments.

THERMAL LENSING

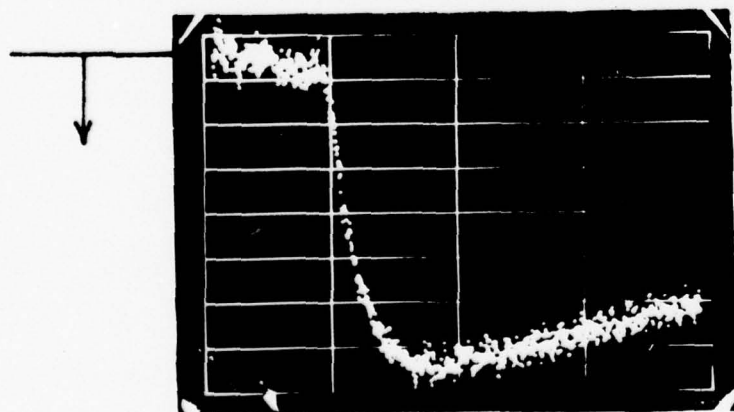
204.8 μ sec FULL SCALE



10.032 t CF_3Cl



4.200 t CF_3Cl

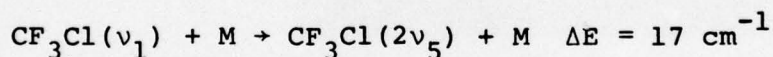


4.200 t CF_3Cl
+ 17.340 t ARGON

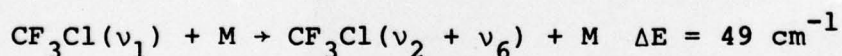
Figure 6

Discussion:

Analysis of the rise and falltimes of emission from the various energy levels of CF_3Cl immediately suggests a rapid collision induced redistribution of energy from the pumped mode to the remaining vibrational modes. The filling rate of the ν_2 and ν_3 modes is given by the measured rate constant of $\approx 350 \text{ msec}^{-1} \text{ torr}^{-1}$, and at 60 torr this corresponds to approximately 50 nsec. In the experiments of Grunwald,⁽¹⁾ also at pressures of 60 torr with laser pulsewidths of 200 nsec, it seems likely that the pumped mode (C-F stretch, ν_1) is not efficiently locking-in energy and that transfer to other modes is efficient and rapid during the laser pulse. CF_3Cl , in fact, appears to be an excellent species in which to demonstrate rapid equilibration of the vibrational modes. Referring to Figure 3, the laser pumps into the low energy end of the ν_1 mode at 1083 cm^{-1} . The $2\nu_5$ level at 1100 cm^{-1} and the $\nu_2 + \nu_6$ level at 1132 cm^{-1} are nearby and collisions of the type



and



would permit efficient transfer of energy from the pumped mode. The energy defect would be taken from the translational energies of CF_3Cl or the collision partner M. Also, since the ν_1 mode and ν_2 are of the same symmetry class (A_1), Fermi coupling⁽⁸⁾ between

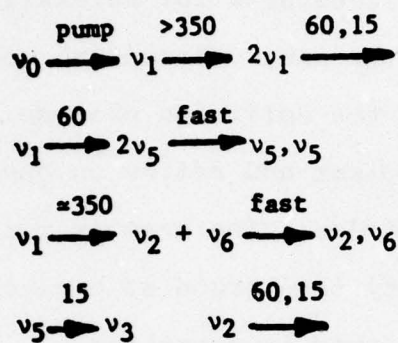
v_1 and $v_2 + v_6$ may result in the more rapid rate for filling of $v_2 + v_6$ ($350 \text{ msec}^{-1} \text{ torr}^{-1}$) versus the $2v_5$ filling ($\sim 60 \text{ ms}^{-1} \text{ torr}^{-1}$). The proposed scheme for energy transfer is given in Table IV.

The efficiencies of various collision partners in the relaxation processes is also given in Table III. Self quenching is most efficient (fastest rate constants for relaxation) and this is reasonable in light of the many vibrational modes that can transfer or accept energy in the collision process. Quenching with rare gases is less efficient and relies on energy transfer to and from the translational modes. The heavier rare gas, krypton, has a slower average velocity than argon at a given temperature and is less efficient than argon in quenching.

The overall deposition of energy from vibrational to translational energies as measured with the thermal lensing apparatus has a rate constant of $6 \text{ ms}^{-1} \text{ torr}^{-1} \text{ CF}_3\text{Cl}$. At 60 torr CF_3Cl the timescale for V-T/R relaxation is $\sim 3 \text{ } \mu\text{sec}$ and the rate of thermal diffusion with its inverse pressure dependence is approximately a factor of 1000 slower. This would suggest that there is rapid (μsec) deposition of energy to thermal heating following IR laser excitation and that the slower thermal diffusion allows for trapping of this 'heat' in a small volume element resulting in elevated temperatures. We must recall that Grunwald's studies gave thermal reaction products at high efficiencies, the later descriptive of elevated temperatures ($\sim 1000^\circ\text{C}$) in the reaction cell. Furthermore in studies of other freons,⁽⁹⁾ it was found that

Table IV

RATE CONSTANTS ($\text{msec}^{-1} \text{ torr}^{-1}$)
 CF_3Cl



$$V \rightarrow T/R \approx 6$$

RATE ($\text{ms}^{-1} \text{ torr}^{-1}$)	350	100	60	15	6
GAS KINETIC RATE (# Collisions)	28	100	167	667	1667

the IR pumping of either of two absorbing modes led to equivalent chemistry. The results tend to indicate a rapid randomization of energy from the pumped C-F mode to other modes. Much of the chemistry may in fact be basically thermal in nature at these pressures (10 to 60 torr CF_3Cl) and similar to chemistry at a higher effective cell temperature, i.e. laser induced pyrolysis. The results also tend to illuminate the number of theoretical models recently presented to explain the observed chemistry.⁽¹⁰⁾⁽¹¹⁾ It appears that the single oscillator model (C-F mode highly excited only) is probably inappropriate. The fast V-T/R rate and slow diffusion rate would tend to favor a thermal mechanism,⁽¹⁰⁾ although a steady-state approach⁽¹²⁾ (vibrations equilibrated but not translational modes) may play a role in the overall chemistry. It is important to appreciate, however, that even at high pressures (10-60 torr) the initial stages of a TEA CO_2 laser pulse can induce multiphoton, collision free dissociation. Thus a combination of effects is likely to be important in explaining laser chemistry results on CF_3Cl .

* This work was also supported by the National Science Foundation under Grant NSF-CHE76-04118.

- (1) D. F. Dever and E. Grunwald, J. Amer. Chem. Soc. 98, 5055 (1976).
- (2) A. S. Sudbo, P. A. Schulz, E. R. Grant, Y. R. Shen, and Y. T. Lee, J. Chem. Phys. 68, 1306 (1978).
- (3) D. S. King and J. C. Stephenson, Chem. Phys. Lett. 51, 48 (1977).
- (4) E. Grunwald, K. J. Olszyna, D. F. Dever, and B. Knishkowsky, J. Amer. Chem. Soc. 99, 6515 (1977).

- (5) R. D. Bates, Jr., G. W. Flynn, J. T. Knudtson, and A. M. Ronn, J. Chem. Phys. 53, 3621 (1970).
- (6) W. G. Golden, D. A. Horner, and J. Overend, J. Chem. Phys. 68, 964 (1978).
- (7) D. R. Siebert, F. R. Grabiner, and G. W. Flynn, J. Chem. Phys. 60, 1564 (1974).
- (8) G. Heryberg, Molecular Spectra and Molecular Structure II, D. Van Nostrand, Princeton, NJ (1945). p. 214.
- (9) G. A. Hill, E. Grunwald, and P. Keehn, J. Amer. Chem. Soc. 99, 6521 (1977).
- (10) I. Oref and B. S. Rabinovitch, J. Phys. Chem. 81, 2587 (1977).
- (11) S. Mukamel and J. Ross, J. Chem. Phys. 66, 5235 (1977).
- (12) I. Shamah and G. W. Flynn, J. Amer. Chem. Soc. 99, 3191 (1977).

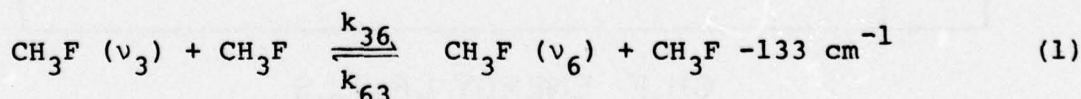
B. LASER STUDIES OF INTERMODE ENERGY TRANSFER EVENTS IN SMALL MOLECULES

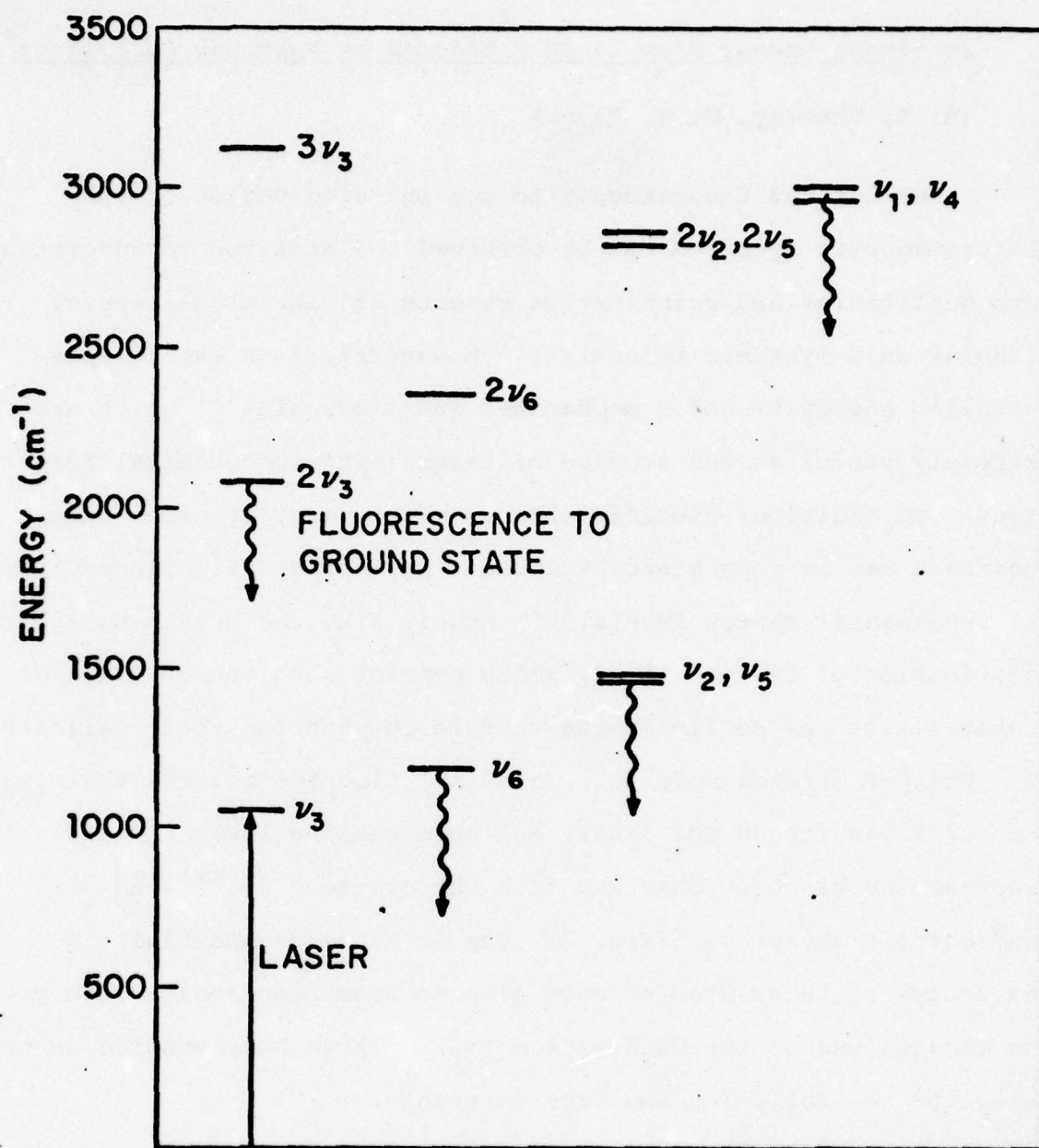
1. Intermode Energy Flow in CH₃F Induced by Rare Gas Collisions*

(R. S. Sheorey, G. W. Flynn)

Laser induced fluorescence in the infrared region of the electromagnetic spectrum can be observed and analyzed to understand both qualitative and quantitative aspects of vibrational energy transfer in polyatomic molecules. In general, such experiments establish energy transfer mechanisms and timescales⁽¹⁾ which are extremely useful in the studies of laser initiated chemical reactions. In addition, specific mode to mode energy transfer rate constants can be determined by monitoring infrared fluorescence from all fundamental energy levels.⁽²⁾ Models like the breathing sphere modification of the SSH theory which predict such energy transfer probabilities per collision can thus be checked for their validity.

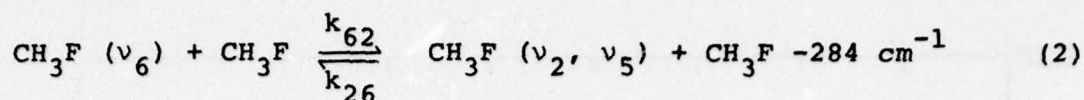
The C-F stretch mode (ν_3) in methyl fluoride absorbs the P₍₂₀₎ line of a Q-switched CO₂ laser, and upon pumping laser induced fluorescence has been observed from the overtone $2\nu_3$ ⁽¹⁾ and all fundamentals except ν_3 . (Fig. 7) The multiple exponential rises and decays of these fluorescence signals have been analyzed to yield the eigenvalues of the CH₃F rate matrix. These have enabled us to determine the following two rate constants.





CH_3F ENERGY LEVELS

Figure 7



Because the Q-switched CO_2 laser puts out very weak pulses, the vibrational temperature does not vary significantly from the translational temperature during the experiment. It is then reasonable to assume that population deviations can be described by simple Boltzmann statistics. Together the ν_3 , ν_6 and ν_2 , ν_5 levels have a 99% share of total vibrationally excited CH_3F population. Therefore, processes coupling these three low lying levels to the others simply do not contribute significantly to the CH_3F rate matrix. It is thus possible to obtain the two rate constants of processes (1) and (2) from a measurement of the two eigenvalues of the linearly coupled ν_3 , ν_6 and (ν_2, ν_5) states which form a three level system.

The decay of $2\nu_3$ fluorescence yields the eigenvalues $596 \pm 48 \text{ msec}^{-1} \text{ torr}^{-1}$ and $198 \pm 43 \text{ msec}^{-1} \text{ torr}^{-1}$ (Fig. 8) and the rise of ν_6 and ν_2 , ν_5 fluorescences yield $609 \pm 68 \text{ msec}^{-1} \text{ torr}^{-1}$ and $192 \pm 41 \text{ msec}^{-1} \text{ torr}^{-1}$ where the error limits indicate two standard deviations. The three level system described by processes (1) and (2) yields the two eigenvalues

$$2 r_{\pm} = -b \pm (b^2 - 4c)^{1/2}$$

where

$$b = (1.95 k_{36} + 3.615 k_{62}) \quad \text{and}$$

$$c = 6.09 k_{36} k_{62}.$$

The values for k_{36} and k_{62} are then found to be:

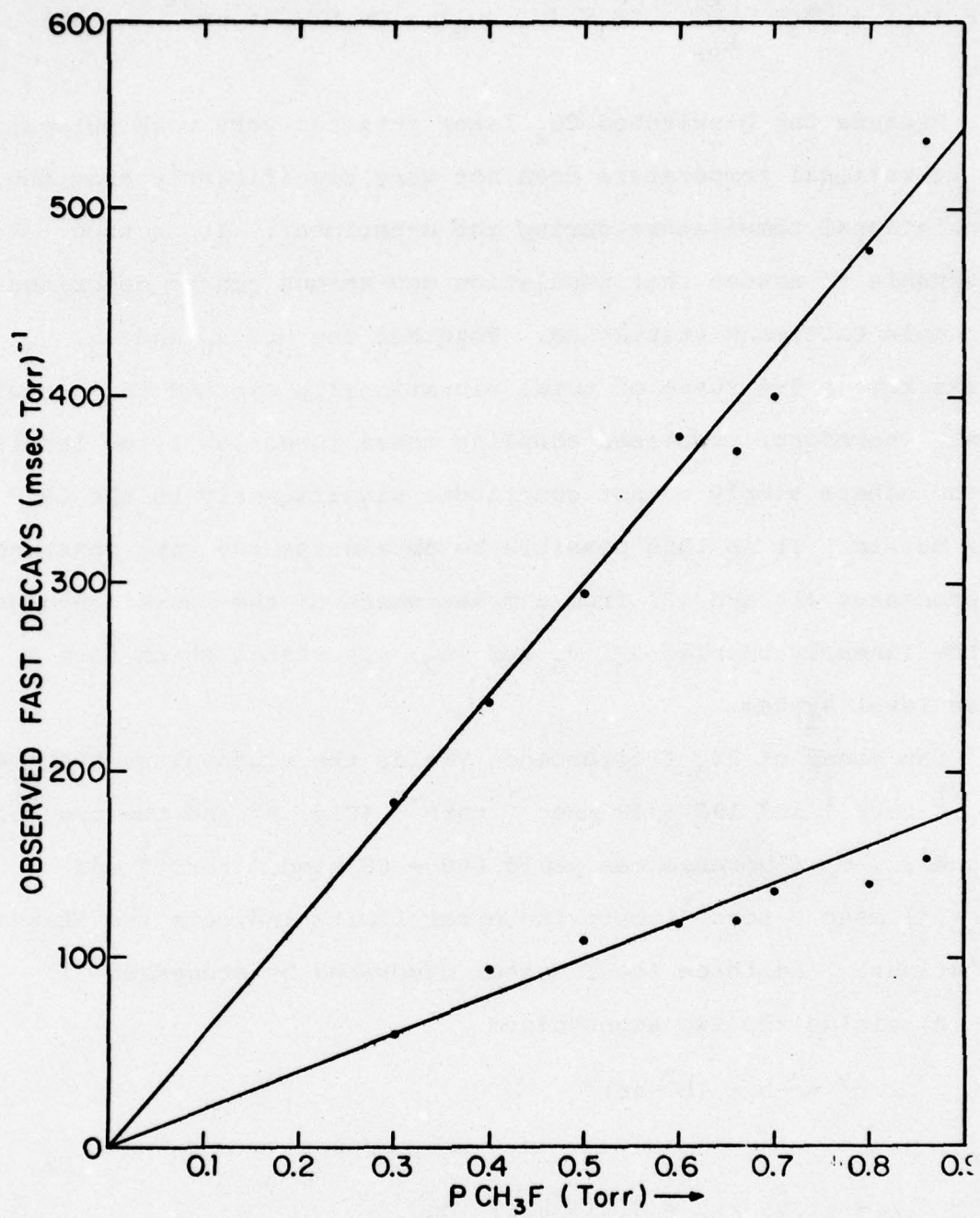


Figure 8

$$k_{36} = 285 \pm 25 \text{ (msec torr)}^{-1}$$

$$k_{62} = 65 \pm 14 \text{ (msec torr)}^{-1}$$

Using a CH_3F gas kinetic collision rate of $8.5 \times 10^6 \text{ sec}^{-1} \text{ torr}^{-1}$, the rate constants k_{36} and k_{62} yield the probabilities $p_{36} = 0.033$ (30 collisions) for $\nu_3 \rightarrow \nu_6$ transfer and $p_{62} = 0.076$ (130 collisions) for $\nu_6 \rightarrow \nu_2, \nu_5$ transfer. These values appear as dotted lines in Fig. 9 where calculated probabilities using the breathing sphere model⁽³⁾⁻⁽⁶⁾ are also presented as a function of $\alpha (\text{cm}^{-1})$ the range parameter for the spherically symmetric intermolecular potential. Specifically, the probabilities were calculated as outlined in Ref. 3 with breathing sphere amplitude factors in Ref. 7. Since the breathing sphere model assumes that the vibrational motion of the surface atoms is in the direction of the collision, the calculated probabilities are expected to be too large. As is apparent in Fig. 9, although the calculated probabilities are indeed too large for the $\nu_6 \rightarrow \nu_2, \nu_5$ V-V energy transfer process, they are actually smaller than the experimental probability for the process $\nu_3 \rightarrow \nu_6$ for all reasonable α values. This suggests that the prescription for obtaining vibrational matrix elements (breathing sphere amplitudes) is not particularly reliable in predicting relative intermode transition probabilities, or that a spherically symmetric potential simply cannot describe such a complex collision event.

Intermode energy transfer probabilities have also been measured for CH_3F - rare gas collisions. The rare gases which were used in these experiments were ^3He , ^4He , He, Ar & Xe. The measured rates were plotted versus the corresponding rare gas pressure. In all cases the dependence was linear with the rate at zero rare gas

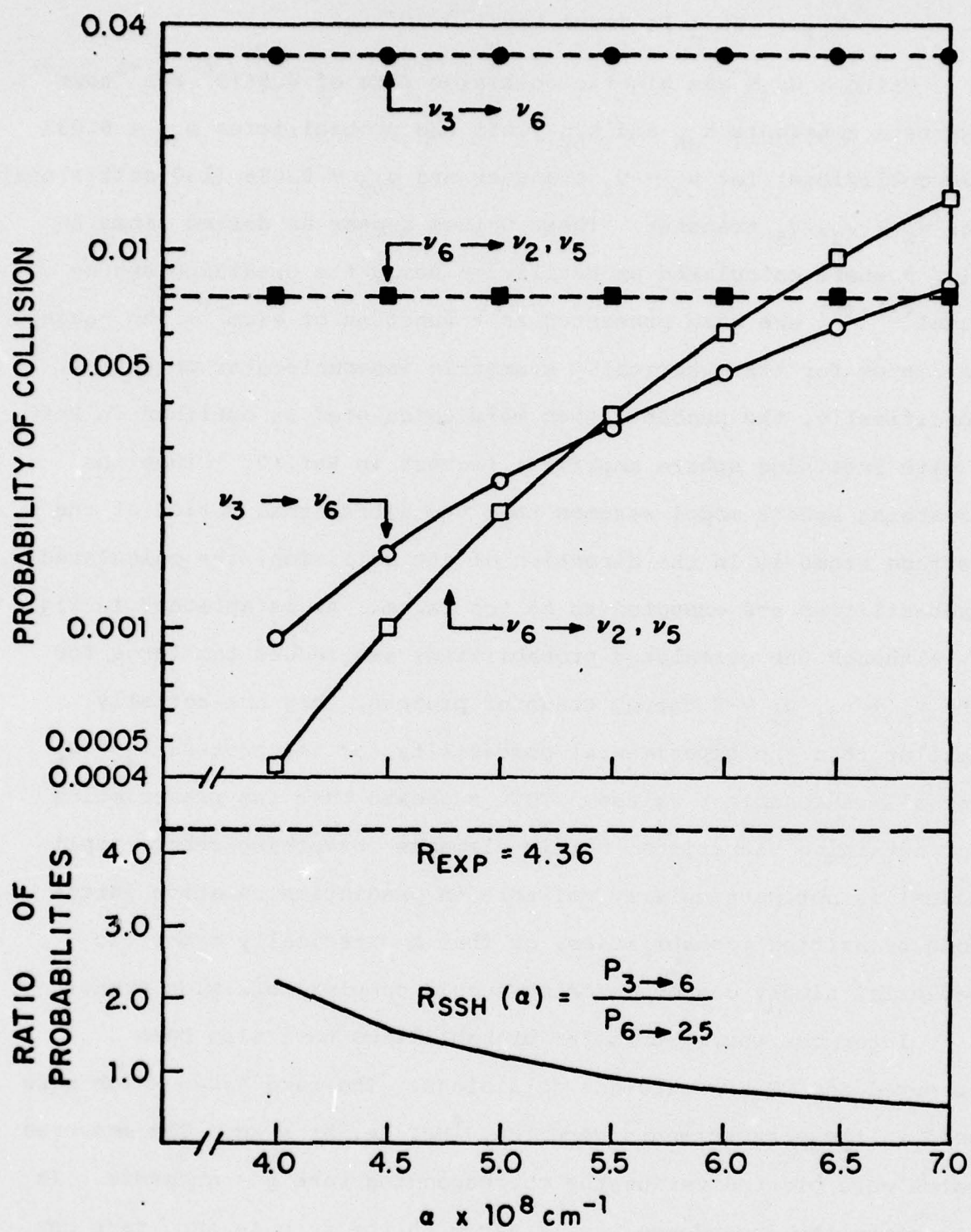


Figure 9

pressure (intercept) consistent with the pure CH_3F rate. Fig. 10 shows the Xe dependence of the two v_2 , v_5 rates, and Table V is a summary of the rare gas data. In Fig. 10a the experimentally determined probabilities per collision for the two energy gaps are plotted versus the square root of the reduced mass of the collision partners (dotted lines). Also plotted are the calculated SSH probabilities per collision (I). The range parameter α used is $7 \times 10^8 \text{ cm}^{-1}$ ($L = .14 \text{ \AA}$). It appears that the SSH model has a great deal more success in predicting energy transfer probabilities in the case of polyatomic-rare gas atom collisions than in the case of polyatomic-polyatomic collision.

Work is in progress to compare the rare gas results with the predictions of the mode matching model of Miklavc & Fischer.⁽⁸⁾

* This work was also supported by the National Science Foundation under Grant NSF-CHE76-04118.

- (1) R. S. Sheorey, R. C. Slater and G. W. Flynn, J. Chem. Phys. 68, 1058 (1978).
- (2) R. S. Sheorey and G. W. Flynn (unpublished work).
- (3) J. T. Yardley and C. B. Moore, J. Chem. Phys. 49, 1111 (1968).
- (4) R. N. Schwartz, Z. I. Slawsky, and K. F. Herzfeld, J. Chem. Phys. 20, 1951 (1952).
- (5) F. I. Tanczos, J. Chem. Phys. 25, 439 (1956).
- (6) J. L. Stretton, Trans. Faraday Soc. 61, 1053 (1965).
- (7) E. Weitz and G. W. Flynn, J. Chem. Phys. 58, 2781 (1973).
- (8) Adolf Miklavc and Sighart Fischer, Chem. Phys. Lett. 44, 20 (1976).

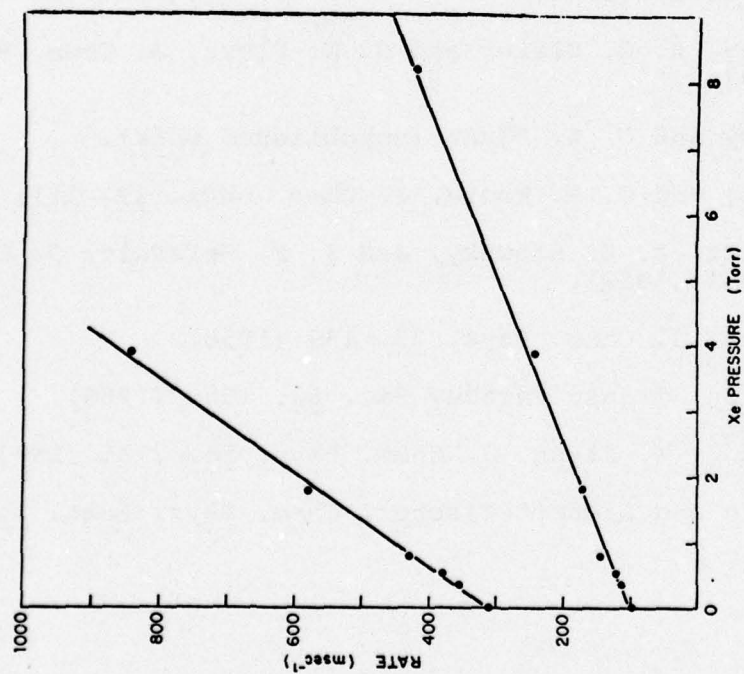


Figure 10

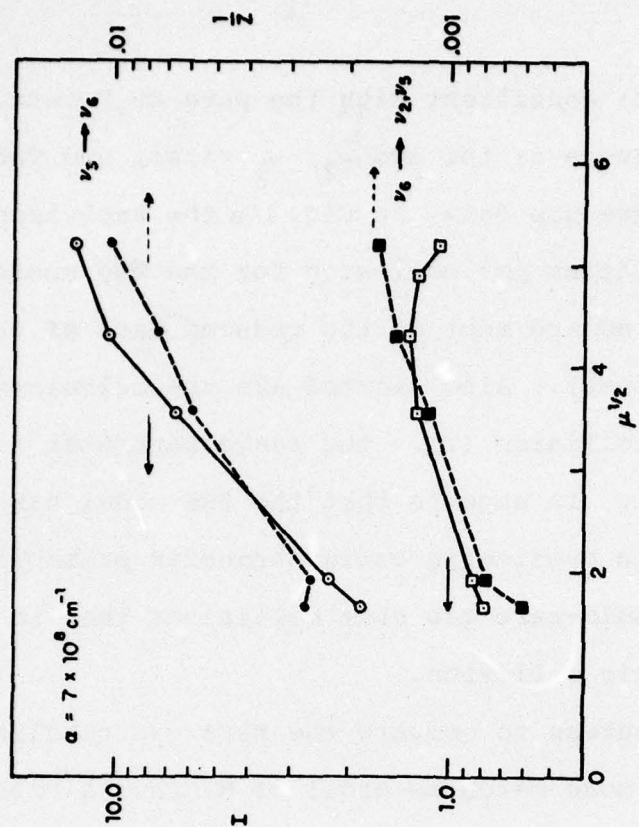


Figure 10a

TABLE V

Collision Partner	$\mu_{\text{CH}_3\text{F-X}}^{\frac{1}{2}}$ (amu)	σ_0^2 (Å)	r_-^* (msec torr) ⁻¹		k^{36} (msec torr) ⁻¹		Prob $v_3 + v_6$	Prob $v_6 + v_{25}$
CH ₃ F	4.12	13.9	-596	-198	285	65	.0330	.00753
³ He	1.66	9.9	-670	-224	41.47	9.15	.00272	.00060
⁴ He	1.92	9.9	-655	-230	34.63	10.39	.00262	.00079
Ne	3.56	10.5	-678	-226	45.83	9.58	.00607	.00127
Ar	4.29	12.7	-693	-232	54.27	10.89	.00716	.00144
Xe	5.20	15.3	-736	-238	76.89	12.31	.01021	.00163

*measured rates for 1T CH₃F + 1T collision partner.

2. Collision Controlled Vibrational Energy Exchange In COF₂:
Equilibration of the ν_2 , ν_6 , and $\nu_{3,5}$ Modes*

(K. R. Casleton, Y. V. C. Rao, G. W. Flynn)

Detailed studies of vibrational energy transfer processes have been undertaken for only a few polyatomic molecules with more than three atoms. One of these, methyl fluoride, has been the most intensely studied and has provided a wealth of information. Carbonyl fluoride, a planar molecule resembling formaldehyde, has been the focus of similar recent studies.⁽¹⁾⁽²⁾ This molecule strongly absorbs CO₂ laser radiation near $\lambda = 10\mu$. Following collisional redistribution of this energy which is absorbed by the ν_2 C-F stretch mode, strong infrared fluorescence can be observed from a variety of other vibrational levels in the molecule, as shown in Figure 11. The previous investigations⁽¹⁾⁽²⁾ focussed primarily on understanding the mechanism for collisional filling of the ν_1 and $2\nu_2$ levels from the pumped ν_2 level.

In order to more fully understand the overall mechanism for collision induced vibrational energy transfer in COF₂, we have undertaken a detailed study of the time resolved, infrared fluorescence emanating from the three lowest vibrational modes, ν_6 and $\nu_{3,5}$, following excitation of ν_2 , the symmetric C-F stretch. The ν_3 , ν_5 and ν_6 normal modes of COF₂ are, respectively, the FCF bend, FCF wag, and out-of-plane bending vibrations. These are the only normal modes whose frequencies lie below that for the laser pumped symmetric C-F stretch mode at 962 cm^{-1} . We expect that effects of vibration to translation/rotation (V-T/R) energy exchange should be most

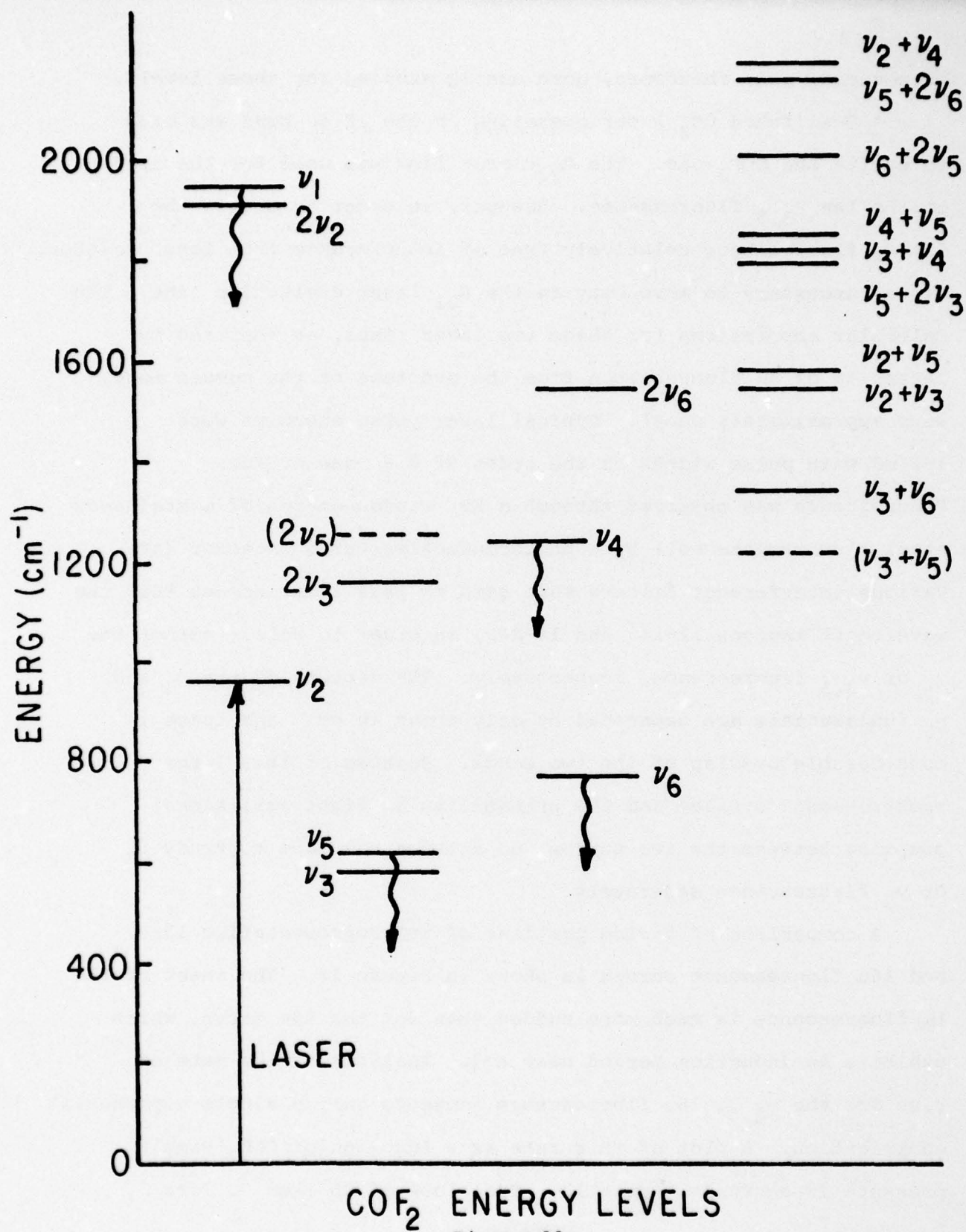


Figure 11

pronounced, and, therefore, more easily studied for these levels.

A Q-switched CO_2 laser operating in the 10.6μ band was used to excite the COF_2 gas. The P_{22} laser line was used for the studies of the 16μ $\nu_{3,5}$ fluorescence. However, in order to obtain the 13μ ν_6 fluorescence relatively free of interference from laser scatter, it was necessary to move away to the R_{22} laser excitation line. The molecular absorptions for these two laser lines, as measured by intensity of 5μ fluorescence from the overtone of the pumped mode, were approximately equal. Typical laser pulse energies were 1-2 mJ with pulse widths on the order of $0.6 \mu\text{sec}$ or less. Fluorescence was observed through a KB window on top of a stainless steel fluorescence cell by a photoconductive Cu:Ge detector (4K). Various interference filters were used to pass fluorescence from the wavelength regions $11\text{-}14\mu$ and $14\text{-}20\mu$, in order to select either the ν_6 or $\nu_{3,5}$ fluorescence, respectively. The centers of the ν_3 and ν_5 fundamentals are separated by only about 40 cm^{-1} and there is considerable overlap of the two bands. Because of this large spectroscopic overlap and the probability of tight collisional coupling between the two states, no attempt was made to study ν_3 or ν_5 fluorescence separately.

A comparison of rising portions of two representative 13μ and 16μ fluorescence curves is shown in Figure 12. The onset of the 16μ fluorescence is much more sudden than for the 13μ curve, which exhibits an induction period near $t=0$. Analysis of the rate of rise for the $\nu_{3,5}$, 16μ fluorescence suggests only a single exponential contribution. A plot of this rate as a function of COF_2 sample pressure is shown in Figure 13. The slope of $35 \text{ msec}^{-1} \cdot \text{Torr}^{-1}$,

COF₂ FLUORESCENCE

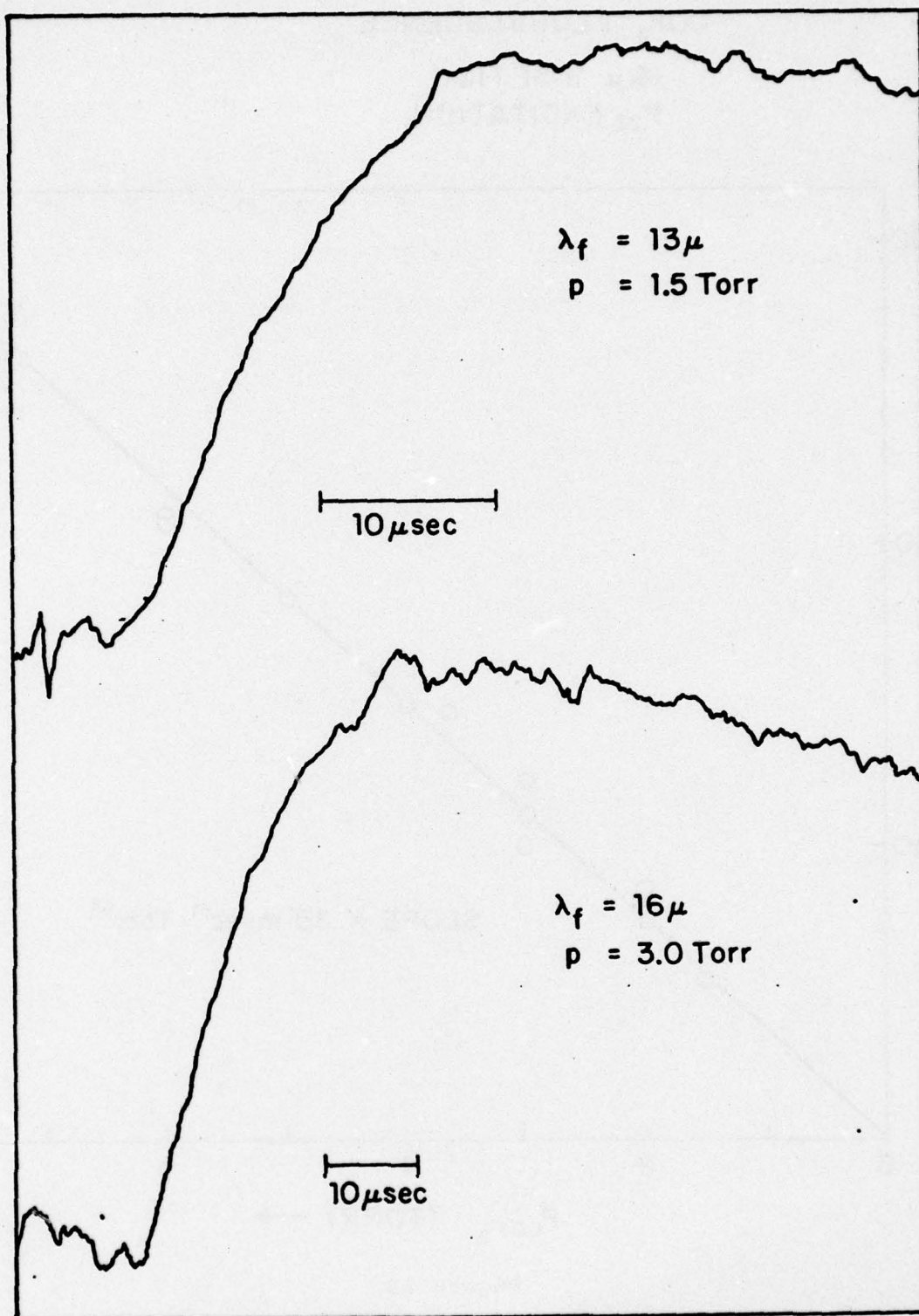


Figure 12

COF₂ FLUORESCENCE

16 μ RISETIME
P₂₂ EXCITATION

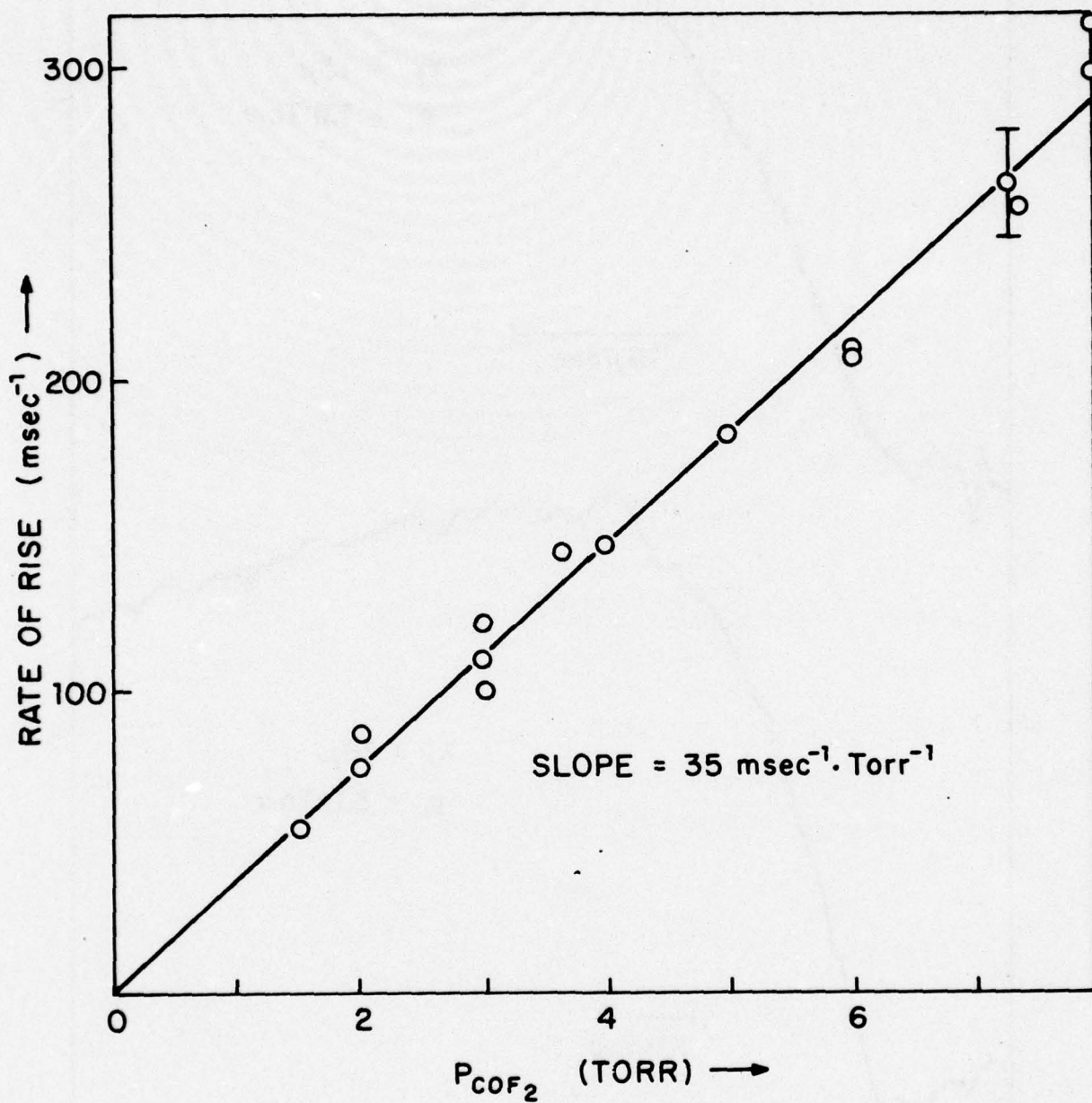


Figure 13

determined from a least squares analysis is consistent with eigenvalues seen in the decay of the ν_1 , $2\nu_2$, 5μ fluorescence⁽¹⁾⁽²⁾⁽³⁾ and rise of the ν_4 , 8μ fluorescence.⁽⁴⁾ This suggests that the process leading to the filling of $\nu_{3,5}$ from the ν_2 pumped mode is the process which has the largest amplitude for deactivation of ν_2 . In addition, this same process appears to be involved in the overall filling mechanism for the ν_4 asymmetric C-F stretch mode.

In contrast to the single exponential nature of the $\nu_{3,5}$, 16μ rise, semi-log plots of fluorescence intensity versus time for the 13μ data clearly show two exponential contributions, where the associated amplitudes are of opposite sign. Figure 14 shows a plot of rate versus COF_2 pressure for the slower of these two processes. The least squares fit slope for these data is $95 \text{ msec}^{-1} \cdot \text{Torr}^{-1}$. An eigenvalue of corresponding magnitude has been observed in a study of the 5μ fluorescence of COF_2 rare gas mixtures.⁽³⁾ It appears that this collisional process which is involved in the filling of the ν_6 mode also contributes to the overall deactivation of ν_2 , although its amplitude is presumably small relative to that for the $35 \text{ msec}^{-1} \cdot \text{Torr}^{-1}$ process. The eigenvalue for the second, faster process seen in the rise of the 13μ fluorescence is approximately $200\text{-}250 \text{ msec}^{-1} \cdot \text{Torr}^{-1}$. The uncertainty here is considerably larger because of the propagation of error due to subtraction of the slower component from the raw data. It does appear, however, that the amplitude of the slow component is approximately 3-4 times larger in absolute value than that for the fast component.

Finally, the decay of the $\nu_{3,5}$, 16μ fluorescence has been

COF₂ FLUORESCENCE

13 μ RISE TIME

SLOW COMPONENT

R₂₂ EXCITATION

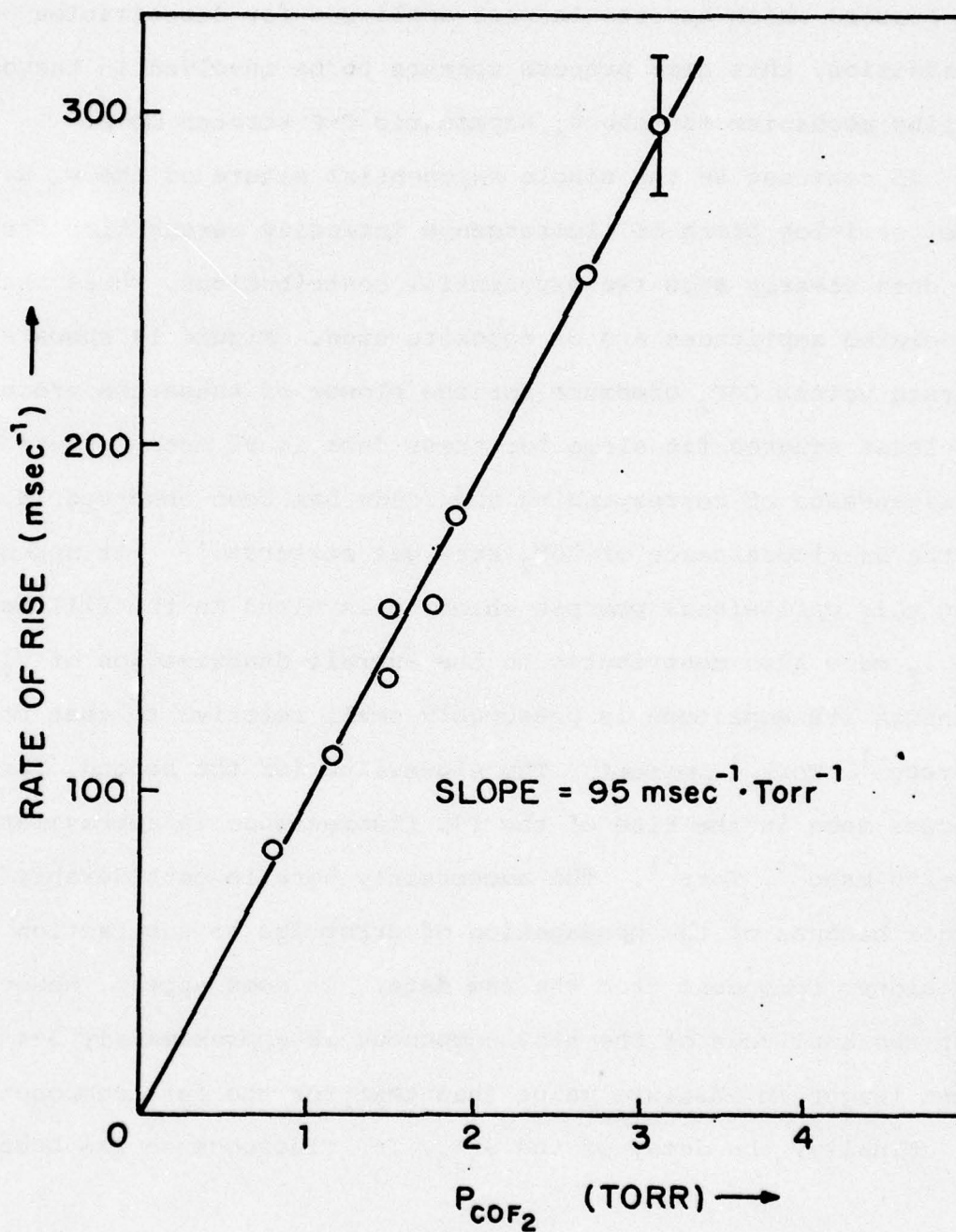


Figure 14

studied in some detail. The part of this decay due to collisional deactivation is single exponential, and the corresponding eigenvalue is $8.6 \text{ msec}^{-1} \cdot \text{Torr}^{-1}$. This agrees quite well with results from studies of 5μ decay⁽¹⁾⁽²⁾⁽³⁾ and 8μ fluorescence decay.⁽⁴⁾

Calculations of COF_2 rare gas collisional energy exchange probabilities using the SSH breathing sphere model⁽⁴⁾⁽⁵⁾⁽⁶⁾ suggest that this eigenvalue may be identified with the V-T process in COF_2 .

Approximately 90% of the total ambient excited state population of COF_2 resides in the v_3 , v_5 , v_6 and v_2 levels. It seems natural to expect that no higher energy levels need be considered in order to explain the primary energy transfer processes for these states. We have constructed a simplified kinetic model, depicted in Figure 15, and considered processes which couple these excited states. The population deviation for v_2 , v_6 and $v_{3,5}$ were written as functions of the rate constants, k_{ij} , in the limit of infinitely slow V-T deactivation. Using experimental limits on ratios of amplitudes and eigenvalues, it appears that k_{63} is larger than k_{26} by at least a factor of 3-5, and k_{23} may exceed k_{26} by a factor of 5 or more. However, in order to reduce the rather large uncertainties in these values, it will be necessary to study the v_6 , 13μ fluorescence and determine more accurate values for both the eigenvalues and ratio of amplitudes.

* This work was also supported by the National Science Foundation under Grant NSF-CHE76-04118.

(1) K. Casleton and G. Flynn, JCP 67, 3133 (1977).

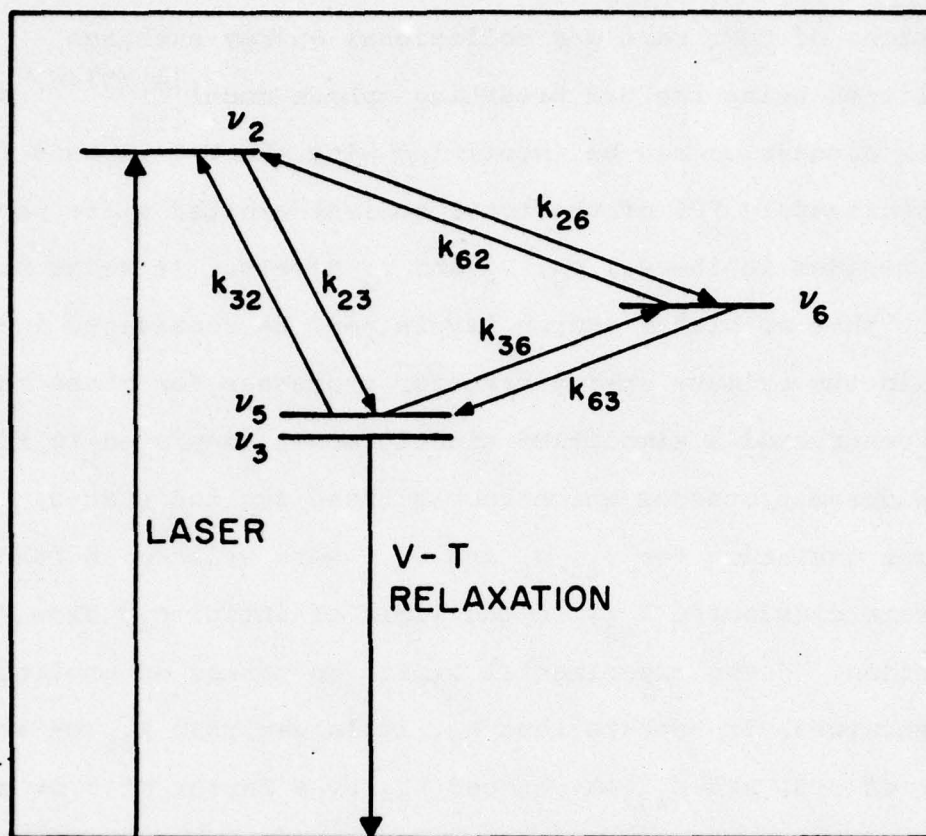


Figure 15

- (2) K. Casleton and G. Flynn, CRL Progress Report No. 27, July 1, 1976-March 31, 1977.
- (3) Y. V. C. Rao, K. Casleton and G. Flynn, 5μ COF_2 Fluorescence: The Effects of Rare Gases, work in process.
- (4) K. Casleton, YVC Rao and G. Flynn, 8μ COF_2 Fluorescence in COF_2 , work in progress.
- (5) R. V. Schwartz, Z. I. Slawsky, K. F. Herzfeld, JCP 20, 1951 (1952).
- (6) J. L. Stretton, Trans. Faraday Soc. 61, 1053 (1965).

3. Intermode Energy Transfer in COF₂ Induced by Rare Gases*

(Y. V. C. Rao, K. R. Casleton, G. W. Flynn)

Laser induced fluorescence studies in the infrared region have provided information on molecular energy transfer processes. Theories have been developed, which take into account either short range repulsive forces or long range attractive forces, to predict energy transfer rates. These theories have satisfactorily explained energy transfer rates in the case of diatomic and some simple polyatomic molecules; however, the complex energy transfer mechanism in polyatomic molecules is yet to be unravelled. An understanding of these energy transfer mechanisms in polyatomic molecules is of considerable importance in laser chemistry and in the development of lasers. The present study was undertaken in an attempt to unravel the complex energy transfer process in the 4 atom polyatomic molecule COF₂. The C-F stretching mode ν_2 of COF₂ strongly absorbs CO₂ laser radiation, while the C=O stretching mode ν_1 exhibits intense infrared emission. The other vibrational modes are widely separated from each other. Such a vibrational energy level spacing is well suited to study the flow of energy from one level to the other. Earlier studies⁽¹⁾ have shown that the levels ν_2 and ν_1 equilibrate by a V-V "up-the-ladder" process within a short period of time requiring ~30 collisions. Because of such tight coupling between the levels ν_2 and ν_1 , monitoring the temporal behavior of excess population in ν_1 is equivalent to monitoring the time history of the population deviation of the ν_2 level.

A detailed description of the experimental apparatus used to study the laser induced fluorescence of COF_2 has been given elsewhere. ^{(2) (3)} In brief, a Q-switched CO_2 laser operating on P(22) of the 10.6μ band excites the COF_2 v_2 mode, and fluorescence near 6μ is observed from the $2v_2$, v_1 fermi mixed states. The band width of the detected fluorescence was $4.6 - 5.5\mu$ the limits being established by a 4.6μ long pass filter and the cut off point for the detector. The decay of the 5μ fluorescence was studied in mixtures of COF_2 with rare gases at room temperature.

The fluorescence signal exhibited a double exponential decay. Fig. 16 shows a typical plot for the fast rate of fluorescence decay versus rare gas pressure, with a constant COF_2 partial pressure of 0.2 torr. One can observe two linear regions with different slopes in Fig. 16. When they are extrapolated to zero rare gas pressure, the intercepts, corresponding to pure COF_2 rates, were found to be $35 \text{ ms}^{-1} \text{ Torr}^{-1}$ (fast rate 1) and $90 \text{ ms}^{-1} \text{ Torr}^{-1}$ (fast rate 2). Such a behavior was also observed with different COF_2 partial pressures in COF_2 -rare gas mixtures. The slopes of these lines indicate the rare gas rates for COF_2 -X collisions. Earlier measurements with pure COF_2 ⁽¹⁾ showed a decay rate of $35 \text{ ms}^{-1} \text{ Torr}^{-1}$ but the other rate ($90 \text{ ms}^{-1} \text{ Torr}^{-1}$) was never observed. It appears that in the decay of 5μ fluorescence, only one eigenvalue, (35 or $90 \text{ ms}^{-1} \text{ Torr}^{-1}$) can be detected experimentally depending upon the rare gas pressure. It is likely that the relative amplitude of the decay corresponding to the missing eigenvalue is too small to be experimentally detected. In Table VI, the rare gas rates for the two fast decay processes are presented. It can be observed from Table VI that the

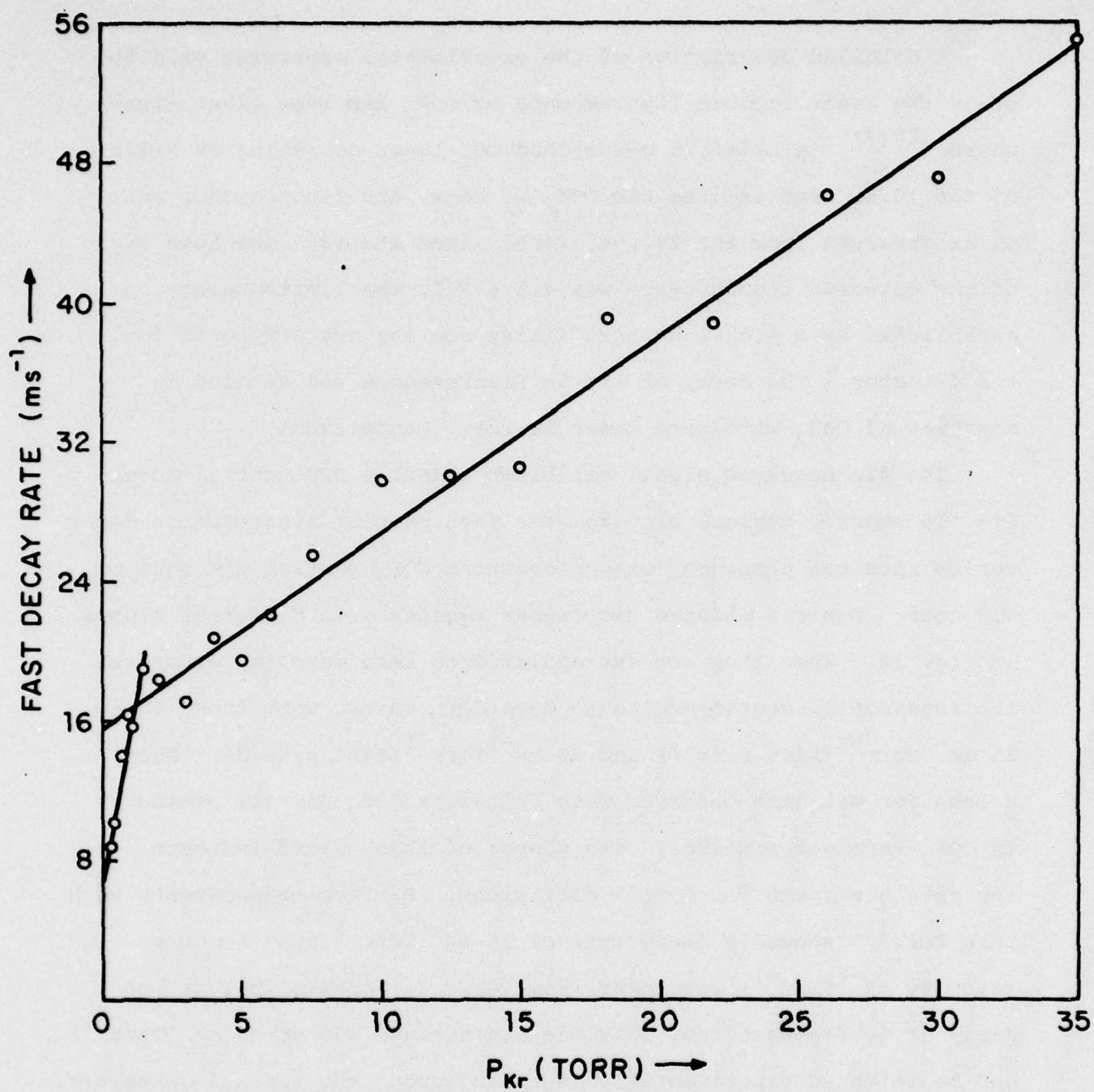


Figure 16

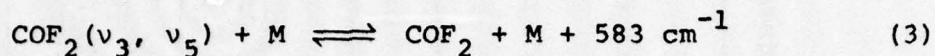
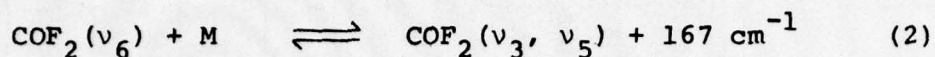
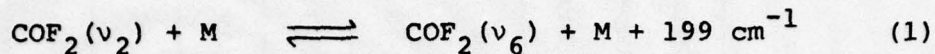
Table VI

Rare gas rates for the two fast decay processes

Rare Gas	Decay Process 1 Pure COF ₂ rate = 35 ms ⁻¹ Torr ⁻¹ (ms ⁻¹ Torr ⁻¹)	Decay Process 2 Pure COF ₂ rate = 90 ms ⁻¹ Torr ⁻¹ (ms ⁻¹ Torr ⁻¹)
³ He	23.6	21.29
He	15.03	11.53
Ne	5.04	2.63
Ar	2.79	1.39
Kr	4.9	0.85
Xe	2.28	0.82

rare gas rates for the $35 \text{ ms}^{-1}\text{Torr}^{-1}$ process are in general larger than the corresponding rates for the $90 \text{ ms}^{-1}\text{Torr}^{-1}$ process.

The major processes responsible for the deactivation of COF_2 (ν_2) are expected to be



It can be qualitatively argued that process (1) is slow compared to (2), in which case one can observe a fast decay followed by a slow decay. The fast rate ($35 \text{ ms}^{-1}\text{Torr}^{-1}$) being the rate of process (1) and the slow rate ($7\text{--}8 \text{ ms}^{-1}\text{Torr}^{-1}$) corresponding to process (3). Upon the addition of rare gas process (1) becomes faster, since the rare gas rate is high for that process, and process (2) becomes the rate limiting step. Thus one can explain the switching over of the eigenvalues in the decay of $\text{COF}_2 \nu_2$ mode. A detailed kinetic analysis of the complex collisional deactivation processes may yield information on the relative rates of the various processes involved. Such a kinetic analysis is in progress.

A typical pressure dependence of the slow rate of fluorescence decay in COF_2 -X mixtures is shown in Fig. 17, and the slope of this line gives the rare gas rate. On extrapolating to zero rare gas pressure, the intercept was found to be $7.8 - 8 \text{ ms}^{-1}\text{Torr}^{-1}$ corresponding to the pure COF_2 rate. This rate is in good agreement with the earlier observations in pure COF_2 , where the decay of (ν_3, ν_5) modes of COF_2 was measured. This clearly indicates that

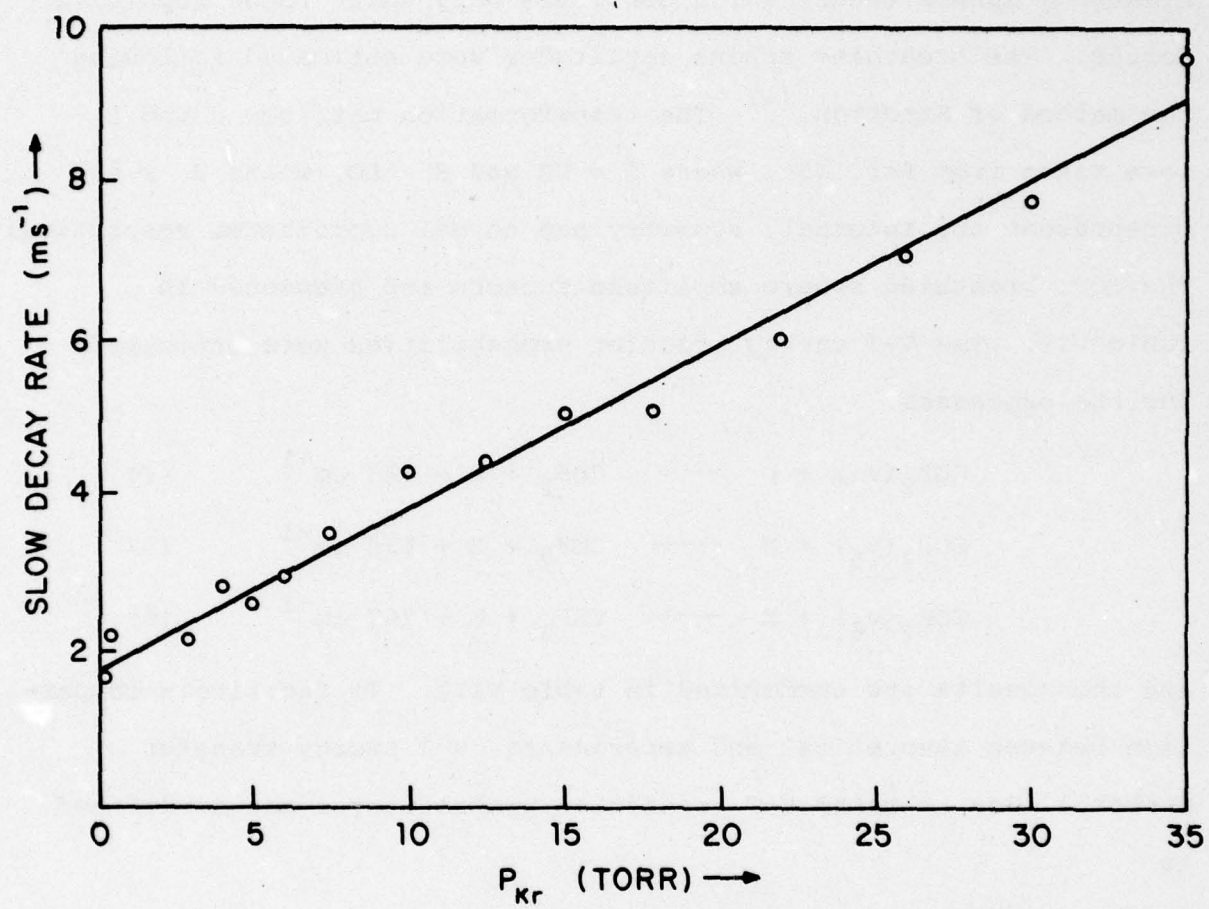
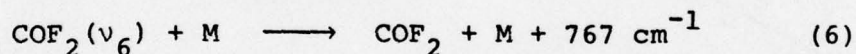
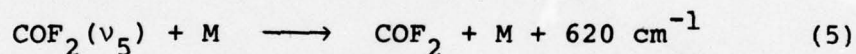
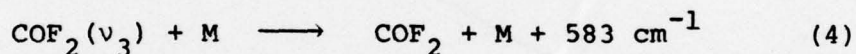


Figure 17

the slow decay rate can be attributed to the V-T process, where the energy flows from the low lying vibrational modes (ν_3 , ν_5) to the ground state. Probabilities of energy transfer per COF_2 -X collision were derived from the rate constants and are presented in Fig. 18. The V-T energy transfer probabilities were estimated using the breathing sphere theory which considers only short range repulsive forces. The breathing sphere amplitudes were estimated following the method of Stretton.⁽⁴⁾ The transformation matrices U and L were taken from Ref. (5), where $S = UR$ and $S = LQ$, where R, S and Q represent the internal, symmetry and normal coordinates respectively. The COF_2 breathing sphere amplitude factors are presented in Table VII. The V-T energy transfer probabilities were estimated for the processes



and the results are summarized in table VIII. To facilitate comparison between theoretical and experimental V-T energy transfer probabilities, a total V-T transition probability P can be defined as

$$p = p_3 f_3 + p_5 f_5 + p_6 f_6$$

where p_i is the V-T transition probability for state i and f_i is the fraction of vibrationally excited molecules in state i. The calculated probabilities for three different range parameters α , are indicated by solid lines in Fig. 18, and the experimental

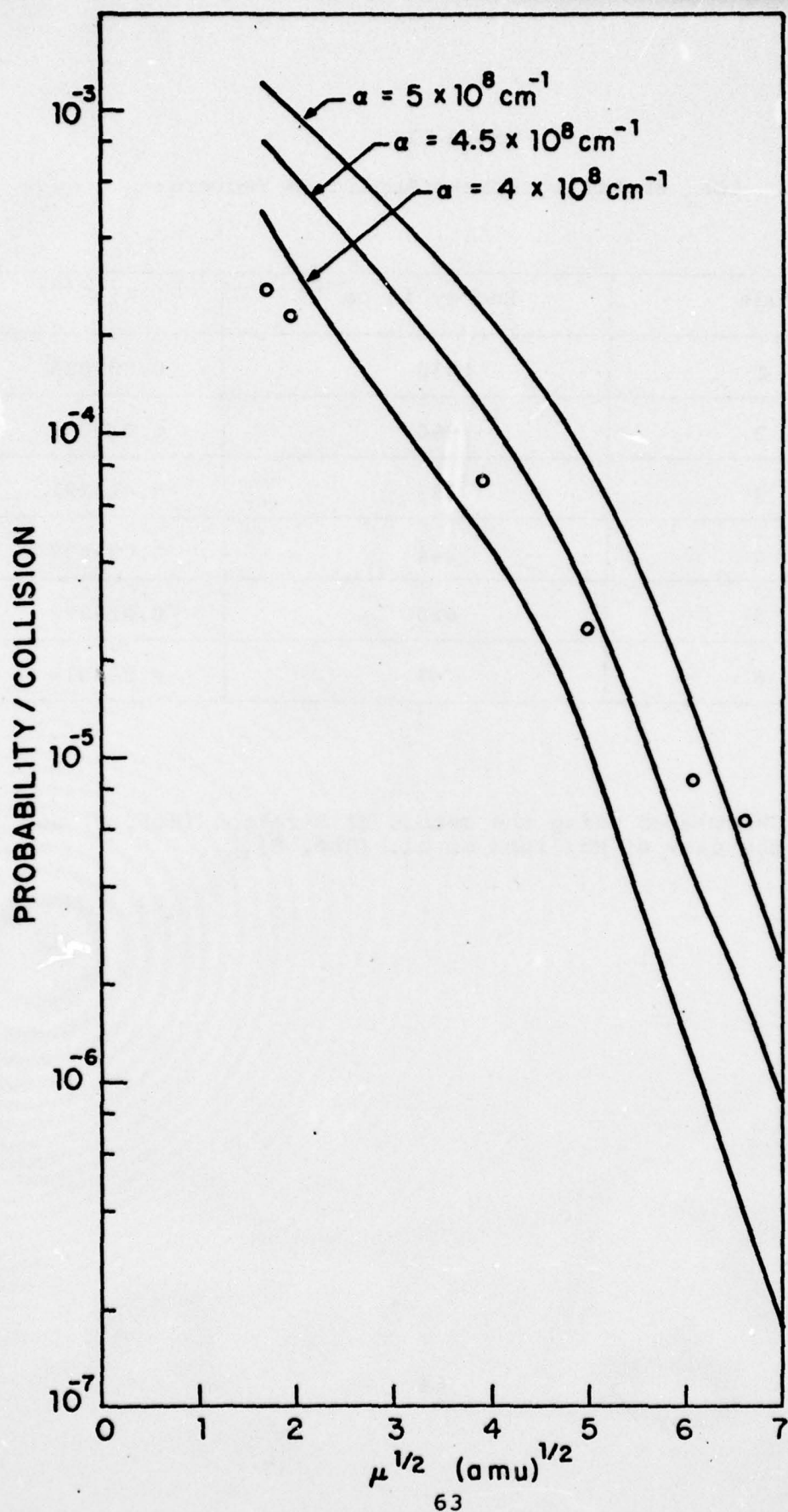


Figure 18

Table VII

COF₂ Breathing Sphere Amplitude Factors:

Mode	Energy in cm ⁻¹	A _J ^{2(a)}
1	1930	0.007028
2	966	0.017001
3	583	0.013291
4	1244	0.004602
5	620	0.025862
6	767	0.003514

(a) Calculated using the method of Stretton (Ref. 4) and the data of Mallison et al. (Ref. 5).

Table VIII
Breathing Sphere Theory. V-T Probabilities.

Process	$\text{COF}_2(\nu_3) + M \xrightarrow{\ddagger} \text{COF}_2 + M + 583 \text{ cm}^{-1}$ $f_3 = 0.4079$ Prob/Collision (a)	$\text{COF}_2(\nu_5) + M \xrightarrow{\ddagger} \text{COF}_2 + M + 620 \text{ cm}^{-1}$ $f_5 = 0.3414$ Prob/Collision (a)	$\text{COF}_2 + M \xrightarrow{\ddagger} \text{COF}_2 + M + 767 \text{ cm}^{-1}$ $f_6 = 0.1684$ Prob/Collision (2)	$P = \sum P_i f_i$
^3He	7.5914×10^{-4}	1.4106×10^{-3}	5.7×10^{-5}	8.01×10^{-4}
He	5.5092×10^{-4}	9.8678×10^{-4}	3.4×10^{-5}	5.67×10^{-4}
Ne	1.268×10^{-4}	1.9784×10^{-4}	4.1×10^{-6}	1.2×10^{-4}
Ar	3.7067×10^{-5}	5.2225×10^{-5}	7.3×10^{-7}	3.3×10^{-5}
Kr	6.0456×10^{-6}	5.7044×10^{-6}	5×10^{-8}	4×10^{-6}
Xe	1.9609×10^{-6}	2.2802×10^{-6}	1.55×10^{-8}	2×10^{-6}

(a) The values of probability/collision were calculated with $\alpha = 4.5 \times 10^8 \text{ cm}^{-1}$, and (t/k) for $\text{COF}_2 = 111.9^\circ\text{K}$ obtained from Ref. 6.

probabilities are indicated by points. From Fig. 18 it can be observed that the experimentally determined probabilities are in very good agreement with those predicted by the breathing sphere theory.

* This work was also supported by the National Science Foundation under Grant NSF-CHE76-04118.

- (1) K. Casleton and G. Flynn, J. Chem. Phys. 67, 3133 (1977).
- (2) L. O. Hocker, M. A. Kovacs, C. K. Rhodes, G. Flynn and A. Javan, Phys. Rev. Lett. 17, 233 (1966).
- (3) R. D. Bates. Jr., G. Flynn, J. T. Knudtson and A. M. Ronn, J. Chem. Phys. 53, 3621 (1970).
- (4) J.L. Stretton, Trans. Faraday Soc. 61, 1053 (1965).
- (5) P. D. Mallison, D. C. McKean, J. H. Holloway and I. A. Oxtan Spectrochimica Acta 31A, 143 (1975).
- (6) Y. Yonezawa and T. Fueno, Bull. Chem. Soc. Japan 47, 1894 (1974).

C. OPTICAL PUMPING OF FLAMES*

(W. Happer, A. C. Tam, S. M. Curry, T. Yabuzaki)

There is a great deal of interest in the combustion process in flames.⁽¹⁾ Methods used for studying flames include, for example, microprobing,⁽²⁾ emission and absorption spectroscopy, electron spin resonance,⁽³⁾ and recently CARS techniques.⁽⁴⁾ Also, excitation transfer cross sections of alkali atoms in flames have been determined.^(5,6) We have recently demonstrated⁽⁷⁾ a new method to investigate collisional relaxation rates of paramagnetic particles (alkali atoms in our present study) in a flame. Presumably other paramagnetic species in a flame (like H or free radicals) can be similarly studied. In this preliminary investigation, we used a circularly polarized CW dye laser beam at the sodium-D₁ wavelength to spin-polarize⁽⁸⁾ ground-state sodium atoms in hydrocarbon flames. The Hanle effect⁽⁹⁾ is used to measure the spin relaxation rate as a function of position within the flame, and we have found this rate to be highly position-dependent. Such a map of relaxation rates provides useful information about compositions and processes at various positions in a flame. We have also demonstrated that large RF magnetic resonance signals for sodium ground-state atoms are readily observable in a flame. This implies the possibility of RF spectroscopy of various ions and free radicals in flames using direct laser pumping or indirect spin-exchange pumping.

The arrangement of our Hanle effect experiment is shown schematically in Fig. 19. The single mode CW dye laser (Spectra Physics model 580) produces about 160 mW of power at 5896 Å. The circularly polarized laser beam is directed into the flame by a convex lens of focal length about 17 cm such that the laser beam diameter is about 1 mm in the flame. A typical flame that we have studied in detail is obtained by burning in air the following gas mixture: 67% methane, 1% ethane, and 32% oxygen by volume at atmospheric pressure and at a total flow rate of 132 cc/min. A stainless-steel wire-mesh (hole size about 1 mm^2) is mounted at the exit orifice of the burner, of diameter about 10 mm. The mesh is coated with NaCl to dope the flame with sodium atoms such that about 10% of the circularly polarized laser light is absorbed. The laser-excited fluorescence from a small spot (about $1/4 \text{ mm} \times 1/4 \text{ mm}$ size) is focused into the entrance slit of a 0.3 m monochromator (instrumental full width $\approx 1 \text{ Å}$) set at 5890 Å. The D_2 fluorescence from the Na atoms is found to be of about twice the intensity of the D_1 fluorescence (i.e. the $^3P_{1/2}$ and $^3P_{3/2}$ states are strongly mixed), and D_2 fluorescence is detected instead of the D_1 fluorescence to avoid instrumental scattering. The position of the observation spot in the flame can be changed by moving the burner horizontally and vertically with translational stages (accuracy of positioning $\approx 0.2 \text{ mm}$). The fluorescence is detected with a cooled S-20 photomultiplier, whose output is amplified and fed to the vertical scale of an

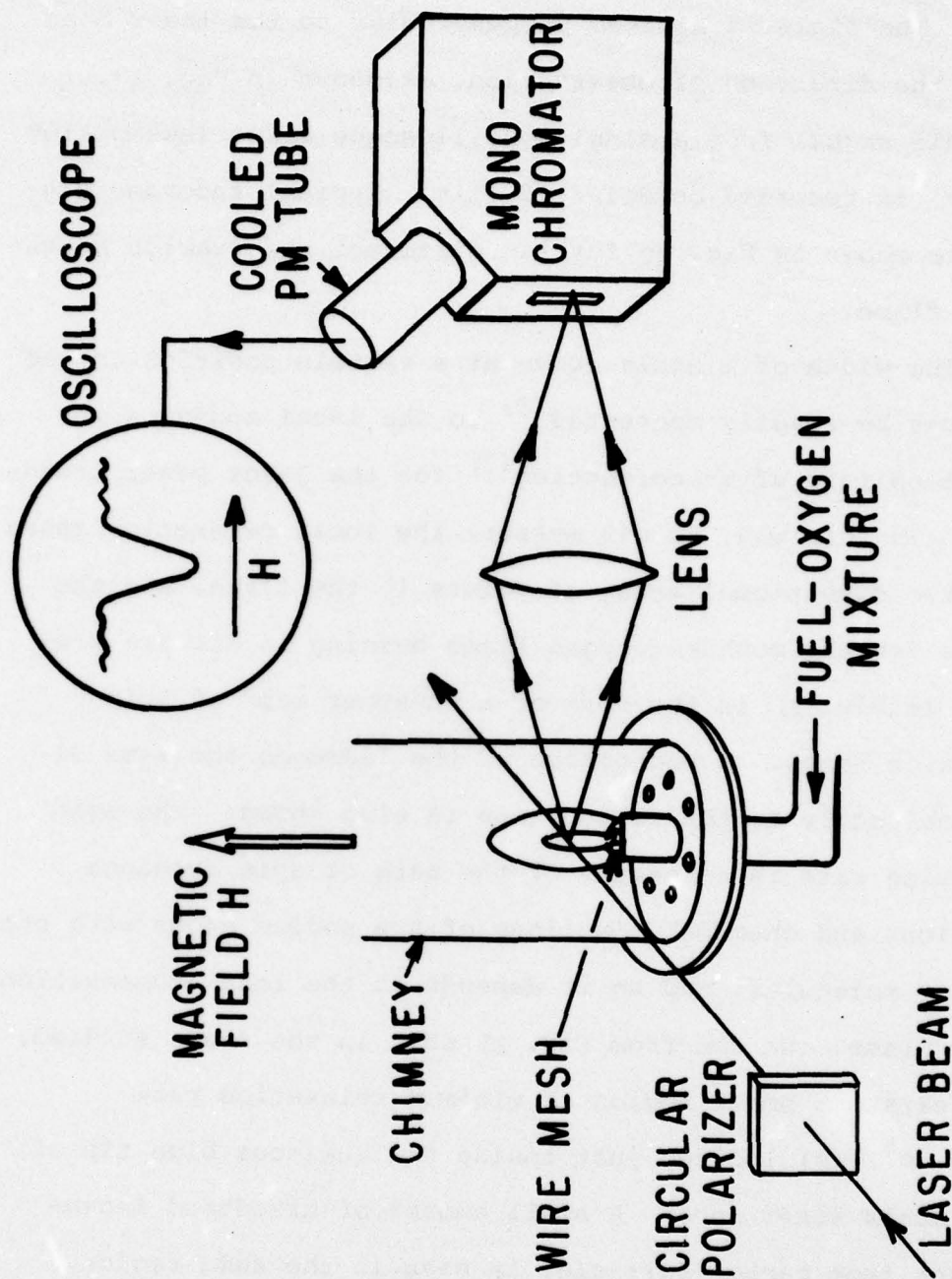


Figure 19: Experimental arrangement to observe optical pumping signals in a flame.

oscilloscope. The horizontal sweep of the oscilloscope is used to sweep a magnetic field from about -32×10^{-4} to $+32 \times 10^{-4}$ Tesla. The field is applied perpendicular to the laser beam and to the direction of observation, as shown in Fig. 19. The Hanle signal from a single oscilloscope trace (sweep time ≈ 5 sec) is recorded on Polaroid film. Typical recorded signals are shown in Fig. 20 for two different observation spots in the flame.

The width of a Hanle curve at a certain position in the flame can be readily converted⁽⁷⁾ to the local sodium spin-relaxation rate after correcting⁽⁷⁾ for the laser power broadening. In this way, we can measure the local relaxation rates for a two dimensional array of points in the flame, and the results for the methane-oxygen flame burning in air are presented in Fig. 21 in the form of a "contour map" of spin relaxation rates. A photograph of the flame on the same dimensional scale as the contour map is also shown. The spin relaxation rate is a measure of the rate of spin exchange collisions and chemical reactions of the sodium atoms with other atoms or molecules, and so it depends on the local composition of the flame. We see from Fig. 21 that in the flame studied, there exists a small region of minimum relaxation rate ($< 3 \times 10^6/\text{sec}$) located just inside the luminous blue tip of the flame's inner cone. A small amount of broadband incandescence from carbon particles is seen in the same region. A platinum thermocouple is used to estimate the flame temperature at various points. The contours of constant relaxa-




Figure 20: Typical Hanle signal observed for different positions on the flame axis: (a) 18 mm from the bottom of the flame (b) 10 mm from the bottom of the flame.

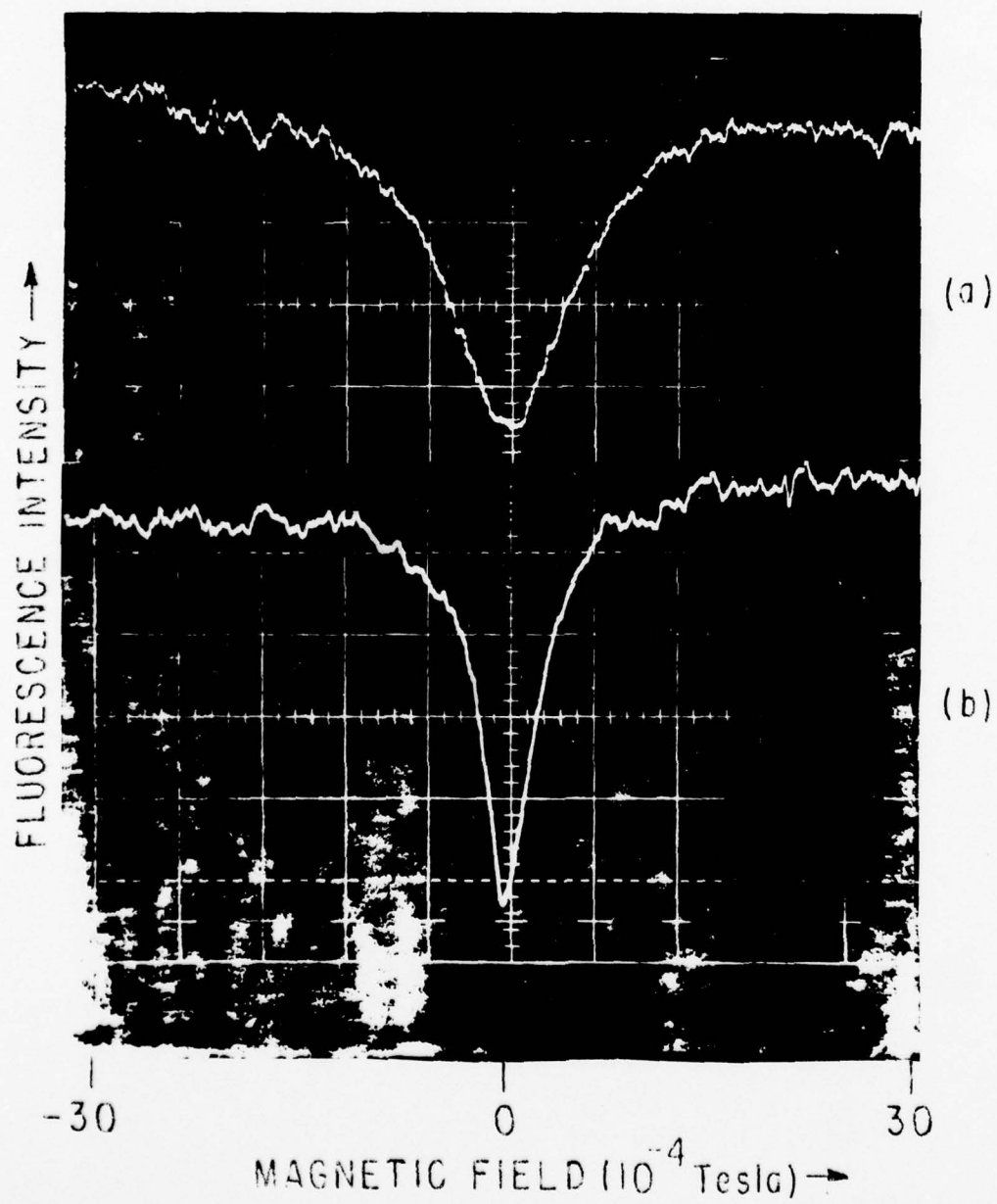


Figure 20

Figure 21: Left: Photograph of the methane-oxygen flame being studied. Right: Contour map of the observed spin-relaxation rates in the flame, drawn to the same scale as the photograph. The numbers on the contours give relaxation rates when multiplied by $2\pi \times 10^6/\text{sec}$. The height indicated is measured from the top of the wire mesh seen in the photograph.

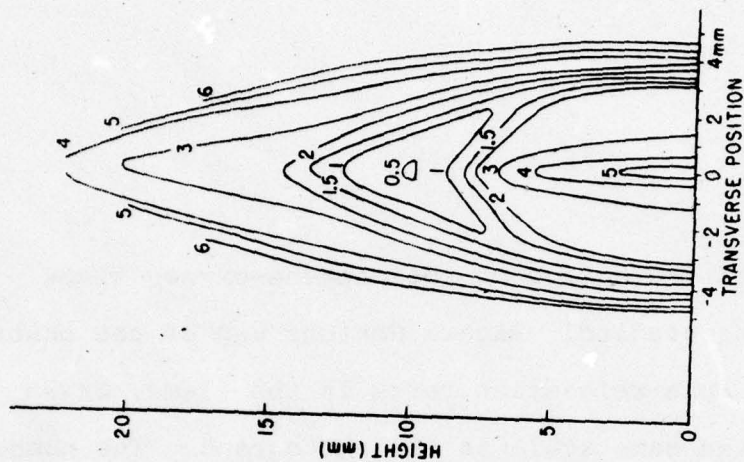


Figure 21

tion frequency (Fig. 21) are found to be roughly parallel to the measured isotherms. The maximum temperature from the thermocouple measurements is 1350°C (not corrected for conduction or radiation loss) at the tip of the inner cone.

With the laser beam spread into a sheet with a cylindrical lens and the magnetic field sweeping at a rate of the order of 1 Hz, the modulation of fluorescence from the most strongly pumped parts of the flame can be clearly seen with the naked eye. The modulated fluorescence comes from a thin, well-defined surface within the flame. This surface appears just inside the flame's inner cone.

Similar results are obtained with a propane-oxygen flame. The fuel mixture consists of 53% propane and 47% O_2 by volume, flowing at 120 cc/min. This flame shows a considerably greater amount of carbon incandescence. A minimum spin relaxation rate of $1.9 \times 10^6/\text{sec}$ is observed in the incandescent tip of the inner cone. Strong spin polarization is achieved over a much larger volume for the propane flame than for the methane flame. We have also tried a diffusion flame of H_2 burning in air, with a small amount of O_2 (5% by volume) premixed with the H_2 to raise the flame temperature enough to release sodium from the NaCl on the wire mesh. In this H_2 flame, the spin relaxation rate is comparatively large ($\approx 12.6 \times 10^6/\text{sec}$) and quite uniform over a large region in the flame. Hence our studies indicate that the contour map of the relaxation rates depends strongly on the type of flame.

AD-A056 767

COLUMBIA RADIATION LAB NEW YORK

F/G 7/4

RESEARCH INVESTIGATION DIRECTED TOWARD EXTENDING THE USEFUL RAN--ETC(U)

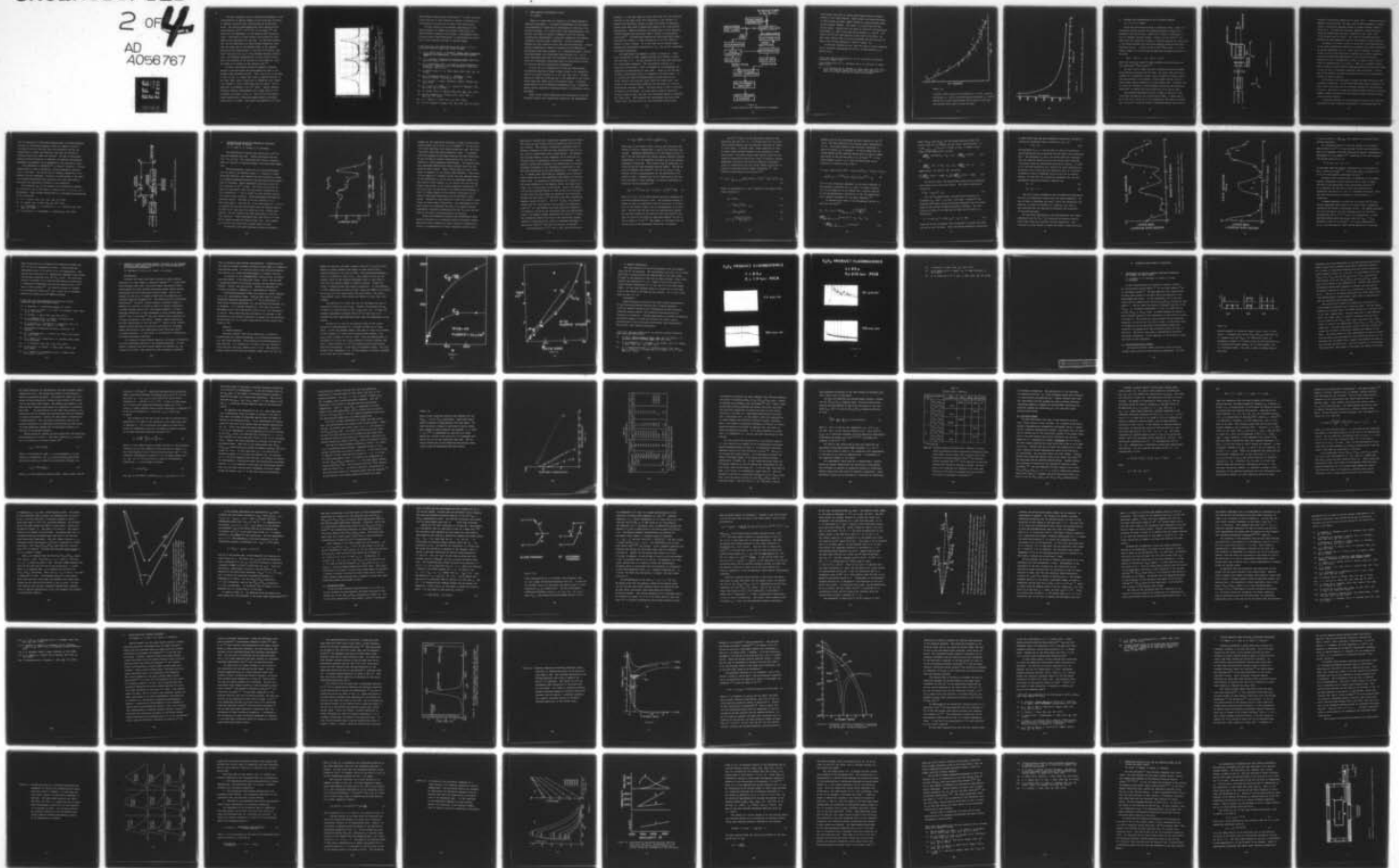
MAR 78 W HAPPER

DAAG29-77-C-0019

NL

UNCLASSIFIED

2 of 4
AD
A056 767



1

The spin relaxation rate is sensitively dependent on the concentrations of species capable of spin exchange collisions or chemical reactions with the polarized Na ground-state atoms. The neutral hydrocarbons have small depolarization cross sections ($10^{-22} - 10^{-24} \text{ cm}^2$) for Na atoms,⁽¹⁰⁾ and should not be responsible for the observed spin relaxation rates. The effect of finite transit time across the laser beam is also negligible for our case. One possible explanation for our observation of sharp minimum relaxation rates near the inner cone of the methane flame is the complete burning of the oxygen present in the fuel-rich mixture used, since collisions with O_2 or O are probably strongly depolarizing. The residual depolarization in this region could be due to the presence of OH radicals or other radicals, which are known to be present in the reaction zone.⁽³⁾

We have also observed strong RF magnetic resonance signals of spin-polarized optically-pumped Na atoms in the propane flame described earlier. Here, the set-up is the same as that in Fig. 19, except that H now is applied parallel to the laser beam, using a small pair of Helmholtz coils (about 3 cm diameter, 9 turns) positioned near the flame. The RF amplitude is estimated to be $\sim 10^{-5}$ Tesla. Typical magnetic resonance signals, photographed with a sweep time for H of 2 seconds, are shown in Fig. 22. This is the first experimental observation of optically pumped magnetic resonance transitions in a flame. This opens the possibility of using

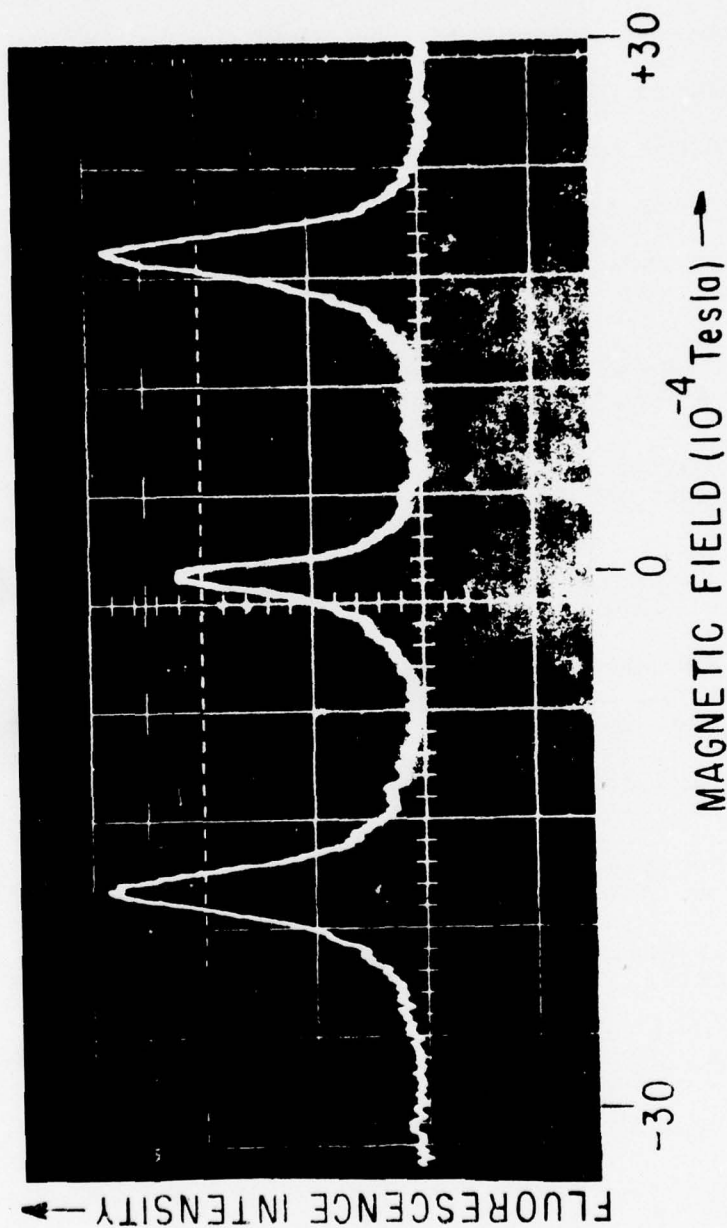


Figure 22: Oscilloscope trace showing RF magnetic resonance transitions (at $\pm 18 \times 10^4$ Tesla) and Hanle signal (at 0 Tesla) of optically pumped Na ground state atoms in flames. The RF frequency applied to the flame is 12 MHz.

spin-exchange spectroscopic techniques⁽¹¹⁾ to study the molecular structure of free radicals in flames or measuring the concentrations of radicals and other flame constituents.

Further studies of the possible applications of the optical pumping of flames with various constituents and under different pressures are planned. Such possible applications include flame diagnostics, or spectroscopy and detection of free radicals and ions in various flames.

* This work was also supported by the Air Force Office of Scientific Research under Grant AFOSR-74-2685.

- (1) A. G. Gaydon and H. G. Wolfhard, Flames, Their Structure, Radiation and Temperature, (Chapman and Hall, London, 1953).
- (2) C. P. Fenimore, Chemistry in Premixed Flames (Macmillan, New York 1964) p. 7.
- (3) A. A. Westenberg and R. M. Fristrom, Tenth Symposium on Combustion, Cambridge, 1964 (The Combustion Institute, Pittsburg, 1965) p. 473.
- (4) P. Regnier and J. P. E. Taran, Appl. Phys. Lett. 23, 240 (1973).
- (5) H. P. Hooymayers and C. Th. J. Alkemade, J. Quant. Spectros. Radiat. Transfer 6, 847 (1966).
- (6) P. L. Lijnse, J. Quant. Spectrosc. Radiat. Transfer 14, 1195 (1974).
- (7) S. M. Curry, W. Happer, A. C. Tam and T. Yabuzaki, Phys. Rev. Lett. 40, 67 (1978).
- (8) W. Franzen and A. G. Emslie, Phys. Rev. 108, 1453 (1957).
- (9) See for example R. L. DeZafra and W. Kirk, Amer. J. Phys. 35, 573 (1967).
- (10) R. J. McNeal, J. Chem. Phys. 37, 2726 (1962).
- (11) See for example W. Happer, Rev. Mod. Phys. 44, 216 (1972).

D. TIME RESOLVED SPECTROSCOPY OF NO_2^*

(R. Gupta†)

There is a great deal of interest in the understanding of combustion phenomenon. A thorough understanding of the combustion phenomenon is essential for development of efficient, non-polluting engines. As a first step in the understanding of combustion, one needs to develop diagnostic tools for species concentration measurements in practical combustion environments (luminous, particle-laden, turbulent). Optical diagnostic methods are very attractive since they are non-perturbing. Several optical techniques for species concentration and temperature measurements have been proposed, e.g., spontaneous Raman, coherent antistokes Raman, and fluorescence spectroscopy, etc. All of these techniques have their own advantages and we have chosen to study the fluorescence techniques which are particularly suited for minority species concentration measurements.

We have set up an experiment to study the time-resolved fluorescence spectrum of gases normally found in the combustion region of aircraft engines (e.g., NO , NO_2 , SO_2 , etc.). We have started to study NO_2 since NO_2 has a rich spectrum in the visible region where dye lasers can be conveniently used. A thorough understanding of the fluorescence properties of NO_2 is essential before optical diagnostic techniques based on fluorescence can be developed.

Study of the visible absorption and fluorescence of NO_2 has presented several very interesting theoretical and experimental

problems. It has been known for quite some time that the radiative lifetime of the upper state (for absorption in the visible) as deduced from absorption studies is about two orders of magnitude shorter than that found by phase-shift method or by time-resolved spectroscopy. Numerous extensive investigations of this anomalous lifetime problem have been made under a variety of experimental conditions.⁽¹⁾ Although much progress has been made toward understanding this anomaly, a clear explanation of all the observed effects is still lacking. It is with this aim of further understanding the fluorescence properties of NO_2 that we have undertaken the present experiment.

Our experimental arrangement is shown in Figure 23. Light from a Molelectron N_2 laser pumped dye-laser goes through a quartz cell with NO_2 in it. The NO_2 pressure can be varied and monitored by a capacitance manometer. The fluorescence from NO_2 in a relatively narrow band ($\sim 10\text{\AA}$) is selected by a spectrometer and detected by a photomultiplier tube (PMT). Output of the PMT goes through a discriminator which is operated in the gated mode, i.e., it accepts only those fluorescent photon pulses which arrive within certain time-interval (gate) after the laser pulse. The output of the discriminator supplies the stop pulse to a time to pulse-height converter (TPHC). The start pulse to TPHC is provided by output of a PIN diode. By using neutral density filters we arrange things so that less than one fluorescent photon is detected per laser pulse. TPHC measures the time between the laser pulse (start pulse) and the arrival of the fluorescent photon pulse

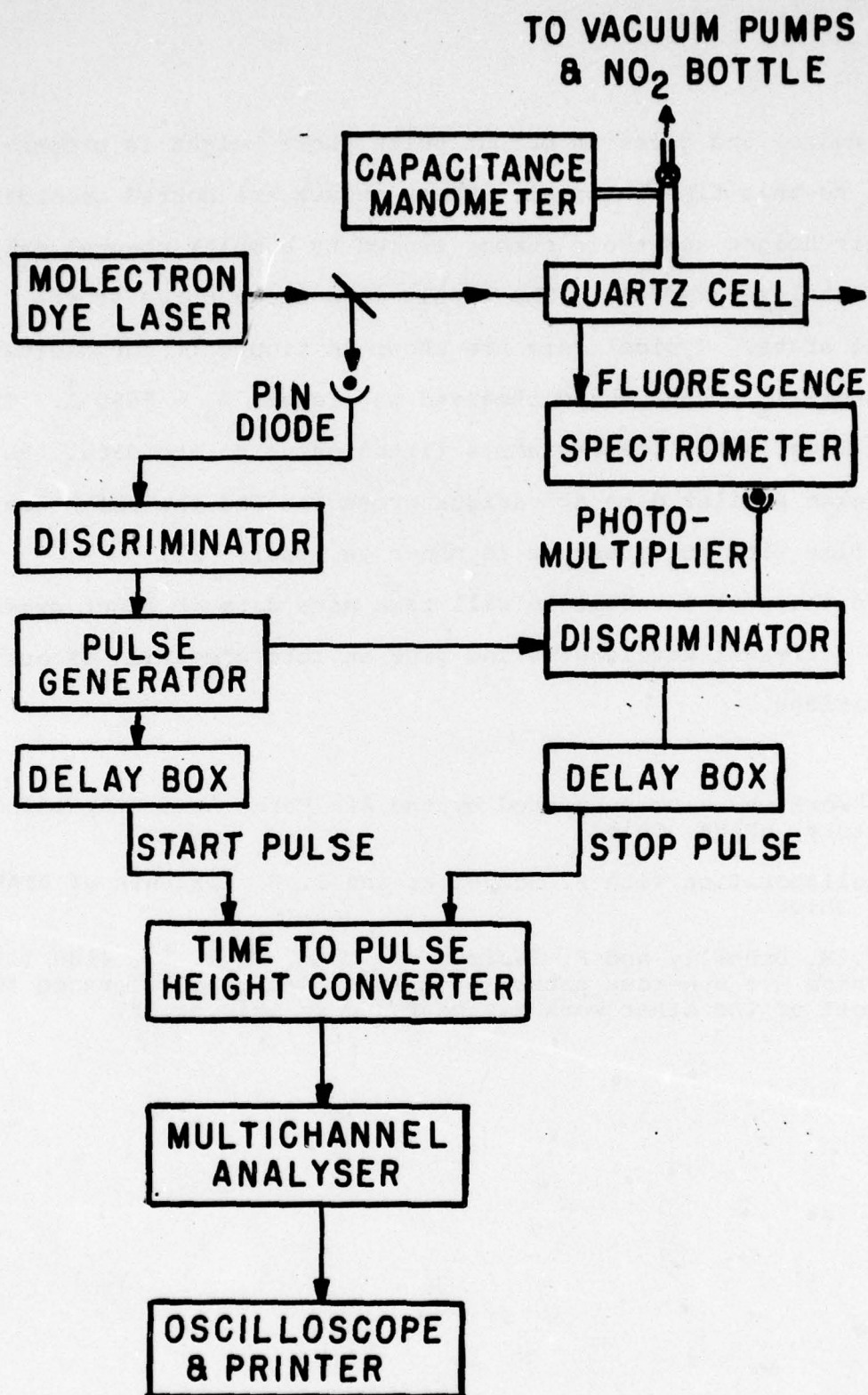


Figure 23
A block diagram of our experimental arrangement.

(stop pulse) and gives an output pulse whose height is proportional to this time interval. These pulses are sorted according to their height and their number stored by a multi-channel pulse height analyzer (MCPHA). The result is a decay curve of the excited state. Typical data are shown in Figure 24 for excitation wavelength $\lambda_E = 4505 \text{ \AA}$ and observed wavelength $\lambda_O = 5950 \text{ \AA}$. The smooth line is the least-squares fitted curve to the data. We have taken similar data at various pressures and the variation of decay time with NO_2 pressure is shown in Figure 25.

In the next interval we will take more data at lower pressures and at different wavelengths and give an interpretation of our observations.

* This work was also supported by the Air Force Aero Propulsion Laboratory, WPAFB, Ohio.

† In collaboration with P. Schreiber and S. W. Kizirnis of AFAPL, WPAFB, Ohio.

- (1) V. M. Donnelly and F. Faufman, J. Chem. Phys. 66, 4100 (1977). There are numerous papers on this subject and reference to most of the other work may be found in this paper.

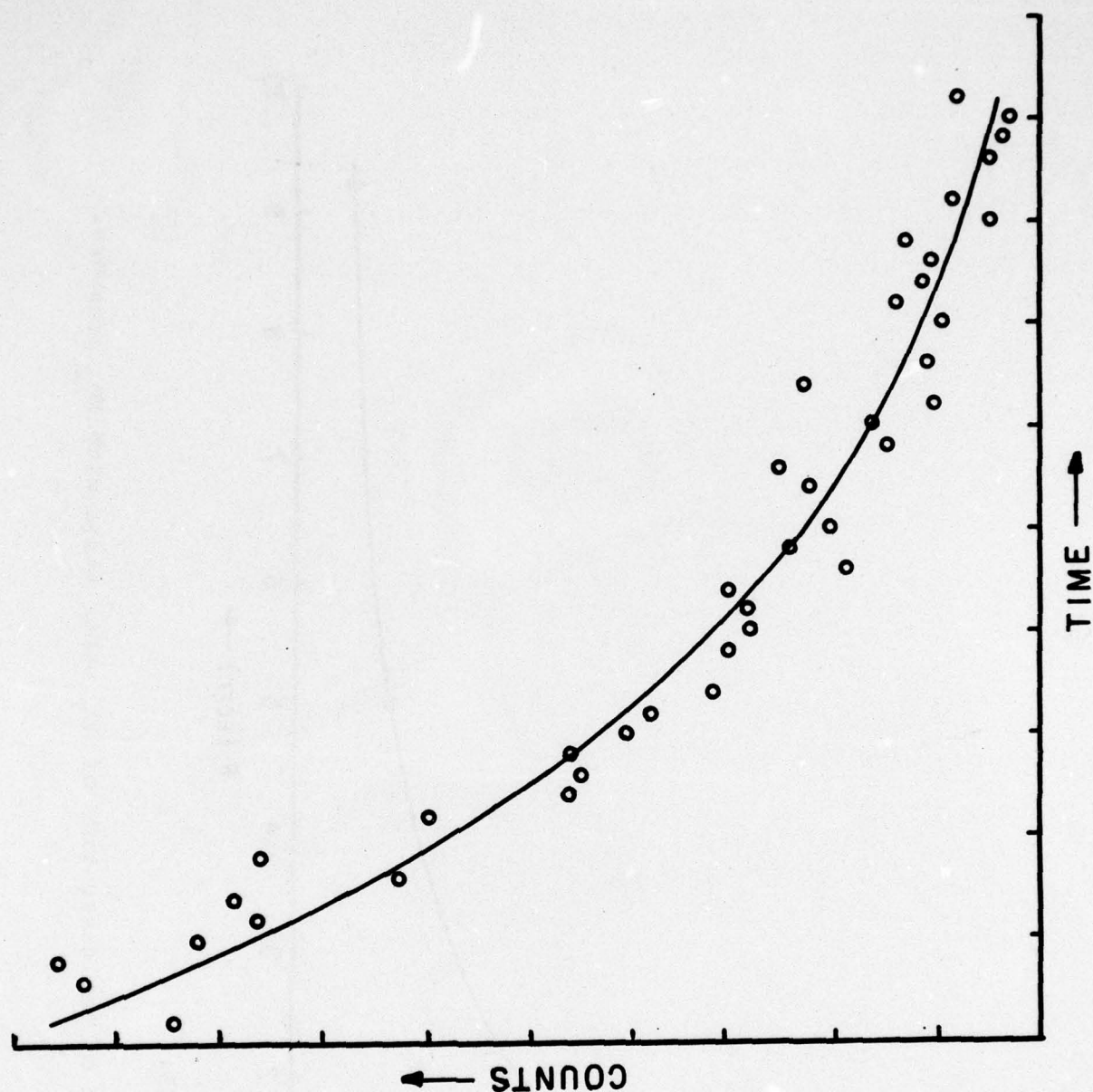


Figure 24 :

A typical decay curve for NO_2 pressure $P = 5$ Torr, exciting wavelength $\lambda_E = 4505 \text{ \AA}$ and observation wavelength $\lambda_O = 5950 \text{ \AA}$. Smooth line is the least-squares fitted curve to the data. The abscissa full scale is about 200 nsec.

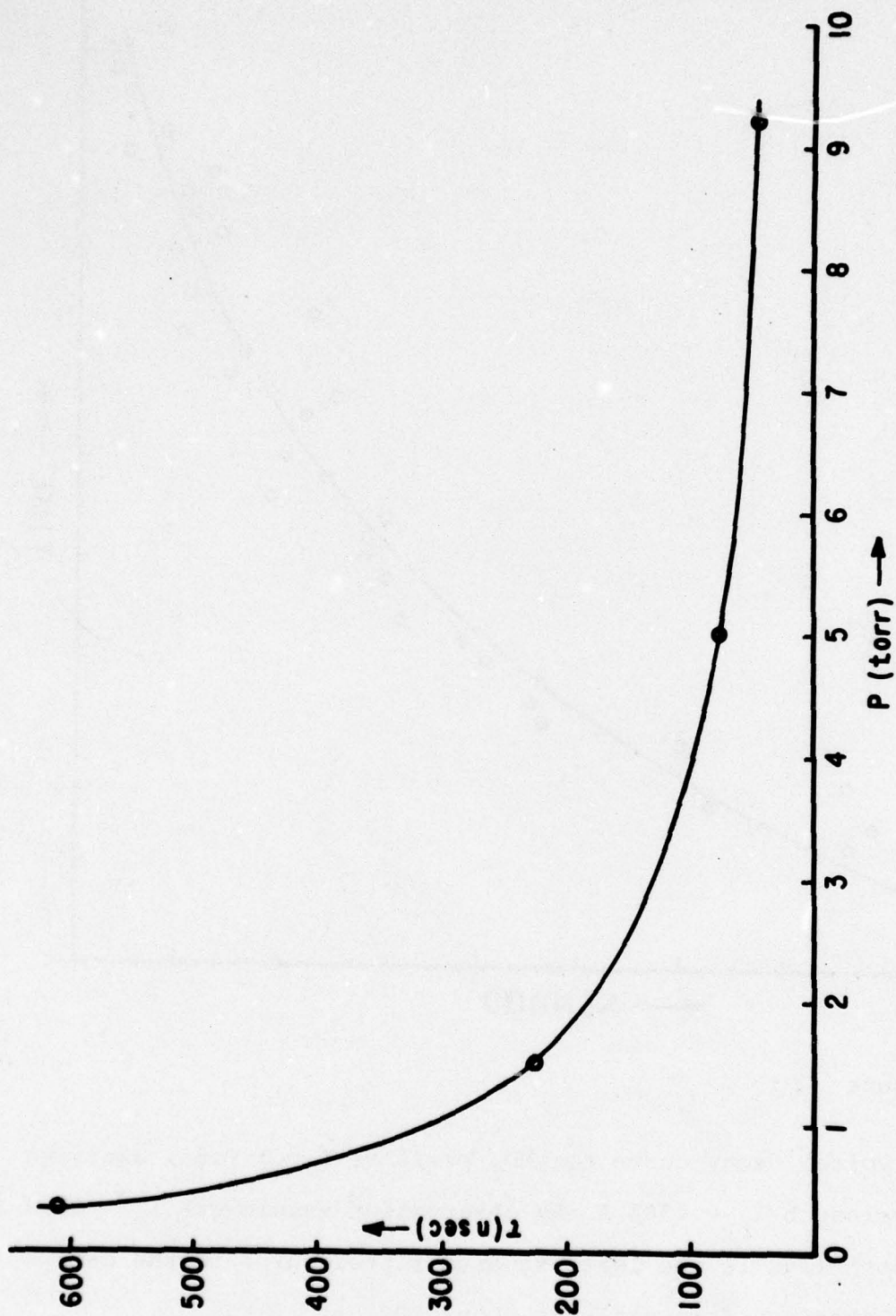


Figure 25:

Variation of the decay time of NO₂ upper state with NO₂ pressure.

E. NUCLEAR SPIN POLARIZATION OF Xe BY OPTICAL PUMPING

(M. Y. Hou, W. Happer)

Physicists have found sources of polarized nuclei useful for performing nuclear physics and elementary-particle experiments. Systems of polarized nuclei might also be used in gyroscopes, or even in computer storage systems. Recent work by Grover⁽¹⁾ has shown that very efficient transfer of angular momentum can take place in collisions between spin polarized Rubidium atoms and the heavy noble-gas nuclei. As many as 10% of the ^{129}Xe nuclei in a low density sample can be polarized through spin-exchange collisions of the form,



where the optically pumped Rb atom transfers its polarization to the unpolarized ^{129}Xe nucleus.⁽²⁾

We would like to apply the spin exchange polarization method using sodium to polarize the Xe atoms. By using laser excitation instead of a conventional alkali lamp, we expect to obtain significant polarization in Xe samples of much higher density since we could supply angular momentum at a much higher rate. We would like to study the influence of spin exchange collisions and relaxation mechanisms in samples with high densities of Xe and Na vapor.

One proposed experimental setup is shown in Figure 26: A 5ml 1720 glass cylindrical cell containing Na metal, a buffer gas of N_2 at 500 torr, and Xe or Kr at a pressure on the order of several torr or more is contained within a resistance-heated oven which is

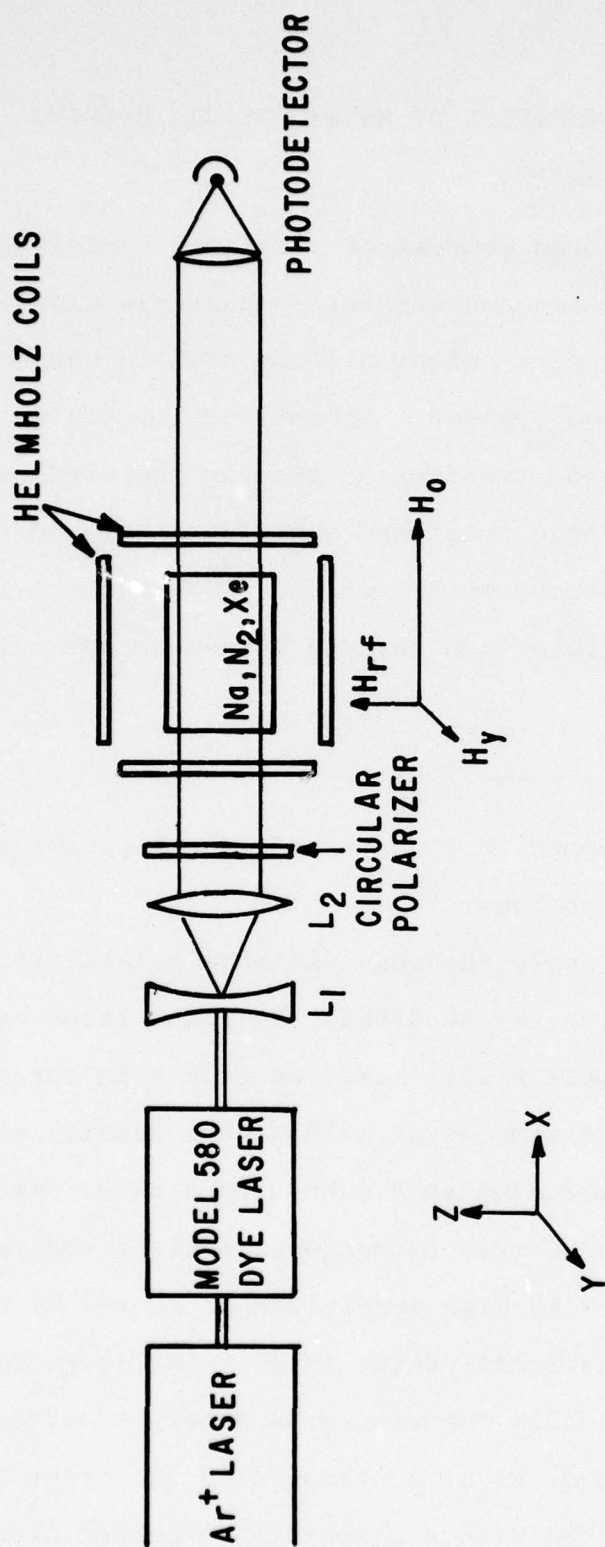


Figure 26
NG Polarization Experimental Setup

capable of controlled temperature to about 150°C. A three-axis set of Helmholtz coils surround the oven, and the whole assembly is placed within a cylindrical magnetic shield to reduce external fields to below 10 μ G. Na atoms are optically pumped by a Spectra-Physics model 580 single mode dye laser, pumped by an Ar^+ laser, with 100 mw output power at 5896 Å. The light is directed along the shield axis and transmitted light is collected by a photo detector.

We apply a rf field, $H_1 \cos \omega t$, along the z-axis perpendicular to the light transmitting direction to modulate the light transmitted at various harmonics $p\omega$ of ω . Since the $p=1$ component is proportional to the Z-axis field and is insensitive to other components, we want the noble-gas magnetization to be oriented along the sensitive Z axis. Besides the H_0 field, we apply a small field H_y which is perpendicular to H_0 and H_{rf} . When H_0 is suddenly turned off the noble gas magnetization precesses slowly and coherently about H_y and can give a sinusoidal component along the Z-axis. In this way we can measure the noble gas magnetization and its exponential growth and decay constants.

Also efforts are being made to study the NaXe collisional spin relaxation mechanism. In the system described above, relaxation is due to wall collisions and to collisions between Xe and polarized Na atoms. There are at least two possible types of Na-Xe collisions; sudden, binary collisions and three-body sticking collisions which lead to bound molecules.

Convincing evidence for the existence of alkali atom-inert gas molecules has been presented by Bouchiat,⁽³⁾ who showed that the

rate of relaxation of polarized rubidium atoms in krypton depended strongly on the external magnetic field for magnetic fields in the range of 0-100 G and also that the relaxation rate was not proportional to buffer gas pressure, even when the effects of diffusion were fully taken into account. We wish to investigate whether molecule formation is important by observing the pressure dependence and magnetic field dependence of the relaxation rates.

The experimental arrangement⁽⁴⁾ is shown in Figure 27. A strong pumping beam is used to establish a large ground-state polarization in the vapor. The strong beam is suddenly removed by a fast shutter, and the subsequent evolution of polarization in the vapor is followed by monitoring the absorption of a very weak probing beam which has negligible influence on the relaxation.

By monitoring $\langle S_z \rangle$ of the system, we are planning to measure the relaxation over a wide range of pressure from .1 torr to 2 or 3 atmospheres. These studies should help us to determine the mechanisms of the relaxation.

- (1) B. C. Grover, Phys. Rev. Lett. 40, 391 (1978).
- (2) W. Happer, Rev. of Mod. Phys. 44, 169 (1972).
- (3) C. C. Bouchiat, M. A. Bouchiat & L. C. L. Pottier, Phys. Rev. 181, 144 (1969).
- (4) M. Bouchiat & F. Grossetête, J. Physique 27, 353 (1966).

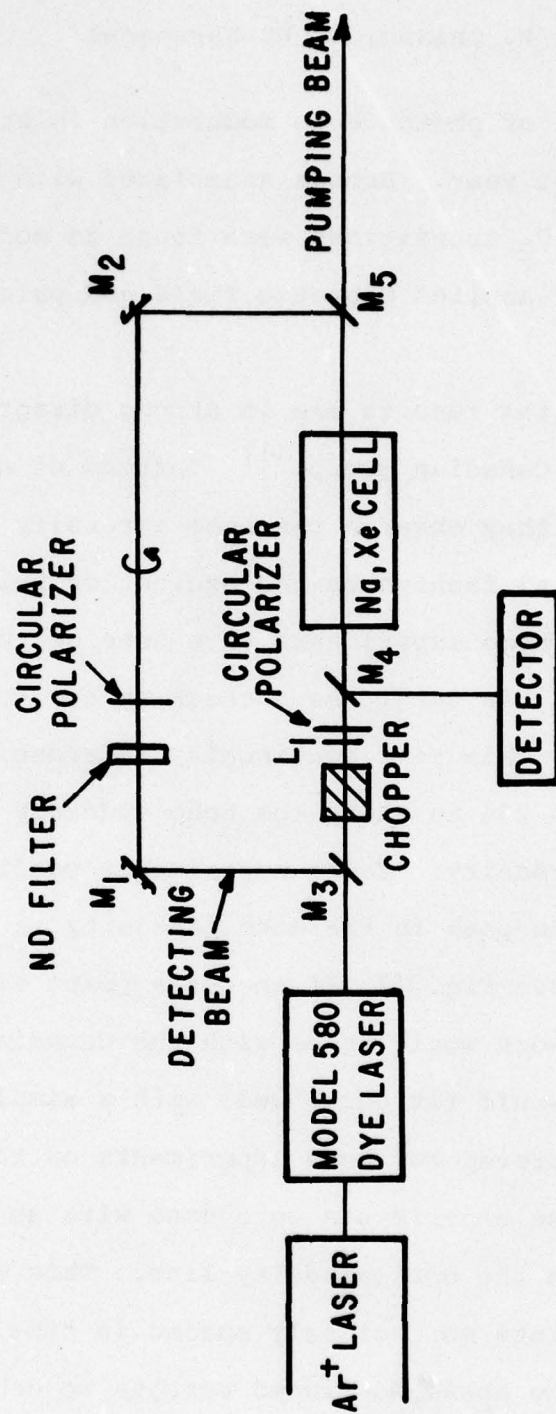


Figure 27
Experimental Arrangement for Relaxation Measurement

F. RELAXATION AND EXCITATION TRANSFER OF OPTICALLY EXCITED STATES IN SOLIDS*

(Y. C. Chen, K. P. Chiang, S. R. Hartmann)

The observation of photon echo modulation in Pr^{3+} in LaF_3 was reported last year. Echoes associated with the $^3\text{H}_4 \leftrightarrow ^3\text{P}_0$ and $^3\text{H}_4 \leftrightarrow ^1\text{D}_2$ transitions were found to modulate both as a function of applied magnetic field and pulse separation.

These experimental results are in strong disagreement with the work of the Canadian group.⁽¹⁾ Instead of a modulated echo behavior, they observe the echo intensity to decay in a simple exponential fashion as the excitation pulse separation is increased. These experiments were done on the $^3\text{H}_4 - ^3\text{P}_0$ transition of Pr^{3+} in LaF_3 . As a check on our work we redid our experiment, this time continually referencing the echo intensity at $\tau = 234$ ns where the echo suddenly regains its initial large intensity. These experiments confirmed our previous results. The peak in the echo intensity is in fact quite sharp. (See Fig. 28) If the data point at $\tau = 234$ ns is deleted then our work would agree with the Canadian work in as much as our data would fit quite well with a simple exponential. We also improved our echo experiments on the $^3\text{H}_4 - ^3\text{P}_0$ transition. These experiments were done with an odd number of passes through the optical delay line. This enabled us to obtain data points more closely spaced in time.

On obtaining the above mentioned results we decided to

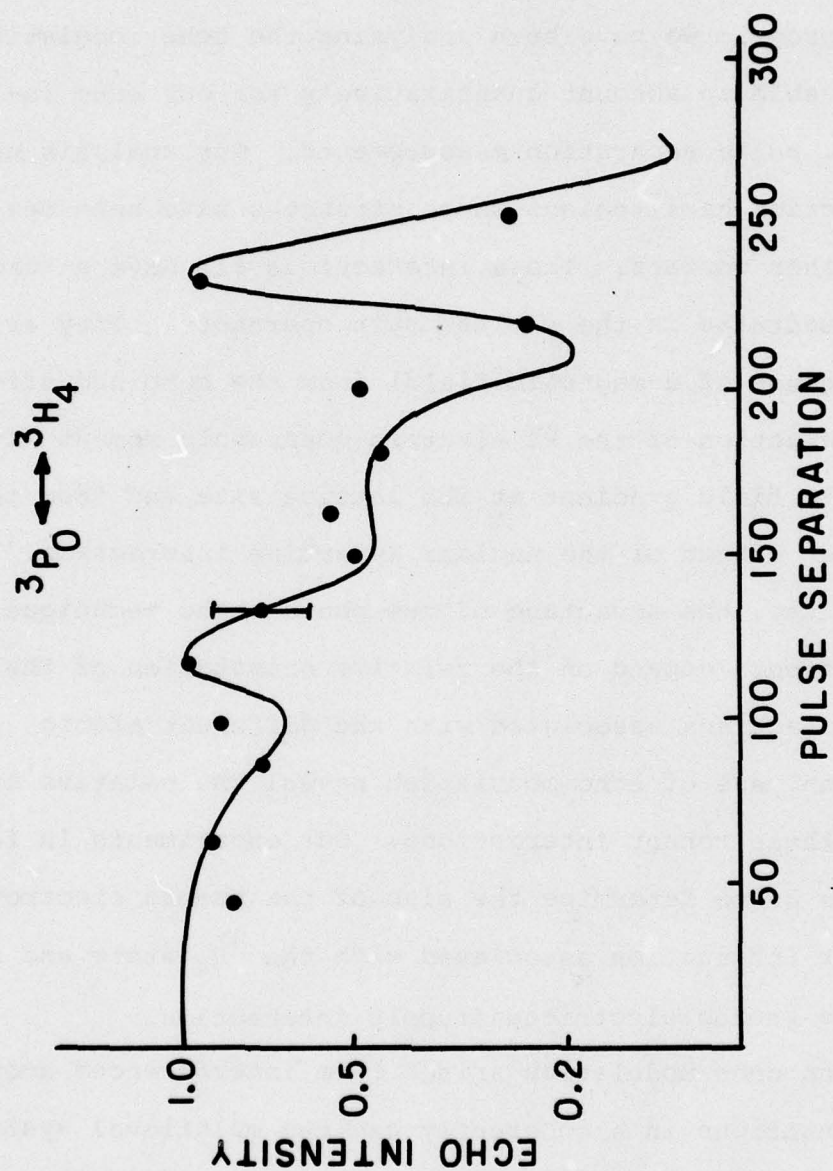


Figure 28:

Echo intensity vs pulse separation for ${}^3\text{P}_0 \leftrightarrow {}^3\text{H}_4$ transition.

The impurity concentration is 0.1%.

change our echo generating technique in order to obtain more stable echoes and to allow us to do PENDOR.⁽²⁾ We are building a high repetition rate double pulsed dye laser with electronically controlled pulse separation times. In parallel with this program we have been analyzing the echo modulation. We are now able to account quantitatively for our echo intensity vs. pulse separation measurements. Our analysis uses the interaction hamiltonians whose strengths have been measured by other workers. These interactions all have a form which is quadratic in the nuclear spin operators. They arise (in the absence of a magnetic field) from the combined effect of the interaction of the Pr electric quadrupole moment with the electric field gradient at its lattice site and from the second order effect of the nuclear hyperfine interaction.⁽³⁾ As we will see, the advantage of the photon echo technique is that its effects depend on the relative orientation of the tensor interactions associated with the different atomic states. Analysis of echo modulation reveal the relative orientation of these tensor interactions. Our experiments, in fact, also enable us to determine the sign of the pseudo electroquadrupolar interaction associated with the 3H_4 state and the sign of the pseudo electricquadrupole interaction.

Photon echo modulation arises from interferences among atomic transitions in a coherently excited multilevel system. Modulation occurs whenever an atomic system is coherently excited to a superposition of nearly degenerate energy levels.

Each atom is excited into a multilevel superposition and beats with itself as the various excited transitions come into and out of phase. This process is physically different from incoherent relaxation in that the echo degradation does not result from an irreversible loss of phase memory. The apparent loss of phase memory is only temporary and is partially recoverable when an appropriate condition is satisfied. Local maxima of photon echo intensity are expected when the angular frequency difference of two interfering transitions is such that when multiplied by the pulse separation τ its product is 2π . If energy level splittings are dependent on an external field, there will be echo modulation with respect to the magnetic field. By studying the echo behavior as a function of the pulse separation or the magnetic field, the energy splittings can, in principle, be determined. Photon echo modulation has been observed before in ruby as well as in $\text{LaF}_3:\text{Nd}^{3+}$. In both cases the multilevels are caused by the interaction between the echo atoms (Cr^{3+} and Nd^{3+}) with their neighboring magnetic nuclei (Al and F). For Pr^{3+} in LaF_3 , the coupling between the Pr^{3+} ions and the F or La nuclei is negligible since Pr^{3+} is a non-Kramers ion whose electronic degeneracy is completely lifted by the crystalline field and consequently there is no magnetic moment associated with the Pr^{3+} in LaF_3 . The interaction which gives rise to the "multilevel system" capable of interfering with itself is therefore different in the case of $\text{LaF}_3:\text{Pr}^{3+}$ than that in ruby and in $\text{LaF}_3:\text{Nd}^{3+}$.

The hamiltonian of Pr^{3+} ions in LaF_3 can be written as

$$H = H_{CF} + g\beta\vec{H}\cdot\vec{J} + A\vec{I}\cdot\vec{J} + g_n\beta_n\vec{H}\cdot\vec{J} + H_Q \quad (1)$$

where H_{CF} is the crystal field, g and g_n are electronic and nuclear g factors, respectively, β and β_n are electronic and nuclear magnetons, respectively, \vec{H} is the magnetic field, \vec{J} and \vec{I} are the electronic and nuclear angular momentum vectors, respectively, A is the hyperfine constant, H_Q is the electric quadrupole interaction. The nuclear electric quadrupole interaction has not been measured directly before. The nQR results of Anderson and Proctor⁽⁴⁾ for the La nuclei in LaF_3 provide us with an approximation for the hamiltonian of Pr nuclei in LaF_3 . Assuming that the Pr impurities do not disturb the electric field gradient, the nuclear quadrupole interaction can be expressed as⁽⁴⁾

$$H_Q = \pm e^{-i\theta J_Y} (0.42 I_Z^2 + 0.26 (I_X^2 - I_Y^2)) e^{i\theta J_Y} \text{ MHz} \quad (2)$$

where $\theta (= 53.6^\circ)$ is the angle between the major component of the field gradient and the \hat{z} axis. The coordinate system is chosen so that \hat{y} is parallel to the two fold axis, \hat{z} is parallel to the crystal C-axis, and \hat{x} is perpendicular to \hat{y} and \hat{z} axis. We have used the fact that the antishielding factors for the rare earths are the same for each rare earth⁽⁵⁾ and that the ratio of the electric quadrupole moments for the Pr and La nuclei is -0.32 .⁽⁶⁾ The symbol (\pm) indicates that the overall sign of the quadrupole interaction is unknown.

For Pr^{3+} in LaF_3 , all the electronic levels are non-degenerate and have $\langle \vec{J} \rangle = 0$. It follows then that the electronic Zeeman coupling and the hyperfine coupling all vanish to first order. In second order, these couplings all have an effect which strength depends on the proximity of near lying levels. The major second order effects come from the hyperfine interaction acting with itself to provide a pseudo-quadrupole interaction and with the hyperfine interaction acting in combination with the nuclear Zeeman interaction to produce an enhanced nuclear Zeeman interaction.⁽³⁾ The effective hamiltonian can be written as⁽⁷⁾

$$H = H_{\text{CF}} + \sum_{i=x',y',z'} g_n \beta_n H_i (1+K_i) I_i + \left[P I_y^2 + \frac{\eta}{3} (I_z^2 - I_x^2) \right] + H_Q \quad (3)$$

where the parameters K_i , P and η depend on the crystal field level according to

$$K_i = 2g\beta\Lambda_{ii} \quad (4)$$

$$P = \frac{\Lambda_{x'x'} + \Lambda_{z'z'}}{2} - \Lambda_{y'y'} \quad (5)$$

$$\tau = \frac{\Lambda_{z'z'} - \Lambda_{x'x'}}{2} \quad (6)$$

$$\Lambda_{ij} = \sum_n \frac{A \langle 0 | J_i | n \rangle \langle n | J_j | 0 \rangle}{E_n - E_0} \quad (7)$$

where E_n and $|n\rangle$ are the energy and wave function of the n^{th} level. The wave function of the singlet under consideration is $|0\rangle$. The primed system is the principle coordinate in which the tensor Λ_{ij} is diagonal. It can be shown that the primed system and the unprimed system share at least a common axis which is the two fold axis of C_2 (\hat{y} axis).⁽⁸⁾ If the angle between \hat{z} and \hat{z}' is θ , then the hamiltonian can be written as a function of K_i 's and θ .

$$H = H_{CF} + g\beta_n \{ [(1+K_z) \cos^2 \theta + (1+K_x) \sin^2 \theta] I_z + [(1+K_z) - (1+K_x)] \frac{1}{2} \sin^2 \theta I_x \} + e^{-iJ_y \theta} P [I_y^2 + \frac{\eta}{3} (I_z^2 - I_x^2)] e^{iJ_y \theta} + H_Q \quad (8)$$

If P is the interaction parameter for the major component of the principle coordinate of Λ_{ij} , then P is always negative. If P is not negative, we can always add a constant operator to the pseudoquadrupole interaction so that the hamiltonian has a negative parameter for the major component.⁽⁸⁾

To determine the range of the enhancement factors, we work out sum rules⁽⁸⁾

$$K_{x'} + K_{y'} + K_{z'} = 2g\beta A \sum_{i=x',y',z'} \sum_n \frac{|\langle 0 | J_i | n \rangle|^2}{\Delta E_n} \quad (9)$$

$$\frac{2g\beta A}{(\Delta E)_{\max}} \sum_{i=x',y',z'} \sum_n |\langle 0 | J_i | n \rangle|^2 < K_{x'} + K_{y'} + K_{z'}$$

$$< \frac{2g\beta A}{(\Delta E)_{\min}} \sum_{i=x',y',z'} \sum_n |\langle 0 | J_i | n \rangle|^2 \quad (10)$$

where $(\Delta E)_{\max}$ and $(\Delta E)_{\min}$ are the energy spacings between the ground state and the highest and the lowest excited states. If a term $\sum_{i=x',y',z'} |\langle 0 | J_i | 0 \rangle|^2$, which is zero, is added to both sides of the inequalities, we have

$$\frac{2g\beta A}{(\Delta E)_{\max}} \langle 0 | J^2 | 0 \rangle < K_{x'} + K_{y'} + K_{z'} < \frac{2g\beta A}{(\Delta E)_{\min}} \langle 0 | J^2 | 0 \rangle \quad (11)$$

or

$$\frac{2g\beta A}{(\Delta E)_{\max}} J(J+1) < K_{x'} + K_{y'} + K_{z'} < \frac{2g\beta A}{(\Delta E)_{\min}} J(J+1) \quad (12)$$

Combining Eq. (5) and Eq. (12), we obtain

$$\frac{1}{3} \left[\frac{2g\beta A}{(\Delta E)_{\max}} J(J+1) - 4\beta g p \right] < K_{y'} < \frac{1}{3} \left[\frac{2g\beta A}{(\Delta E)_{\min}} J(J+1) - 4\beta g p \right] \quad (13)$$

For the 3P_0 state, the second order effects can be neglected since there are no near lying levels. The nuclear hamiltonian is given by

$$H(^3P_0) = g_n \beta_n \vec{H} \cdot \vec{I} + H_Q \quad (14)$$

For the 3H_4 ground state, the hamiltonian contains two variables, $K_{y'}$, and θ , if p and n are known. Erickson⁽⁹⁾ has measured the nuclear energy splittings associated with the ground state by the optical RF double resonance technique. The zero field splittings of 8.47 MHz and 16.7 MHz can be fitted by a hamiltonian

$$H = -4.185 [I_z''^2 + 0.036 (I_x''^2 - I_y''^2)] \text{ MHz} \quad (15)$$

where one of the coordinate axis is parallel to \hat{y} while the other two are in the \hat{x} - \hat{z} plane. Since the pseudo quadrupole interaction

is much larger than the pure quadrupole interaction, Erickson's interaction parameters imply, according to Eq. (13),

$$6 < K_y' < 12 \quad . \quad (16)$$

The magnitude of K_y , θ , and the over all sign of the excited state hamiltonian can be obtained from the photon echo modulation data. The parameters K_y and θ are varied under the constraint that the combined effect of H_Q and the second order hyperfine interaction gives the hamiltonian obtained by Erikson. In order to fit the echo modulation as a function of pulse separation as presented in Fig.28 and the echo modulation data as a function of magnetic field as presented in Fig.29 and Fig.30 simultaneously, we find that the interaction parameters for the pure quadrupole interaction should be negative and

$$K_y' = 8 \quad (17)$$

$$K_x + K_z, \approx 1.3 \quad . \quad (18)$$

The solid curves accompanying the corresponding experimental data are the theoretical curves using the above parameters. We are not able to determine the angle θ since the theoretical echo behavior is found not sensitive to θ when $K_y' \gg K_x'$ and K_z' . More detailed data are required to determine the orientation of the principle axes.

We have shown theoretically and experimentally that echoes associated with the $^3H_4 \leftrightarrow ^3P_0$ transition do modulate significantly when taken as a function of pulse separation. The locations of local maxima of echoes are simply integer multiples

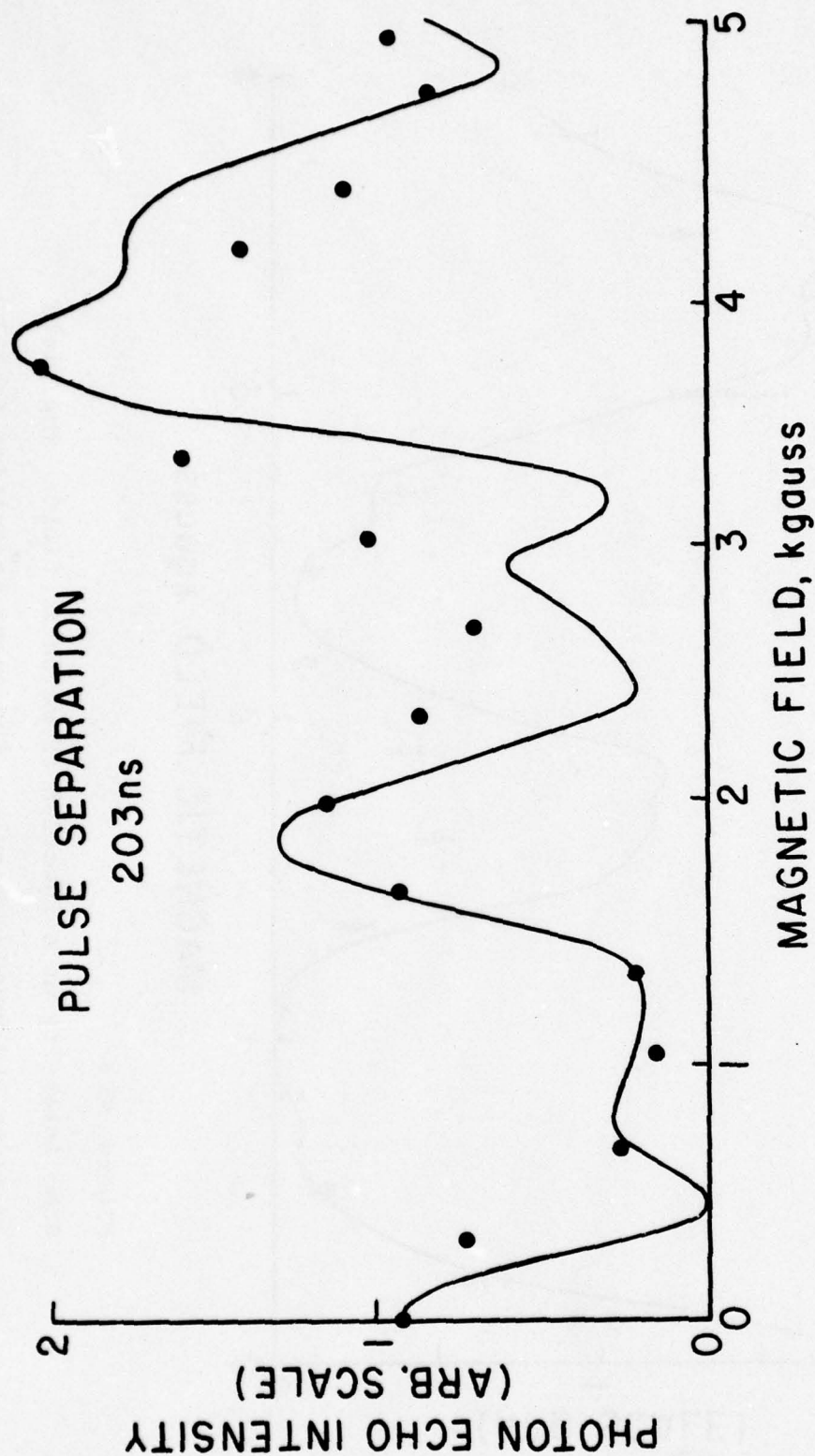


Figure 29 :

Echo intensity as a function of magnetic field. The field is along the crystal c-axis. The pulse separation is 200 ns.

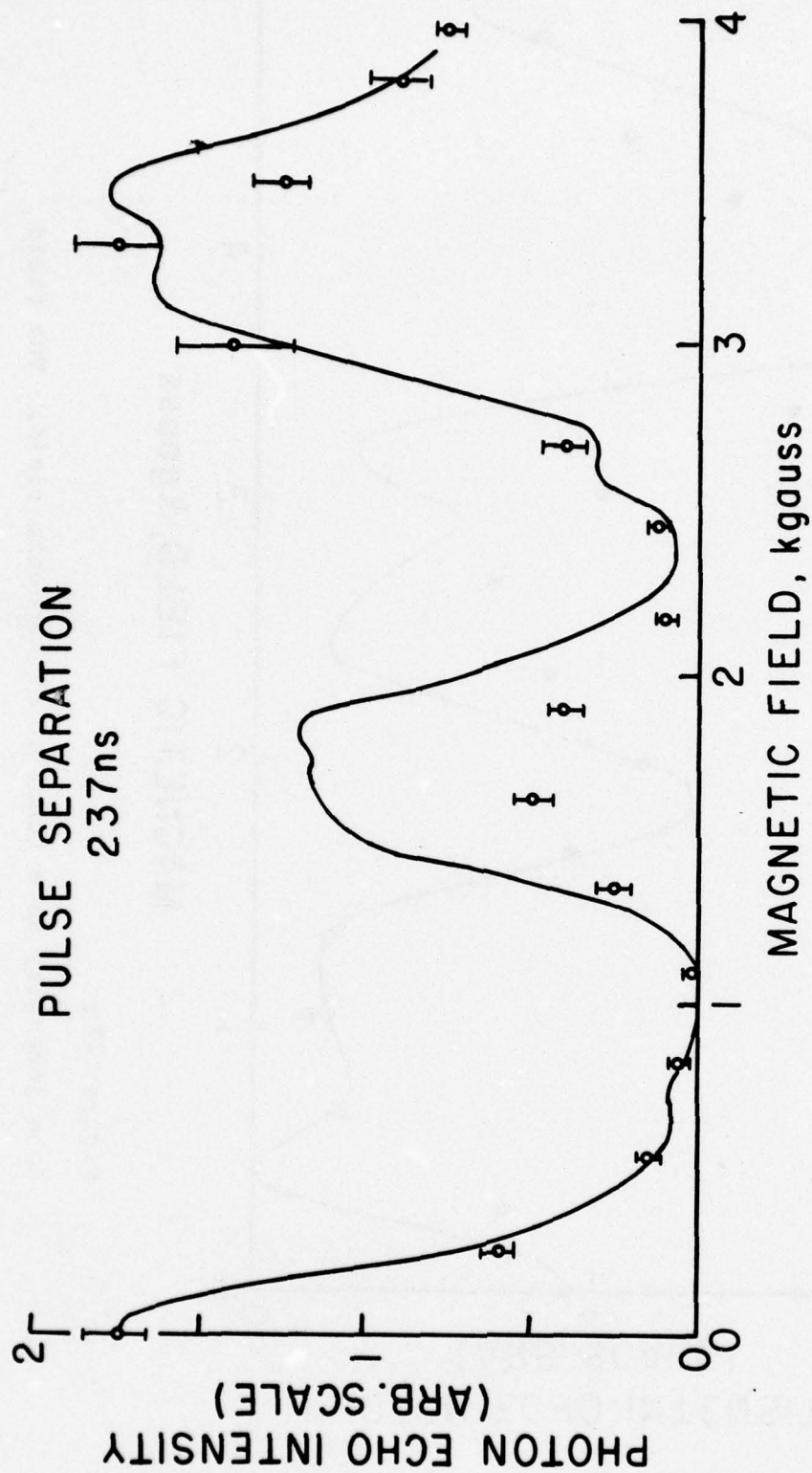


Figure 30 :

Echo intensity as a function of magnetic field. The field is along the crystal c-axis. The pulse separation is 237 ns.

of 115 ns, which is $\frac{1}{8.37}$ MHz, the inverse of the ground state nuclear splittings.

An interesting result is that the average of the enhancement factors for Pr^{3+} in LaF_3 inferred from the echo modulation data is in agreement with that obtained by magnetic susceptibility measurement in PrF_3 powders.⁽¹⁰⁾ According to our data analysis, the average value of K_i 's is

$$\bar{K} = \frac{1}{3} (K_x + K_y + K_z) = 3.1 \quad (19)$$

On the other hand the magnetic susceptibility of the powder of PrF_3 is found to be $\frac{1}{60}$ ⁽¹⁰⁾, which also gives an average value of 3.1 for the magnetic enhancement factors.⁽⁷⁾

We would like to mention that the magnitude of the largest magnetic enhancement factor inferred from our data is almost one half of the enhancement factor obtained by Erickson.⁽⁹⁾

It is possible that Erickson's result was obtained by an inadvertant excitation of a $\Delta M = \pm 2$ forbidden transition which had twice the transition frequency as the allowed $\Delta M = \pm 1$ transition.

A PENDOR experiment is under way to resolve the 3P_0 state nuclear quadrupole splittings and to obtain direct information concerning the magnetic enhancement factors. The PENDOR technique will also provide us with the knowledge about the electronic antishielding factor of Pr^{3+} ion at low temperatures. We have generated photon echoes associated with the $^4I_{15/2} \leftrightarrow ^4S_{3/2}$ transition (5387 Å) of $\text{LaF}_3:\text{Er}^{3+}$. At a pulse separation of 64 ns, a strong magnetic field induced modulation is observed.

This is believed to be caused by the interaction between the Er^{3+} ion and its neighboring F nuclei. Photon echoes are observable only at 41 ns and 64 ns in low temperatures. This implies that there must be a temperature independent fast relaxation process associated with the $^4\text{S}_{3/2}$ state. The relaxation process is probably a non radiative multiphoton process which is temperature independent and has been observed also in Er^{3+} ions in oxide glasses.⁽¹¹⁾ We intend to pursue our studies of the relaxation process Er^{3+} ions in LaF_3 and in amorphous materials by photon echo and PENDOR technique.

* This work was also supported by the National Science Foundation under Grant NSF-DMR77-05995.

- (1) N. Takeuchi, J. Luminescence 12/13, 743 (1976).
- (2) P. F. Liao, R. Leigh, P. Hu, and S. R. Hartmann, Phys. Lett. 41 A, 285 (1972).
- (3) B. Bleaney, J. Appl. Phys. 34, 1024 (1963).
- (4) L. O. Anderson and W. G. Proctor, Zeitschrift für Kristallographie 127, 366 (1968).
- (5) R. G. Barnes, R. L. Mössbauer, E. Kankelict, and J. M. Poindexter, Phys. Rev. 136 A, 175 (1964).
- (6) The Handbook of American Institute of Physics. 3rd Edition.
- (7) F. L. Aukhadeev and I. S. Konov, Sov. Phys. Solid State 15, 1929 (1974).
- (8) Y. C. Chen, K. P. Chiang and S. R. Hartmann, Optic Comm. to be published.
- (9) L. E. Erickson, Phys. Rev. B 16, 4731 (1977).
- (10) S. Kern and P. M. Raccach, J. Phys. Chem. Solids. 26, 1625 (1965).
- (11) C. B. Layne, W. H. Lowdermilk and M. J. Weber, Phys. Rev. B 16, 10 (1977).

G. DYNAMICS OF LASER INITIATED CHEMICAL REACTIONS IN LOW PRESSURE GASES WITH MODE SPECIFIC EXCITATION (CO₂ LASER DECOMPOSITION OF PERFLUOROCYCLOBUTANONE)*

(K. Casleton, G. Hill, N. J. Turro, G. W. Flynn)

Introduction:

Infrared (IR) lasers have been utilized to induce chemical reactions in a large number of molecular systems.⁽¹⁾ In some cases, such reactions occur from a molecular energy distribution which exists before the laser excited vibrational energy levels achieve equilibrium with the translational energy levels. Part of the interest in the use of IR lasers arises from the possibility of selective molecular decomposition. The selectivity may be molecular selectivity⁽²⁾ (in which a single isotope, structural isomer or molecule in a mixture is caused to react) or channel selectivity (in which reaction occurs via a non-thermal pathway). To date, molecular selectivity is well documented in laser isotope separations⁽³⁾ and, in one case,⁽⁴⁾ BCl₃ was freed of COCl₂ impurity via IR laser irradiation of the COCl₂. However, channel selectivity has been demonstrated in only one case.⁽²⁾ Results which indicate channel selectivity must be carefully scrutinized as, following energy equilibration, high temperatures exist which may lead⁽⁵⁾ to thermal reaction. In such cases, it is difficult to deconvolute the laser and thermal reactions.

In a typical IR laser-induced reaction, the energy is deposited into the vibrational manifold of the absorbing molecule. If this energy is greater than the critical energy for reaction, E_0 , the molecule will react. The reaction of such a molecule is defined

here as infrared laser-induced photochemistry. Competitive with the reactive process is energy relaxation which leads to a thermally equilibrated system. If reaction occurs after this equilibration, the reaction is a laser-induced photolysis, or thermal reaction.

In addition to the aforementioned selectivities, IR lasers may prove useful in two additional areas. First, they provide a convenient method of initiating reactions for gas phase kinetic studies. Second, they may provide method for modeling the internal conversion component in a photochemical reaction.

Perfluorocyclobutanone (PFCB) was chosen as a model compound for an IR photochemical study. PFCB has been shown to exhibit wavelength dependent photochemistry.⁽⁶⁾ The UV photolysis of PFCB yields tetrafluoroethylene (C_2) and perfluorocyclopropane (C_3) as products. At a constant pressure of 1 torr the C_3/C_2 ratio decreases from 23 for irradiation at 405 nm to 0.2 for irradiation at 313 nm. This effect has been ascribed to an increase in the efficiency of the internal conversion of energy from the electronic excited state (1S) to a highly vibrationally excited ground state molecule (0S).

Results:

a. Product Analysis

The major product, from the IR photolysis of perfluorocyclobutanone are tetrafluoroethylene, (C_2) perfluorocyclopropane, (C_3) and carbon monoxide. Trace amounts of perfluoropropene are also observed. At a fluence of 0.75 J/cm^2 , with low conversion (less than 10%) the C_2/C_3 product ratio is ≈ 6.5 . The amounts of product formed varies with gas pressure, added inert gas (N_2 , Ar),

extent of reaction, and laser fluence. Figure 31 is a plot of the amount of product formed vs the number of laser events with a starting pressure of 0.4 torr of PFCB. The perfluorocyclopropane rises to a plateau of 6×10^{-3} torr. This plateau occurs for two reasons, first as the reaction progresses there is less PFCB to react and the products appear to inhibit reaction. Second the $c\text{-C}_3\text{F}_6$ is unstable under the reaction conditions. In high pressure (1 torr) experiments in which 0.5 torr $c\text{-C}_3\text{F}_6$ was added as a diluent, the $c\text{-C}_3\text{F}_6$ was $\approx 90\%$ reacted after 250 laser events. The tetrafluoroethylene (C_2F_4) rises quickly and begins to level after ≈ 200 flashes.

The addition of an inert gas (Ar , N_2) decreases the rate of formation of both C_2F_4 and $c\text{-C}_3\text{F}_6$. However, the decrease of C_2F_4 is about 2.5 times as great as for $c\text{-C}_3\text{F}_6$ (Fig. 31). In these low pressure experiments the major effect of the inert gas is to increase the heat capacitance and hence lower the temperature of the system.

Figure 32 is a plot of the reaction yield vs the initial pressure of PFCB photolized at a constant fluence for 10 laser shots. In the low pressure regime (less than 0.4 torr) the increase in both products is linear with increasing PFCB pressure. The C_2/C_3 ratio is about 6.5 for all cases. When the PFCB pressure is increased to 0.8 torr the $c\text{-C}_3\text{F}_6$ increase is slightly greater than what a linear extension of the low pressure points would predict, while the nonlinearity in the C_2F_4 is noticeably larger. The C_2/C_3 product ratio increases to 13. If the pressure is further increased to 4.8 torr this ratio becomes 40.

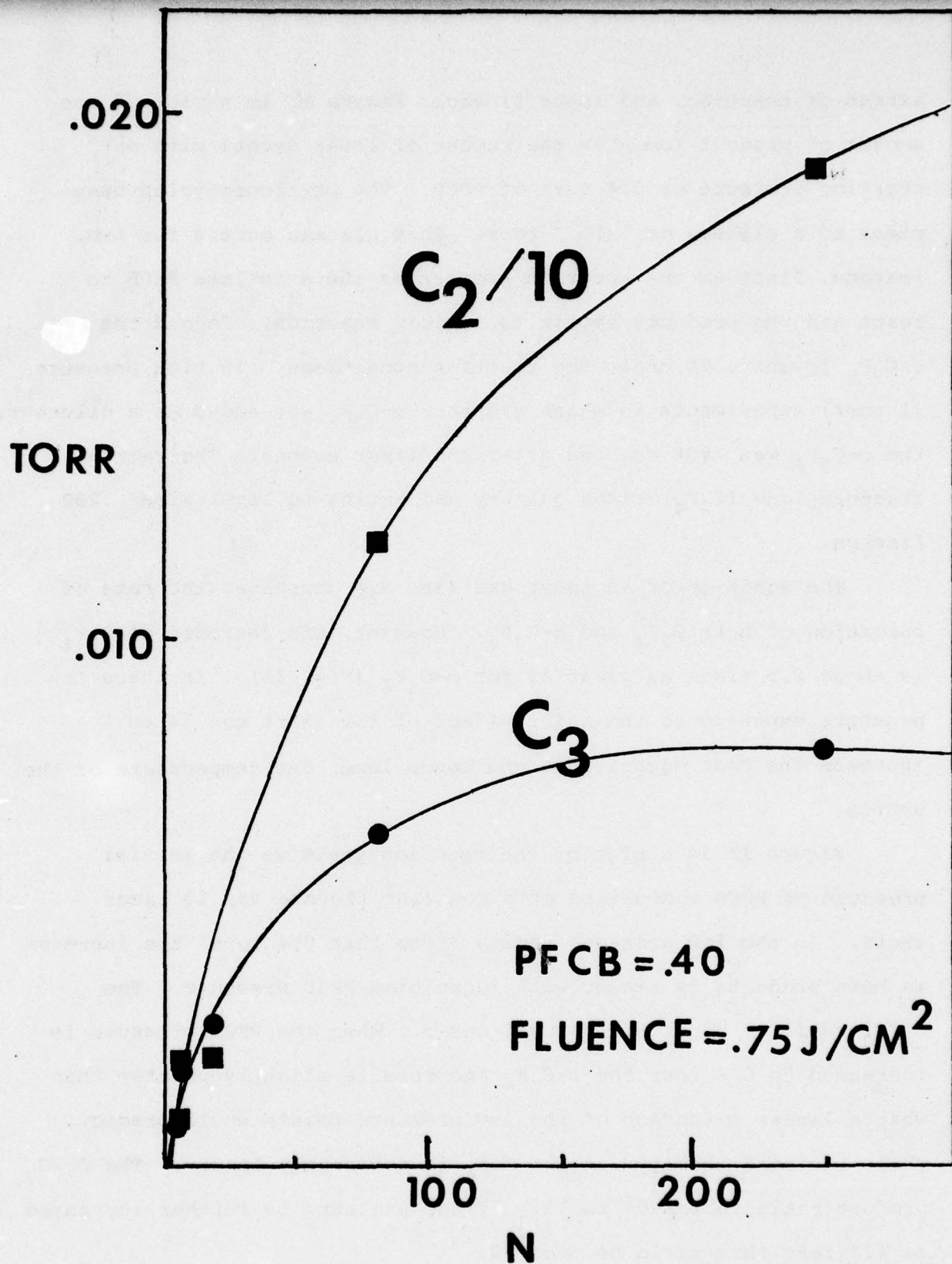


Figure 31

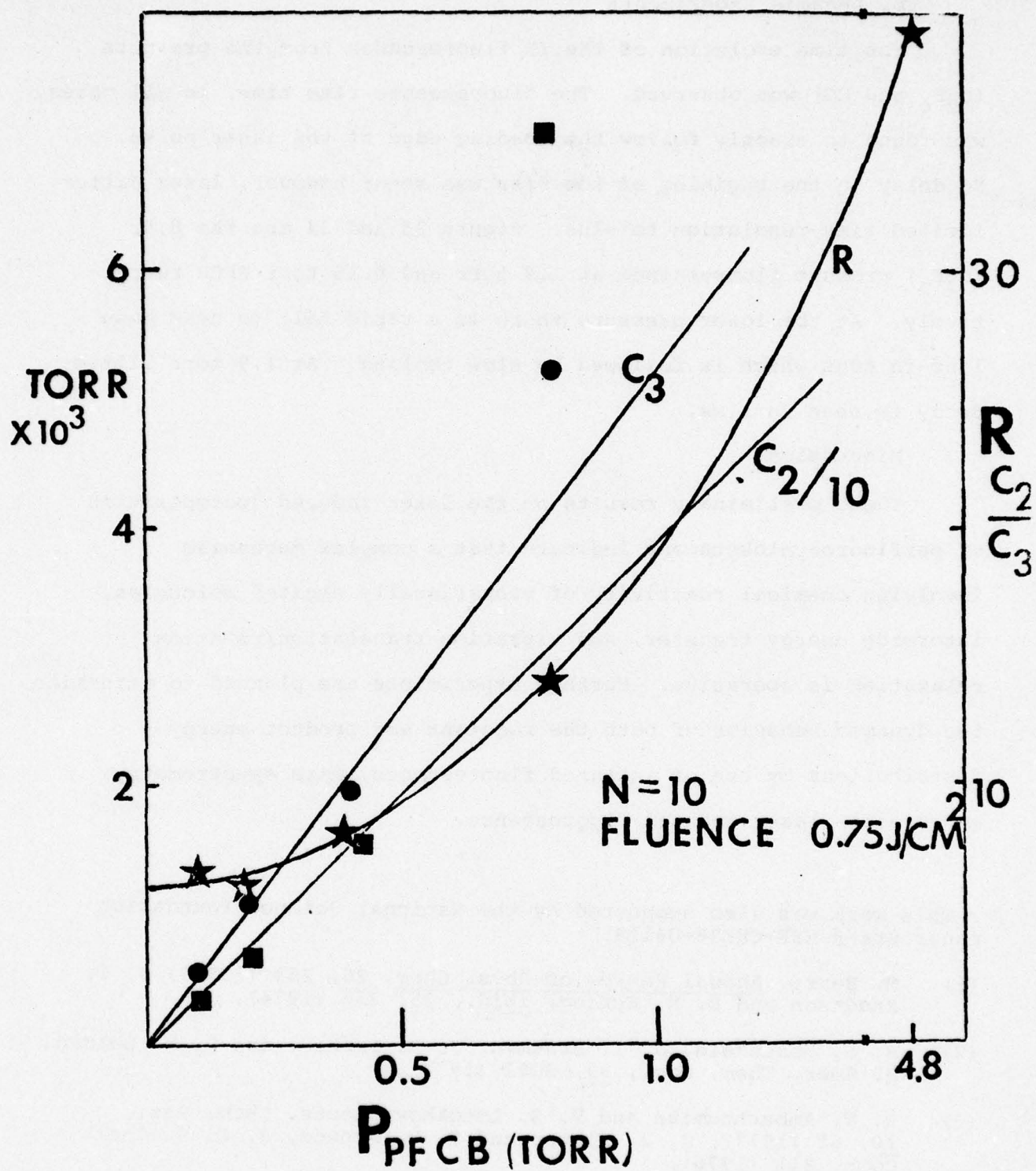


Figure 32

b. Dynamic Experiments

The time evolution of the IR fluorescence from the products (C_2F_4 and CO) was observed. The fluorescence rise time, in all cases, was found to exactly follow the leading edge of the laser pulse. No delay in the beginning of the rise was seen; however, laser jitter limited time resolution to $\sim 1\mu s$. Figure 33 and 34 are the 8.5μ (C_2F_4) product fluorescence at 1.9 torr and 0.15 torr PFCB respectively. At the lower pressure there is a rapid fall to near baseline in $60\mu s$ which is followed by slow cooling. At 1.9 torr little decay is seen in 1 ms.

Discussion:

These preliminary results on the laser induced decomposition of perfluorocyclobutanone indicate that a complex mechanism involving chemical reactivity of vibrationally excited molecules, intermode energy transfer, and vibration-translation/rotation relaxation is operative. Further experiments are planned to determine the dynamic behavior of both the reactant and product energy distributions by use of infrared fluorescence, mass spectrometry, and visible laser induced fluorescence.

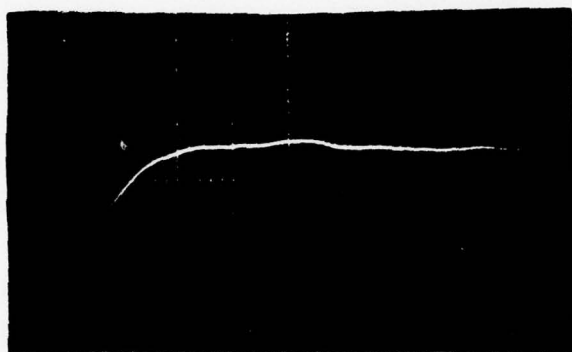
* This work was also supported by the National Science Foundation under Grant NSF-CHE76-04118.

- (1) M. Berry, Annual Review of Phys. Chem. 26, 263 (1975); J. T. Knudtson and E. M. Eyring, ibid., 25, 255 (1974).
- (2) R. N. Rosenfeld, J. I. Brauman, J. R. Barker, and D. M. Golden, J. Amer. Chem. Soc., 99, 8063 (1977).
- (3) R. V. Ambartzumian and V. S. Letokhov, Accts. Chem. Res., 10, 61 (1977); J. J. Ritter and S. M. Freund, J. C. S. Chem. Comm. 811 (1976).

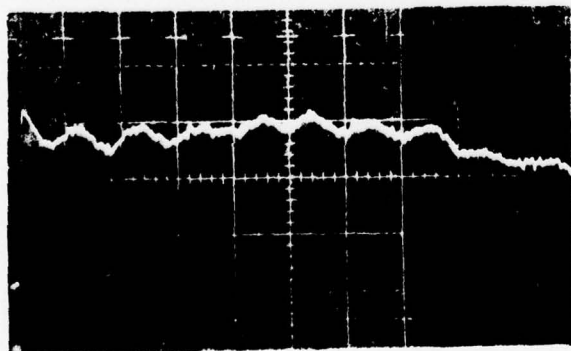
C_2F_4 PRODUCT FLUORESCENCE

$$\lambda = 8.5 \mu$$

$$P_0 = 1.9 \text{ torr PFCB}$$



2.5 $\mu\text{sec/div}$



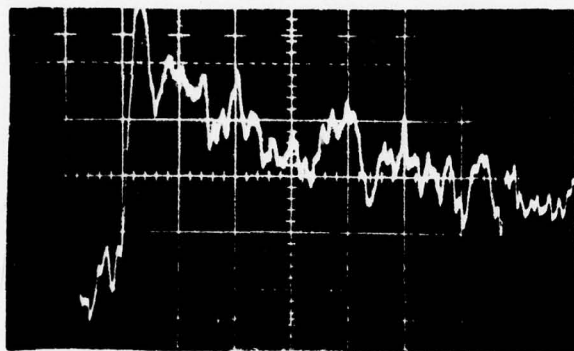
100 $\mu\text{sec/div}$

Figure 33

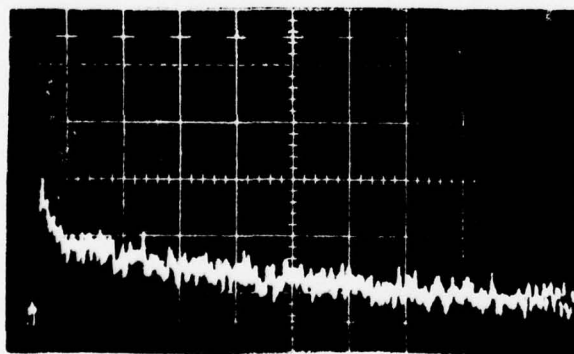
C_2F_4 PRODUCT FLUORESCENCE

$\lambda = 8.5 \mu$

$P_0 = 0.15$ torr PFCB



20 μ sec/div



100 μ sec/div

Figure 34

- (4) D. Merritt, J. Chem. Phys. 67, 3544 (1977).
- (5) W. M. Shaub and S. H. Bauer, Int. J. Chem. Kinetics, 7, 509 (1975).
- (6) R. S. Lewis and E. K. C. Lee, J. Phys. Chem. 79, 187 (1974)

PRECEDING PAGE BLANK - NOT FIL

II. GENERATION AND CONTROL OF RADIATION

A. SPONTANEOUS AND INDUCED COHERENT RADIATION GENERATION AND CONTROL IN ATOMIC VAPORS

(A. Flusberg, S. R. Hartmann, R. Kachru, K. Leung, T. Mossberg)

We have observed three new transient coherent effects:

(a) excited-state photon echoes,⁽¹⁾ (b) tri-level echoes,⁽²⁾ and (c) two-photon echoes.⁽³⁾ We have made the first observations of these three effects in Na vapor using the same pair of N_2 -laser-pumped dye lasers. In each experiment, one of the dye lasers used is resonant with the Na $3^2S_{1/2}$ - $3^2P_{1/2}$ transition wavelength $\lambda' = 589$ nm, while the second is resonant with one of the $3^2P_{1/2} - |c\rangle$ transition wavelength λ'' ; here $|c\rangle$ stands for an excited $n^2D_{3/2}$ or $n^2S_{1/2}$ state. A sample sequence of pulses of each frequency applied in the observation of each effect is shown in Figure 35. The excitation pulse sequence and the rephasing mechanism is distinct for each type of echo, a distinction which is brought out by the particular relationships between the direction of propagation of the excitation pulses and that of each echo. The size of each echo is determined by different relaxation parameters. In the remainder of this report we treat each type of echo separately.

a) Excited-state photon echoes.

Excited-state photon echoes are photon echoes produced between states which are both thermally unpopulated. Our work

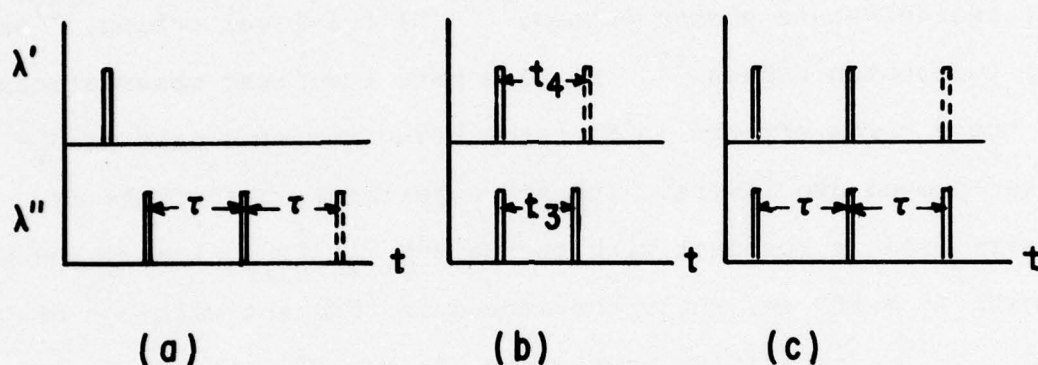


Figure 35 :

Applied sequence of excitation pulses (solid lines) of wavelength λ' (resonant with the Na $3^2S_{1/2}-3^2P_{1/2}$ transition) and λ'' (resonant with the $3^2P_{1/2}-|c\rangle$ transition, where $|c\rangle$ represents a higher S or D state of Na) for the observation of (a) excited-state photon echoes, (b) tri-level echoes, and (c) two-photon echoes. The echo is shown in dashed lines in each case.

represents the first observation of the excited-state photon echo, which we have used to measure collisional relaxation constants for a number of transitions between optically excited states of atomic sodium in either Ar or He gas. In the presence of Ar the $3^2P_{1/2}-(5,6) \ 2^2S_{1/2}$ and the $3^2P_{1/2}-(4,5,6,7) \ 2^2D_{3/2}$ transitions were studied, while the $3^2P_{1/2}-5^2S_{1/2}$ and $3^2P_{1/2}-4^2D_{3/2}$ transitions were studied in the presence of He. We have also used the conventional photon-echo technique to measure the collisional relaxation constants of the Na $D_{1,2}$ transitions in the presence of Ar. The use of the photon-echo effect to study these transitions demonstrates a significantly wider range of applicability than has previously been appreciated.

The excited-state echoes are produced by two pulsed dye lasers pumped transversely by a single N_2 laser. The dye lasers produce 1(3) kW peak power, 7-ns-FWHM pulses with a spectral width of 1(7) GHz, respectively. The dye laser with a 7-GHz spectral width (the "pump" laser) is tuned to resonance with the Na D_1 line to populate the $3^2P_{1/2}$ state, while the other (the "echo" laser) is tuned to the appropriate $3^2P_{1/2}-n^2S_{1/2}$ or $3^2P_{1/2}-n^2D_{3/2}$ transition. The echo laser pulse is split into two "excitation" pulses, one of which is optically delayed with respect to the other. All three pulses are then superimposed and made collinear, with the pump pulse preceding the first excitation pulse by 4 ns. The beams are collimated with a common 3-mm diameter and made to pass through the sodium cell. The cell consists of a 65-cm-long stainless-steel tube heated in the center and cooled at the ends.

The sodium densities are determined by the vapor pressure versus temperature curve. The foreign gas pressure is monitored by a Baratron capacitance manometer. Following the sodium cell are a series of three Pockels-cell shutters which provide $>10^9$ extinction of the three laser pulses. The shutters are opened at the echo time by a krytron switch which is triggered by a transistor Marx bank. The polarization of the three laser pulses is not controlled, but the Pockels-cell shutters pass only one component of linear polarization. Finally the echo signal is detected by a photomultiplier. The collisional relaxation rates for the various transitions are determined by monitoring the echo signal (at fixed separation between the two excitation pulses) as a function of foreign-gas pressure.

Photon echoes are largest and most stable when the excitation-pulse sequence is $\pi/2$ and π . The laser intensity $I_{\pi/2}$ necessary for a $\pi/2$ pulse on a two-level system is⁽⁴⁾

$$I_{\pi/2} = \pi^4 \hbar c / 3 \lambda^3 \tau_p^2 A, \quad (1)$$

where c is the speed of light, λ is the wavelength, A is the Einstein A coefficient, and τ_p is the excitation pulse width. This can be written in terms of the oscillator strength f as

$$I_{\pi/2} \approx \pi^2 \hbar / 24 \tau_p^2 r_e^2 \lambda f, \quad (2)$$

where r_e is the classical electron radius. Here we have used the

relation $A = 8\pi^2 r_e c f / \lambda^2$. Using the semi-empirically calculated alkali oscillator strengths of Anderson and Zilitis,⁽⁵⁾ we find that with $\tau_p = 7$ ns, $I_{\pi/2}$ is only 8 W/cm^2 for the Na 3P-7D transition ($\lambda = 450 \text{ nm}$, $f \approx 8 \times 10^{-3}$). In Ref. (5) the values of f for the 3P-nD transitions decrease roughly as n^{-3} for large n , a result familiar from an exact calculation in hydrogen.⁽⁶⁾ At the 3P-14D transition ($\lambda = 420 \text{ nm}$), $I_{\pi/2}$ is still only 70 W/cm^2 .

The intensity of the echo signal can best be appreciated by expressing it in terms of the intensity of the laser pulse used to generate it. For an optically thin sample of atoms with a single non-degenerate transition the number of photons radiated in the echo neglecting relaxation effects is⁽⁴⁾

$$N = \frac{\rho}{2} \frac{3\lambda^2 L}{8\pi} \frac{T_2^*}{\tau_p} \frac{\rho}{2} (aL) \frac{T_2^*}{\tau_p} A \tau_p, \quad (3)$$

where ρ is the number density of atoms initially in the populated (thermally or by laser pumping, as the case may be) state; a is the cross sectional area of the excitation pulses, $(T_2^*)^{-1}$ is the transition inhomogeneous linewidth, L is the sample length, and $\tau_p > T_2^*$. Eq. (3) can be written in terms of the absorption coefficient $\alpha = (3/4\pi)\rho\lambda^2 A T_2^*$ as follows:

$$N = (\alpha L / \pi)^2 N_{\text{ex}}. \quad (4)$$

Here N_{ex} is the number of photons $N_{\pi/2} = I_{\pi/2} \lambda a \tau_p / hc$ in a $\pi/2$

excitation pulse if the pulse is Fourier-transform limited and the transition is nondegenerate. In the more general case, we set N_{ex} equal to the number of excitation photons required to equalize the upper- and lower-state populations. This can be obtained from $N_{\text{ex}} \approx (\tau_p/\tau')N_{\pi/2}$, where τ' is the greater of T_2^* and τ_L , τ_L being the inverse spectral width of the excitation pulses.

We emphasize the importance of Eq. (4), which shows that for αL approaching unity the number of photons in the echo is only about two orders of magnitude smaller than the number of photons in an excitation pulse. In our experiments two factors cause the echo size to be smaller than the maximum predicted by Eq. (4). First, the excitation-pulse separation τ , typically 21 ns in our experiments, is long compared to the 16-ns lifetime of the $3^2P_{1/2}$ state; the observed echo intensity at $\tau = 2$ ns is thus reduced to no more than $\exp[(-21/8)] \approx 0.07$ of its unrelaxed value. Second, the laser pump beam is collinear with the echo excitation beams. Thus only on the conventional echo $3^2S_{1/2} - 3^2P_{1/2,3/2}$ transitions do we excite the sample uniformly and still attain $\alpha L = O(1)$. In this case with $\tau_p/\tau' \approx 20$ and with the relaxation factor of 0.07 taken into account, Eq. (4) predicts $N \approx 4 \times 10^7$, which compares well with the $\approx 10^7$ photons we observe. For experiments on transitions within the excited-state manifolds, however, it is not possible to both pump the ground-state population into the lower excited state throughout the entire sample length and achieve $\alpha_E L = 1$ at the echo transition wavelength.

This difficulty results from the fact that the absorption coefficient of the pump pulse is much larger than that of the excitation pulses. For $\alpha_p L \gg 1$, only a length of sample $L_{\text{eff}} \sim \alpha_p^{-1}$ is pumped, with ρ being negligible elsewhere. Here the subscripts P and E refer to the pump and echo transitions, respectively. Then $N \propto (\alpha_E/\alpha_p)^2 N_{\text{ex}}$ is independent of atomic density (for fixed pump power), and it follows from the definition of α and N_{ex} that $N \propto \lambda^2 f$ for Doppler-broadened transitions. Our observations roughly bear out these predictions.

If we were to pump transversely or bleach the pump transition, the excited-state echo signals could be much larger. Nevertheless, our signals were quite large, e.g. $\approx 3 \times 10^6$ photons in the $3^2P_{1/2} - 4^2D_{3/2}$ echo. Our signal-to-noise ratios were large, as well, and were typified by Fig. 36 where we have shown echo intensities versus Ar gas pressure at fixed pulse separation for several transitions between the $3^2P_{1/2}$ state and various S states.

The data of Figure 36 behave according to $dI/dP = -\beta I$, where β is a collisional decay constant. Measured values of β for several transitions are listed in Table IX. In the fifth column of Table IX we have tabulated the values of $\gamma = \tau/\beta$ in ns-torr. To within experimental error γ is found to be independent of τ for the $3^2P_{1/2} - 4^2D_{3/2}$ transition, i.e. this echo decays exponentially with delay time. This contrasts with the $^{13}\text{CH}_3\text{F}$ measurements of Schmidt et al., in which an $\exp(-k\tau^3)$ contribution to the collisional decay of a two-pulse photon echo was observed.⁽⁷⁾ We may conclude that either population-changing or phase-

Figure 36 :

Decay of echo intensity versus Ar gas pressure for the $3^2P_{1/2} - (3,5,6) 2^2S_{1/2}$ transitions. Each point represents an average of approximately 100 laser shots. For each transition a number of such sets of points giving echo intensity versus pressure are obtained. A β (from $I = I_0 e^{-\beta P}$) is determined for each set by a least-square fit, and our final value of β is a weighted average of the β 's for the individual data sets. The relative intensities of the echoes for the various transitions cannot be determined from this figure.

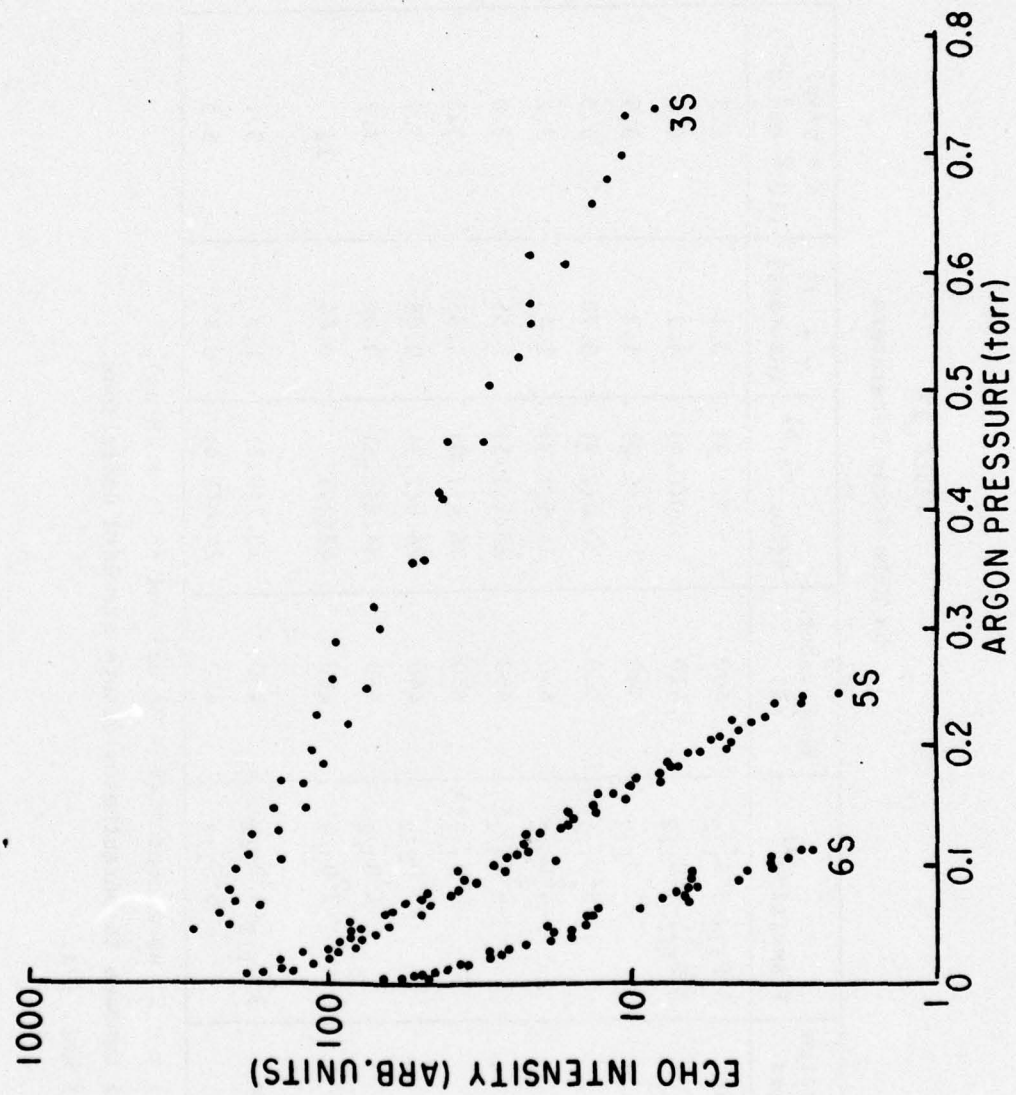


Figure 36

TABLE IX
Na Echo-decay Parameters

Foreign gas	Transition ^{a)}	Temperature (K)	β (torr ⁻¹) ^{b)}	$\gamma = \tau/\beta$ (ns-torr)	$K = p/\gamma\rho f$ (10 ⁻⁸ cm ³ s ⁻¹)	$K^{(c)}$ (10 ⁻⁸ cm ³ s ⁻¹)
Ar	$3^2P_{3/2}-3^2S_{1/2}$	400	5.9(1.3)	3.6	1.2	
	$3^2P_{1/2}-3^2S_{1/2}$	410	5.0(0.4)	4.2	1.0	
	$-5^2S_{1/2}$	440	17.7(1.0)	1.2	3.9	
	$-6^2S_{1/2}$	440	30.0(2.9)	0.70	6.5	
	$-4^2D_{3/2}$	440	14.6(1.3)	1.44	3.2	
	$-4^2D_{3/2}^*$	450	23.2(1.5)	1.55	3.0	
	$-4^2D_{3/2}^{**}$	450	36.1(7.0)	1.33	3.5	0.23(0.09)
	$-5^2D_{3/2}$	440	24.0(2.3)	0.88	5.2	0.41(0.14)
	$-6^2D_{3/2}$	450	34.8(2.6)	0.60	7.7	1.20(0.29)
	$-7^2D_{3/2}$	460	48(24)	0.44	11	
He	$3^2P_{1/2}-4^2D_{3/2}$	450	13.7(0.2)	1.5	3.1	
	$-5^2S_{1/2}$	450	24.6(1.4)	0.85	5.5	

a) $\tau = 21$ ns except * ($\tau = 36$ ns) and ** ($\tau = 48$ ns).

b) Numbers in parentheses denote standard deviations.

c) Ref. (9).

interrupting collisions (or both) dominate over velocity-changing collisions in producing decay of the $3^2P_{1/2}-4^2D_{3/2}$ echo. Indeed, as pointed out by Berman, Levy and Brewer,⁽⁸⁾ the τ^3 decay, which arises from velocity-changing collisions, may occur only when the collision interaction is nearly the same for both states involved in the echo, i.e. when phase-interrupting collisions play a negligible role. In the present study the superposition is always between two different electronic states; therefore, even in the absence of population-changing collisions, we expect phase-interrupting collisions to dominate over the effect of velocity-changing collisions. It is thus reasonable to assume that γ is independent of τ for all the echo transitions we have studied.

Our data allows the calculation of a collisional constant $K = p/\gamma\rho_f$ which we can compare to the corresponding collisional angular-momentum-mixing constant K' , as measured by Gallagher, Edelstein and Hill for the various Na D states.⁽⁹⁾ Here ρ_f is the foreign gas atomic density. Our collisional constants and those of Gallagher appear in the sixth and seventh columns, respectively, of Table IX. If only those collisions which mix the angular momentum of the n^2D states were responsible for the echo decay, then K would equal $2K'$. It can be seen from Table IX that in all cases K is considerably larger than $2K'$. The discrepancy is not due to collisional relaxation in the $3^2P_{1/2}$ state only, since the value of $K(\text{Ar})$ for the $3^2S_{1/2}-3^2P_{1/2}$ echo is relatively small. The fact that $K \gg 2K'$ indicates, instead,

that quenching collisions of the type studied by Gallagher play only a minor role in echo decay.

We have also measured the pressure-decay constant $\gamma(\text{argon})$ for the $3^2P_{1/2}-3^2S_{1/2}$ resonance echo. From its value we may predict the contribution of the Ar-Na collisions to the line-width $\tilde{\nu}_{1/2} \text{ (cm}^{-1}\text{)}$ of the Na $3^2P_{1/2}-3^2S_{1/2}$ absorption profile. We find

$$\frac{\tilde{\nu}_{1/2}}{\mu} = \frac{1}{4\pi\gamma c} \frac{T}{T_0} P_0 = 0.72(0.06) \text{ cm}^{-1}, \quad (5)$$

where $T = 410 \text{ K}$ is the Na cell temperature, $T_0 = 273 \text{ K}$, $P_0 = 760 \text{ torr}$, and μ is the relative density of Ar. This value of $\tilde{\nu}_{1/2}/\mu$ is in excellent agreement with the absorption measurements of Margenau and Watson (0.72 cm^{-1})⁽¹⁰⁾⁽¹¹⁾ and Kleman and Lindholm (0.742 cm^{-1}).⁽¹²⁾

For some of the transitions we have also tabulated the equivalent foreign-gas-induced FWHM linewidth, $\Delta\nu = (4\pi\gamma)^{-1}$ in the fifth column of Table X for comparison with measurements of the decay of S-S and S-D superpositions. A discussion of the comparison appears in (b) below.

Our experiments, which make use of modest-power, tunable, pulsed dye lasers, demonstrate the versatility of the photon-echo technique as applied to relaxation studies of transitions between states even when both are thermally unpopulated. Large analyzable signals can be produced on a multitude of transitions

TABLE X

Relaxation Rate $\Delta\nu$ (MHz/torr)

Foreign Gas	Superposition	ESPE [440-460°K] ^(a)	TLE [410°K]	TPE [400°K]	TPA [563°K]	TPCT [670°K]
Ar	$3^2S_{1/2}-4^2D_{3/2}$	57(5)	60(10)	57(10)	61(6)	60
	$3^2P_{1/2}-4^2D_{3/2}$					
	$3^2S_{1/2}-5^2S_{1/2}$	64(4)			69(5)	
	$3^2P_{1/2}-5^2S_{1/2}$					
	$3^2S_{1/2}-7^2D_{3/2}$	192(95)	160(20)			
	$3^2P_{1/2}-7^2D_{3/2}$					
He	$3^2S_{1/2}-4^2D_{3/2}$	55(4)			49(6)	
	$3^2P_{1/2}-4^2D_{3/2}$					
	$3^2S_{1/2}-5^2S_{1/2}$	98(6)			87(4)	
	$3^2P_{1/2}-5^2S_{1/2}$					

(a) See Table IX.

Table X: Foreign-gas induced relaxation rates $\Delta\nu$ (MHz/torr) of various atomic Na superposition states as measured by excited-state photon echoes (ESPE), tri-level echoes (TLE), two-photon echoes (TPE), Doppler-free two-photon absorption (TPA),⁽¹⁷⁾ and two-photon coherent transients (TPCT).⁽¹⁶⁾ The Na temperature at which each experiment was performed is indicated in brackets. The rates given in each column have been normalized to the values they would have at 410°K under the assumption that the collisional cross section is independent of temperature.⁽²⁾

of different frequencies. The practicality of the technique is understood from Eq. (4), which expresses photon-echo intensity in a particularly enlightening way. Pumping schemes other than our longitudinal one can probably be used to better advantage. Transverse pumping or pumping via E1-forbidden transitions are practical schemes for achieving $\alpha_E L = O(1)$ and even larger excited-state echoes.

b) Tri-level echoes.

We have discovered a new type of echo peculiar to multi-level (three levels or more) systems: for a sample of multilevel systems inhomogeneously broadened by the Doppler effect a rephasing of a coherent superposition between a particular pair of levels can be induced even if the constituent systems of the sample spend most of the time between their first excitation and the echo dephasing in a superposition between a different pair of levels. The echo signals produced are large since they arise on an allowed transition. Through them one can study the relaxation of a step-wise, resonantly excited superposition which would ordinarily be inaccessible. We term this effect tri-level echoes. Similar effects were predicted several years ago by Aihara and Inaba,⁽¹³⁾ who described them as anomalous photon echoes. Related effects were observed in three-level spin systems by Hatanaka, Terao, and Hashi.⁽¹⁴⁾ We have observed tri-level echoes in Na on the $3^2S_{1/2}-3^2P_{1/2}-n^2D_{3/2}$ ($n = 4, 6, 7, 8$ and 9) three-level systems, and we have used it to measure the Ar-Na collisional decay constant of the Na $3^2S_{1/2}-4^2D_{3/2}$ and $3^2S_{1/2}-7^2D_{3/2}$ superpositions.

Consider a gaseous sample of three-level systems whose atomic states $|a\rangle$, $|b\rangle$, and $|c\rangle$ have respective eigenenergies $\hbar\Omega_a$, $\hbar\Omega_b$, and $\hbar\Omega_c$ ordered for simplicity as $\Omega_a < \Omega_b < \Omega_c$. The atoms are initially in state $|a\rangle$. The transitions a-b and b-c are E1 allowed. The sample is irradiated at times $t_1 \leq t_2 < t_3$; the i th excitation pulse has central frequency ω_i and wave vector \vec{k}_i . We specialize to $\omega_1 = \Omega_{ba}$ and $\omega_2 = \omega_3 = \Omega_{cb}$, where $\Omega_{ij} = |\Omega_i - \Omega_j|$. Under these conditions, complete rephasing on the resonance transition producing an echo at $\omega_4 = \omega_1 + \omega_2 - \omega_3$ will occur at $t = t_4$ when and if all atoms at \vec{x} are in superposition states of identical relative phase ϕ and are phase matched according to $\phi(\vec{x}) = \vec{k}_4 \cdot \vec{x}$. In the absence of velocity-changing collisions, an atom having velocity \vec{v} and position \vec{x} at time t must have come from $\vec{x}_i = \vec{x} - \vec{v}(t - t_i)$ at $t = t_i$. The atomic superposition created between states $|a\rangle$ and $|c\rangle$ by excitation pulses 1 and 2 has the phase factor $\exp[i(\vec{k}_1 \cdot \vec{x}_1 + \vec{k}_2 \cdot \vec{x}_2)]$. The third pulse transforms this $|a\rangle - |c\rangle$ superposition into an $|a\rangle - |b\rangle$ superposition, introducing an additional phase factor $\exp(-i\vec{k}_3 \cdot \vec{x}_3)$. For this atom the net phase of the $|a\rangle - |b\rangle$ superposition is thus

$$\phi = \vec{k}_1 \cdot \vec{x}_1 + \vec{k}_2 \cdot \vec{x}_2 - \vec{k}_3 \cdot \vec{x}_3 = \phi_0 - \vec{v} \cdot \vec{A}(t), \quad (6)$$

where

$$\phi_0 = (\vec{k}_1 + \vec{k}_2 - \vec{k}_3) \cdot \vec{x}$$

and

$$\vec{A}(t) = (t - t_1)\vec{k}_1 + (t - t_2)\vec{k}_2 - (t - t_3)\vec{k}_3.$$

Under the assumption that the entire Doppler distribution is equally excited, the dipole moment of frequency ω_4 , produced at \vec{x} when $t > t_3$, is proportional to $\langle e^{i\phi} \rangle$, where the brackets indicate an average over the velocity distribution. Assuming perfect phase matching, i.e., $\vec{k}_4 = \vec{k}_1 + \vec{k}_2 - \vec{k}_3$, the radiated intensity I at ω_4 is proportional to $\exp(-\frac{1}{2}v_0^2 |\vec{A}|^2)$, where $v_0 = (2kT/m)^{1/2}$, k is Boltzmann's constant, T is the temperature, and m is the mass of the atom. The intensity peaks when the various atomic dipoles rephase so as to minimize $|\vec{A}(t)|$. Setting $t_1 = 0$, this occurs at the "echo" time t_4 given by $t_4 = (t_2\vec{k}_2 - t_3\vec{k}_3) \cdot \vec{k}_4 / |\vec{k}_4|^2$. In terms of t_4 , $\vec{A}(t)$ can be expressed as $\vec{A}(t) = (t - t_4)\vec{k}_4 - t_2\vec{k}_{2\perp} + t_3\vec{k}_{3\perp}$, where $\vec{k}_{i\perp}$ is the component of \vec{k}_i normal to \vec{k}_4 . From the above it should be clear that complete rephasing, i.e., $\vec{A}(t_4) = 0$, can only occur if the \vec{k} vectors are coplanar. A case of special interest is $\hat{k}_1 \cdot \hat{k}_2 = -1$ and $\vec{k}_2 = \vec{k}_3$, for which $\vec{k}_4 = \vec{k}_1$ and $\vec{A}(t) = (t - t_4)\vec{k}_4$. Under the assumption that dispersion may be neglected, rephasing will in this case occur at $t_4 = (t_3 - t_2)\omega_2/\omega_1$ as long as $t_4 > t_3$; the latter condition is insured if $\omega_2 > \omega_1 t_3 / (t_3 - t_2)$. Since $\vec{k}_4 = \vec{k}_1$, the echo is in this case emitted along the direction of propagation of pulse 1. Non-collinear excitation, however, is desirable in order to avoid saturation of the detection system by the first excitation pulse. Unlike photon echoes, tri-level echoes may easily be phase

matched in the noncollinear configuration. Like photon echoes,⁽¹⁵⁾ however, tri-level echoes do not, in general, rephase perfectly when the beams are not collinear. For tri-level echoes perfect rephasing in the noncollinear case, which requires that the quantity $t_2 \vec{k}_{2\perp} - t_3 \vec{k}_{3\perp}$ vanish, only occurs for certain values of t_2 and t_3 when $\vec{k}_{2\perp} \parallel \vec{k}_{3\perp}$. For small departures from our case of special interest this quantity is, however, always rather small. We may evaluate the echo intensity I for the geometry of Figure 36 ($\theta \ll 1$) and find

$$I = I_0 \exp \left(- \frac{\theta^2 v_0^2 \omega_2^2}{2c^2} \left[\frac{(\omega_2 - \omega_1)}{2\omega_1} (t_3 - t_2) - t_2 \right]^2 \right), \quad (7)$$

where I_0 is the intensity when $\theta = 0$, and where we have neglected the effect of the noncollinearity on the size of the beam-overlap volume. For the relatively unfavorable case of $\omega_2/\omega_1 = 1.5$, with $t_2 = 0$, $I(\theta = 0.02 \text{ rad})$ is smaller than $I(\theta = 0)$ by only a factor of 10 at $t_3 = 50 \text{ nsec}$. Also, for the experimental situations that we have examined, t_4 differs insignificantly from the value it has when the excitation is collinear.

In our experiment the Na $3^2S_{1/2}$, $3^2P_{1/2}$, and $n^2D_{3/2}$ states ($n = 4, 6, 7, 8, 9$) correspond to $|a\rangle$, $|b\rangle$, and $|c\rangle$, respectively. The $5^2S_{1/2}$ state has also served as state $|c\rangle$. These states are excited by 7-nsec (full width at half-maximum) FWHM excitation pulses produced by our two nitrogen-laser-pumped dye lasers. The first dye laser, of frequency ω_1 resonant with D_1 -line transition, has a 750-MHz spectral width, while the second,

of frequency ω_2 ($= \omega_3$) has a 10-GHz spectral width. The output of the second dye laser is split; an undelayed part is used as pulse 2, and the other part is optically delayed as pulse 3. Laser peak power is ~ 50 W for 3-mm beam diameters. By suitable optics the laser pulses are made to cross inside a sodium cell as shown in Figure 37. The angle θ of Figure 37 was usually chosen to lie between 20 and 50 mrad. The sodium vapor cell is the same 65-cm-long stainless-steel tube used in the excited-state photon-echo experiment. The echo, whose frequency is ω_1 , propagates nearly antiparallel to \vec{k}_3 and is detected on a photomultiplier. The $3^2S_{1/2}$ - $3^2P_{1/2}$ - $4^2D_{3/2}$ echo typically contains about 10^6 - 10^7 photons. The echo size decreases quite slowly as we go to higher D states.

When ω_2 is resonant with the 568.3-nm $3^2P_{1/2}$ - $4^2D_{3/2}$ transition, $\omega_2/\omega_1 = 1.038$. Thus when $t_1 = t_2 = 0$ and $t_3 = 195$ nsec, $\Delta t = t_4 - t_3$ should be about 7 nsec. We have indeed observed this delay of the echo from the time of the third pulse. A longer delay Δt is expected when ω_2 is resonant with the 449.4-nm $3^2P_{1/2}$ - $7^2D_{3/2}$ transition. Here, with $t_1 = t_2 = 0$ and $t_3 = 81$ nsec, Δt should be ~ 25 nsec. The observed delay of 23 nsec agrees quite well with this value when one considers the 7-nsec pulse widths and the difficulty of making t_1 and t_2 equal. We have also observed that the echo intensity changes when a magnetic field is applied perpendicular to \vec{k}_4 ; this suggests the presence of quantum-beat effects.

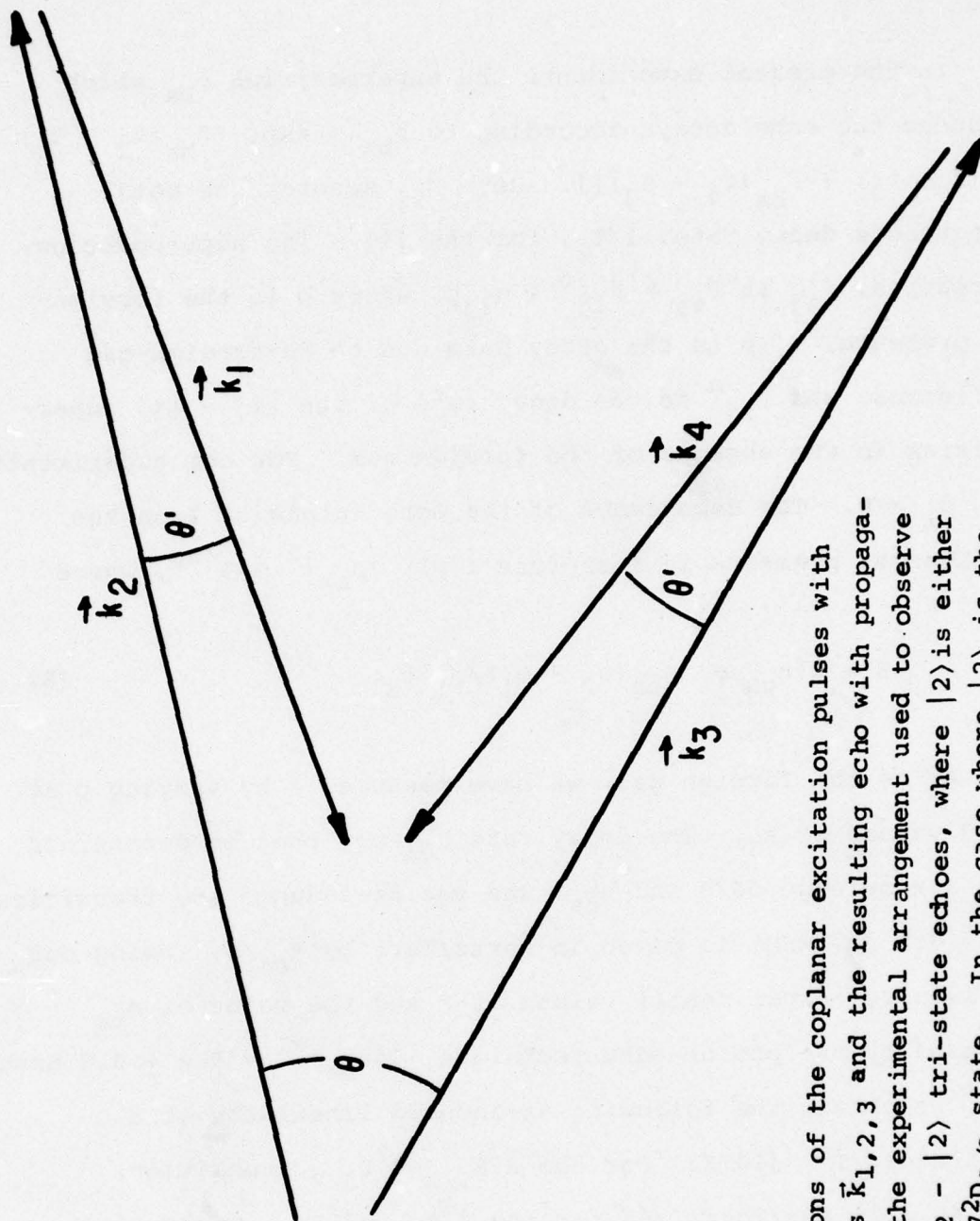


Figure 37:

Relative orientations of the coplanar excitation pulses with propagation vectors $\vec{k}_{1,2,3}$ and the resulting echo with propagation vector \vec{k}_4 in the experimental arrangement used to observe the $3^2S_{1/2} - 3^2P_{1/2} - |2\rangle$ tri-state echoes, where $|2\rangle$ is either the $4^2D_{3/2}$ or the $7^2D_{3/2}$ state. In the case where $|2\rangle$ is the $4^2D_{3/2}$ state $\theta' < 1$ mrad when $\theta \approx 50$ mrad.

In the present experiments the superposition ρ_{ba} which produces the echo decays according to $\rho_{ba} \sim \exp\{-[\Gamma_{ba}(t_2 - t_1) + \Gamma_{ca}(t_3 - t_2) + \Gamma_{ba}(t_4 - t_3)]\}$. Here Γ_{ij} denotes the total homogeneous decay rate, $1/T_2$, for the $|i\rangle - |j\rangle$ superposition. We rewrite, Γ_{ij} as $\Gamma_{ij} = \Gamma_{ij}^0 + \eta_{ij}p$, where p is the foreign-gas pressure, $\eta_{ij}p$ is the decay rate due to Na-foreign-gas collisions, and Γ_{ij}^0 is the decay rate of the $|i\rangle - |j\rangle$ superposition in the absence of the foreign gas. For our experiments $t_2 \cong t_1 = 0$. The dependence of the echo intensity I on the foreign-gas pressure is therefore $I(p) \sim |\rho_{ba}|^2 \sim e^{-\beta p}$, where

$$\beta = 2\{\eta_{ca} + \eta_{ba}(\omega_2 - \omega_1)/\omega_1\}t_3. \quad (8)$$

With Ar as the foreign gas, we have measured β by varying p at fixed values of t_3 . The decay rate η_{ca} may thus be determined from a knowledge of β and η_{ba} , and the Ar-induced a-c transition linewidth $\Delta\nu$ (FWHM) is given in hertz/Torr by η_{ca}/π . Using our preliminary experimental values of β and the value of η_{ba} measured by the photon-echo technique, $(4\eta_{ba})^{-1} = 4.2 \pm 0.3$ nsec Torr, we obtain the following Ar-induced linewidths at a temperature $T \cong 410^\circ\text{K}$: For the $3^2S_{1/2} - 4^2D_{3/2}$ transition, $\Delta\nu = 60 \pm 10$ MHz/Torr; and for the $3^2S_{1/2} - 7^2D_{3/2}$ transition, $\Delta\nu = 160 \pm 20$ MHz/Torr. In the former case no change in $\Delta\nu$ is observed as t_3 is varied from 27 to 106 nsec.

As shown in Table X, our observed 3S-4D Ar-induced linewidth agrees with that measured in two other recent experiments.⁽¹⁶⁻¹⁷⁾

Even more interesting is the fact that to within experimental uncertainty our values of $\Delta\nu$ are identical with the $3^2P_{1/2}$ - $4^2D_{3/2}$ and $3^2P_{1/2}$ - $7^2D_{3/2}$ Ar-induced decay measurements made by the excited-state photon-echo technique. Similarly, the He and Ar collisionally induced decay rates of the $3^2S_{1/2}$ and $5^2S_{1/2}$ state⁽¹⁷⁾ are respectively identical to within experimental error with those of the $3^2P_{1/2}$ - $5^2S_{1/2}$ state. This result suggests that the P state plays a small role in the foreign-gas-induced decay of these P-D and P-S superpositions.

Other examples of tri-level echoes are the following: Let $\omega_1 = \omega_3 = \Omega_{ba}$ and $\omega_2 = \Omega_{cb}$. If $\vec{k}_3 = \vec{k}_1$ and either (i) \vec{k}_1 and \vec{k}_2 are antiparallel, and $\Omega_a < \Omega_b < \Omega_c$, or (ii) \vec{k}_1 and \vec{k}_2 are parallel, and $\Omega_a < \Omega_c < \Omega_b$, then an echo of wave vector \vec{k}_2 is formed at $t_4 = t_3\omega_1/\omega_2 + t_2$ if $t_1 = 0$ and $t_4 \geq t_3$. Furthermore, if $\Omega_a < \Omega_b < \Omega_c$, $\omega_1 = \omega_2 = \Omega_{ba}$, $\omega_3 = \Omega_{cb}$, $\vec{k}_{1,2,3}$ are all parallel and $t_1 = 0$, then an echo of frequency $\omega_4 = \Omega_{cb}$ occurs at $t_4 = t_3 + t_2\omega_2/\omega_3$. We have already observed the latter echo. Many other variations of the basic tri-level echo scheme should be possible. A variety of echoes involving more than three levels ("multi-level" echoes) and/or arising from a sequence of more than three excitation pulses are possible as well.

c) Two-photon echoes.

Using the same apparatus described above in (a) and (b), we have produced the sum-frequency two-photon analogue of the photon echo on the $3^2S_{1/2}$ - $4^2D_{3/2}$ transition of atomic Na. This is the first observation of this effect, called a "two-photon"

echo, in which all the electromagnetic-wave frequencies are in the optical regime. We have used the two-photon echo to measure the argon-gas-induced relaxation behavior of the $\text{Na } 3^2S_{1/2} - 4^2D_{3/2}$ superposition state. The observed relaxation rate agrees with our measurements made with the tri-level echo technique.

Except for the level configuration (Figure 38), the dynamics of a two-photon echo are identical to that of a Raman echo.⁽¹⁸⁾ The two-photon echo dynamics can most easily be visualized by approximating each atom by a three-level system with energy levels $\hbar\Omega_a < \hbar\Omega_b < \hbar\Omega_c$, such that the $|a\rangle - |b\rangle$ and $|b\rangle - |c\rangle$ transitions are electric-dipole allowed, while the $|a\rangle - |c\rangle$ transition is not. We restrict our discussion to a dilute gas. The atoms are excited by a sequence of two "pulses", each of length τ_p and each containing two optical fields denoted by $[']$ and $["]$. Let $t_1=0$ ($t_2=\tau$) be the time at which the first (second) pulse is centered, and let t_3 be the two-photon echo time. The travelling-wave fields are given by $E_i' \exp[i(\vec{k}_i' \cdot \vec{x} - \omega_i' t)] + \text{c.c.}$ and $E_i'' \exp[i(\vec{k}_i'' \cdot \vec{x} - \omega_i'' t)] + \text{c.c.}$, where the subscript i refers to the fields present at $t = t_i$. We require that $\omega_i' + \omega_i'' = \Omega_{ca} \equiv \Omega_c - \Omega_a$, assume that $|\omega_i' - \Omega_{ba}| \ll |\omega_i'' - \Omega_{ba}|$, and define $\Delta\omega = \omega_i - \Omega_{ba}$, $\vec{k}_i = \vec{k}_i' + \vec{k}_i''$. Let \vec{x}_i denote the position of a particular atom of velocity \vec{v} at the time t_i . The $|a\rangle - |c\rangle$ superpositions dephase between the two pulses, but rephase at a later time t_3 to the extent to which the relative phase ϕ of the atoms at each point \vec{x}_3 , given by

$$\phi = 2\vec{k}_2 \cdot (\vec{x}_3 - \vec{x}_2) - \vec{k}_1 \cdot (\vec{x}_3 - \vec{x}_1) \quad (9)$$

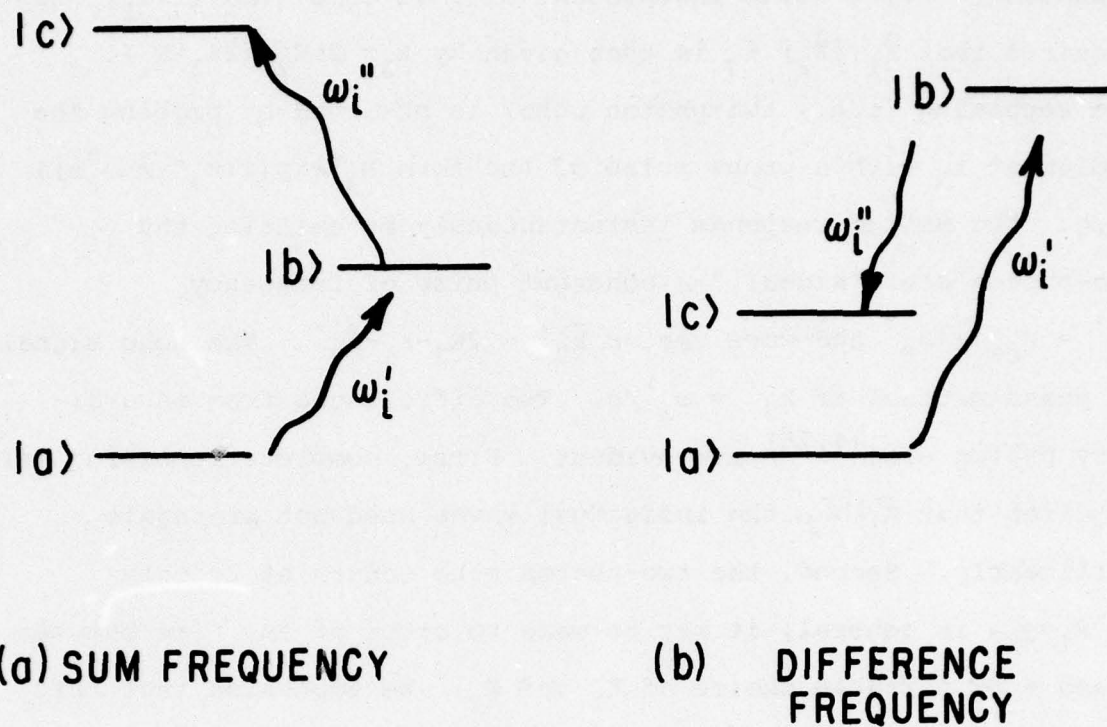


Figure 38:

Level configuration for a two-photon (sum-frequency) echo (a) and a Raman (difference-frequency) echo (b). In each the two incident waves of a particular excitation pulse "i" have frequencies ω_i' , ω_i'' , respectively. For the sum-frequency (difference-frequency) case $\omega_i' + \omega_i'' = \Omega_{ca}$ ($\omega_i' - \omega_i'' = \Omega_{ca}$), where $\hbar\Omega_{ca}$ is the energy splitting between states c and a.

is independent of \vec{v} ; this is a simple generalization of the condition for photon-echo rephasing in a gas.⁽¹⁵⁾ Complete rephasing, i.e. ϕ being independent of \vec{v} at some time $t_3 > t_2$, only requires that $\vec{k}_1 \parallel \vec{k}_2$; t_3 is then given by $t_3 = 2\tau K_2 / (2K_2 - K_1)$. The rephasing (i.e., two-photon echo) is observed by probing the medium at t_3 with a probe pulse of the form $E_3 \exp[i(\vec{k}_3 \cdot \vec{x} - \omega_3 t)] + \text{c.c.}$ The medium responds instantaneously by emitting the two-photon echo "signal," a coherent pulse of frequency $\omega_3' = \Omega_{ca} - \omega_3''$ and wave vector $\vec{k}_3' = 2\vec{k}_2 - \vec{k}_1 - \vec{k}_3''$. The echo signal is phase matched if $k_3' = \omega_3'/c$. Two differences from an ordinary photon echo^(4,15) are evident. First, complete rephasing only requires that $\vec{k}_1 \parallel \vec{k}_2$; the individual waves need not propagate collinearly. Second, the two-photon echo occurs at 2τ only if $K_1 = K_2$; in general, it may be made to occur at any time between τ and ∞ by suitable choice of K_1 and K_2 . We emphasize that this result applies only to a medium in which the inhomogeneous frequency shift is correlated with the directions of propagation of the electromagnetic waves, e.g. a Doppler-broadened gas. In a solid, for which this correlation is absent, the echo always occurs at 2τ .

We now specialize to the case $\omega_1' = \omega_2' = \omega_3'$, $\vec{k}_1 = \vec{k}_2$. We assume first that the spectral widths of the optical waves are so wide that the entire Doppler profile is equally excited by each pulse, and second, that these waves are Fourier-transform limited. (The second assumption will be dropped below.) We consider two cases; (a) If $\Delta\omega$ is so large that for each atom state $|b\rangle$ is excited nonresonantly during each excitation pulse,

then the dipole moment of frequency ω' induced in any atom located at \vec{x} at the echo time is given in the "small-angle" limit of weak excitation by

$$p(\omega' = \Omega_{ba} + \Delta\omega) = p_{cb}^4 p_{ba}^3 E_1' E_1'' (E_2' E_2'')^2 \tau_p^3 (\hbar \Delta\omega)^{-4} e^{i(\vec{k}_3' \cdot \vec{x} - \omega' t)} \quad (10)$$

where $p_{\alpha\beta}$ is the dipole matrix element between states α and β .⁽¹⁸⁾ The echo signal intensity is proportional to $|p(\omega')|^2$.

(b) If $\Delta\omega = 0$, then state $|b\rangle$ is excited resonantly. The same two-photon echo, whose signature is the signal direction of propagation \vec{k}_3' , still occurs. From the work of Aihara and Inaba⁽¹³⁾ it follows that in the limit of weak excitation the induced dipole moment $p(\omega' = \Omega_{ca})$ has the same form as Eq. (10), but is a factor of $(\tau_p \Delta\omega)^{(4)}$ larger. It may also be shown that the ratio $p(\omega' = \Omega_{ba})/p(\omega' = \Omega_{ba} + \Delta\omega)$ is not modified if the optical excitation waves are not Fourier-transform limited, provided that the spectral width of at least one of the waves making up a pulse is comparable to the corresponding single-photon inhomogeneous linewidth.

Since our steering optics deliver no more than a few watts peak power of each laser beam into the sample volume, we optimize the size of the $3^2S_{1/2} - 4^2D_{3/2}$ ($|a\rangle - |c\rangle$) superposition by exciting resonantly via the $3^2P_{1/2}$ ($|b\rangle$) state. Each of the two dye lasers oscillates at one of the frequencies ω' (wavelength $\lambda' = 589\text{nm}$) and ω'' (wavelength $\lambda'' = 568\text{nm}$) corresponding respectively to the S-P and P-D transitions. The lasers, which produce pulses of length $\tau_p = 7 \text{ nsec}$, are simultaneously pumped transversely

by the same 120-kW-peak-power N_2 laser. The spectral width (FWHM) of the pulse of frequency ω' (ω'') is 0.8 GHz (10 GHz). The dye-laser pulses are divided, steered to a white-cell delay line, recombined, and recollimated to a 4 mm^2 area such that: (1) at $t = 0$ the pulses at ω' and ω'' overlap in the interaction region with their wave vectors \vec{k}_1' and \vec{k}_1'' making an angle ϕ with respect to each other; (2) at $t = \tau$ the pulse configuration in the sample volume is the same as it was at $t = 0$; (3) at $t = 2\tau$ the "probe" pulse at ω'' is directed in to the sample cell along the direction $\hat{k}_3'' \approx \hat{k}'$ where $\vec{k}' \equiv \vec{k}_1' = \vec{k}_2'$. The angle ϕ can be adjusted from 0 to 20 mrad, while τ can be adjusted from 21 to 40 nsec. Since $\vec{k}_1' = \vec{k}_2'$, the rephasing condition is satisfied at $t = 2\tau$. The phase-matching condition ($k_3' = 2\pi/\lambda'$) demands that \vec{k}_1' make the same angle with \vec{k}_3'' as it does with \vec{k}'' where $\vec{k}'' \equiv \vec{k}_1'' = \vec{k}_2''$. (See Fig. 39) With \vec{k}_3'' coplanar with \vec{k}' and \vec{k}'' , $|\vec{k}' - \vec{k}''| \ll k'$, and $\phi \ll 1$, it follows that \vec{k}_3'' should make an angle $\theta = 2\phi|k' - k''|/k'$ with \vec{k}' . Since in our case θ is smaller than the laser divergence of 1 mrad, the two-photon echo signal should be phase-matched with $\hat{k}_3'' \approx \hat{k}'$. Since the two-photon echo at ω' propagates along $\hat{k}_3' \approx \hat{k}''$, for ϕ sufficiently large the echo is not masked by excitation pulses at ω' . Furthermore, no single-photon coherent emission at ω' propagates in the direction of the two-photon echo signal. To eliminate stray light, the photomultiplier set up to detect the echo signal along \hat{k}'' is protected by an interference filter and two Pockels-cell shutters which are electronically gated to transmit at $t = 2\tau$.

The experiment is begun with \vec{k}' and \vec{k}'' parallel so that

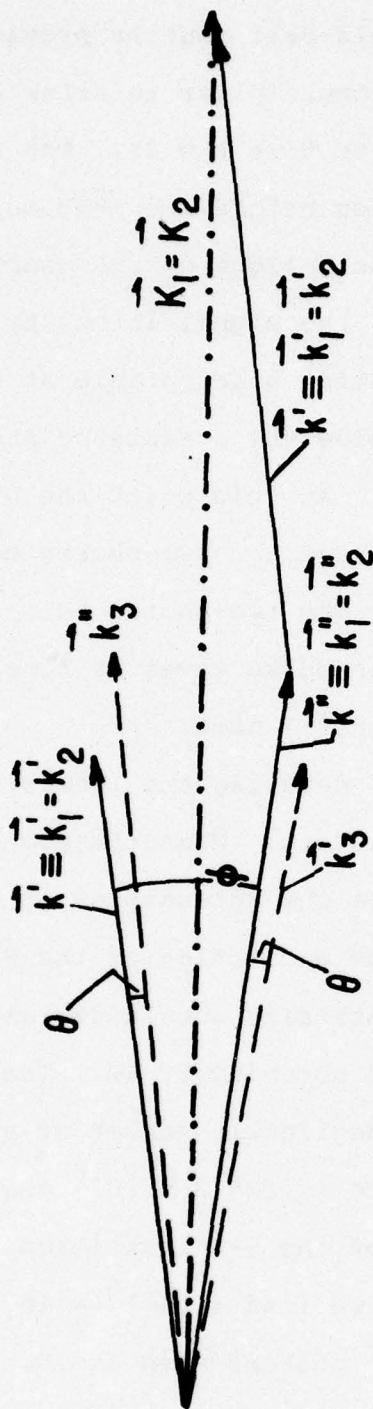


Figure 39:

The angular orientation of the pulses involved in the two-photon echo experiment as they emerge from the sample region is shown. The excitation pulses (solid arrows) at $\omega'(\omega'')$ propagate along $\vec{k}'(\vec{k}'')$. The probe pulse and two-photon echo "signal" (dashed arrows) propagate along \vec{k}_3 and \vec{k}_3 , respectively. \vec{k}' , \vec{k}'' and \vec{k}_3 , \vec{k}_3 form the sides of a parallelogram with $\vec{K}_1 = \vec{K}_2$ as a diagonal. \vec{k}' is drawn twice to illustrate this fact. Note that for $k' \approx k''$, $\theta \ll \phi$.

ordinary and excited-state photon echoes may be observed. No probe pulse is applied. The Pockels-cell shutter provides sufficient protection for the photomultiplier to allow in-line detection of both echoes at the gate time $t = 2\tau$. The next step is to insert the interference filter before the photomultiplier, so that the photomultiplier sees only light of frequency ω' . Then as \hat{k}' is tilted away from \hat{k}'' , the signal intensity observed at ω' continually diminishes, becoming undetectable at $\phi = 10$ mrad, for which the direction \hat{k}' is outside the acceptance angle (centered at \hat{k}'') of the phototube. At this point the probe pulse at ω'' along $\hat{k}_3'' \cong \hat{k}'$ is unblocked, and the two-photon echo signal at ω' along $\hat{k}_3' \cong \hat{k}''$ is observed. The two-photon echo signal disappears if any of the excitation-pulse waves is blocked or if the probe is delayed by an additional 7 nsec.

We now consider the effect of detuning the lasers by $\Delta\omega$ from resonance with the intermediate P state. Measurements of the dependence of the echo intensity on the intensities of the excitation pulses indicate that our excitation of the S-D superposition is weak; thus the echo intensity should decrease by a factor of $(\tau_p \Delta\omega)^8$ as a result of detuning by $\Delta\omega$. The minimum feasible value of $\Delta\omega$ for which a negligible number of atoms is resonantly excited into the P state is $\Delta\omega \cong 2 \times 10^{10} \text{ sec}^{-1}$, which is about twice the Doppler width of the S-P transition. For this value of $\Delta\omega$ and with $\tau_p = 7$ nsec, we find $(\tau_p \Delta\omega)^8 = 10^{17}$. Since our largest echo contains $\sim 2 \times 10^5$ photons when $\Delta\omega = 0$, it is not surprising that we are able to observe the two-photon echo only

when ω' is tuned to lie within the Doppler profile of the S-P transition. With respect to the observed echo size, we make two additional remarks: First, this size compares well with the tri-level echo photon number of $10^6 - 10^7$ photons when we note that the optics used in the two-photon echo experiment could only deliver "weak" excitation pulses. Second, the two-photon echo intensity is about a factor of 30 smaller than the signal observed at $t=\tau$ when the probe pulse is also made to occur at $t=\tau$; the latter signal may be viewed as arising from ordinary four-wave mixing.

Although the intermediate P state was always resonantly excited in our experiment, its decay is not expected to contribute to decay of the two-photon echo. To check this, we measured the ratio $I_e(\tau)/I_e(\tau+13 \text{ nsec})$ for $\tau=21$ and 27 nsec ; here $I_e(\tau)$ represents the echo intensity at the pulse separation τ in the absence of foreign gas ($p_{\text{Ar}} < 5 \text{ mTorr}$). In both cases the ratio was found to be 3. This is significantly smaller than the factor of five expected on the basis of the relaxation of the 16-nsec-lifetime⁽¹⁹⁾ $3^2P_{1/2}$ state alone if its relaxation contributed to the decay of our signal. We believe that the observed decrease in echo intensity is due instead to the decay of the 50-nsec-lifetime⁽²⁰⁾ $4^2D_{3/2}$ state and the additional $\sim 10\%$ reflection loss in power of the delayed laser pulses.

The value of the two-photon echo as a technique is its ability to directly measure the relaxation of a superposition state which cannot relax by an allowed single-photon decay. In

the present experiment this is accomplished by introducing Ar gas into the Na cell and monitoring the echo signal intensity (at fixed τ) as a function of the Ar pressure p . We find that the echo signal intensity decreases as $\exp(-4n\pi\tau)$, with $(4n)^{-1} = 1.4 \pm .5$ nsec-torr. This compares well with $(4n)^{-1} = 1.3 \pm .2$ nsec-torr obtained indirectly for this S-D state from the tri-level measurements and agrees with the results of other Doppler-free two-photon-excitation techniques⁽¹⁶⁾⁽¹⁷⁾ (Table X).

The intensity of the two-photon echo has also been observed qualitatively in the presence of a DC magnetic field H of up to 80 G at a pulse delay time of $\tau = 27$ nsec. With H applied perpendicular to the propagation direction of the echo, the echo intensity is modulated as a function of H in an oscillatory fashion, with the first null occurring in the region of 10-20 G. The modulation is a type of quantum-beat effect which occurs because each atom is driven into a linear superposition of several ground and excited states.

We emphasize that the two-photon echo experiment was performed with excitation pulses of very modest power. Improved optics together with readily available, more powerful lasers could easily result in signals several orders of magnitude greater than reported here. The extension to other transitions, such as the series $3^2S_{1/2} - n^2D_{3/2}$, where $n > 4$, is also straightforward. Although transient experiments utilizing two-photon excitation, e.g. two-photon echoes and two-photon free decay, generally require excitation pulses of high peak power, our experiment demonstrates that in the case of the two-photon echo the excitation

frequencies can be tuned to utilize resonant enhancement of the two-photon transition, thus permitting the use of relatively low-power excitation pulses without destroying the Doppler-free nature of the effect.

- (1) A. Flusberg, T. Mossberg, and S. R. Hartmann, *Opt. Commun.* 24, 207 (1978).
- (2) T. Mossberg, A. Flusberg, R. Kachru, and S. R. Hartmann, *Phys. Rev. Lett.* 39, 1523 (1977).
- (3) T. Mossberg, A. Flusberg, R. Kachru, and S. R. Hartmann, *Bull. Am. Phys. Soc.* 23, 33 (1978).
- (4) I. D. Abella, N. A. Kurnit, and S. R. Hartmann, *Phys. Rev.* 141, 391 (1966).
- (5) E. M. Anderson and V. A. Zilitis, *Opt. and Spectr. (USSR)* 16, 99 (1964).
- (6) E. U. Condon and G. H. Shortley, *The Theory of Atomic Spectra*, (Cambridge University Press, London, 1970).
- (7) J. Schmidt, P. R. Berman, and R. G. Brewer, *Phys. Rev. Lett.* 31, 1103 (1973).
- (8) P. R. Berman, J. M. Levy, and R. G. Brewer, *Phys. Rev. A* 11, 1668 (1975).
- (9) T. F. Gallagher, S. A. Edelstein, and R. M. Hill, *Phys. Rev. Lett.* 35, 644 (1975).
- (10) H. Margenau and W. W. Watson, *Phys. Rev.* 44, 92 (1933).
- (11) S. Y. Chen and M. Takeo, *Rev. Mod. Phys.* 29, 20 (1957).
- (12) B. Kleman and E. Lindholm, *Arkiv. Mat. Astron. Phys.* 32B, no. 4, paper 10 (1946).
- (13) M. Aihara and H. Inaba, *Opt. Commun.* 8, 280 (1973), and *J. Phys. A* 6, 1709, 1725 (1973).
- (14) Hiroshi Hatanaka, Takehiko Terao, and Tsuneo Hashi, *J. Phys. Soc. Jpn. Lett.* 39, 835 (1975).
- (15) M. Scully, M. J. Stephen, and D. C. Burnham, *Phys. Rev.* 171, 213 (1968).

- (16) P. F. Liao, N. P. Economou, and R. R. Freeman, Phys. Rev. Lett. 39, 1473 (1977).
- (17) F. Biraben, B. Cagnac, E. Giacobino, and G. Grynberg, J. Phys. B 10, 2369 (1977); G. Grynberg, private communication.
- (18) S. R. Hartmann, IEEE J. Quant. Electron. 4, 802 (1968).
- (19) T. A. Erdmann, H. Figger, and H. Walther, Opt. Comm. 6, 166 (1972).
- (20) F. Karstensen and J. Schramm, Z. Phys. 195, 370 (1966).

B. ALKALI-NOBLE-GAS DIATOMIC EXCIMERS*

(W. Happer, A. C. Tam, S. M. Curry, T. Yabuzaki)

Emission bands from the lower excimer states of alkali-noble-gas molecules (correlated with the lowest excited P alkali atom and unexcited noble gas atom) have been studied extensively by Gallagher and coworkers⁽¹⁾ in the past several years. Recently, emission bands from higher excimer states (correlated with the lowest excited S alkali atom and unexcited noble gas atom) were observed,⁽²⁾ and numerous further investigations of these higher excimer bands have followed. These visible excimer bands, correlated with the lowest forbidden atomic S-S transitions, are frequently very strong compared to the other excimer bands (except those bands⁽¹⁾ in or near the IR correlated with the lowest P-S resonance doublet); in fact, the visible excimer band frequently dominates the entire visible spectrum for selective laser excitation in the case of Xe (Ref. 2 and present report for KXe), and it is also a very prominent feature for other noble gases or for other experimental configurations we studied (e.g. discharges or absorption measurements). However, a quantitative understanding of the lineshapes of these higher excimer bands was lacking. Now a more quantitative understanding is possible because recently, Pascale⁽³⁾ calculated the oscillator strengths of the higher excimer bands correlated with forbidden alkali S-S or S-D transitions, and he reported oscillator strengths as large as 10^{-1} at

certain interatomic separations. Using the calculated oscillator strengths⁽³⁾ and molecular potential curves,⁽⁴⁾ Sayer et al.⁽⁵⁾ have recently calculated some of the higher excimer bands in alkali-noble-gas molecules, and they have made comparisons of the calculated bands with available experimental data. For the case of K-noble-gas and Na-noble-gas bands, only a very rough comparison was made, because our previously published experimental data⁽⁶⁾ were not detailed enough.

We report here our recent progress in the studies of the K-noble-gas and Na-noble-gas excimer bands. We have observed experimentally the visible emission bands from K(5S)Xe, K(5S)Kr, Na(4S)Xe and Na(4S)Kr excimers, the potassium excimers being produced by a violet Kr⁺ laser excitation and the sodium excimers by a discharge. We have also calculated these emission profiles, using Gallagher's quasi-static theory⁽¹⁾ and Pascale's molecular potentials⁽⁴⁾ and oscillator strengths.⁽³⁾ We have made comparison of the observed profiles with the calculated profiles, and this comparison is more quantitative than that of Sayer, et al.⁽⁵⁾ Such comparisons provide a critical test of the calculated molecular potential curves⁽⁴⁾ and oscillator strengths,⁽³⁾ and we shall draw some qualitative conclusions about the accuracies of these calculated parameters. A knowledge of the limitations of these calculated parameters is important if one uses these calculated values for guidance to develop alkali-noble-gas excimer lasers.

The emission profile of the KG ($G =$ a noble gas atom) green band near 5200 \AA due to the $K(5S)G \rightarrow K(4S)G$ molecular transition has been reported previously.⁽⁶⁾ This green band was excited by the 4579 \AA Ar^+ laser line, and the emission profile⁽⁶⁾ was somewhat distorted by strong alkali dimer emission bands and by atomic emission lines. We find that a much stronger emission profile of the KG green band can be obtained by exciting with the 4067 \AA Kr^+ line, which populates the $K(5P)$ excited state through absorption in the noble-gas-induced red wing of the $4045/4047 \text{ \AA}$ resonance doublet. A typical observed spectrum is shown in Fig. 40. Note that the entire visible spectrum is dominated by the single green band peaked near 5215 \AA .

The origin of the KG green band, as discussed previously,⁽⁶⁾ can be understood by examining the molecular potential curves calculated by Pascale and Vandeplanque,⁽⁴⁾ and the relevant KXe curves are shown in Fig. 41. Rapid collisions in our high density systems favor population of the $K(5S)\text{Xe}$ potential curve near the bottom of the well, and this population can radiate either to the $K(4P)\text{Xe}$ states (radiation bands in the IR) or to the $K(4S)\text{Xe}$ dissociative ground state (green excimer band). While the $K(5S)\text{Xe} \rightarrow K(4S)\text{Xe}$ transition is highly forbidden for large interatomic separation R , it is strongly allowed near the bottom of the potential well. (A very similar emission band is the Xe-induced green band in oxygen, $\text{O}(^1S)\text{Xe} \rightarrow \text{O}(^1D)\text{Xe}$, which has received much attention

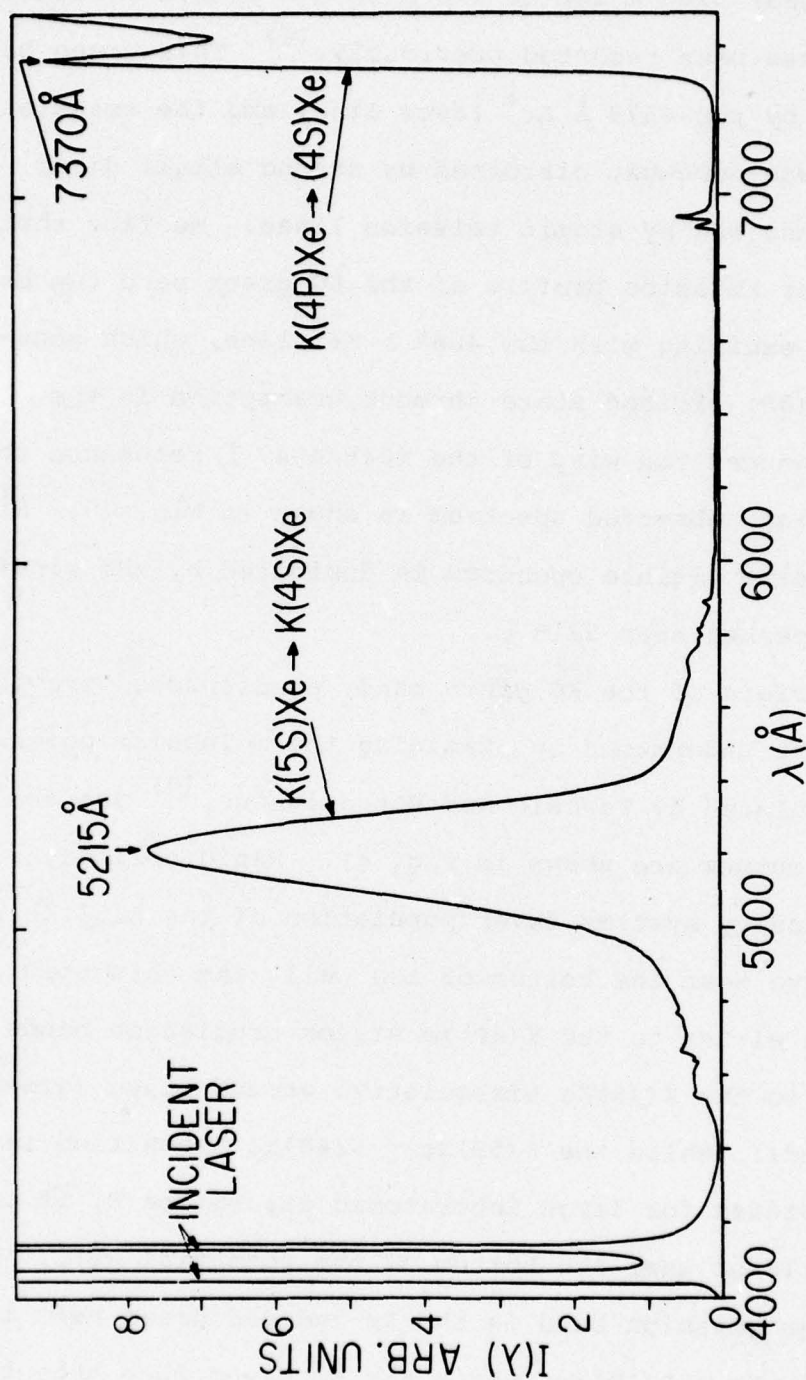


Figure 40: The visible emission spectrum from a KXe cell (Xe density = 2.4 amagats; cell temperature = 253°C) excited by the violet Kr^+ laser lines at 4067 Å (140 mW) and 4131 Å (240 mW).

Figure 41: Relevant theoretical molecular potential curves (from Ref. 4) showing the origin of the green excimer band in KXe. The Boltzman population of the K(5S)Xe potential well within a depth of $kT \sim 350 \text{ cm}^{-1}$ is indicated. The limits of R for approximately half-intensities of the green band are also shown. For larger R, emission intensity rapidly decreases because of vanishing oscillator strength; and for smaller R, emission intensity also rapidly decreases because of vanishing Boltzman population in the K(5S)Xe state.

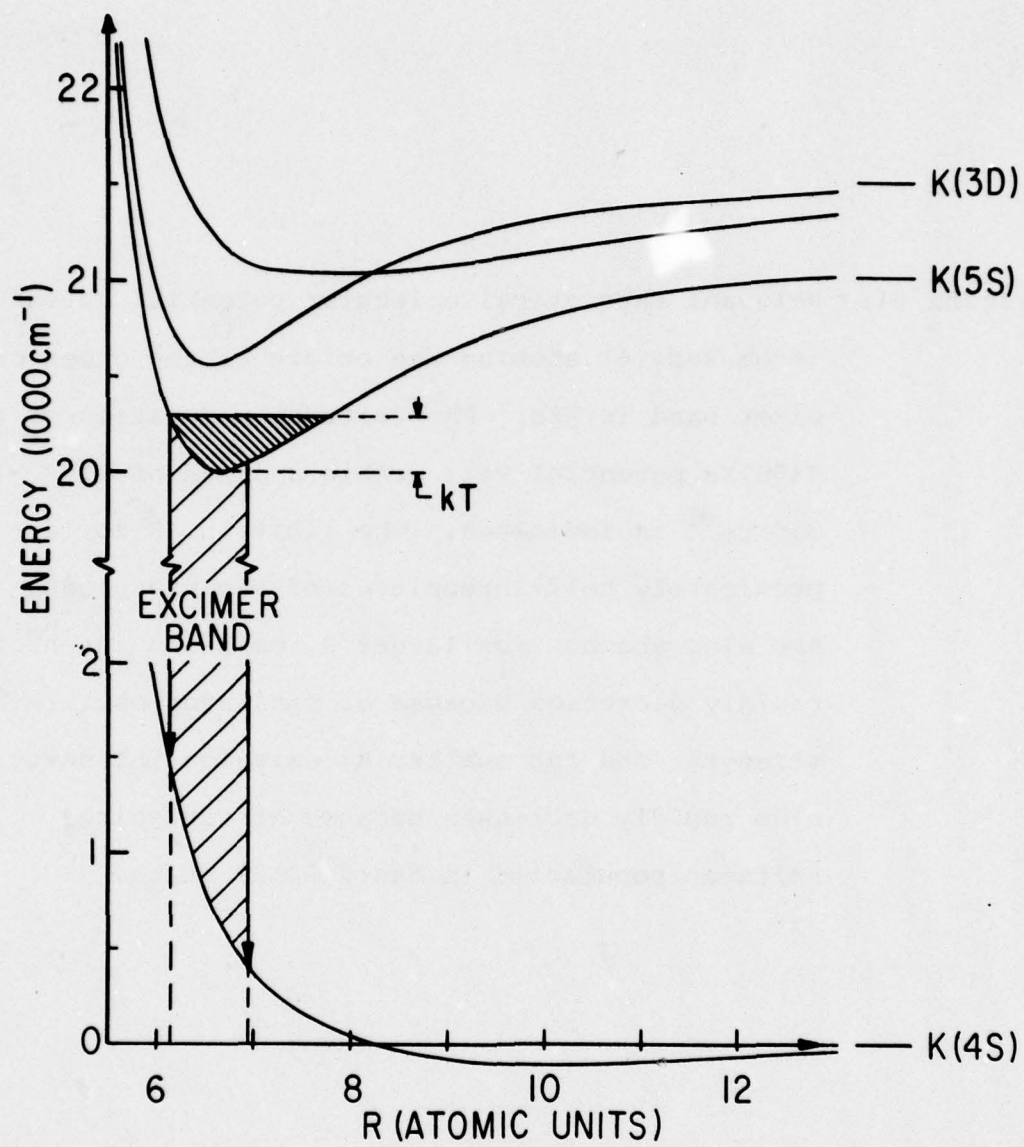


Figure 41

because it is a proven⁽⁷⁾ lasing transition.) The relevant calculated oscillator strengths⁽³⁾ f are shown in Fig. 42. For KG, we see that f decreases rapidly with increasing R , and at $R > 10$ atomic units, f becomes $< 1\%$ of the oscillator strength at the bottom of the potential well (at $R \approx 6$ atomic units). Hence the excimer band we observed ($K(5S)G \rightarrow K(4S)G$ for the case of potassium) is bound on the red side (small R) by the Boltzman factor in the upper state population, and on the blue side (large R) by vanishing f .

The emission intensity $I(\nu)$ at frequency ν due to the $K(5S)G \rightarrow K(4S)G$ or the $Na(4S)G \rightarrow Na(3S)G$ molecular transition can be calculated by the quasistatic theory of Gallagher and coworkers,⁽¹⁾ as done by Sayer et al.⁽⁵⁾:

$$I(\nu)d\nu = a N_u N_g \nu^3 f(R)R^2 dR \exp [(V^*(\infty)-V^*(R))/kT] \quad (1)$$

where a is a constant, N_u and N_g are the alkali (excited) and Xe atomic densities respectively, and $V^*(R)$ is the excited molecular potential energy at separation R . Details of this calculation are published.⁽⁸⁾ Here we shall only list the conclusions drawn from the comparison of the calculated KG and NaG profiles and the observed profiles. In all the cases we studied, the upper state potential well is found to be too shallow, and they should be deeper by about 200 cm^{-1} , 230 cm^{-1} , 735 cm^{-1} and 445 cm^{-1} for the $K(5S)Xe$, $K(5S)Kr$, $Na(4S)Xe$ and $Na(4S)Kr$ molecular excited states re-

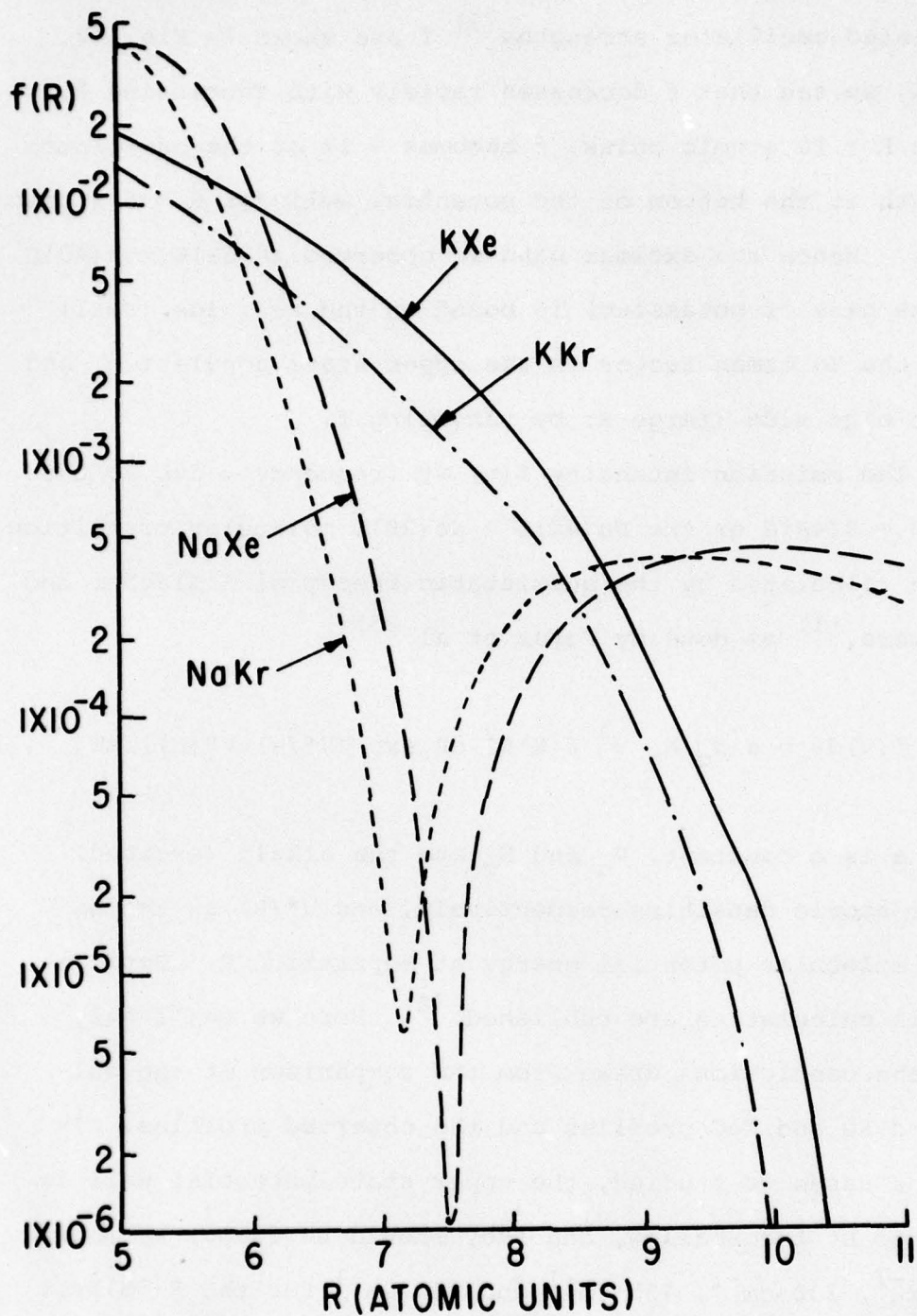


Figure 42: Theoretical oscillator strength $f(R)$ calculated by Pascale (Ref. 3) for the $K(5S)G \rightarrow K(4S)G$ and for the $Na(4S)G \rightarrow Na(3S)G$ transitions.

spectively in order to produce the observed peak positions of the emission profiles. The predicted linewidth is too broad by about 35% for the green KG excimer bands; this may be due to the calculated K(5S)G potential curves being too broad. The calculated Na(4S)G emission linewidths are in excellent agreement with the observed blue band linewidths if the oscillator strengths in the NaG system are taken to be the calculated oscillator strengths⁽³⁾ in the KG system. Pascale's calculated abrupt change of NaG oscillator strengths, as indicated in Fig.42, is not favored by the experimentally observed emission profiles.

The excimer band of Na(4S)Xe is probably the most interesting, because the strong binding in the upper state (estimated as 1900 cm^{-1} at the equilibrium separation R_0) and the strong repulsion of the lower state (1150 cm^{-1} at R_0) and the large value for the oscillator strength ($\sim 10^{-2}$) at R_0 greatly favor the Na(4S)Xe \rightarrow Na(3S)Xe transition for possible excimer laser applications similar to the O(¹S)Xe \rightarrow O(¹D)Xe case.⁽⁷⁾

By approximating the theoretical emission profile in an analytical form,⁽⁸⁾ we have predicted that the linewidth in the KG and NaG excimer bands should increase with temperature roughly as $T^{1/2}$. This prediction is borne out in our experimental observations for KXe in a limited temperature range. A line shift δV_0 proportional to T is also predicted but not clearly observed.

We have been concerned only with the main emission band

in the KG or NaG system, at $R \sim 6$ atomic units. A much weaker satellite band has been predicted⁽⁵⁾ very near the forbidden atomic S-S transition, due to the upper and lower adiabatic potential curves being parallel at $R \sim 11$ atomic units. Perhaps one of the small peaks near 4700 \AA in Fig. 40 is actually this predicted weak satellite band.

In the present report, we have studied only relatively low noble gas densities, where mainly binary molecules are important. We find that at high Xe densities (e.g. 10 amagats) and low cell temperatures ($\leq 150^\circ\text{C}$), polyatomic exciplex molecules $\text{K}(5\text{S})\text{Xe}_n$ (with n being 2, 3, or 4 mainly) become very important radiating species in the KXe system excited by the 4067 \AA Kr^+ laser line. Such exciplex radiation occurs in the spectral region of $5400 \text{ \AA} - 6400 \text{ \AA}$, and the study of these exciplexes is reported in another section of this progress report.

* This work also supported by the Army Research Office (Durham) under Grant DAAG29-77-G-0015.

- (1) A. Gallagher, Atomic Physics 4, edited by G. Zupulitz, E. W. Weber, and A. Winnacker (Plenum Press, N.Y. 1975).
- (2) A. C. Tam, G. Moe, W. Park and W. Happer, Phys. Rev. Lett. **35**, 85 (1975).
- (3) J. Pascale, J. Chem. Phys. **67**, 204 (1977).
- (4) J. Pascale and J. Vandeplanque, J. Chem. Phys. **60**, 2278 (1974).
- (5) B. Sayer, J. P. Visticot and J. Pascale, "Band Profiles Associated with Induced Dipole Transitions in Alkali-Rare-Gas System", to appear in J. Physique.
- (6) A. C. Tam, G. Moe, B. R. Bulos and W. Happer, Optics Comm. **16**, 376 (1976).

- (7) H. T. Powell, J. R. Murray and C. K. Rhodes, Appl. Phys. Lett. 25, 730 (1974).
- (8) "Visible Excimer Bands of the K-Noble-Gas and Na-Noble-Gas Molecules: Comparison of Experiments with Theory," A. C. Tam, T. Yabuzaki, S. M. Curry and W. Happer, to appear in Phys. Rev. A

C. VISIBLE EMISSION BANDS FROM KXe_n POLYATOMIC EXCIPLEXES*

(W. Happer, A. C. Tam, S. M. Curry, T. Yabuzaki)

Radiative processes in dense gases have received considerable attention in the past few years. One of the motivations for the study of such systems has been the great success of excimer (excited dimers) lasers in producing efficient, high power visible and ultraviolet radiation. At sufficiently high gas pressures, excited atoms often react to form bound electronically excited states of rather improbable molecules (noble gas fluorides⁽¹⁾ and alkali-noble-gas combinations⁽²⁾) which are dissociative in the ground electronic states. These "exciplex" (excited complex) molecules are often good laser species since the ground states self-destruct by dissociation and do not accumulate in sufficient numbers to reabsorb the laser light.

The visible excimer bands from alkali-noble-gas molecules were discovered⁽³⁾ in this laboratory three years ago, and more studies of these bands in selective laser excitations, discharges,⁽⁴⁾ and absorptions⁽⁵⁾ have followed. In our recent investigation of the emission spectra from K-noble-gas systems using selective laser excitation, we have discovered an unusual class of polyatomic exciplexes, $KXe_n(5S)$ molecules, which can be thought of as cluster ions KXe_n^+ with $n = 1, 2, 3, \dots$ and a rather extended valence electron in an orbit which resembles the first excited S state (5S) of the potassium atom. By exciting a vapor system of K mixed with ~ 10 amagats of

Xe, we have observed strong emission bands from $\text{KXe}(5\text{S})$, $\text{KXe}_2(5\text{S})$, $\text{KXe}_3(5\text{S})$ and $\text{KXe}_4(5\text{S})$ molecules, centered near 5220 Å, 5500 Å, 5900 Å and 6400 Å respectively. At low Xe density (< 5 amagats) and high temperature ($> 200^\circ\text{C}$), the emission is dominated by the $\text{KXe}(5\text{S})$ "monoxenide" radiation; while at high Xe density (> 5 amagats) and low temperatures ($< 150^\circ\text{C}$), it is dominated by overlapping $\text{KXe}_n(5\text{S})$ "polyxenide" radiation.

We produce these exciplex molecules by exciting a glass cell containing saturated potassium vapor in high density xenon gas with the 4067 Å line of a krypton-ion laser. This laser line, which has a power of 140 mW, excites the pressure-broadened red wing of the 4044/4047 Å second resonance line of potassium. The fluorescence from the cell is observed with a monochromator. The entire visible region of the spectrum is dominated by an intense green emission band. The most striking features of this band are illustrated in Fig. 43. The band consists of two parts, a well-defined, narrow peak centered near 5220 Å, which is known⁽⁴⁾ to be an emission band of potassium monoxenide $\text{KXe}(5\text{S}) \rightarrow \text{KXe}(4\text{S})$, and a broad asymmetric emission band between 5300 Å and 7000 Å which we attribute to the superposed emission bands of polyatomic exciplexes: $\text{KXe}_n(5\text{S}) \rightarrow \text{KXe}_n(4\text{S})$ with $n = 2, 3, 4, \dots$. We shall henceforth refer to these bands as the monoxenide and polyxenide bands respectively.

This system is particularly convenient for quantitative

Figure 43: Fluorescence spectra of potassium monoxenide and polyxenide at various cell temperatures and xenon densities (given in amagats). At low xenon density (lower curves), the monoxenide component is dominant. The small peaks observed near 4600 Å and 5750 Å for $[Xe] = 0.9$ amagat are due to alkali dimer fluorescence, since they are also observed in the absence of xenon. At high xenon density, the relative intensity of the red-shifted polyxenide component becomes progressively greater as the temperature is reduced.

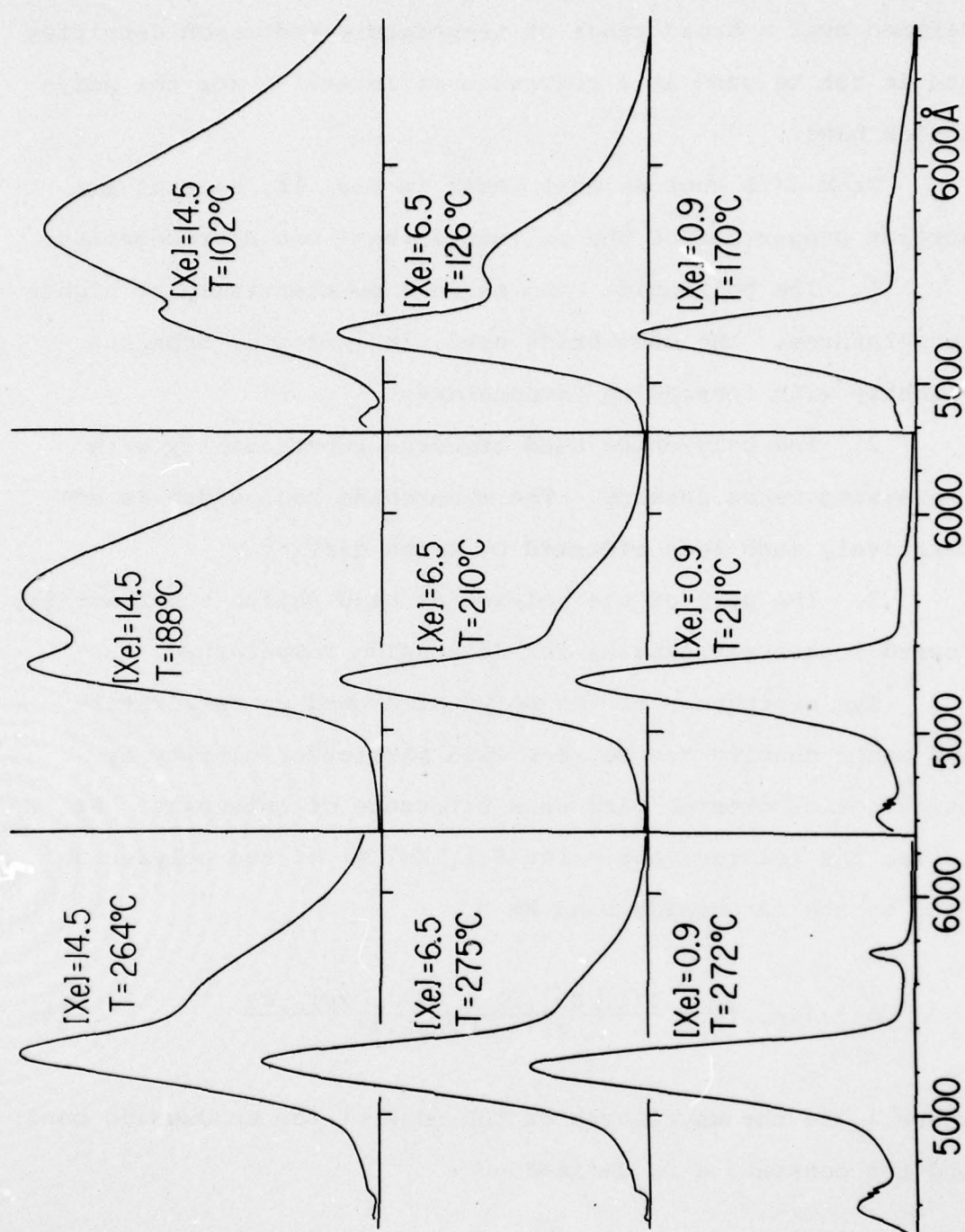


Figure 43

study since the narrow monoxenide emission peak remains well defined over a broad range of temperature and xenon densities and it can be used as a reference of intensity for the polyxenide band.

From data such as that shown in Fig. 43, several important properties of the polyxenide band can be recognized:

1. The polyxenide band narrows substantially at higher temperatures. The monoxenide band, in contrast, broadens slightly with increasing temperature.

2. The polyxenide band broadens substantially with increasing xenon density. The monoxenide band width is comparatively much less affected by xenon density.

3. The peak of the polyxenide band shifts substantially toward longer wavelengths for decreasing temperature.

The dependence of the polyxenide band on temperature and xenon density can be seen with particular clarity by using the monoxenide band as a reference of intensity. We define the relative intensity $S(\lambda, [\text{Xe}], T)$ of the polyxenide band to the monoxenide band by

$$S(\lambda, [\text{Xe}], T) = \frac{I(\lambda, [\text{Xe}], T) - \alpha I(\lambda, [\text{Xe}]_0, T)}{\alpha I(\lambda_0, [\text{Xe}]_0, T)} \quad (1)$$

where λ_0 is the wavelength of the peak of the monoxenide band, and the constant α is defined by

$$\frac{I(\lambda, [\text{Xe}], T)}{I(\lambda, [\text{Xe}]_0, T)} \rightarrow \alpha \quad \text{for } \lambda < 5220 \text{ \AA} \quad (2)$$

Here $I(\lambda, [\text{Xe}]_0, T)$ is defined as the fluorescence spectrum at low xenon densities, when only the monoxenide spectrum is present. We have found that the polyxenide spectrum is negligible at $[\text{Xe}] \approx 0.9$ amagat, and so we can take $I(\lambda, [\text{Xe}]_0, T)$ as the fluorescence spectrum at $[\text{Xe}] \approx 0.9$ amagat.

The relative intensity S at a xenon density of 8.4 amagats is shown in Fig. 44a. By doing temperature dependence measurements (as indicated in Fig. 44b) and Xe density (i.e. $[\text{Xe}]$) dependence measurements of the polyxenide signal S at various wavelengths λ , we found⁽⁶⁾ that S can be fitted over a rather large range of temperature and xenon density by a rather suggestive formula:

$$S(\lambda, [\text{Xe}], T) = G(\lambda) [\text{Xe}]^{n(\lambda)-1} \exp \frac{E(\lambda)}{kT} \quad (3)$$

where parameters $E(\lambda)$, $n(\lambda)$ and $G(\lambda)$ are plotted in Fig. 45.

Because nothing is yet known about the potential surfaces for polyxenide molecules we cannot give a detailed theoretical analysis of the experimental data. However, we can assign a plausible physical meaning to the empirically determined parameters of Eq. (3). We may assume that each polyxenide species KXe_n has a characteristic emission band, similar to but broader than the monoxenide band, for integer values of n ($n = 2, 3, 4, \dots$). The peaks of the emission bands of KXe_n shift systematically to longer wavelengths for increasing values of n . A large part of the red shift is due to the binding energy of Xe atoms to $\text{K}(5S)$. The polyxenide

Figure 44: (a) Spectra of the polyxenide component at a xenon density of 8.4 amagats, measured at various temperatures. The polyxenide spectra are obtained by subtracting the monoxenide component from the original data and then normalizing to the amplitude of the monoxenide peak. (b) The logarithm of the polyxenide component is shown plotted against the reciprocal of the absolute temperature for several different fluorescence wavelengths.

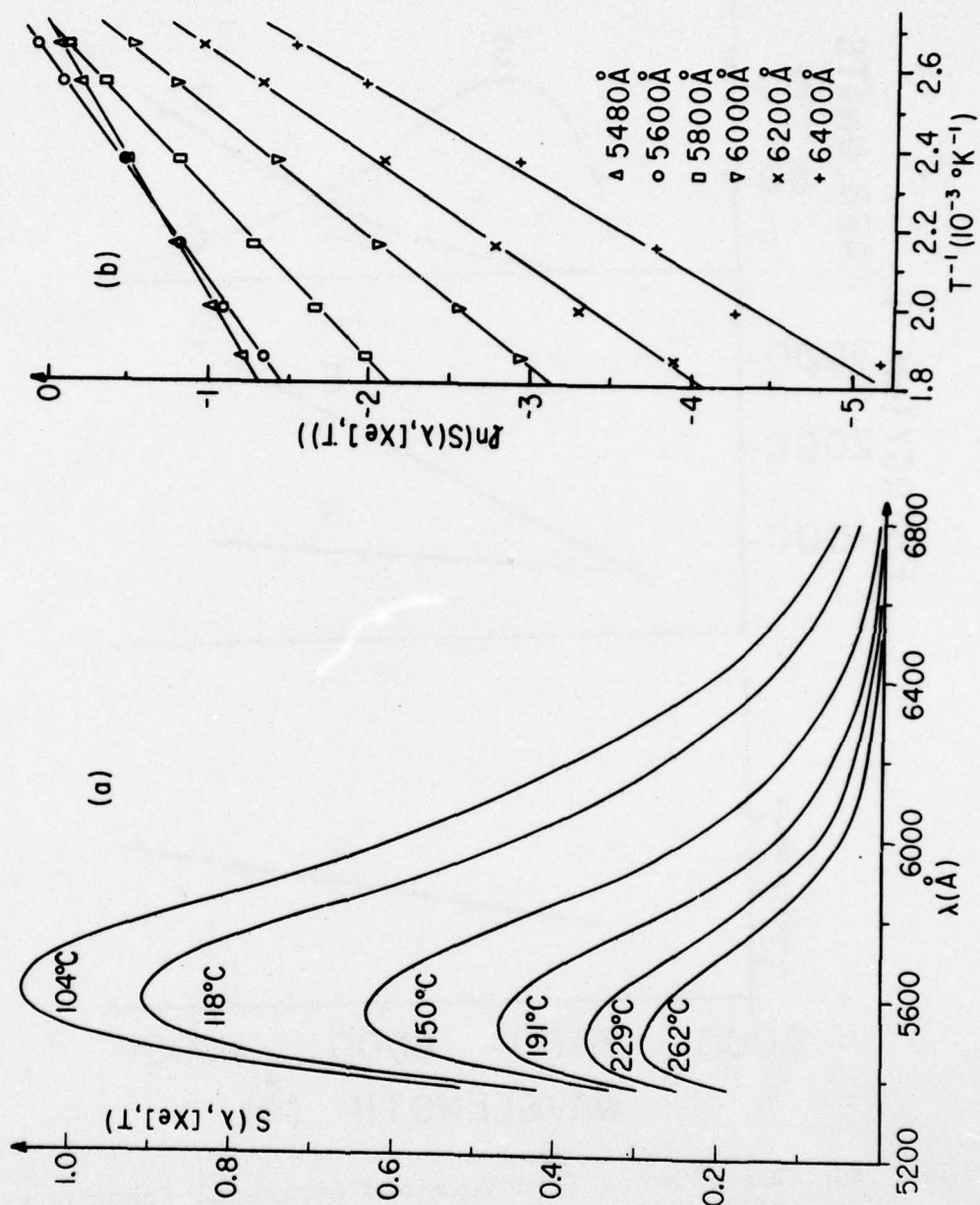


Figure 44

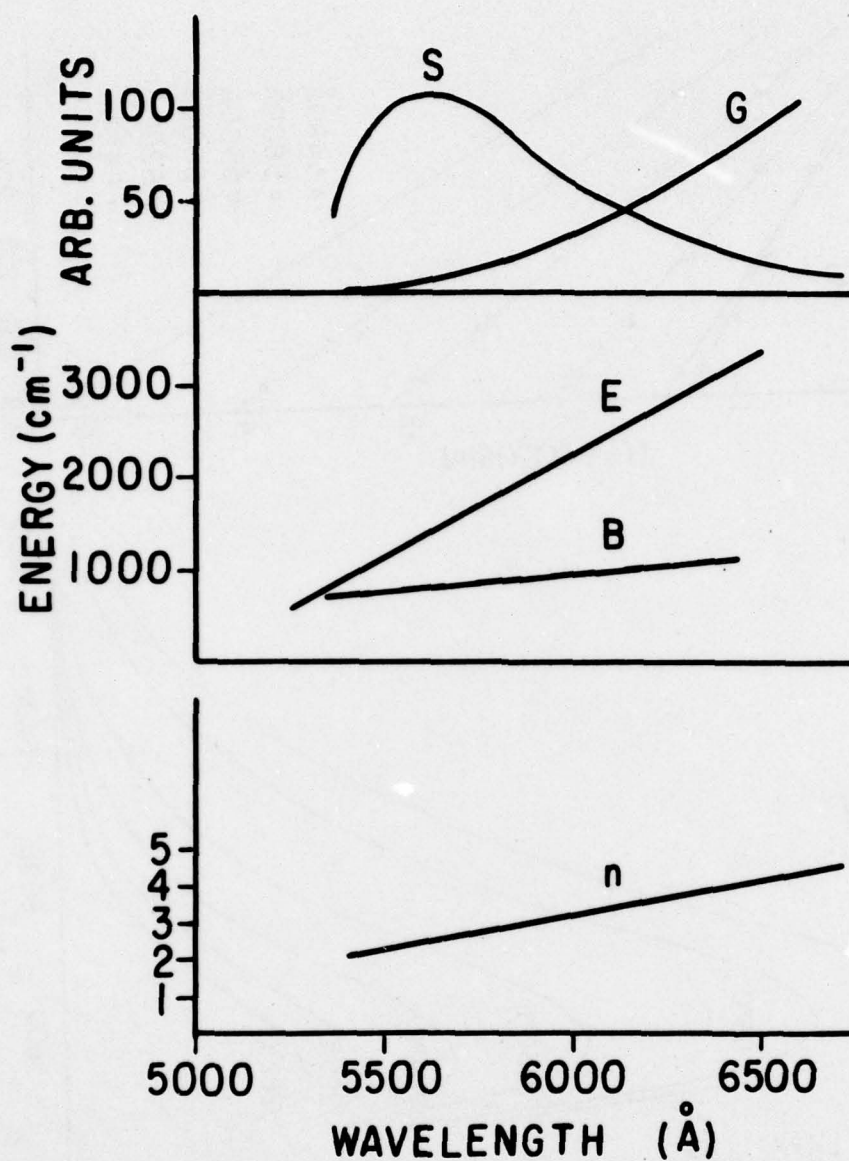
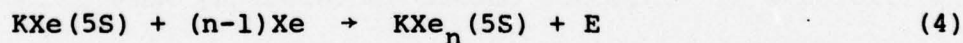


Figure 45: Experimentally determined empirical functions $n(\lambda)$, $E(\lambda)$, and $G(\lambda)$. The function $B(\lambda)$, representing the average binding energy, and a typical polyxenide lineshape $S(\lambda)$ are also shown.

bands of Fig. 44 therefore consist of the superposed and unresolved emission bands of KXe_2 , KXe_3 , KXe_4 , etc. We expect the intensity of the emission band due to KXe_n to be proportional to $[Xe]^n$ with $n = 2, 3, 4$, etc. Since there is substantial overlap of these bands the apparent density dependence of the fluorescence of wavelength λ is $[Xe]^{n(\lambda)}$ where $n(\lambda)$ is the measured non-integer exponent and $n(\lambda)$ can be interpreted as the average number of xenon atoms attached to a potassium atom when the fluorescent wavelength is λ . The values λ_p defined by $n(\lambda_p) = p$ with $p = 2, 3, 4$, etc. can be identified approximately as the peak wavelengths of the emission bands of KXe_2 , KXe_3 , KXe_4 , etc. From Fig. 45 we see that $\lambda_2 = 5500 \text{ \AA}$, $\lambda_3 = 5900 \text{ \AA}$, and $\lambda_4 = 6400 \text{ \AA}$. The peak of the well-resolved monoxenide spectrum occurs at $\lambda_1 = 5220 \text{ \AA}$.

The energy $E(\lambda)$ can be thought of as the internal energy (not enthalpy because of our conditions of constant density rather than constant pressure) released in the reaction



The mean binding energy per xenon atom attached to the monoxenide KXe^* is thus

$$B(\lambda) = \frac{E(\lambda)}{n(\lambda)-1} \quad (5)$$

The binding energy, which is plotted in Fig. 45, is of the order of 1000 cm^{-1} per xenon, and it increases slightly as more xenons are added.

The line shape factor $G(\lambda)$ is perhaps the most remarkable property of the polyxenide band. The function $G(\lambda)$ is proportional to a factor which measures the statistical weight of the configurations of potassium polyxenide molecules which radiate at λ , and a mean transition rate of the configurations. Since the statistical weight factor decreases with increasing n , the rapid growth of $G(\lambda)$ with increasing λ must be due to an increase in the decay rate with λ . Indeed we expect a substantial increase in the radiative transition rate with λ , that is, with the number of attached xenon atoms, because both the monoxenide and polyxenide emission bands of Fig. 43 correlate with a highly forbidden electronic transition of the free atom $K(5S) \rightarrow K(4S)$. Each additional xenon atom in $KXe_n(5S)$ will cause further mixing of the electronic wave functions of the free potassium atom, and the radiative transition will therefore become increasingly more allowed as more xenons are attached. The unprecedented prominence of the green potassium polyxenide band is due to the fact that it originates from a forbidden electronic transition of the free potassium atom. This seems to be one of the main reasons that multiple perturber effects are so much more striking in the data presented in this paper than in the pressure-broadened resonance lines of the alkali atoms.⁽⁷⁾

Since the first excited P states of free alkali atoms have fully allowed transition rates to the ground state, they can only be weakened by multiple perturber effects, while forbidden lines are strongly enhanced.

The nature of these polyxenide exciplexes is still uncertain, but it is interesting to note that cluster ions of the form $K^+(H_2O)_n$ have been extensively studied,^(8,9) and six or more waters of hydration are observed by mass spectroscopic techniques. Similar bonding of alkali ions to other neutral molecules (O_2 , N_2 , and CO_2) has been observed⁽¹⁰⁾ and calculated theoretically.⁽¹¹⁾ The highly polarizable noble gas xenon ($\alpha = 4 \text{ \AA}^3$) can be expected to form analogous cluster ions K^+Xe_n , and an electron could bind to such a cluster ion to form the initial and final states of the polyxenide transitions we have observed.

Further work to understand the nature and possible applications of the potassium polyxenides and other similar exciplexes is being planned.

*This work also supported by the Army Research Office (Durham) under Grant DAAG29-77-G-0015.

- (1) See for example, M. Rokni, J. H. Jacob, J. A. Mangano, and R. Brochu, *Appl. Phys. Lett.* 32, 223 (1978).
- (2) See for example, G. York, R. Schleps, and A. Gallagher, *J. Chem. Phys.* 63, 1052 (1975).
- (3) A. C. Tam, G. Moe, W. Park and W. Happer, *Phys. Rev. Lett.* 35, 85 (1975).
- (4) A. C. Tam, G. Moe, B. R. Bulos and W. Happer, *Optics Comm.* 16, 376 (1976).
- (5) G. Moe, A. C. Tam and W. Happer, *Phys. Rev. A* 14, 349 (1976).

- (6) "Visible Emission Bands of KXe_n Polyatomic Exciplexes", T. Yabuzaki, A. C. Tam, S. M. Curry and W. Happer, submitted for publication.
- (7) W. P. West, P. Shuker and Alan Gallagher, "The Effects of Multi-Perturber Interactions on the Sodium-Rare Gas Excimer Bands", to appear in J. Chem. Phys.
- (8) I. Džidić and P. Kebarle, J. Phys. Chem. 74, 1466 (1970).
- (9) K. G. Spears and S. H. Kim, J. Phys. Chem. 80, 673 (1976).
- (10) G. E. Keller and R. A. Beyer, J. Geophys. Res. 76, 289 (1970); Trans. Am. Geophys. Union 52, 303 (1971).
- (11) K. G. Spears, J. Chem. Phys. 57, 1850 (1972).

D. ABSORPTION STUDIES OF Cs_2 AND Rb_2 MOLECULAR BANDS IN THE VISIBLE AND NEAR VISIBLE

(R. Gupta, W. Happer, J. Wagner, E. Wennmyr)

York and Gallagher⁽¹⁾ have recently suggested that alkali dimers may show promise for high power tunable lasers. Lasing has already been observed in Na molecular bands by several groups.⁽²⁾⁽³⁾⁽⁴⁾⁽⁵⁾ In order to assess the potential of Rb_2 and Cs_2 as possible lasing media, Schlie and coworkers⁽⁶⁾⁽⁷⁾ at Air Force Weapons Laboratory have studied the absorption spectrum of Rb_2 and Cs_2 in the infrared region. In their experiments Schlie et.al. note that the precision of their results is limited by uncertainties associated with the saturated vapor pressure of alkali vapors. We have extended the work of Schlie et.al. to the visible region of the spectrum of Rb_2 and Cs_2 . We have, however, used a two temperature oven, to be described below, and we have thus almost completely eliminated uncertainties associated with the saturated vapor pressure of Rb and Cs.

By analyzing the temperature dependence of the absorption spectrum of Cs_2 in the visible region, we have demonstrated that a group of unusually narrow bands near 7100 Å originates from a very shallow and possibly slightly repulsive part of a ground state potential curve. This may be part of the $^3\Sigma$ ground-state potential curve. An analogous set of narrow bands occurs for Rb_2 near 6000 Å. The remaining prominent visible absorption bands of Cs_2 and Rb_2 all originate from molecules near the bottom of the $^1\Sigma$ ground state. A preliminary report of this work was presented in the last Progress Report.

Our experimental arrangement was the classical absorption spectroscopy arrangement and has been described in the previous Progress Report. Our absorption cell, however, had a unique design, as shown in Fig. 46. The cell was made of alkali resistant Corning 1720 glass and the main body of the cell was 2.5 cm in dia. and 7.5 cm long. The main body of the cell was kept at temperature T_2 . The cell had a long side-arm which was kept at temperature T_1 . The temperature T_1 was always kept lower than T_2 . Thus all the alkali metal was in the side-arm and the vapor pressure of alkali vapor was determined by T_1 . During our runs we maintained the vapor pressure of Cs constant by holding T_1 constant while we varied the temperature of the main cell T_2 to obtain different absorption curves. Typical results for Cs_2 are shown in Fig. 47, where $T_1 = 660^\circ\text{K}$ and T_2 is varied between 685°K and 761°K .

The intensity $I(\nu)$ of the light transmitted through a cell of length z is given by

$$I(\nu) = I_0(\nu) e^{-\alpha(\nu)z} \quad (1)$$

where $I_0(\nu)$ is the intensity of the incident light and $\alpha(\nu)$ is the absorption coefficient given by

$$\alpha(\nu) \propto N^2 e^{-V_\ell(R)/kT_2} \quad (2)$$

N is the number density of Cs atoms and $V_\ell(R)$ is the molecular potential of the lower state at internuclear distance R (we have set $V_\ell(\infty) = 0$). The total vapor pressure in our cell is determined by the temperature T_1 of the Cs metal in the sidearm. Under our experimental conditions the cesium vapor consists predominantly

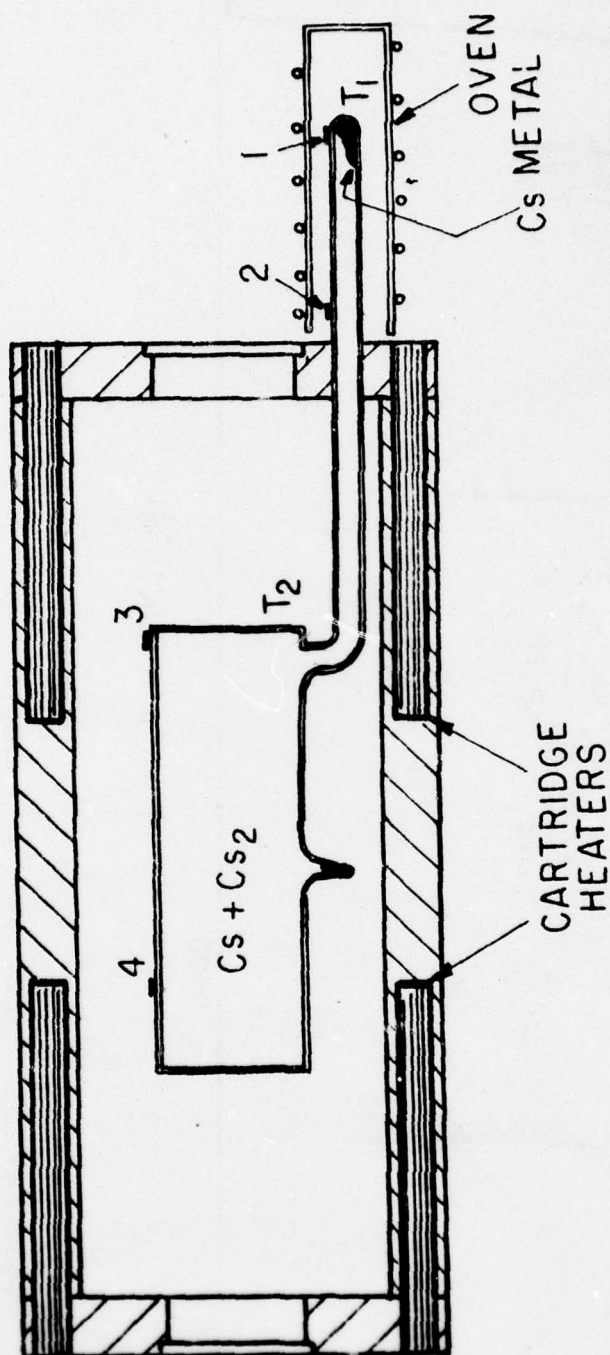


Figure 46 :

Schematic illustration of two-oven arrangement to superheat the Cs cell.

AD-A056 767

COLUMBIA RADIATION LAB NEW YORK

F/G 7/4

RESEARCH INVESTIGATION DIRECTED TOWARD EXTENDING THE USEFUL RAN--ETC(U)

DAAG29-77-C-0019

NL

UNCLASSIFIED

3 of 4
AD
A056 767



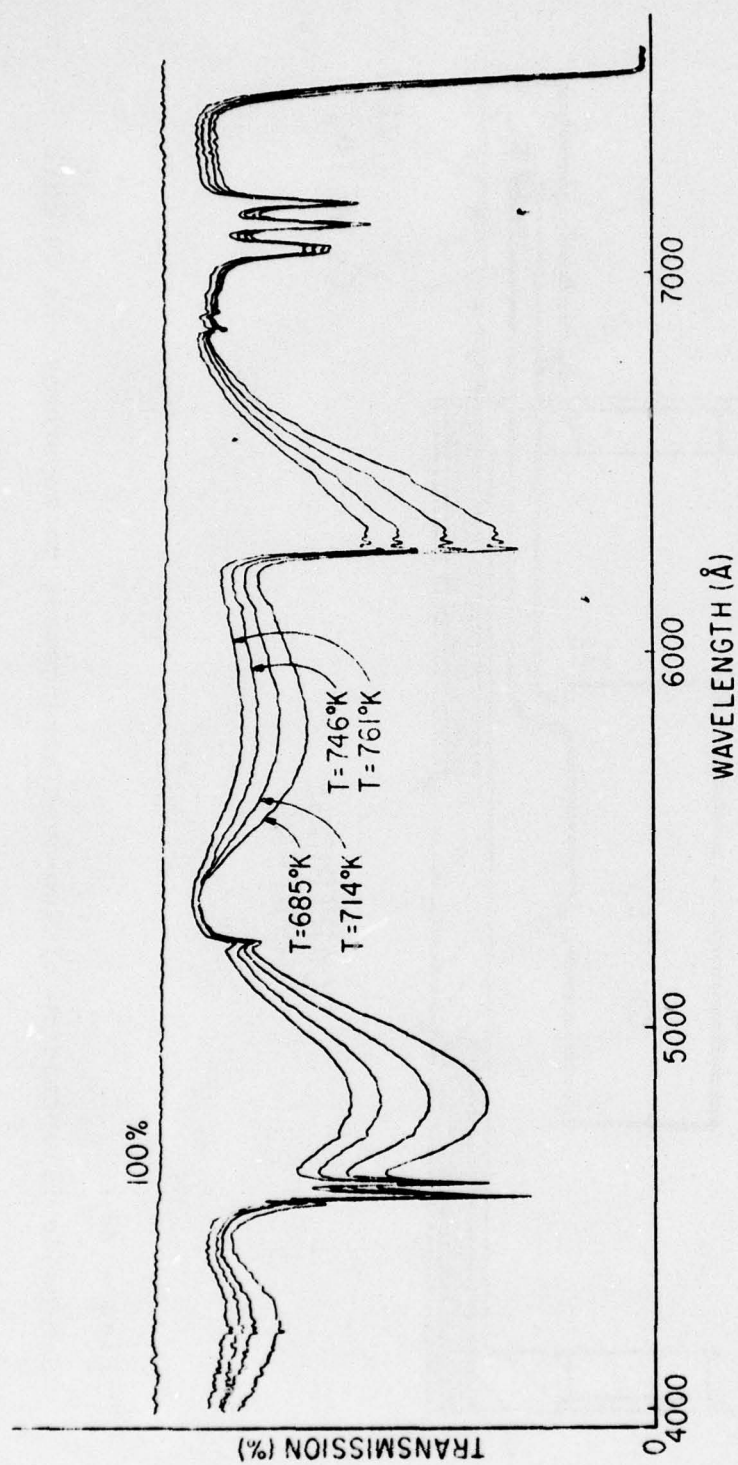


Figure 47 :
Absorption spectrum of Cs_2 molecules. These curves were taken for
 $T_1 = 660^\circ\text{K}$. T_2 was varied between 685°K to 761°K .

of Cs atoms. The partial pressure NkT_2 of Cs atoms in the main body of the cell is therefore very nearly equal to the saturated vapor pressure $P(T_1)$ of the liquid Cs in the side-arm, i.e.,

$$NkT_2 = P(T_1) \quad (3)$$

Combining (1), (2) and (3), we get

$$-\frac{V_\ell(R)}{kT_2} = \ln[-T_2^2 \ln(I(v)/I_0(v))] + \text{constant}. \quad (4)$$

Therefore, plots of $\frac{1}{T_2}$ against $[-T_2^2 \ln(I/I_0)]$ at fixed frequencies on semilog scale should be straight lines with slopes proportional to V_ℓ . Fig. 48 shows such plots for various frequencies and the straight lines and the least-squares fit to the data. The values of V_ℓ , deduced from the slopes of these lines are shown in Table XI. We have taken similar data for the 7600 Å band at lower temperatures (this band is optically thick in Fig. 47), and the results are given in Table XI. The quoted error bars represent two standard deviations of the mean.

Our results (Table XI) indicate that most of the structure in the visible and near visible spectrum of Cs_2 originate from an attractive potential well. Therefore it must originate from the 1Σ ground state. The exception is the structure near 7100 Å which appears to originate from a slightly repulsive ground-state potential. Although we get small positive values for V_ℓ (a repulsive intermolecular potential), the uncertainties are such that we cannot completely exclude a small negative value of V_ℓ for the peaks near 7100 Å.

Since the peaks near 7100 Å correspond to very small potentials

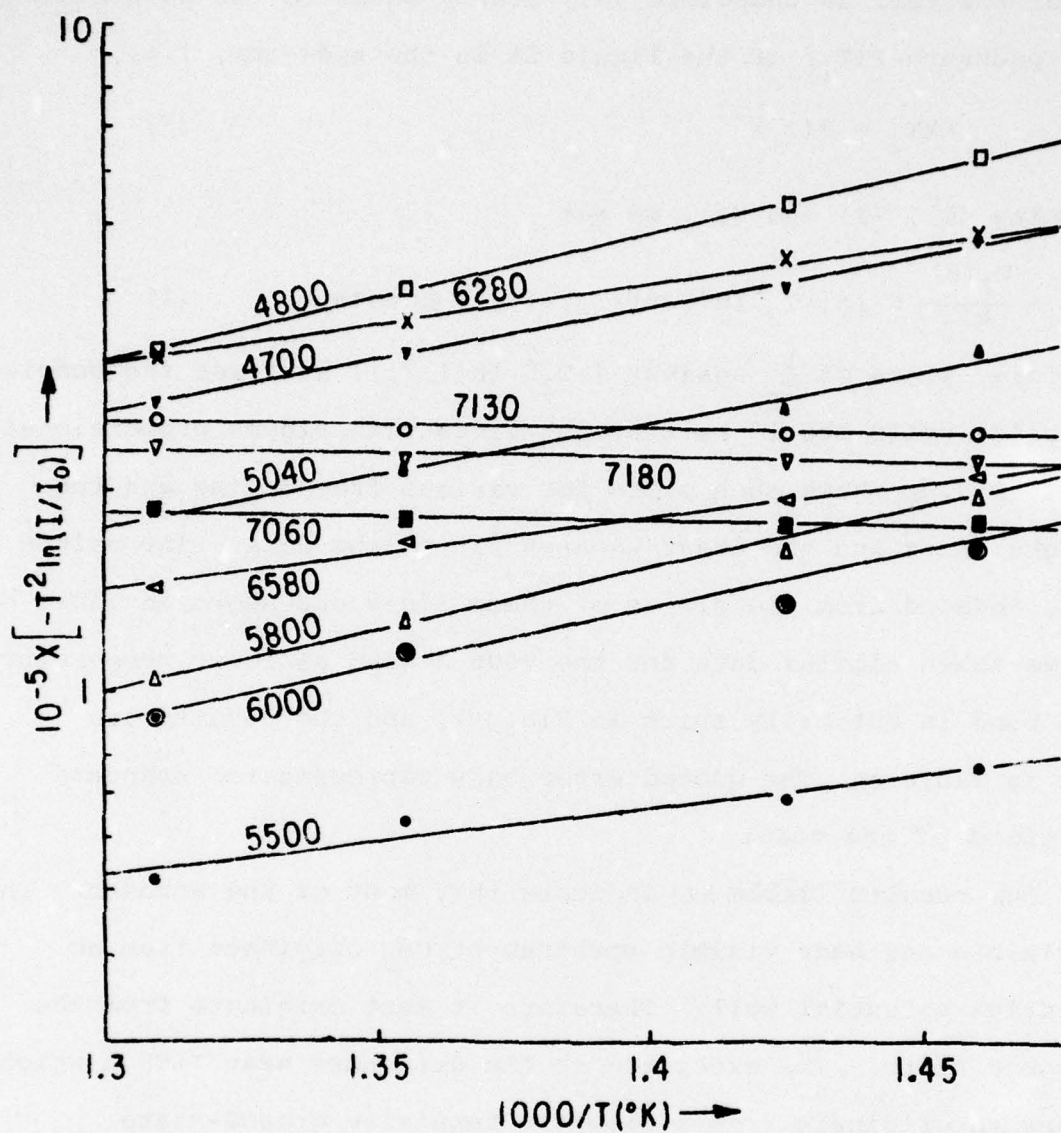


Figure 48 :

$[-T \ln(I(v)/I_0(v))]$ is plotted against $1000/T$ for various wavelengths. The straight lines are least squares fitted lines.

TABLE XI

Wavelength (\AA)	V_g (eV)
4230*	-0.33(5)
4700	-0.347(14)
4800*	-0.383(12)
5040	-0.287(16)
5500	-0.278(62)
5800*	-0.390(34)
6000	-0.330(32)
6580	-0.240(28)
7070*	+0.022(22)
7130*	+0.032(20)
7180*	+0.028(20)
7600*	-0.396(18)
7650	-0.386(22)
7700	-0.388(19)
7880	-0.379(30)

* peaks

V_ℓ , and since the magnitudes of the lowest singlet and triplet potentials of the Cs_2 molecule are thought to be large near the equilibrium internuclear separation it is natural to assume that the peaks at 7100 \AA originate from transitions at large internuclear separations where V_ℓ is small. There is no way to tell for certain from our data whether the peaks near 7100 \AA correspond to transitions from the singlet or triplet ground states, but if the lower state potential V_ℓ is indeed positive, as is indicated in our data, the peaks at 7100 \AA would be the first identified optical transitions out of the repulsive triplet ground state of Cs_2 molecules.

We have taken similar data for Rb_2 . Unfortunately, Rb reacted with the 1720 glass at these elevated temperatures, changing the transmission characteristics of the glass. Therefore, we were unable to get very quantitative data. However, we were able to ascertain that most the structure in Rb_2 absorption bands in the visible region originates deep in the attractive part of the ground state potential curve. The exception is a structure near 6000 \AA which seems to originate from a very shallow or possibly repulsive part of the potential. There is little doubt the narrow peaks around 6000 \AA in the spectrum of Rb_2 are analogous to the similar peaks around 7100 \AA for Cs_2 .

- (1) G. York and A. Gallagher, Joint Institute for Lab. Astrophysics, University of Colorado, Report No. 114, 1974.
- (2) M. A. Henesian, R. L. Herbst, and R. L. Byer, J. Appl. Phys. 47, 1515 (1976).
- (3) A. Bauer and K. S. Sreenivasa Murthy, Appl. Phys. 12, 391 (1977).

- (4) B. Wellinghauser, S. Shahdim, D. Friede, and H. Welling, Appl. Phys. 13, 97 (1977).
- (5) H. Itoh, H. Uchiki, and M. Matsuoka, Opt. Comm. 18, 271 (1976).
- (6) D. L. Drummond and L. A. Schlie, J. Chem. Phys. 65, 2116 (1976).
- (7) R. P. Benedict, D. L. Drummond, and L. A. Schlie, J. Chem. Phys. 66, 4600 (1977).

E. PHOTOIONIZATION AND STIMULATED EMISSION IN ALKALI-NOBLE
GAS VAPORS*

(G. Moe, W. Happer)

During the previous year experiments were begun to measure collisionally-induced decay rates and excitation transfer rates in the excited states of alkali atoms in the presence of high pressure noble gas atmospheres. Our early results disclosed that additional processes were taking place which had to be thoroughly understood and eliminated in order that the experiments actually measure the desired physical parameters. These additional processes, which involve photoionization and stimulated emission, were found to be quite interesting in their own right.

The apparatus used in these experiments is shown in Figure 49. A glass sample cell containing either pure cesium metal or cesium with several atmospheres of a noble gas such as xenon or krypton is contained in a glass oven. The oven is heated electrically to a temperature as high as 400°C. The sample is irradiated with light from a pulsed tunable dye laser which is pumped by a nitrogen laser. Both of these lasers were constructed in this laboratory and are discussed in Progress Report number 27. The laser light is focussed into the cell with a 5 cm fl. lens and the light emerging from the cell in the forward direction (or at other times at right angles to the incident laser beam) is collected by a lens of 89 mm focal length and focused into the entrance slit of a 3/4 meter SPEX grating monochromator. The light is

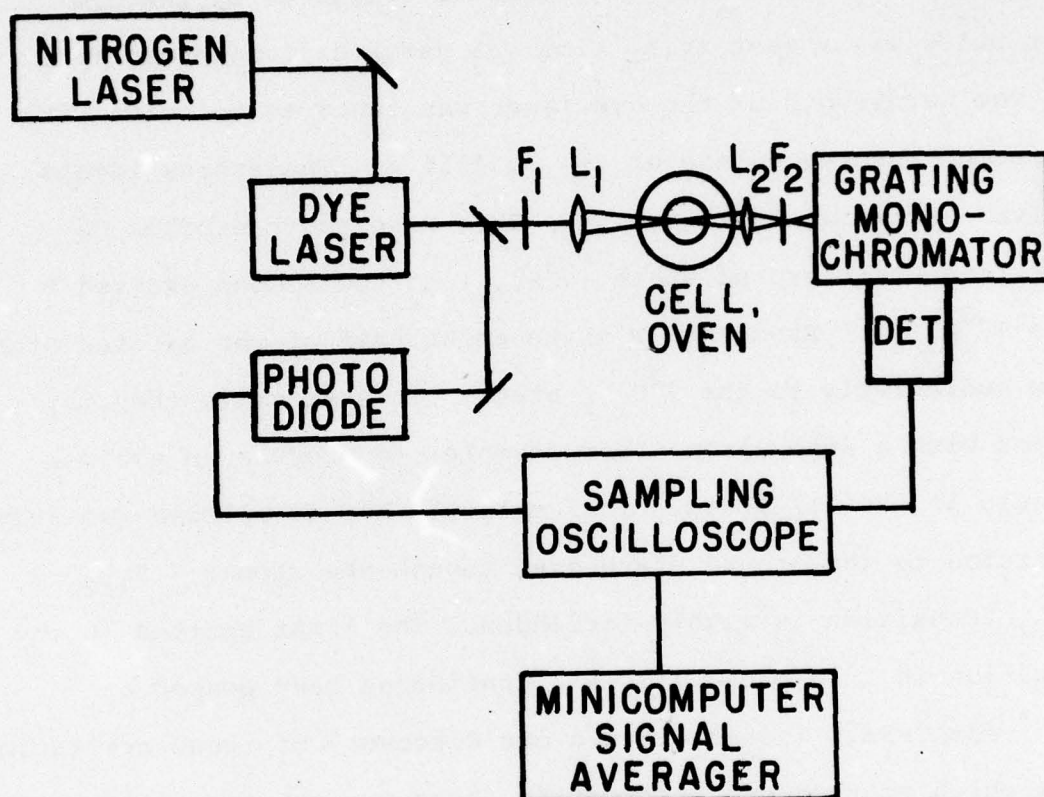


Figure 49: Schematic of experimental apparatus for time-resolved spectroscopy.

detected by a fast photomultiplier tube. The anode current from this tube is sent into the input of a sampling oscilloscope which is interfaced to a PDP 8/E minicomputer operating as a signal averager. The sampling scope-signal averager combination functions as an averaging transient digitizer with sub nanosecond time resolution. The sampling scope is triggered by the dye laser pulse via a fast (rise time $< .5$ nsec) silicon photodiode.

The wavelength of the dye laser was tuned to coincide with the second resonance line of Cs at 4555 \AA . The energy levels involved are shown in Figure 50. This wavelength excites Cs atoms from their ground state ($6^2S_{1/2}$) to the second excited P state ($7^2P_{3/2}$). From the 7P state about half of the excited atoms decay radiatively to the $7^2S_{1/2}$ state. In that state they may combine with a xenon atom (for example) to produce an excimer molecule in the $7s\text{]} \text{ state}$. This molecule has an allowed radiative transition to the ground state even though the atomic $7^2S_{1/2} \rightarrow 6^2S_{1/2}$ transition is highly forbidden. The light emitted in the transition is in a broad ($\sim 50 \text{ \AA}$), continuous band peaked at 5723 \AA for CsXe. Indeed, it was our discovery of these new excimer bands which sparked our interest in these excimer transitions as discussed in Progress Report number 26 and number 27.

Our intention was to study the rate of decay of fluorescence from the excimer molecule, but in the process we discovered something unexpected and quite interesting. We observed strong fluorescence from a multitude of excited states of Cs, states with

energies considerably higher than the 7P level we were exciting. Some of these emissions are shown as wavy lines in Figure 50. The states involved are S, D, and even F states. Their energies are such that it would not be possible to excite them with a single 4555 Å dye laser photon.

The fluorescence from these high-lying states was observed to have a very fast rise time, nearly as fast as the laser excitation pulse. Figure 51 shows the time history of the fluorescence from three of the high-lying D states. The cell temperature is 230°C, which corresponds to a Cs vapor density of 4.4×10^{15} . This will be true for all the results discussed in this report, although similar effects were seen over a broad range of temperatures. No noble gas was present for the results to be discussed here, although similar effects were observed in cells with an atmosphere of Ar or Kr. Figure 52 shows a detail of the initial peak of one of these decay curves, for the $8D \rightarrow 6P$ transition, with greater time resolution. The rise time of the fluorescence is seen to be about the same as that of the laser pulse. In addition, the decay of the fluorescence was observed to be definitely nonexponential. This is demonstrated in Figure 53, which shows the time history of the $8^2S_{1/2} \rightarrow 6^2P_{1/2}$ transition. The upper trace shows the log of the fluorescence curve, which would be a straight line if the decay were a simple exponential.

The very fast rise time of the fluorescence (a few nanoseconds) demonstrates conclusively that this fast fluorescence is not the

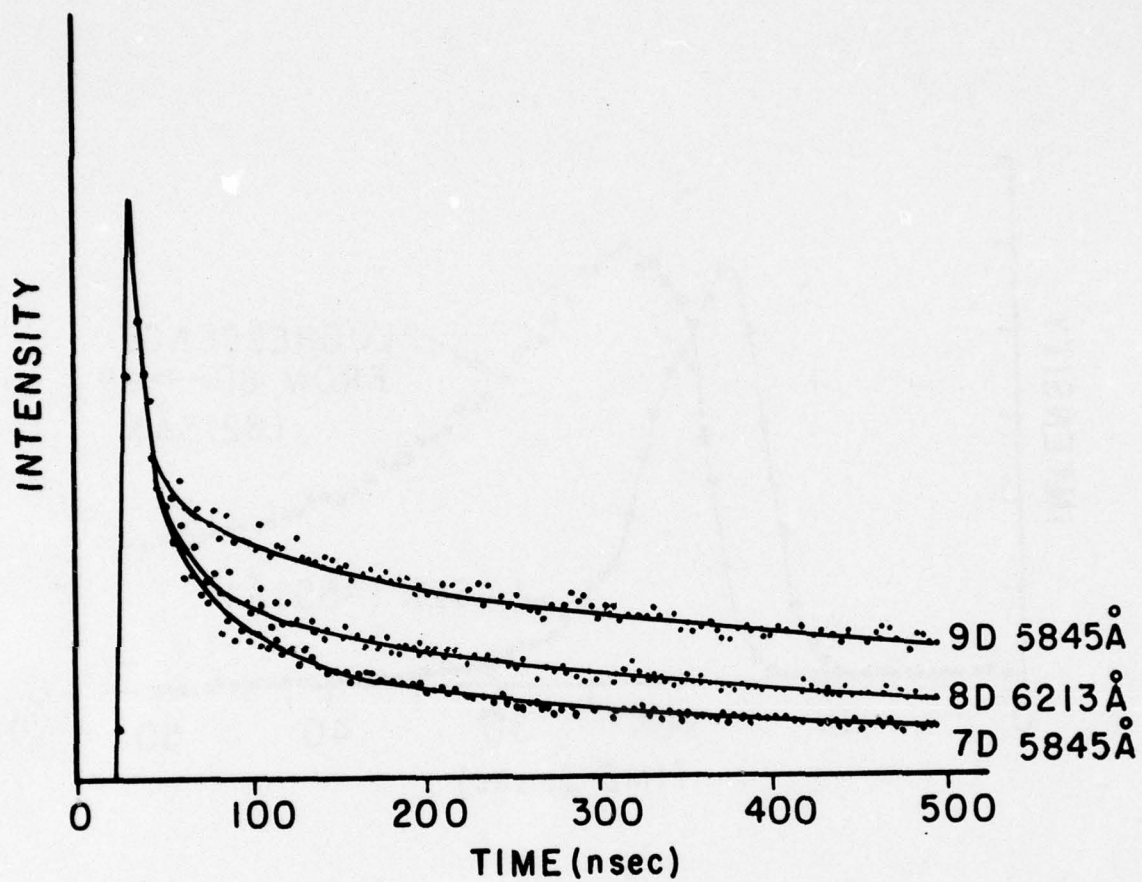


Figure 51: Fluorescence from nD-6P transitions in Cs as a function of time. The D states lie considerably higher in energy than the 7P level populated by the laser.

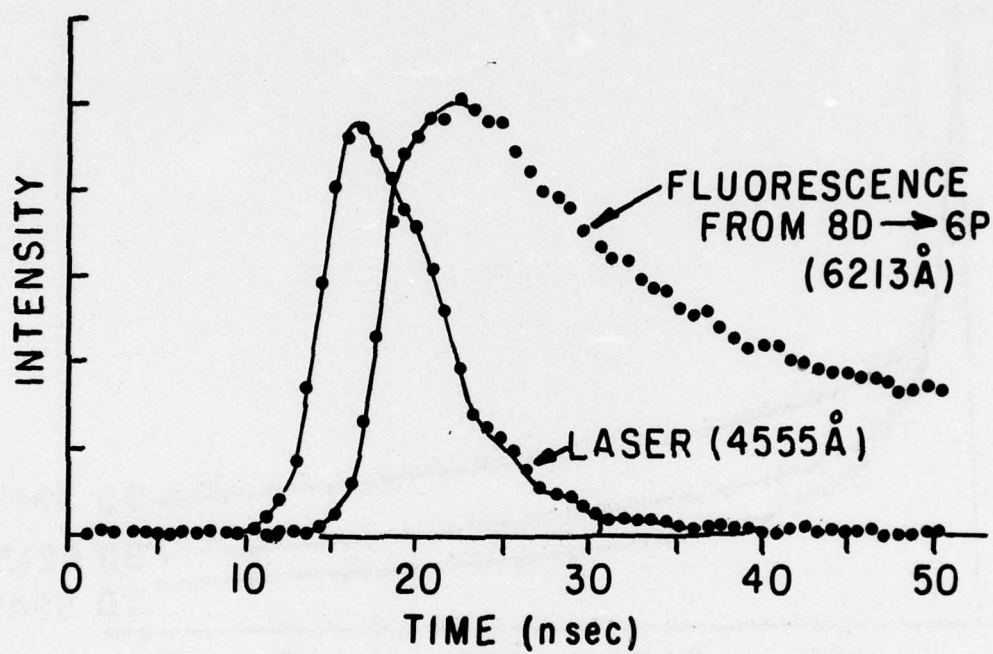


Figure 52: Detail of the initial peak for the $8^2D_{5/2} \rightarrow 6^2P_{3/2}$ transition in cesium.

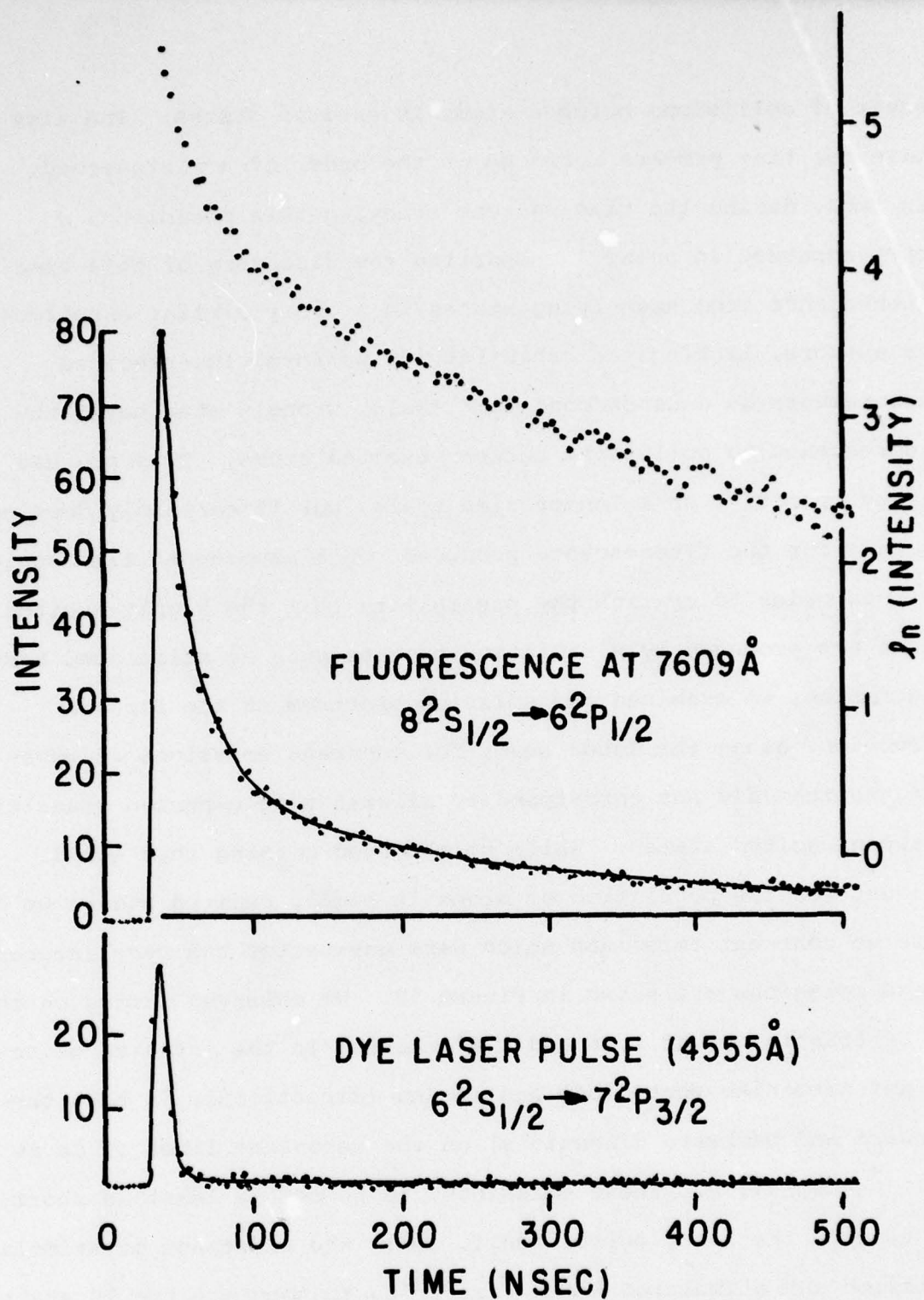


Figure 53: Decay of the fluorescence from the $8^2S_{1/2}$ state in Cs.

result of collisions between atoms in excited states. The time scale for that process would be on the order of a microsecond. (In fact, during the time we were studying this phenomenon a paper appeared in print⁽¹⁾ reporting the discovery of this same fluorescence from high-lying states in a very similar experiment. The authors, lacking the capability to perform time-resolved measurements on a nanosecond time scale, wrongly attributed the fluorescence to collisions between excited atoms. This process may be operative on a longer time scale, but it certainly does not account for the fluorescence produced on a nanosecond time scale.

In order to examine the possibility that the highly-excited atoms are produced by a radiative process such as stimulated Raman scattering, we examined the emission spectrum in the forward direction, along the laser beam, for coherent emissions at wavelengths that did not correspond to allowed single-photon transitions between excited states. While we observed nothing that would account for the population of atoms in highly excited states we did observe coherent emissions which were unexpected and very interesting. These emissions are shown in Figure 50. We observed lasing on the 7S-6P transitions at 1.36 and 1.47 microns in the infrared using a fast germanium photodiode and lasing (directional, in both the forward and backward directions) on the resonance lines of Cs at 8521 \AA and 8943 \AA . These emissions, in pulses at least as short in time as the laser pulse itself, imply the existence of stimulated emission and stimulated Raman scattering to populate the 7S state

from the 7P state. We were quite surprised to see the stimulated emission on the resonance lines of Cs, since the optical thickness of the Cs vapor in the resonance lines at this density is on the order of 10^4 or 10^{15} and fluorescence is highly trapped. The stimulated emission could not be produced by populating the 6P state directly from the 6S state, as one could at most saturate the transitions and equalize the populations. There is, however, nothing to prevent achieving a population inversion on this transition via the 7P state, in a process similar to that used in a 3-level laser. Thus this process is not so surprising, and could have been expected. A literature search revealed that it had been reported during the last year by Kung and Itzkan,⁽²⁾ who also discuss the Raman processes discussed above.

We also observed coherent emissions at approximately 6606 \AA , as shown in Figure 50, which results from a four-wave mixing process involving a laser photon and two 2.93μ photons from the $7P \rightarrow 7S$ transition. The wavelength of this emission tunable over a range of about 10 \AA by tuning the wavelength of the pump laser. This emission is produced by the same 4-wave mixing process as that observed in potassium vapor by Sorokin, Wynne, and Lankard in 1972.⁽³⁾

All the coherent emissions discussed up to this point are produced by mechanisms that are easily understood. However we also observed a coherent emission at 5393.5 \AA , the wavelength of the $7^2S_{1/2} \rightarrow 6^2S_{1/2}$ transition in cesium, which is not as readily

explained. This transition is highly forbidden. The electric dipole moment is zero for an isolated atom because of parity violating considerations and the magnetic dipole moment is known to be anomalously small by some four orders of magnitudes. This makes it much too small to account for the emissions we observe. This is in fact the reason this transition was selected by M.A. Bouchiat and C. Bouchiat to look for an electric dipole moment induced by parity-violating weak neutral current effects.⁽⁴⁾ The coherent emissions on the 7S - 6S transition had also been independently and previously observed by Flusberg, Mossberg and Hartmann⁽⁵⁾ of this laboratory in an unrelated experiment.

Figure 54 shows the time history of the 5394 Å 7S - 6S emission above that of the laser pulse. Much of the pulse width is instrumental due to the finite band width of the photomultiplier tube used (Amperex TUV56). The laser pulse itself has a full width at half maximum of about 5 nsec when observed with a biplanar photodiode with a rise time less than .5 nsec.

The rise of the 7S - 6S emission is delayed from that of the laser by approximately 1 nsec in Figure 49.

We interpret both the 7S-6S emission and the fluorescence from the high-lying states as due to photoionization of the Cs atoms by the laser pulse. An excited Cs atom can absorb another laser photon and become photoionized, producing an electron with on the order of 1 eV of kinetic energy. Remembering that electrons move ~2000 times more rapidly than atoms for the same kinetic energy) we see that the collision rate between electrons and excited

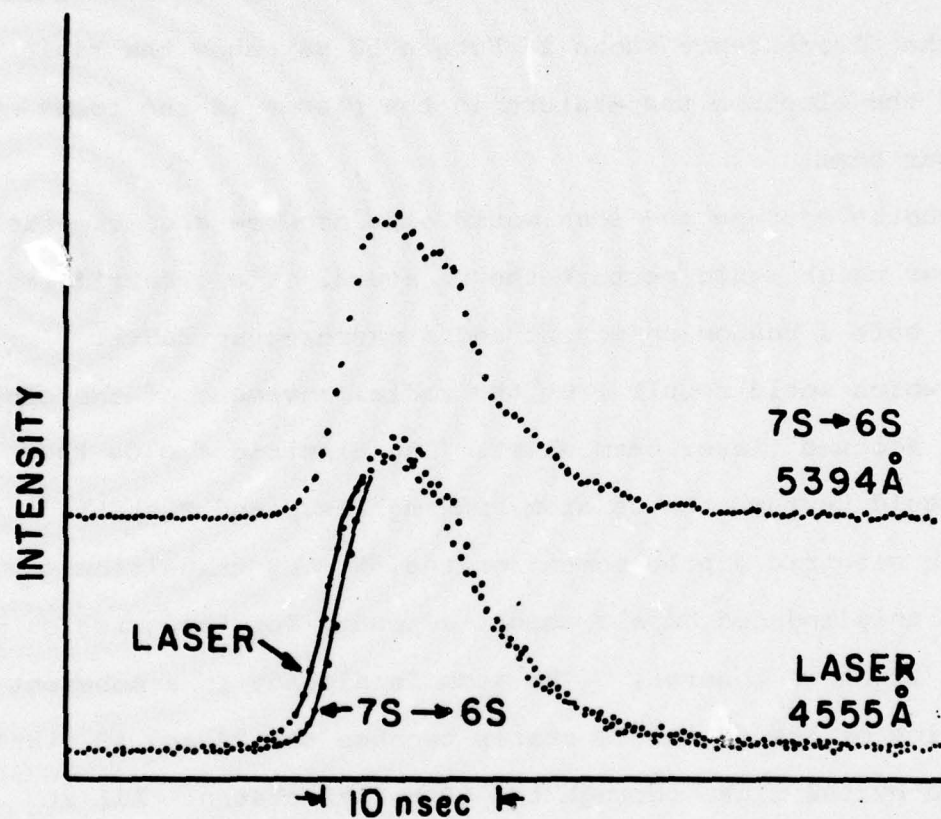


Figure 54: Coherent emission from the $7^2S_{1/2} \rightarrow 6^2S_{1/2}$ transition in Cs perturbed by fields from ions and electrons. The upper trace shows the two lower traces superimposed.

atoms in the laser beam would be large enough to easily account for the fast rise time of the fluorescence. In fact the collision rate is probably rapid enough to establish an equilibrium between the relative populations of the highly excited states and the electron temperature. Thus the very rapid "nonexponential" initial decay of the fluorescence shown in Figure 53 may show the rapid cooling of the electron temperature in the plasma in the focus of the laser beam.

The photoelectrons and ions would also produce electric fields in the vapor which would perturb the Cs atoms. The electric field would have both a random component and a macroscopic radial component which would result from the radial movement of the electrons out of the focused laser beam waist. The electric fields thus produced would perturb the Cs atom, mixing its S and P states and inducing an electric dipole moment on the 7S - 6S transition. We believe this induced dipole moment accounts for the emission of the 5394 Å light we observe. (The atom is already in a coherent superposition of the 6S and 7S states because the 7S and 6S states are coupled by the light through the 6P and 7P states. All it needs is a nonzero expectation value for the dipole moment.)

The electric field induced dipole matrix element E_1 has been calculated as a function of the external electric field E_0 by Bouchiat and Bouchiat.⁽⁴⁾ The result is

$$E_1 = \langle 7S | e r | 6S \rangle = 5.83 \times 10^{-8} e a_0 E_0 \left(\frac{V}{cm} \right) \quad (1)$$

Where $e r$ is the dipole moment operator and $E_1 = e a_0$ corresponds to an oscillator strength $f = 1$.

In order to get some idea of the magnitude of the induced dipole moment we measured the relative intensities of the various emissions. The results are shown in Table XII. If we were to assume that the 7S - 6S and 6P - 6S emissions would have roughly equal intensities for equal oscillator strength, and use the fact that the oscillator strength for the 6P - 6S transition is nearly unity, we come out with a rough estimate of the oscillator strength for the 7S - 6S transition of $(1/3.3 \times 10^4) \approx 3 \times 10^{-5}$. This means an electric dipole moment roughly 1/2% that of a fully allowed transition. (This value is really an upper bound, since it is not certain that most of the light emitted in the resonance lines escapes from the vapor). According to Equation 1, this would imply an rms electric field of $\sim 10^5$ V/cm. This is equal to the field of an electron at a distance of 120 \AA .

In order to confirm our hypothesis that the unexpected effects observed were due to ionization we used a cell with two interior disk-shaped electrodes facing each other about 1 cm apart and measured the amount of charge produced by a laser pulse. We applied a small voltage across the plates and operated in a region (a few volts to ~ 30 volts) where the amount of charge collected was independent of the voltage. To determine the total charge produced we integrated the area under the trace on an oscilloscope as the charge decayed through a known resistance.

TABLE XII

Relative Intensities of the Observed Emissions

Laser	4555 Å	3 kW	2.2×10^7
6P → 6S	8521 Å		3.3×10^4
4-wave	6606 Å		83
7S → 6S	5394 Å		1

The result was 1.2×10^{12} electrons. Under our experimental conditions this corresponds to nearly total ionization of the vapor in the volume of the focused laser beam, which we estimate to be $\sim 100 \mu$ in diameter at the focus.

This finding of near total ionization is in good agreement with our own rough estimate of the number of ions expected using a laser peak intensity of ~ 10 kW in a 5 nsec pulse (this is more than adequate to saturate the 7P - 6S transition) and the value for the photoionization cross section $\sigma = 5 \times 10^{-18} \text{ cm}^2$ at 4555 \AA measured by Nayfeh et al.⁽⁶⁾ (A precise comparison is difficult because some of the electrons detected in the experiment were surely produced after the laser pulse by collisional processes.) Near-total ionization has recently been observed in sodium and cesium vapors by Lucatorto and McIlrath⁽⁷⁾ and by Hurst et al.⁽⁸⁾ respectively using flashlamp-pumped dye lasers. Our results show that nitrogen-pumped dye lasers, which have approximately 10^4 times less energy per pulse and are commonly used in a variety of experiments with atomic vapors, are also easily capable of producing a very high degree of ionization in an atomic vapor. Both ionization and stimulated emission can have substantial effects on the results of experiments designed to study collisional processes in supposedly neutral vapors, such as the decay rate measurements in progress in this laboratory, and these experiments must be designed to eliminate such extraneous effects.

* This work also supported by the Army Research Office (Durham) under Grant DAAG29-77-G-0015.

- (1) S. G. Leslie, J. T. Verdeyen, and W. S. Millar, J. Appl. Phys. 48, 4444 (1977).
- (2) Robert V. Kung and Irving Itzkan, IEEE J. Quant. Elect. QE-13, 73 (1977).
- (3) P. P. Sorokin, J. J. Wynne, and J. R. Lankard, App. Phys. Lett. 22, 342 (1973).
- (4) M. A. Bouchiat and C. Bouchiat, J. Phys. (France) 36, 493 (1975).
- (5) A. Flusberg, T. Mossberg, and S. R. Hartmann, Phys. Rev. Lett. 38, 59 (1977).
- (6) Munir H. Nayfeh, G. S. Hurst, M. G. Payne, and G. P. Young, Phys. Rev. Lett. 39, 604 (1977).
- (7) T. B. Lucatorto and T. J. McIlrath, Phys. Rev. Lett. 37, 428 (1976).
- (8) G. S. Hurst, M. H. Nayfeh, and J. P. Young, Phys. Rev. 15A, 2283 (1977).

III. QUANTUM DETECTION AND SENSING OF RADIATION

A. NONLINEAR HETERODYNE DETECTION AND SENSING IN THE INFRARED AND OPTICAL REGIONS OF THE SPECTRUM.

Progress in this project during the first interval has been achieved in a number of directions, as described in the following subsections: 1. Heterodyne correlation radiometry; 2. Simple threshold detection of a continuous signal in noise with multiple independent observations; and 3. Heterodyne detection of rough targets in the infrared and optical.

1. Heterodyne Correlation Radiometry⁽¹⁾

(M. C. Teich, R. A. Meyers, G. Vannucci)

We have recently shown that three-frequency nonlinear heterodyne detection can be a useful technique for the acquisition of weak communications and radar signals in the presence of substantial Doppler shift.^{(2) (3) (4)} The same concept has also been considered in the context of a multiple-frequency passive configuration, for the selective heterodyne detection of radiation from known remote species moving with unknown velocities.^{(4) (5)} Basically, the system uses a nonlinear element to provide an output signal near a predetermined difference frequency f_c , which is independent of the Doppler shift of the received signals. The quantity f_c may be the frequency difference between two transmitter modes,^{(2) (3) (4) (6)} or the rest difference frequency between two

waves emitted from a remotely radiating source.^{(4) (5)} The signal-to-noise ratio (SNR) obtainable with the nonlinear heterodyne system can be substantially higher than that obtainable with a conventional heterodyne system by virtue of the (often considerable) decrease in receiver bandwidth that is possible and the relatively small amount of receiver noise introduced by the nonlinear element.

The present work considers the use of the same principle in an altered configuration, to sensitively detect the signature of a source whose Doppler feature is known, but whose presence we wish to affirm. A radiating sample of the species to be detected is physically made a part of the laboratory receiver, and serves as a frequency-domain template with which the remote radiation is correlated, after heterodyne detection. The system will be especially useful for the detection of species or sources whose radiated energy is distributed over a large number of lines, with frequencies that are not necessarily known. Examples include the radiation from complex molecules at submillimeter wavelengths and molecular radiation in the infrared and optical. We observed that remote conventional heterodyne radiometry and spectroscopy have recently begun to find use at these higher frequencies.⁽⁷⁻¹⁰⁾ Detailed studies of the sensitivity limits of a real infrared heterodyne spectrometer have been carried out by Abbas et al.⁽¹⁰⁾ Attention has been drawn to a number of multiplexing or correlation techniques useful for increasing the detectability of a weak signal, including Fourier-transform spectrometry,⁽¹¹⁾ gas-cell correlation spectrometry,⁽¹²⁾ and Fabry-Perot interferometry for periodic rotational Raman spectra.⁽¹³⁾ The system described here provides the advantages of heterodyning in conjunction with correlation.

A block diagram of the remote-detection version of the proposed system is illustrated in Figure 55. The remotely radiating source emits electromagnetic radiation at a series J of rest signal frequencies f_j (j integer). Also present in the same source are other undesired species (impurities), emitting radiation at the series K of rest frequencies f_k (k integer). The f_j radiation, as well as the f_k radiation, will in general be Doppler shifted due to the motion of the source, and will arrive at the receiving station with frequencies f'_j and f'_k , respectively. These series are referred to as J' and K' .

The received remote radiation is then combined with the radiation from a local sample of the species to be detected, which is at rest in the laboratory frame and therefore emits at frequencies f_j . The three series of frequencies (f'_j , f_j , and f'_k) are mixed in a heterodyne detector with a strong, coherent, and polarized local oscillator (LO) signal at frequency f_L to produce three series of strong electrical beat signals at $|f'_j - f_L|$, $|f_j - f_L|$, and $|f'_k - f_L|$, along with a dc component that is blocked. This is shown schematically in Figure 56. Signals at $|f'_j - f_j|$, $|f'_j - f'_k|$, and $|f_j - f'_k|$, arising without benefit of the LO, are weak and may be neglected. In the infrared and optical, optimum mixing requires coincident, plane, parallel, and polarized waves normally incident on the photodetector;⁽¹⁴⁾ thus spatial first-order coherence is required over the detector aperture.⁽¹⁵⁾⁻⁽¹⁸⁾ As shown in Fig. 55, the ac output of the heterodyne mixer must then be coupled, through a filter of bandwidth Δf , to a nonlinear device. Provided that

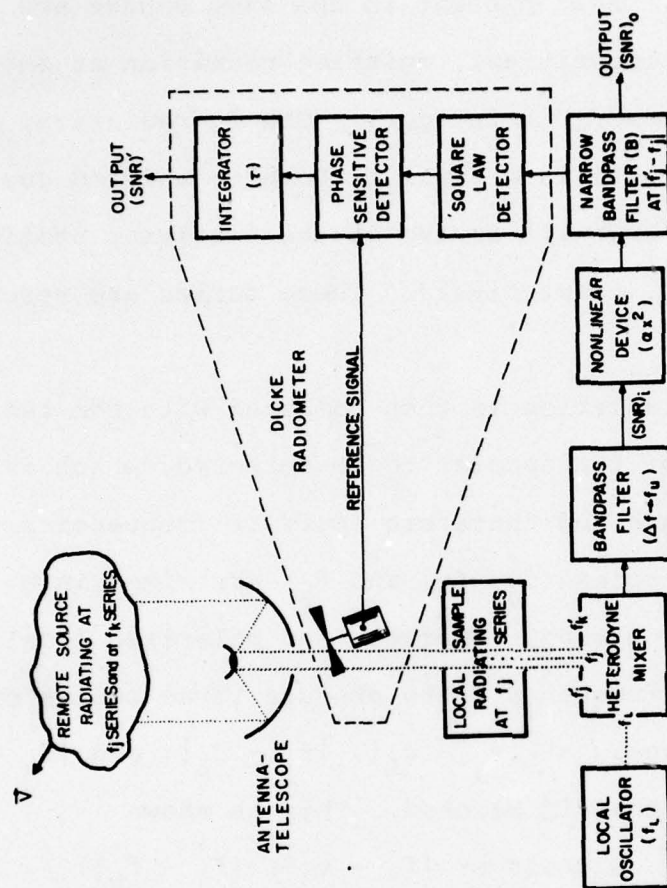


Figure 55:

Block diagram for the heterodyne correlation radiometer. Dotted lines represent radiation signals, solid lines with arrows represent electrical signals, and dashed lines enclose one version of a Dicke radiometer that can be added to the system if required.

Figure 56 :

Schematic representation of frequency mixing in the heterodyne correlation radiometer. The cross-hatched areas represent individual line contributions (from line pairs j) to the over-all detected signal power. The technique is most useful for detecting species whose radiated energy is distributed over a large number of lines. Note that the frequencies f_j and f_L need not be known whereas the Doppler shift frequency $|f'_j - f_j|$ is assumed to be known a priori. The local oscillator may be multimode, non-stabilized, and non-tunable.

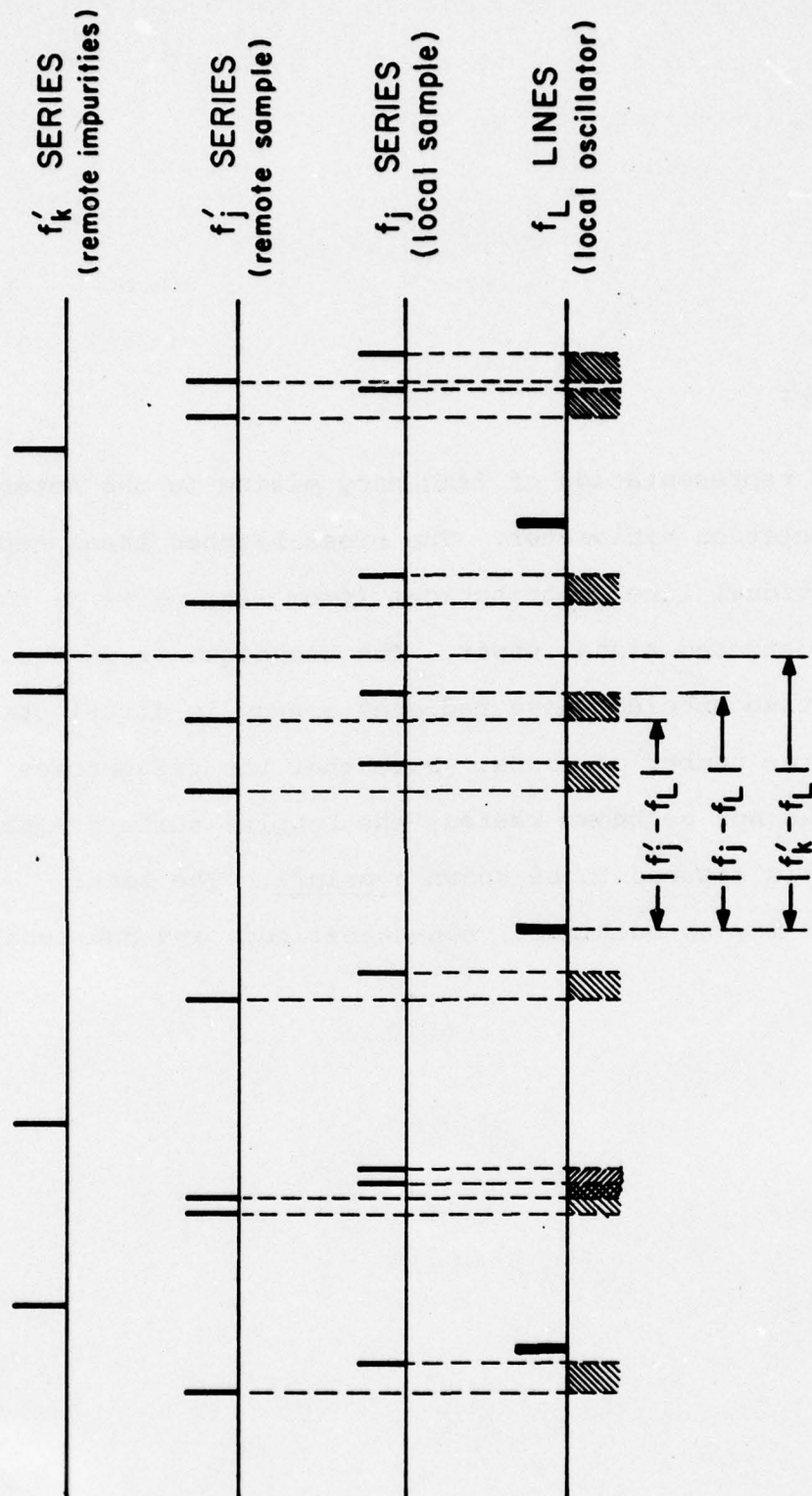


Figure 56

the bandwidth Δf encompasses several lines produced by the species to be detected, its value is not critical. The nonlinear device, which is assumed to have a response over Δf , then generates a component of power at the Doppler shift frequency

$$|f'_j - f_j| = (v_{||}/c)f_j \quad (1)$$

for each j when both $|f'_j - f_L|$ and $|f_j - f_L|$ pass through Δf . Contributions from individual values of j are shown as the cross-hatched areas in Fig. 56. The greater the number n of these line pairs that pass through the filter, the greater the power generated at the Doppler shift frequency. It is also evident from Fig. 56 that a multimode LO (indicated by 3 LO lines in our schematic) may increase the likelihood that several lines are detected from the desired species.

Previous embodiments of the nonlinear heterodyne detection technique⁽²⁾⁽³⁾ assumed that the Doppler shift (represented by $v_{||}$) was unknown within broad limits, but that the difference frequency f_c was known a priori to high accuracy. In the present circumstance, we assume that the radiated line frequencies are unknown but that the Doppler shift is known a priori, at least to good approximation (see Fig. 56). As previously,⁽²⁾⁽³⁾⁽⁴⁾⁽⁵⁾⁽⁶⁾ the nonlinear device output is independent of LO frequency and amplitude fluctuations, within broad limits. (A careful choice of the LO frequency will often be useful, however.) A narrowband filter centered at $|f'_j - f_j|$ and of bandwidth B , placed after the nonlinear device, achieves a low noise bandwidth (see Fig. 55). Only the heterodyne mixer and the nonlinear device need have high-frequency response

in many instances. Thus, amplifiers and other detection apparatus following the nonlinear device, though omitted in the block diagram for simplicity, process electrical signals at (usually) moderate frequencies, which provides ease of matching as well as good receiver noise figure. This, in turn, decreases the LO power necessary for optimum coherent detection. (16) (17) (18) The effect of accidental contributions at $|f'_j - f_j|$ arising from the K' series can generally be neglected.

If warranted, the output of the narrow bandpass filter may be fed into a standard Dicke radiometer⁽¹⁹⁾ (dashed box in Fig. 55) consisting of a (third) detector, a phase-sensitive (synchronous) detector, and an integrator with time constant τ . Although we specify that the third detector is square-law in Fig. 55, its characteristic is not critical and, in fact, a linear detector will often provide the cleanest signal. The modulation may be obtained from a chopper as indicated in Fig. 55, though in some circumstances it might be advantageous to switch the frequency of the narrow bandpass filter instead of the remote radiation (for baseline elimination). The use of a Dicke radiometer will generally provide improvement in the SNR and has been coupled with conventional infrared heterodyne systems in a number of instances. (9) (10) It may also be advantageous to use a balanced mixer in this configuration. (7)

Considerable progress has been made in the theoretical analysis of the heterodyne correlation radiometer and the details will be published shortly. (1) The ideal SNR and MDP at the output of the

system have been obtained for a number of cases of interest, including sinusoidal signals and Gaussian signals with both Gaussian and Lorentzian spectra. Small linewidths and closely spaced lines are seen to enhance detectability, as does a strongly radiating local sample. Of course, the remote source should be as strong as possible for definitive detection. Correction factors for impurity species have been accounted for and are not expected to seriously impair operation of the system. For certain choices of parameters, the SNR at the output of the heterodyne correlation radiometer will provide a sufficient confidence level for detection. For situations in which this is not the case, further improvement can be obtained by using a classical radiometer, a balanced mixer, and/or a multichannel receiver. Though system performance is excellent, the real SNR may be reduced by a variety of deleterious effects in analogy with the conventional system.⁽¹⁰⁾

The technique should operate over a broad frequency range from the microwave to the optical. For the submillimeter region, it may be possible to use a combination Schottky-barrier-diode/harmonic-mixer that would provide an output at low frequencies as long as the high-frequency beat signals are generated and mixed within the detector. LO harmonics are also readily generated in these devices⁽²⁰⁾ so that harmonic-mixing heterodyne correlation radiometry could be performed.⁽²¹⁾ Josephson junctions, which can sometimes be made to produce their own LO power, and metal-oxide-metal diodes could also be used. An IMPATT solid-state oscillator could conveniently be considered as an LO in these regions since

frequency stabilization, which is difficult to achieve in these devices, is not required. At higher frequencies, tunable diode lasers and Schottky-barrier detectors may be useful components.

Because the theoretical solutions we have obtained⁽¹⁾ appear to confirm the attractive features of the technique, we are proceeding with an experimental implementation. In the next interval, we will construct a simple heterodyne correlation receiver using an Ar^+ multimode laser operated at 5145 \AA in conjunction with two scattering targets. That will provide a good experimental indication of the usefulness of heterodyne correlation radiometry and will determine whether we shall proceed with implementation in the infrared, where the technique is likely to provide the most advantage.

- (1) M. C. Teich, Opt. Eng. 17, 170 (1978).
- (2) M. C. Teich, Appl. Phys. Lett. 15, 420 (1969).
- (3) M. C. Teich and R. Y. Yen, Appl. Opt. 14, 666 (1975); 14, 680 (1975).
- (4) M. C. Teich, "Nonlinear Heterodyne Detection," in Topics in Appl. Phys., edited by R. J. Keyes (Springer-Verlag, New York, 1977), vol. 19, Optical and Infrared Detectors, ch. 7.
- (5) M. C. Teich, Rev. Sci. Instr. 46, 1313 (1975).
- (6) R. L. Abrams and R. C. White, Jr., IEEE J. Quantum Electron. QE-8, 13 (1972).
- (7) T. de Graauw and H. van de Stadt, Nature (London) Phys. Sci. 246, 73 (1973).
- (8) J. Gay, A. Journet, B. Christophe, and M. Robert, Appl. Phys. Lett. 22, 448 (1973).
- (9) M. A. Frerking and D. J. Muehlner, Appl. Opt. 16, 526 (1977).

- (10) M. M. Abbas, M. J. Mumma, T. Kostiuk, and D. Buhl, Appl. Opt. 15, 427 (1976).
- (11) P. B. Fellgett, J. Phys. Rad. 19, 187 (1958).
- (12) T. V. Ward and H. H. Zwick, Appl. Opt. 14, 2896 (1975).
- (13) J. J. Barrett and S. A. Meyers, J. Opt. Soc. Am. 61, 1246 (1971); J. J. Barrett, Opt. Eng. 16, 85 (1977).
- (14) A. E. Siegman, Proc. IEEE 54, 1350 (1966).
- (15) M. C. Teich, Appl. Phys. Lett. 14, 201 (1969); "Quantum Theory of Heterodyne Detection," in Proc. Third Photocond. Conf., edited by E. M. Pell (Pergamon, New York, 1971), pp. 1-5.
- (16) M. C. Teich, R. J. Keyes, and R. H. Kingston, Appl. Phys. Lett. 9, 357 (1966).
- (17) M. C. Teich, Proc. IEEE 56, 37 (1968); 57, 786 (1969).
- (18) M. C. Teich, "Coherent Detection in the Infrared," in Semiconductors and Semimetals, edited by R. K. Willardson and A. C. Beer (Academic, New York, 1970), vol. 5, Infrared Detectors, ch. 9.
- (19) R. H. Dicke, Rev. Sci. Instrum 17, 268 (1946).
- (20) H. R. Fetterman, B. J. Clifton, P. E. Tannenwald, C. D. Parker, and H. Penfield, IEEE Trans. Microwave Theory Tech. MTT-22, 1013 (1974).
- (21) P. F. Goldsmith, R. L. Plambeck, and R. Y. Chiao, IEEE Trans. Microwave Theory Tech. MTT-22, 1115 (1974).

2. Simple Threshold Detection of a Continuous Signal in Noise with Multiple Independent Observations

(P. R. Prucnal, M. C. Teich, G. Lachs)

The likelihood-ratio detection of a signal embedded in noise constitutes an important class of classical binary decision problems that has found widespread applicability in the synthesis and analysis of many types of systems.⁽¹⁾ Though the signal-to-noise ratio (which is most useful for analog systems) can frequently provide a rough indication of system performance for digital systems, likelihood-ratio analysis and error probabilities provide more appropriate performance criteria for digital systems. For complex signal and noise statistics, however, it is sometimes difficult or impossible to express the likelihood-ratio in closed form. Even for simple signal and noise statistics, direct implementation of the likelihood-ratio as an optimum detector may be rather difficult. Sometimes it is possible to reduce the likelihood-ratio to a simpler, but equivalent detector by using various ad hoc geometric arguments or lengthy algebraic manipulations.

In the present work we derive a remarkable simple detector that is optimum for a broad range of classical binary decision problems involving likelihood-ratio detection of a signal embedded in noise. The class of problems we consider encompasses the case of N independent (but not necessarily identically distributed) observations of an arbitrary non-negative (or non-positive) continuous signal, embedded in additive, independent, and non-interfering continuous noise. For infrared or optical heterodyne

detection, we can use this method provided we can separate signal, local oscillator, and mixing contributions from such noninterfering noise sources as dark noise and amplifier noise.

We show that a comparison of the sum of the N observations with a unique threshold comprises an optimum detector, provided only that the logarithm of the noise probability density does not contain a point of inflection. This condition on the noise probability density is not necessary, but is sufficient, to imply our simple threshold detector, and does not depend on the signal probability density. Our results are applicable to a spatial array of detectors exposed to a temporal sequence of observations. In many cases, it is not difficult to test the logarithm of the noise density analytically for a point of inflection. In more difficult cases, a graphical representation of the noise density with a logarithmic ordinate scale could be useful in revealing a point of inflection. We also develop a restriction on the form of the likelihood ratio that renders the sum of the N observations a sufficient statistic.

We consider the following general classical binary detection problem. Each of two source outputs corresponds to a hypothesis, H_0 or H_1 . To decide which hypothesis is true, based on the Bayes or Neyman-Pearson criterion, optimum processing of the observation vector \vec{x} is the well-known likelihood-ratio test⁽¹⁾

$$\Lambda(\vec{x}) = \frac{p(\vec{x}|H_1)}{p(\vec{x}|H_0)} \begin{matrix} H_1 \\ \geq 1 \\ < \\ H_0 \end{matrix} \lambda, \quad (1)$$

where $\Lambda(\vec{x})$ represents the likelihood-ratio, $p(\vec{x}|H_1)$ is the probability density of \vec{x} given that H_1 is true, and λ is a constant dependent on the choice of decision criterion. The observation vector $\vec{x} = (x_1, \dots, x_N)$ consists of N independent observations, which may represent a spatial array of N_s detectors sampled during a sequence of N_t time intervals, in which case $N = N_s N_t$.

In the simplest situation, $N_s = N_t = 1$, so that a single detector samples a single observation x_1 . In this case $\Lambda(x_1)$ may be graphically represented by a simple-two-dimensional Cartesian plot. We demonstrate that a simple condition on the noise density, namely that its logarithm does not contain a point of inflection, implies that $\Lambda(x_1)$ is monotonic with respect to x_1 . The monotonicity of $\Lambda(x_1)$ implies, in turn, that Eq. (1) is equivalent to the simple threshold detector

$$x_1 \begin{matrix} H_1 \\ \geq \\ < \\ H_0 \end{matrix} \lambda' , \quad (2)$$

with threshold λ' . Equation (2) completely specifies optimum processing of x_1 .

Considering now the case $N > 1$, we visualize $\Lambda(\vec{x})$ as a N -dimensional surface in $N+1$ space. An N -dimensional hyperplane, orthogonal to the Λ axis at λ , cuts through the surface $\Lambda(\vec{x})$. This is illustrated in Fig. 57 for $N=2$. For an observation $\hat{\vec{x}}$, the test given by Eq. (1) is equivalent to determining whether $\Lambda(\hat{\vec{x}})$ is located above or below the hyperplane: if it is above, H_1 is chosen; if it

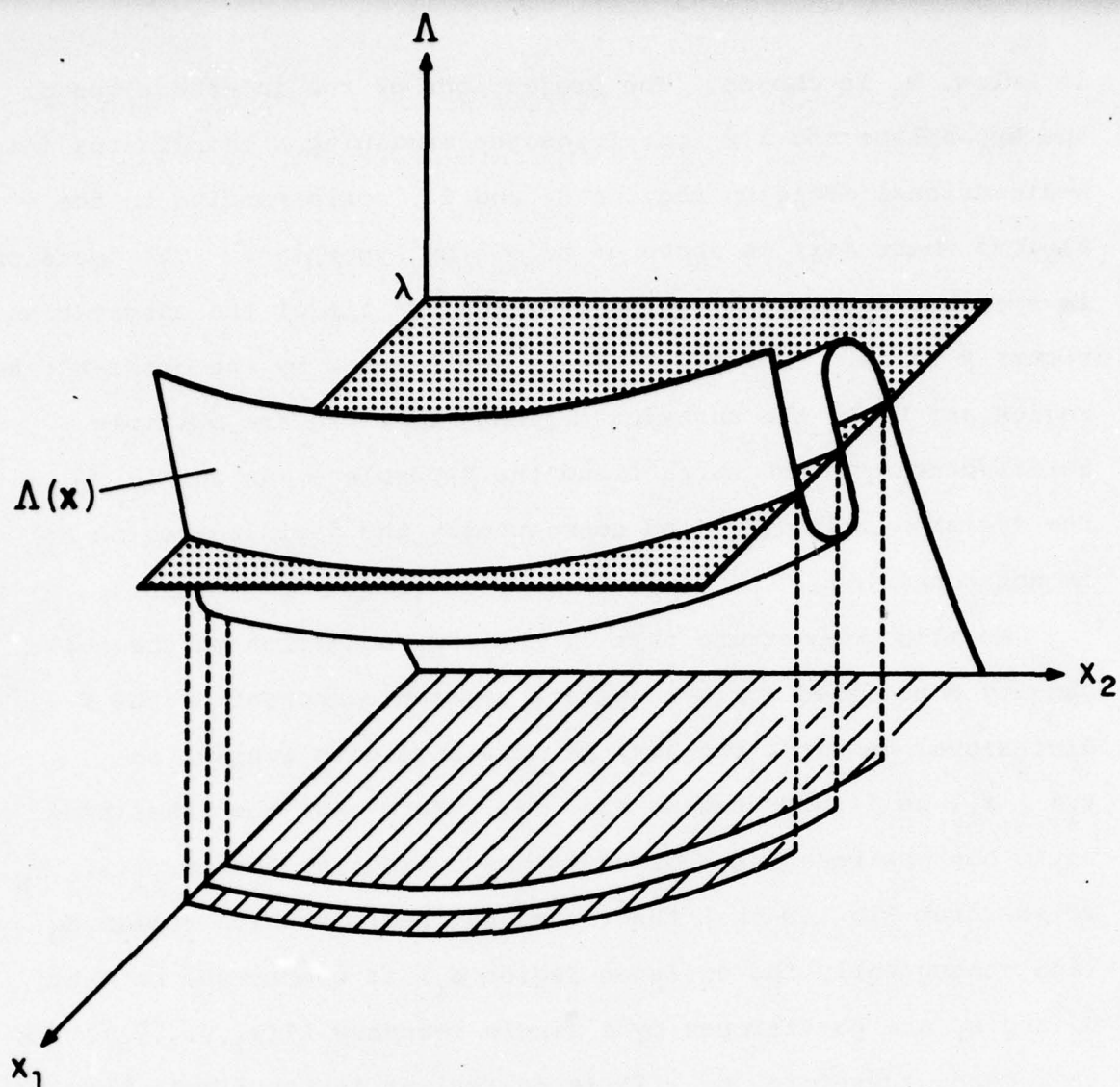


Figure 57 :

The likelihood ratio $\Lambda(\vec{x})$ versus the observations x_i for the case $N = 2$. The solution $\Lambda(\vec{x}) = \lambda$ is represented by the multiple curved intersections of $\Lambda(\vec{x})$ with the dotted plane. The decision regions H_0 are cross-hatched and represent the coordinates (x_1, x_2) for which $\Lambda(\vec{x}) < \lambda$. The decision regions H_1 are unshaded and represent the coordinates (x_1, x_2) for which $\Lambda(\vec{x}) \geq \lambda$. This case exhibits multiple curved decision boundaries.

is below, H_0 is chosen. The projections of the intersections of the hyperplane and $\Lambda(\vec{x})$ partition the remaining N coordinates into N -dimensional decision regions H_1 and H_0 , corresponding to the regions where $\Lambda(\vec{x})$ is above or below the hyperplane. The decision is then based upon the region in which the tip of the observation vector \hat{x} falls. In Fig. 57, H_0 is represented by the cross-hatched region and H_1 by the unshaded region. If there are multiple intersections of the surface and the hyperplane, as in Fig. 57, the decision region H_0 (and consequently the decision region H_1) is not connected.

We also demonstrate that if the same condition on the noise density considered for $N=1$ applies to each component of the N -dimensional density, the $\Lambda(\vec{y})$ is monotonic with respect to $y_1 = \sum_{i=1}^N x_i$, as illustrated in Fig. 58. (Note that the likelihood ratio has now been transformed to the coordinate system y_1, \dots, y_N .) We see from Fig. 58 that the (cross-hatched) decision region H_0 (and consequently the decision region H_1) is connected, so that H_0 and H_1 are partitioned by a single boundary $\lambda''(y_2, \dots, y_N)$. In this case, therefore, Eq. (1) is equivalent to the simple threshold detector

$$y_1 \begin{matrix} H_1 \\ \geq \\ < \\ H_0 \end{matrix} \lambda''(y_2, \dots, y_N) = \lambda''(\vec{x}). \quad (3)$$

This does not completely specify optimum processing, as does the simple threshold detector in the case $N=1$, where λ' is not a

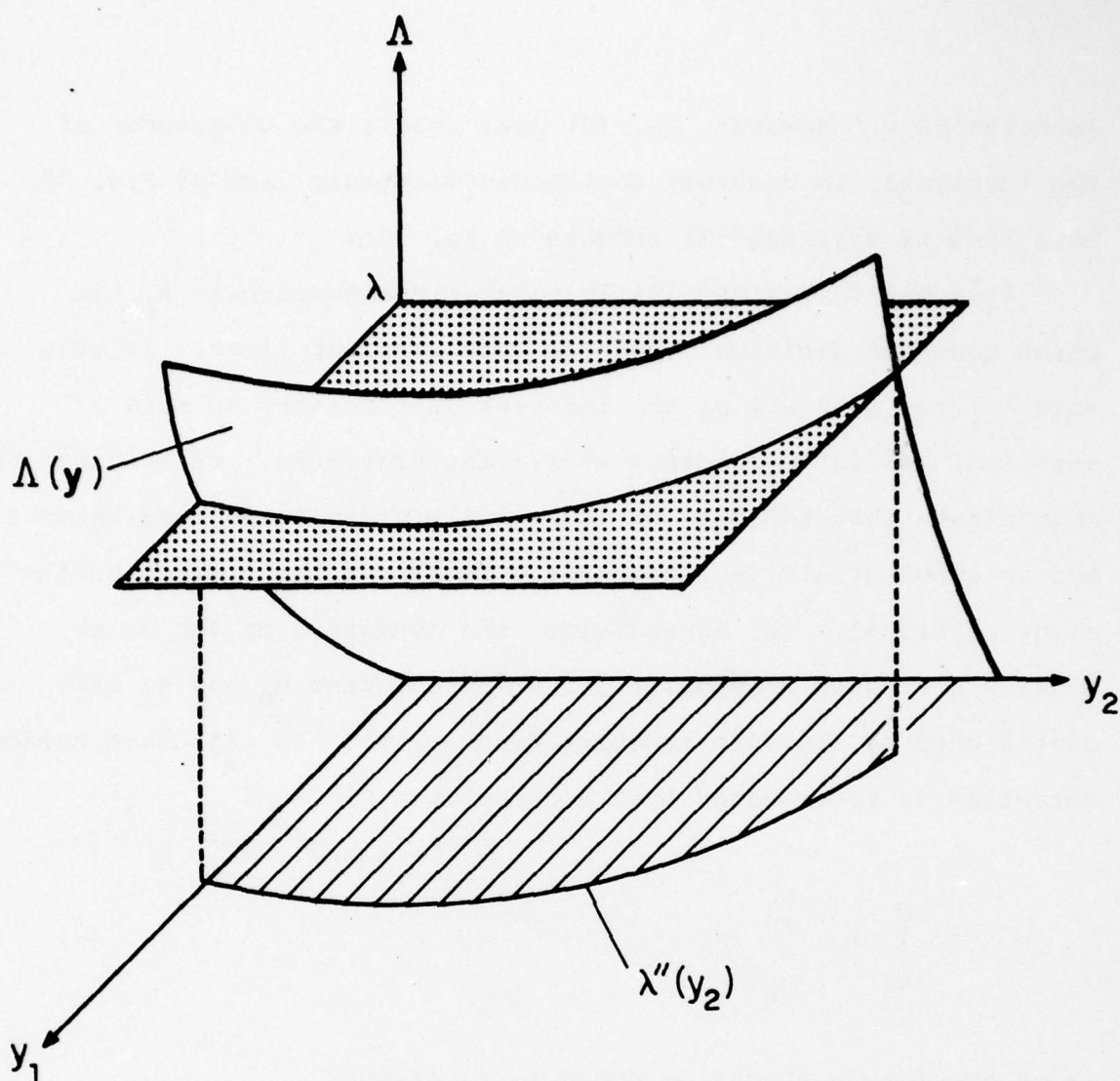


Figure 58 :

The transformed likelihood ratio $\Lambda(\vec{y})$ for the case $N = 2$, where $\Lambda(\vec{y})$ is monotonic with respect to y_1 . The solution $\Lambda(\vec{y}) = \lambda$ is represented by a single curved intersection of $\Lambda(\vec{y})$ with the dotted plane. The region H_0 is cross-hatched and represents the coordinates (y_1, y_2) for which $\Lambda(\vec{y}) < \lambda$. The decision region H_1 is unshaded and represents the coordinates (y_1, y_2) for which $\Lambda(\vec{y}) \geq \lambda$. This case exhibits a single curved decision boundary $\lambda''(y_2)$, and therefore simple threshold detection.

function of \vec{x} . However, Eq. (3) does assure the uniqueness of the threshold, in contrast to the non-monotonic case of Fig. 57. Note that if $N=1$, Eq. (3) reduces to Eq. (2).

$\Lambda(\vec{y})$ may depend explicitly only on the coordinate y_1 , in which case the decision boundaries are straight lines. In this case, y_1 contains all of the information necessary to make a decision, and is therefore a sufficient statistic. We are able to demonstrate that independent identically distributed observations and an exponential likelihood ratio renders $y_1 = \sum_{i=1}^N x_i$ a sufficient statistic. If, in addition, the condition on the noise density discussed previously is satisfied, then H_0 and H_1 are partitioned by a single constant boundary λ' . In this case optimum detection is represented by the comparison

$$\sum_{i=1}^N x_i \underset{H_0}{\overset{H_1}{\geq}} \lambda'. \quad (4)$$

which completely specifies optimum processing.

A manuscript has been prepared documenting the details of these results and has been submitted for publication.⁽²⁾ We have found that the following noise densities satisfy the simple condition cited above: Gaussian, Rayleigh, gamma, and Maxwell. The beta noise density satisfies it only for certain parameter values, whereas the Cauchy noise density never satisfies it.

In short we have demonstrated that simple threshold detection represents optimum processing in many more cases than previously considered. Our work on this problem is now complete.

- (1) H. L. VanTrees, Detection, Estimation, and Modulation Theory, (Wiley, New York, 1968), Part 1.
- (2) P. R. Prucnal and M. C. Teich, "Simple threshold detection of a signal in noise with multiple independent observations: Continuous case," submitted for publication.

3. Heterodyne Detection of Rough Targets in the Infrared and Optical*
(M. Elbaum, M. C. Teich)

Heterodyning in the infrared and optical provides a useful technique for the detection and estimation of a weak signal buried in a strong background (this is true for both the conventional and the nonlinear implementations). In this work, we consider the detection of weak radiation scattered from a laser-illuminated non-cooperative rough target.⁽¹⁾⁻⁽⁶⁾ Taking into account the coherence properties of the scattered radiation enables us to demonstrate that receiver performance is optimized when the degeneracy parameter of the scattered signal light is unity. This result establishes a connection between the mean number of signal photocarriers released and the radar pulse duration. The coherence properties of the scattered radiation are therefore germane to the design of heterodyne laser radar systems and should not be omitted from the formalism as is usual.

The theoretical portion of this work has been largely completed and a manuscript detailing the results is in preparation.

*This research was also supported by DARPA.

- (1) J. W. Goodman, Proc. IEEE 53, 1688 (1965).
- (2) M. C. Teich, R. J. Keyes, and R. H. Kingston, Appl. Phys. Lett. 9, 357 (1966).
- (3) M. C. Teich, Proc. IEEE 56, 37 (1968).
- (4) M. C. Teich, Proc. IEEE 57, 786 (1969).
- (5) E. Jakeman, C. J. Oliver, and E. R. Pike, Adv. Phys. 24, 349 (1975).
- (6) R. M. Gagliardi and S. Karp, Optical Communications (Wiley, New York, 1976).

B. PHOTON COUNTING DETECTION FOR COMMUNICATIONS, RADAR, AND IMAGING

Our efforts in this area have been largely concerned with direct detection photon counting systems operating in the visible region. Substantial progress in the first interval has been made on a number of problems, considered in the following subsections: 1. Optimum photon detection with a simple counting processor; 2. Effects of rate variation on the counting statistics of dead-time-modified Poisson processes; 3. Observation of dead-time-modified photocounting distributions for modulated laser radiation; 4. Information, error, and imaging in dead-time-perturbed doubly-stochastic Poisson counting systems; and 5. Photocounting distributions for exponentially decaying sources.

1. Optimum Photon Detection with a Simple Counting Processor^{*(1)}

(M. C. Teich, P. R. Prucnal, G. Vannucci, G. Lachs)

We have shown that, for an arbitrary discrete process embedded in independent additive discrete noise, the classical binary detection problem using a likelihood-ratio test reduces to a simple comparison of the number of events with a single threshold. Only a weak condition on the noise distribution is required. Our results are appropriate for the analysis of photocounting optical communications and photocounting radar systems.

Let hypothesis "zero" (H_0) represent the situation in which no light is transmitted (noise only) and hypothesis "one" (H_1) represent the transmission of a pulse of light of specified characteristics (signal plus noise). We wish to determine the optimum rule for

deciding which hypothesis is true on the basis of a single observation. This is a simple binary hypothesis-testing problem. It is often convenient to use the Neyman-Pearson criterion, which maximizes the probability of detection P_D with the probability of false alarm P_F constrained to a particular value α . The general solution is most readily obtained using the method of Lagrange multipliers⁽²⁾ and yields the well-known likelihood-ratio test

$$\Lambda(n) = \frac{p(n|H_1)}{p(n|H_0)} \underset{H_0}{\overset{H_1}{\geq}} \lambda, \quad (1)$$

where $\Lambda(n)$ represents the likelihood ratio, $p(n|H_i)$ is the probability of obtaining n counts given that H_i is true, and λ is the threshold. The constraint $P_F = \alpha$ is satisfied by choosing λ appropriately. It should be noted that our results are also valid for other criteria that lead to the likelihood-ratio test (e.g., Bayes).⁽²⁾

Equation (1) indicates that optimum processing can be implemented by using the received data n to compute $\Lambda(n)$, which is then compared with λ , indicating which decision is appropriate. In its existing form, the calculation of $\Lambda(n)$ may be rather involved. However, processing of the received data n can be greatly simplified if $\Lambda(n)$ is a monotonic nondecreasing function of n .

We use the notation $p_s(n)$ to represent the arbitrary (discrete) signal counting distribution, and $p_D(n)$ to represent the (discrete) noise counting distribution, where n is a nonnegative integer. The signal and noise processes are assumed to be independent and additive, so that the overall distribution resulting from signal plus noise

is simply the convolution sum of the individual signal and noise distributions. The noise we consider (e.g. detector dark noise) is assumed not to interfere with the signal;⁽³⁾ interfering superposed radiation⁽⁴⁾ is accounted for in the statistics of $p_S(n)$. The likelihood ratio, defined by Eq. (1), can then be explicitly written as

$$\Lambda(n) = \left[\sum_{k=0}^n p_S(k) p_D(n-k) \right] / p_D(n). \quad (2)$$

Though it is possible to deal with the noise in the discrete form given above, it is somewhat easier to consider a continuous extension of the noise statistics. Let $f_D(x)$ be a continuous extension of $p_D(n)$ obtained by the substitutions $x = n$ and $\Gamma(x+1) = n!$, with x real and nonnegative, so that $f_D(n) = p_D(n)$ for n integer (other continuous extensions are also possible).

We have been able to demonstrate that if the logarithm of $f_D(x)$ is concave downward, i.e., if

$$d^2 [\log f_D(x)] dx^2 \leq 0, \quad (3)$$

then the likelihood ratio $\Lambda(n)$ is monotonic nondecreasing.⁽¹⁾

this condition is sufficient but not necessary. The monotonicity of $\Lambda(n)$ implies that for each value of λ in Eq. (1) there exists a unique integer n_t such that the test

$$\begin{array}{c} H_1 \\ n > n_t \\ < \\ H_0 \end{array} \quad (4)$$

is equivalent to the test specified in Eq. (1). Therefore, if the condition of Eq. (3) is satisfied, optimum processing can be implemented by the simple test given in Eq. (4), which defines a simple counting processor. Here n is called a proper decision variable. Thus, in contrast to the usual ad hoc procedures that can become rather cumbersome for complex signal distributions, Eq. (3) provides a standard sufficiency condition, independent of the signal distribution, for determining whether n is a proper decision variable.

Let us now consider specific signal and noise statistics for a simple laser radar experiment. In the simplest case where speckle is important, the signal distribution arising from the presence of the stimulus alone is given approximately by the negative binomial photon-counting distribution, (5) (6)

$$p_S(n) = \frac{\Gamma(n+M)}{n! \Gamma(M)} \left(1 + \frac{M}{\langle n_0 \rangle}\right)^{-n} \frac{1}{1 + \left(\frac{\langle n_0 \rangle}{M}\right)^{-M}}. \quad (5)$$

Here $p_D(n)$ represents the probability that exactly n photons are detected during the sampling time T , and $\langle n_0 \rangle$ represents the mean number of quanta (or mean light energy in units of $h\nu$) detected in this time. The parameter M is the number of modes ($M \geq 1$); it contains information relative to the spatiotemporal coherence and polarization properties of the light, the flash duration and area, and the detector integration time and area. (7)

We assume that the noise distribution is Poisson with mean $\langle n_D \rangle$, (6) (8)

$$p_D(n) = p(n|H_0) = \langle n_D \rangle^n \exp(-\langle n_D \rangle)/n!; \quad (6)$$

other noise distributions can be dealt with as easily.

Using Eqs. (2), (5), (6), and some rather complex algebra, we can demonstrate by means of a direct calculation that n is a proper decision variable in this particular case. We can obtain the same result more simply, however, by dealing with the noise distribution alone in the manner described above. The continuous extension of Eq. (6) is $f_D(x) = \langle n_D \rangle^x \exp(-\langle n_D \rangle)/\Gamma(x+1)$, $x \geq 0$. Using the series representation for $d^2[\ln \Gamma(x+1)]/dx^2$ provided by Gradshteyn and Ryzhik,⁽⁹⁾ we obtain

$$d^2[\ln f_D(x)]/dx^2 = - \sum_{n=1}^{\infty} (x+n)^{-2} < 0, \quad (7)$$

thereby satisfying Eq. (3). It is important to note that Eq. (5) for the signal distribution did not enter our calculation, indicating the general nature of our method. Thus the optimum processor for chaotic radiation embedded in Poisson noise is the remarkably simple counting processor given by Eq. (4)

In the presence of detector dead time, the additivity and independence assumptions are not obeyed, though it intuitively seems that a similar simple counting processor ought to work. In the next interval, we will investigate the optimum dead-time-perturbed processor.

* This research was also supported by the National Science Foundation under Grant NSF-ENG75-09325.

- (1) M. C. Teich, P. R. Prucnal, and G. Vannucci, Opt. Lett. 1, 208 (1977).
- (2) H. L. Van Trees, Detection Estimation and Modulation Theory (Wiley, New York, 1968), Part I.
- (3) M. C. Teich and R. Y. Yen, IEEE Trans. Aerosp. Electron. Syst. AES-8, 13 (1972).
- (4) M. C. Teich and W. J. McGill, Phys. Rev. Lett. 36, 754; 1473 (1976).
- (5) M. Greenwood and G. U. Yule, J. Royal Stat. Soc. A 83, 255 (1920).
- (6) J. W. Goodman, Proc. IEEE 53, 1688 (1965).
- (7) L. Mandel, Proc. Phys. Soc. 74, 233 (1959).
- (8) G. W. Flint, IEEE Trans. Mil. Electron. MIL-8, 22 (1964).
- (9) I. S. Gradshteyn and I. M. Ryzhik, Table of Integrals, Series, and Products, Yu. V. Geronimus and M. Yu. Tseytlin, eds. (Academic, New York, 1965), 4th ed., p. xxxii.

2. Effects of Rate Variation on the Counting Statistics of Dead-Time-Modified Poisson Processes*⁽¹⁾

(G. Vannucci, M. C. Teich)

The probability distribution for a dead-time-modified pulse counter has been studied by a number of researchers in a broad variety of disciplines such as photon counting,^{(2) (3) (4)} nuclear counting,^{(5) (6) (7)} and neural counting.⁽⁸⁾ Many cases have been studied in detail including paralyzable and nonparalyzable counting under blocked, unblocked, and equilibrium conditions. Attention has also been given to the variable dead time case. Müller has recently compiled a comprehensive bibliography on dead time effects,⁽⁹⁾ and has summarized the results of a number of authors.^{(6) (7)}

Though most of the work cited above is applicable only when the input to the counter is a Poisson point process with constant rate, a few results are also available for the case where the rate is not constant. Cantor and Teich,⁽³⁾ Teich and McGill,⁽⁴⁾ and Bédard⁽²⁾ present expressions for the photon counting distribution when the intensity of the light is a random process, with the sampling interval much smaller than the coherence time of the light.

We have obtained general expressions for the dead-time-modified mean and variance, for a nonparalyzable counter, when the rate of the input process is an arbitrary function of time, under the constraint that it vary slowly with respect to the duration of the dead time.⁽¹⁾ No constraints on the length of the sampling interval are imposed. Of course, the results also apply to a spatial dead-time-modified process under the appropriate conditions. We have also explicitly shown that the counting efficiency is greatest

when the rate of the input process is constant.

To verify the validity of our calculations, we performed a series of photocounting experiments. The source was a Spectra-Physics Model 162 Ar^+ ion laser operated at 514.5 nm. The radiation was fed into an acousto-optic modulator that modulated the intensity of the beam with a ramp or a sinusoid. The modulated radiation was attenuated sufficiently for the photon statistics to be observable and was polarized and detected by an RCA 8575 photomultiplier tube. The output pulses from the anode of the photomultiplier tube were counted by a pulse counter with an electronically-generated nonparalyzable dead time whose value could be set arbitrarily.

Data were taken for a ramp and for sinusoidal modulation with the following parameters (in both cases); Observation time $T = 10$ msec, modulation depth $m = 1$, counting rate $\lambda_0 \approx 33$ counts/msec, and the dead time τ was varied from a minimum of $6 \mu\text{s}$ ($\lambda_0 \tau \approx 0.2$) to a maximum of 1.2 msec ($\lambda_0 \tau \approx 40$). At the low end, τ is sufficiently small so that the theoretical results are expected to be applicable. For the largest values of τ , however, we would expect that the experimental results should depart somewhat from the predictions. The experimentally measured values of the mean and variance of the photocounting distributions are presented in Figs. 59 and 60 respectively, for both ramp and sinusoidally modulated radiation. Though it is clear that the data are in good accord with the theoretical curves, it is evident from Figs. 59 and 60 that, as expected, the experimental points depart somewhat from the theoretical

Figure 59:

Counting efficiency ($\bar{n}/\lambda_0 T$) vs $\lambda_0 \tau$ where \bar{n} is the observed mean count, λ_0 is the average input count rate, T is the sampling time, and τ is the dead time. Theoretical curves are for a Poisson process where the rate is constant (solid curve), a ramp (dashed curve), and a sinusoidal function of time (dotted curve). The dash-dot curve represents the asymptotic behavior, which is the same for all three curves. It is clear that the efficiency is significantly reduced when the rate is not constant (up to 20% for sinusoidal modulation). Experimental values for the ramp (+) and sinusoid (•) are in good accord with the theoretical curves.

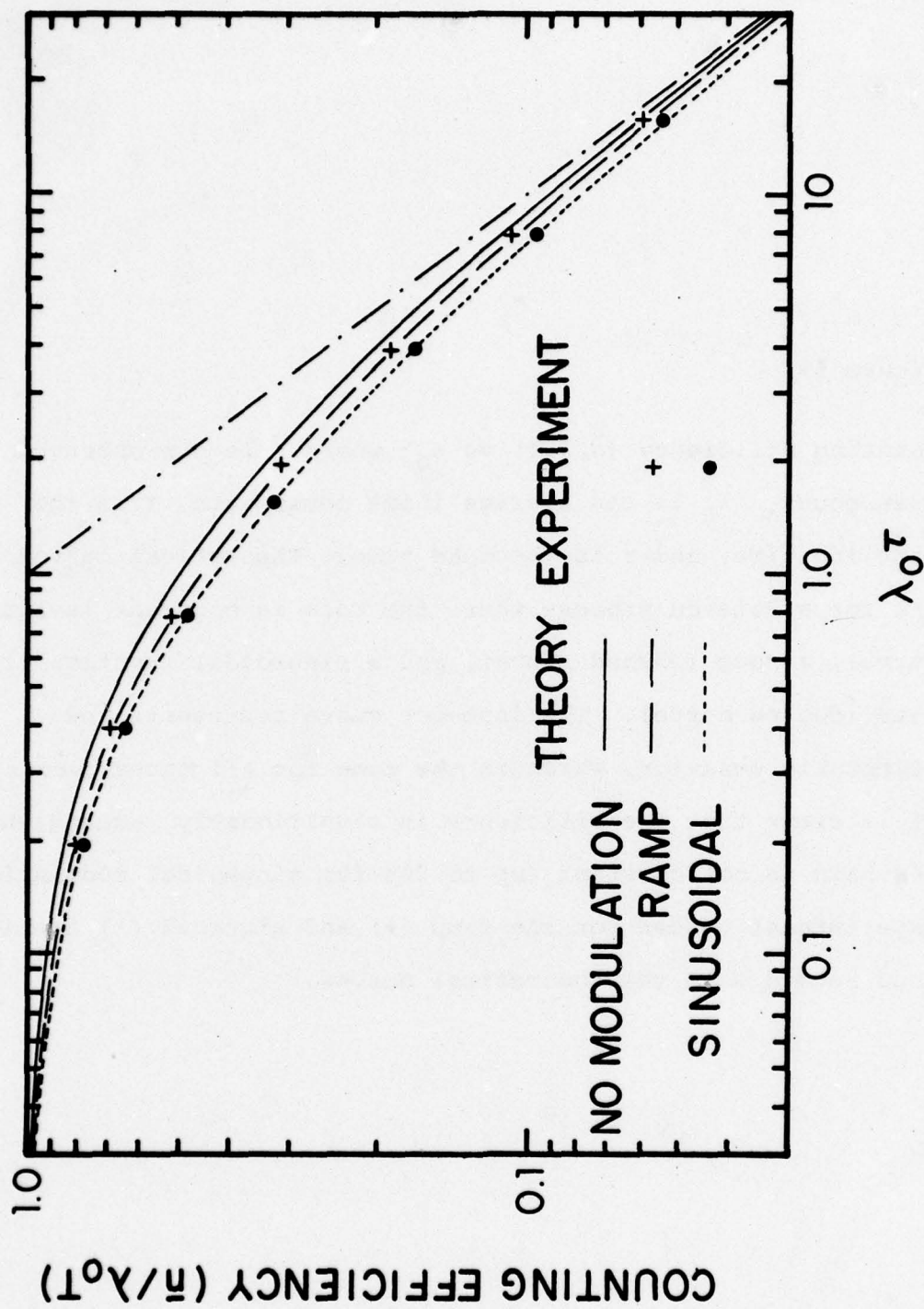


Figure 59

Figure 60:

Normalized dead-time-modified variance ($\sigma^2/\lambda_0 T$) vs $\lambda_0 \tau$. Theoretical curves are for a Poisson process where the rate is constant (solid curve), a ramp (dashed curve), and a sinusoidal function of time (dotted curve). Note that the curves as well as the asymptotic behavior are significantly different. Experimental values for the ramp (+) and sinusoid (•) are in good accord with the theoretical curves.

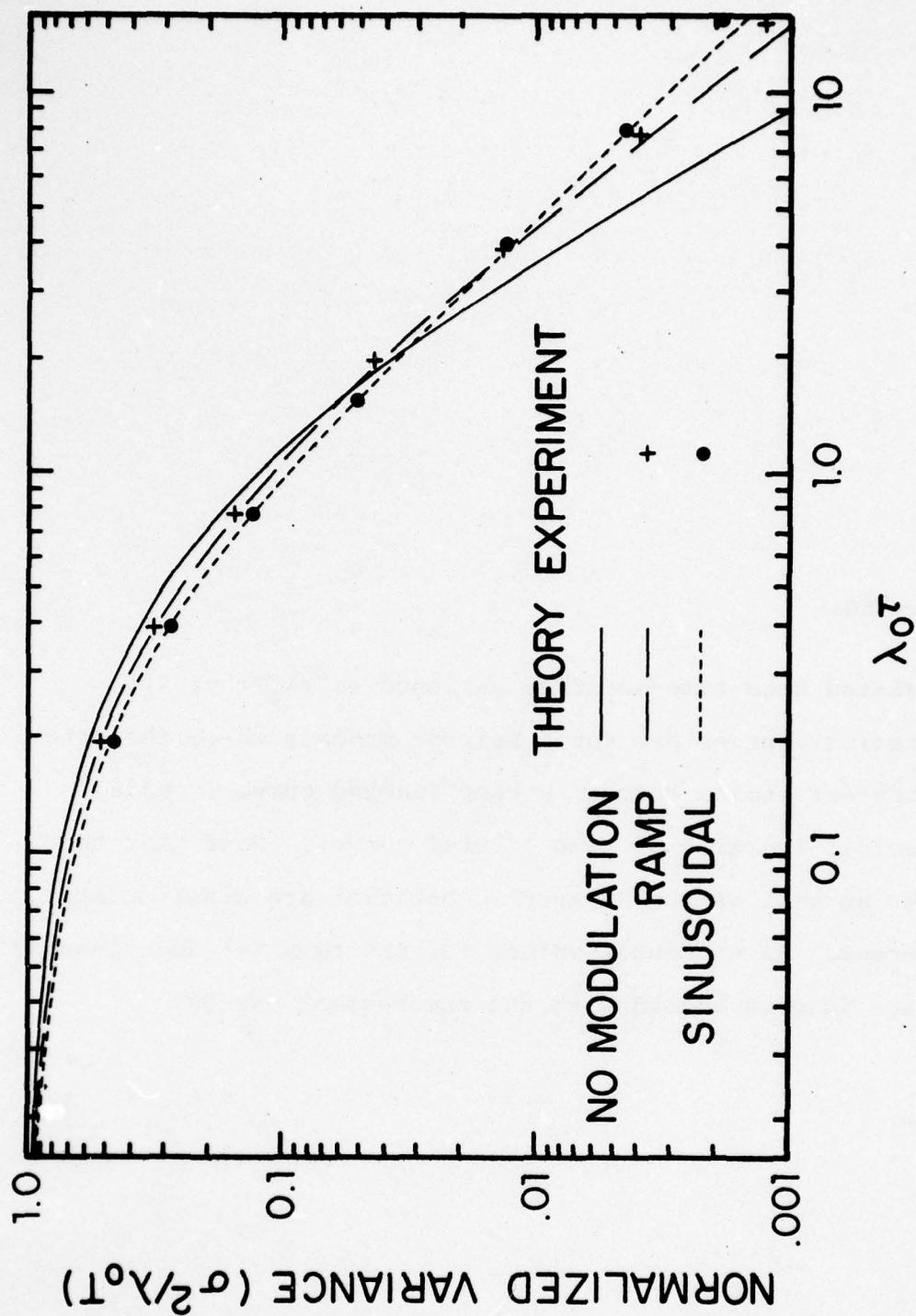


Figure 60

predictions for the largest values of τ .

It is evident from the foregoing that when $\lambda(t)$ is not constant, the statistics of the number of pulses counted by a nonparalyzable dead-time-counter in a given time interval depend on more than just the statistics of the total energy (integrated rate) arriving at the counter during that time. Thus these statistics cannot, in general, be deduced from the statistics of the total energy alone as is the case in the absence of dead time. Our results clearly show that the details of the variation of the rate during the sampling interval must be accounted for in order to correctly evaluate the dead-time-modified counting statistics. The particular cases of the ramp and sinusoidal modulation presented illustrate this point particularly well. This is because the statistics of the integrated rate are the same for both modulation formats and for the no-modulation case, yet the values of the experimental and the theoretical dead-time-modified mean and variance are significantly different. These results underscore the fact that existing formulas for the dead-time-modified counting distribution produced by randomly fluctuating light⁽²⁾⁽³⁾⁽⁴⁾ are valid only in the limit where the sampling interval is much smaller than the coherence (or modulation) time of the light, and cannot be extended in any simple way to cases outside that limit.

We have obtained the dead-time-modified mean and variance when the rate is a known function of time. Kikkawa et al.⁽¹⁰⁾ have calculated the efficiency of a dead-time photon counter with

Gaussian-Lorentzian light (stochastic rate variation). Their results are not of use, however, since they are only valid in the limit where the correlation time is much smaller than the mean time interval between pulses (see remarks following Eq. (10) in Ref. 10). In the next interval we shall attempt to derive expressions for the dead-time-modified mean and variance in the general case where the rate is a stochastic process, and to experimentally test these results. The work reported in the next two subsections complements that reported here.

* This research was also supported by the National Science Foundation under Grant NSF-ENG75-09325.

- (1) G. Vannucci and M. C. Teich, Opt. Comm. 25, in press (1978).
- (2) G. Bédard, Proc. Phys. Soc. 90, 131 (1967).
- (3) B. I. Cantor and M. C. Teich, J. Opt. Soc. Am. 65, 786 (1975).
- (4) M. C. Teich and W. J. McGill, Phys. Rev. Lett. 36, 754 (1976).
- (5) I. DeLotto, P. F. Manfredi, and P. Principi, Energia Nucleare 11, 557 (1964).
- (6) J. W. Müller, Nucl. Instrum. Meth. 112, 47 (1973).
- (7) J. W. Müller, Nucl. Instrum. Meth. 117, 401 (1974).
- (8) L. M. Ricciardi and F. Esposito, Kybernetik 3, 148 (1966).
- (9) "Bibliography on Dead Time Effects," edited by J. W. Müller, Bureau International des Poids et Mesures, Sèvres, France, Report Number BIPM-75/6, 1975 (unpublished).
- (10) A. Kikkawa, K. Ohkubo, H. Satō, and N. Suzuki, Opt. Comm. 12, 227 (1974).

3. Observation of Dead-Time-Modified Photocounting Distributions for Modulated Laser Radiation*

(M. C. Teich, G. Vannucci)

The photocounting statistics for intensity-modulated radiation have been investigated by a number of workers.^{(1) - (9)} In particular, theoretical results for various periodic modulation formats (square-wave, triangular, and sinusoidal) have been obtained by Diamant and Teich^{(4) (5)} for arbitrary modulation depth and short sampling times. There have been few experimental measurements of these counting statistics, however, though some time ago Teich and Diamant observed the flat gamma-ray counting distribution resulting from a linearly swept mean.^{(4) (10)} For an unmodulated (Poisson) source, the effect of detector dead time on the counting statistics has also been studied extensively, primarily in the context of nuclear particle counting and neural pulse counting.^{(11) (12) (13) (14)} In the presence of intensity modulation, the theoretical dead-time-modified counting statistics have been obtained only under the special conditions of a nonparalyzable counter with a sampling time short in comparison with the fluctuation time of the source.^{(15) (16) (17)} A particularly useful form for this distribution has been presented by Cantor and Teich.⁽¹⁶⁾

We have performed a series of experiments that verify the full theoretical photocounting distributions for triangular and sinusoidal modulation given by Diamant and Teich,⁽⁵⁾ and the full nonparalyzable-dead-time-modified versions of these formulas obtained using the method suggested by Cantor and Teich.⁽¹⁶⁾ The

light source was a Spectra-Physics Model 162 Ar^+ ion laser^{(18) (19)} operated at 514.5 nm. The radiation was fed into an acousto-optic modulator that modulated the intensity of the beam with a triangular wave or a sinusoid. The modulated radiation was attenuated sufficiently for the photocounting statistics to be observable and was polarized and detected by an RCA Type 8575 photomultiplier tube. The output pulses from the anode of the photomultiplier tube were counted by an (unblocked) pulse counter with an electronically generated nonparalyzable dead time whose value could be set arbitrarily.

Data were taken for triangular and sinusoidal modulation for various combinations of values of the modulation depth m and the dead-time ratio τ/T . Other experimental parameters were the period of the wave $T_M = 1$ s, the sampling interval $T = 1$ ms, and the number of observation samples $N = 10^5$. These parameters were the same for all sets of data, except where explicitly indicated in the figure captions.

Representative examples of the experimental data (data points indicated by \square , Δ , \times , \uparrow) as well as the theoretical counting distributions for the same parameters (solid curves) are presented in Figs. 61, 62, 63. Figures 61 and 62 provide results for sinusoidal and triangular modulation, respectively, in the absence of dead time. The modulation depth is varied parametrically. The more general case of triangular modulation in the presence of nonparalyzable dead time is presented in Fig. 63.

In examining the figures, it is clear that the theory is in excellent agreement with all of the experimental data. It is also

Figure 61:

Theoretical counting distributions (solid curves) and experimental data for sinusoidally modulated radiation in the absence of dead time ($\tau/T = 0$). The modulation depth m takes on 3 values: $m = 0$ (X), $m = 0.75$ (Δ , $T_M = 5$ s, $T = 10$ ms, $N = 50000$), and $m = 1.0$ (\square , $T_M = 5$ s, $T = 10$ ms, $N = 50000$). The mean count is approximately the same for all 3 distributions ($\langle n \rangle \approx 17$).

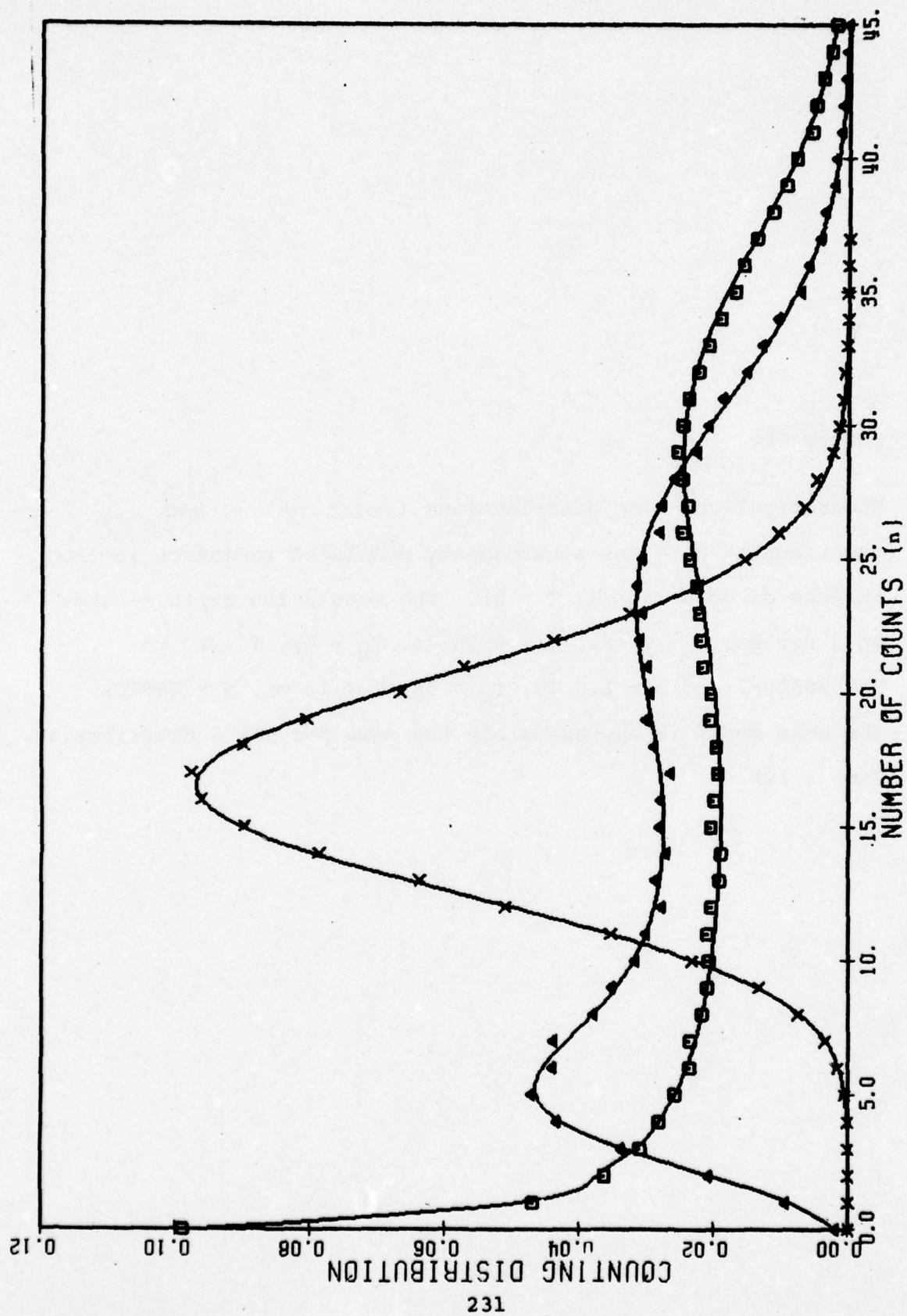


Figure 61

Figure 62:

Theoretical counting distributions (solid curves) and experimental data for triangularly modulated radiation in the absence of dead time ($\tau/T = 0$). The modulation depth m takes on 3 values: $m = 0$ (Δ), $m = 0.74$ (\square , $N = 200000$), and $m = 0.99$ (\times , $N = 200000$). The mean count is approximately the same for all 3 distributions ($\langle n \rangle \approx 15$). Note the flat counting distribution [see Refs. 4,5 and 10] obtained when $m \approx 1$.

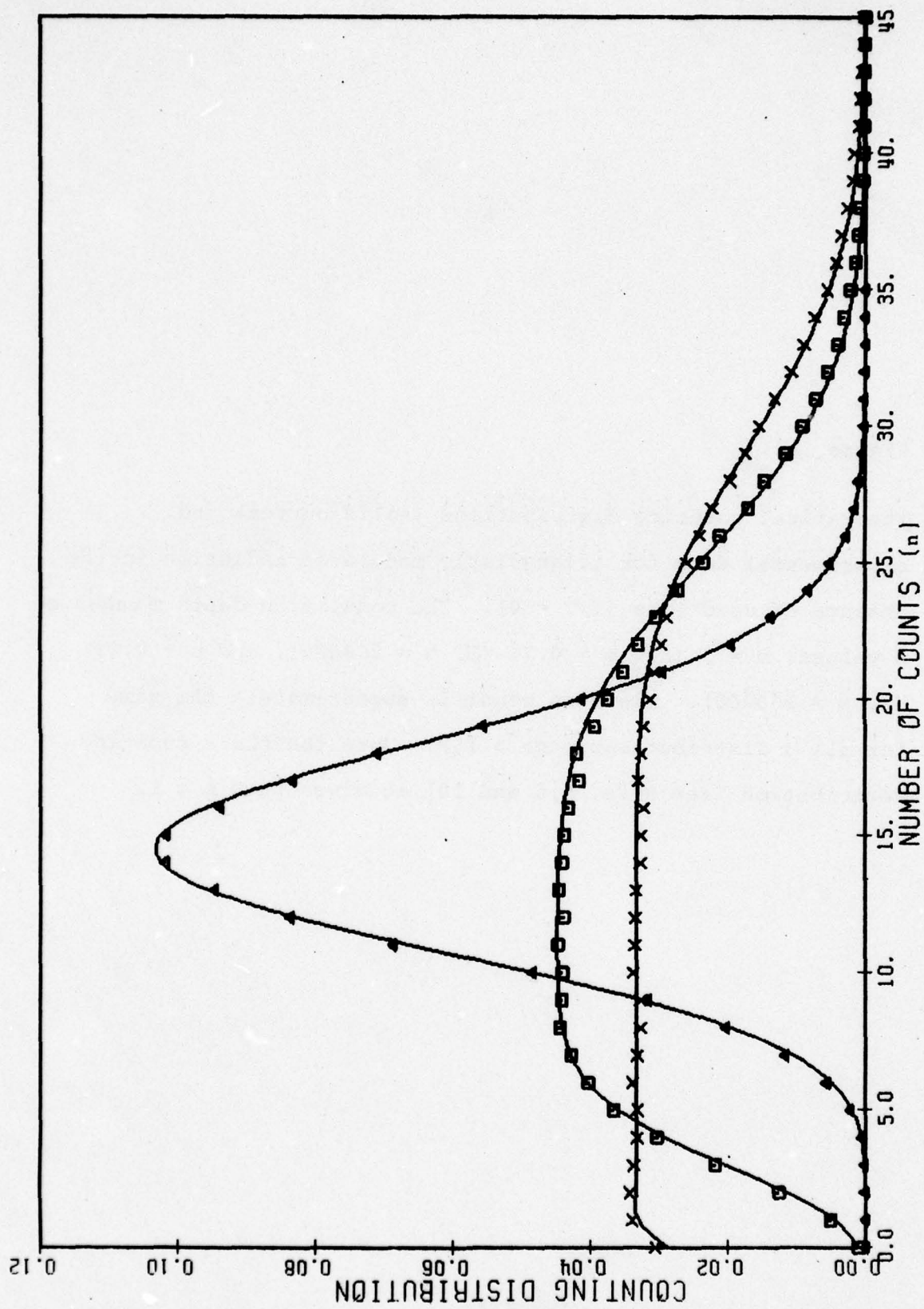


Figure 62

Figure 63:

Theoretical nonparalyzable-dead-time-modified counting distributions (solid curves) and experimental data for triangularly modulated radiation ($m \approx 1$). The dead-time ratio takes on 4 values: $\tau/T = 0$ (\dagger , $N = 200000$), $\tau/T = 0.02$ (\times , $N = 200000$), $\tau/T = 0.05$ (Δ), and $\tau/T = 0.1$ (\square). The unmodified mean count is approximately the same for all 4 distributions ($\langle n \rangle \approx 15$).

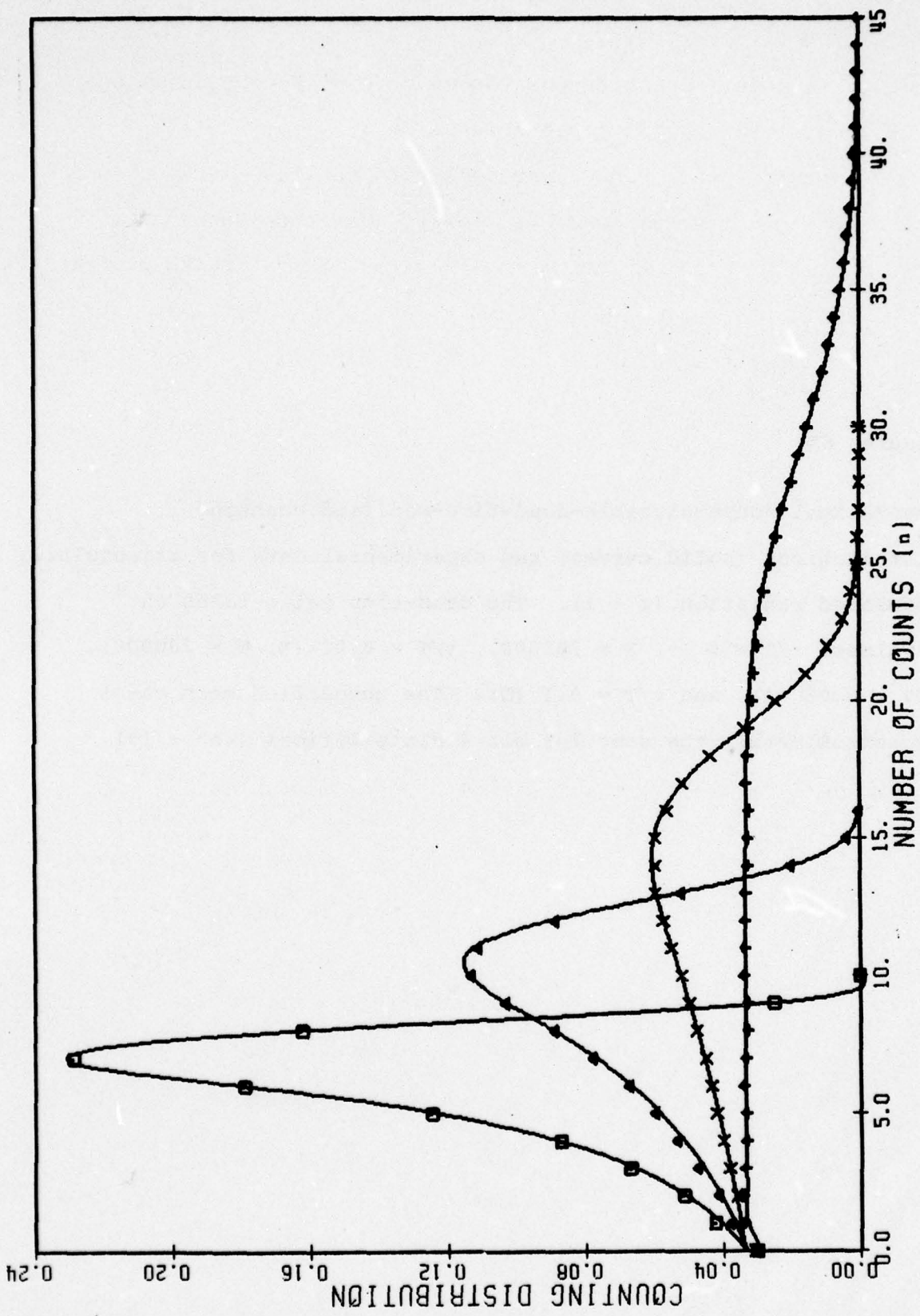


Figure 63

apparent that modulation broadens the counting distributions (see Figs. 61 and 62); this is interpretable as accentuated photon bunching. Dead time, on the other hand, decreases both the mean and variance of the counting distribution as well as the variance-to-mean ratio (see Fig. 63) corresponding to a loss of counts and to count antibunching. The dead-time-modified counting distributions converge to the unmodified distributions for low count numbers n where dead-time effects are least important.

We have also obtained a new theoretical result for the paralyzable-dead-time-modified counting distribution for intensity-modulated radiation and short sampling times. In practice, the discriminator following the photodetector often provides a major contribution to dead time so that the detailed structure of the system is important in determining which formulas should be used.

A thorough investigation of the theoretical and experimental counting distributions briefly described here has been completed, and a manuscript has been prepared and submitted for publication.⁽²⁰⁾ The theoretical and experimental results for the dead-time-modified count mean and variance reported in the preceding subsection complement the results presented here. In the following subsection, we use the nonparalyzable-dead-time formulas discussed here to investigate likelihood-ratio detection, channel capacity, and maximum-likelihood image estimation in dead-time-modified doubly-stochastic Poisson counting systems.

* This research was also supported by the National Science Foundation under Grant NSF-ENG75-09325.

- (1) G. J. Troup, IEEE J. Quantum Electron. QE-1, 398 (1965).
- (2) S. Fray, F. A. Johnson, R. Jones, T. P. McLean, and E. R. Pike, Phys. Rev. 153, 357 (1967).
- (3) P. Pearl and G. J. Troup, Phys. Lett. 27A, 560 (1968).
Equation (3) in this paper is incorrect and should be replaced by Eq. (38) of Ref. 5.
- (4) M. C. Teich and P. Diament, Phys. Lett. 30A, 93 (1969).
- (5) P. Diament and M. C. Teich, J. Opt. Soc. Am. 60, 682 (1970).
- (6) P. Diament and M. C. Teich, J. Opt. Soc. Am. 60, 1489 (1970).
- (7) M. C. Teich and S. Rosenberg, J. Opto-electron. 3, 63 (1971).
- (8) W. G. Clark and E. K. O'Neill, J. Opt. Soc. Am. 61, 934 (1971).
- (9) I. Kitazima, Opt. Comm. 10, 137 (1974).
- (10) M. C. Teich and P. Diament, J. Appl. Phys. 41, 415 (1970).
- (11) I. DeLotto, P. F. Manfredi, and P. Principi, Energia Nucleare 11, 557 (1964).
- (12) L. M. Ricciardi and F. Esposito, Kybernetik 3, 148 (1966).
- (13) J. W. Muller, Nucl. Instr. Meth. 112, 47 (1973).
- (14) J. W. Muller, Nucl. Instr. Meth. 117, 401 (1974).
- (15) G. Bédard, Proc. Phys. Soc. 90, 131 (1967).
- (16) B. I. Cantor and M. C. Teich, J. Opt. Soc. Am. 65, 786 (1975).
- (17) M. C. Teich and W. J. McGill, Phys. Rev. Lett. 36, 754; 1473 (1976).
- (18) G. J. Troup and J. Lyons, Phys. Lett. 29A, 705 (1969).
- (19) T. Aoki, T. Endo, and K. Sakurai, Opt. Comm. 23, 26 (1977).
- (20) M. C. Teich and G. Vannucci, "Observation of dead-time-modified photocounting distributions for modulated laser radiation," submitted for publication.

4. Information, Error, and Imaging in Dead-Time-Perturbed
Doubly-Stochastic Poisson Counting Systems*

(M. C. Teich, B. I. Cantor)

In the past decade, there has been a considerable effort devoted to the analysis of systems that convert a continuous source variable into a discrete counting process. Perhaps the earliest study of this kind was carried out in 1920 by Greenwood and Yule,⁽¹⁾ who in the course of studying the industrial accident rate in a British munitions factory, considered the Poisson transform of a probability density function specifying individual proneness to accident. Though much of the subsequent work on these compound or doubly-stochastic Poisson processes, as they are now called, has specifically dealt with the photon counting detection of light in a fixed time interval, first considered by Purcell⁽²⁾ and Mandel,⁽³⁾ the formalism has also been applied to neural counting by McGill.⁽⁴⁾ Teich and McGill⁽⁵⁾ recently demonstrated that McGill's neural counting model and Mandel's semiclassical photon counting description⁽³⁾ are in fact identical from a mathematical point of view and can be formally represented in terms of Greenwood and Yule's compound Poisson distribution. This equivalence was explicitly demonstrated for McGill's noncentral negative binomial distribution and Peřina's^{(6) (7)} multimode confluent hypergeometric distribution for a coherent signal embedded in chaotic noise (an excellent approximation for the radiation from an amplitude-stabilized single-mode laser operated well above the threshold of oscillation). For all of these problems, the underlying Poisson behavior can arise from the occurrence of independent

events⁽⁸⁾ or from the superposition of a large number of arbitrary stochastic point processes.⁽⁹⁻¹¹⁾

For an optical system, forward photon counting distributions have been studied from both a quantum-mechanical⁽⁷⁾⁽¹²⁻¹⁴⁾ and a semiclassical⁽³⁾⁽⁷⁾ point of view for a broad range of incident field statistics⁽⁷⁾ and modulation formats.⁽¹⁵⁻²⁰⁾ (Recently, increasing consideration has been given to the doubly-stochastic Poisson process where attention is directed to the more general photoelectron arrival times⁽²¹⁾ rather than to their number in a fixed time interval as considered here.) Calculations for direct-detection likelihood-ratio receiver performance⁽²²⁻³¹⁾ and information rate⁽³²⁻³⁶⁾ have also been carried out by a number of researchers.

One factor that can substantially impair the performance of this kind of counting system -- particularly at high data rates -- is dead time. Fortunately, the nonparalyzable-dead-time-perturbed problem can be treated rather easily from a mathematical point of view since Cantor and Teich⁽³⁷⁾ have obtained a closed-form expression for the dead-time-modified counting distribution for a doubly-stochastic Poisson counting process. The special case of the dead-time-modified simple Poisson distribution had been previously dealt with extensively by researchers working in nuclear counting⁽³⁸⁾⁽³⁹⁾ and neural counting.⁽⁴⁰⁾⁽⁴¹⁾ In both cases, the modified distribution is simply expressible in terms of the unmodified distribution and the dead-time ratio τ/T , where τ is the dead time and T is the sampling time. Even small values of

τ/T (~ 0.01) alter the distribution markedly⁽³⁷⁾ so that dead-time effects cannot in general be neglected. In the preceding subsection,⁽²⁰⁾ we presented experimental verification of Diamant and Teich's⁽¹⁵⁻¹⁷⁾ theoretical photon counting distributions for triangularly and sinusoidally modulated laser radiation and of Cantor and Teich's⁽³⁷⁾ nonparalyzable-dead-time-modified versions of these formulas.

In this subsection, we consider likelihood-ratio detection, information transmission, and image detection in the presence of such fixed nonparalyzable dead time. In the counting system we consider, the source is deterministically or stochastically modulated (see Fig. 64). The input u to the detector is the binary-gated modulated signal, and its output v_1 is the number of counts registered in the fixed sampling time interval T . The output of the likelihood-ratio test v_2 is a random variable with value 1 or 0 depending on the decision. Noise arising from background and dark effects is considered to give rise to a dead-time-modified Poisson counting distribution (this may come about from a background that exhibits no intrinsic fluctuations, or from a background that is independent, noninterfering, and additive with the signal, but fluctuates sufficiently rapidly such that its fluctuation time $\tau_n \ll T$). Though the Poisson condition for the background is quite generally obeyed, an arbitrary noise process can be treated within our framework at the price of increased complexity.

The relevant counting distributions were considered in the

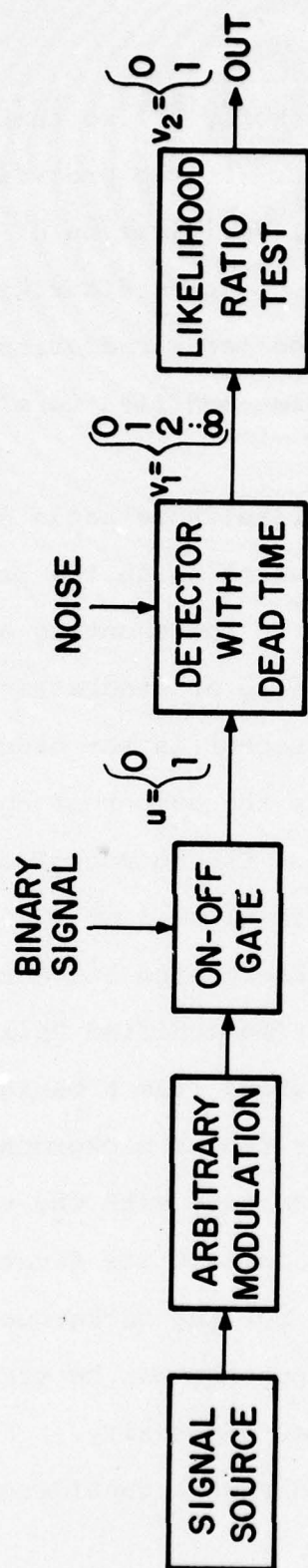


Figure 64

Block diagram of the binary-gated dead-time-modified likelihood-ratio counting receiver for detecting a fluctuating signal.

previous subsection.⁽²⁰⁾ Using the likelihood-ratio test for an on-off system (nonorthogonal signaling format) such as that shown in Fig. 64,⁽²²⁻³¹⁾ the decision threshold n_D is determined by the minimum count number n satisfying the condition

$$p_{S+H}(n, \tau/T)/p_H(n, \tau/T) \geq \Lambda, \quad (1)$$

where $p_{S+H}(n, \tau/T)$ and $p_H(n, \tau/T)$ are the counting distributions for signal plus noise and for noise alone, respectively, and Λ is the decision level. This result assumes the existence of a single decision threshold.⁽²⁵⁾ For simplicity, we assume a Bayes criterion with equal costs so that $\Lambda=(1-Q)/Q$, where Q is the a priori probability that the signal is present. Maximum-likelihood detection is associated with $\Lambda=1$ ($Q=0.5$). In order to construct the receiver operating characteristic (ROC), we write the probability of detection P_d and the probability of false alarm P_f in terms of the parameter n_D as

$$P_d = \sum_{n=n_D}^{\infty} p_{S+H}(n, \tau/T) \quad (2)$$

and

$$P_f = \sum_{n=n_D}^{\infty} p_H(n, \tau/T). \quad (3)$$

The ROC curve is a plot of P_d vs P_f as the decision threshold n_D varies from 0 to ∞ .

In Fig. 65, we present ROC curves corresponding to an unmodulated ($m=0$) amplitude-stabilized signal in the presence of a steady background (Poisson counts). The solid curve corresponds to a detector with zero dead time, whereas the dashed curve corresponds to a ratio of dead time to sampling time $\tau/T = 0.02$ and the dotted curve to $\tau/T = 0.05$. The unmodified (fixed) signal level $\langle n_S \rangle = \lambda_S T = 5$ and the unmodified noise level $\langle n_H \rangle = \lambda_H T = 20$ for all curves. The effect of the dead time is to decrease the probability of detection at a fixed false alarm rate (constant P_f). The small signal level $\lambda_S T = 5$ was used in order to clearly illustrate this effect graphically. It is important to note that although continuous curves are drawn in Fig. 65, the ROC is defined only at discrete points. This is because the decision threshold n_D takes on only integer values. (26)

In terms of the parameter n_D , the total probability of error P_e is

$$P_e = Q \left[1 - \sum_{n=n_D}^{\infty} P_{S+H}(n, \tau/T) \right] + (1-Q) \sum_{n=n_D}^{\infty} P_H(n, \tau/T) \quad (4)$$

Selecting n_D in accordance with Eq. (1) for maximum-likelihood detection ($\Lambda=1$), the total probability of error for an amplitude-stabilized source in the presence of triangular modulation is presented in Fig. 66 as a function of the unmodified mean signal level $\lambda_S T$. The solid curves correspond to a detector with zero dead time, while the dashed curves correspond to the ratio $\tau/T = 0.02$

Figure 65:

Receiver operating characteristic (ROC) curves for a likelihood-ratio receiver (unmodulated amplitude-stabilized signal) in the absence of dead time (solid curve), for the dead-time ratio $\tau/T = 0.02$ (dashed curve), and for $\tau/T = 0.05$ (dotted curve). The (fixed) unmodified signal level is $\lambda_S T = 5$, and the unmodified noise level is $\lambda_H T = 20$ for all curves.

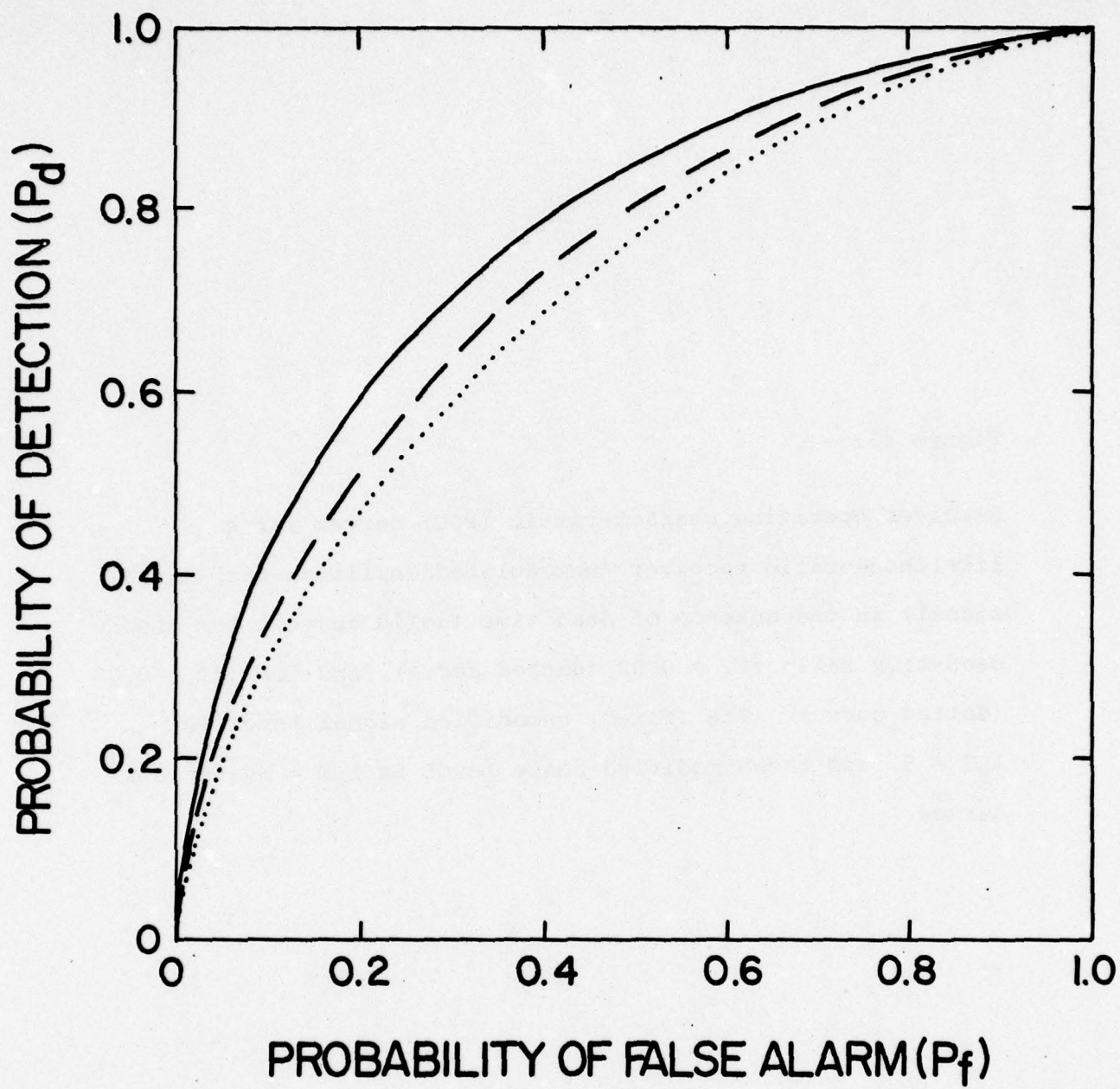


Figure 65

Figure 66:

Probability of error (P_e) versus unmodified mean signal level ($\lambda_S T$) for a triangularly modulated amplitude-stabilized signal in the absence of dead time (solid curves) and with a dead-time ratio $\tau/T = 0.02$ (dashed curves). The unmodified (steady) noise level $\lambda_H T$ is 20 for the upper pair of curves and 10 for the lower pair. The signal modulation depth $m = 0.5$ and the a priori probability $Q = 0.5$ for all curves.

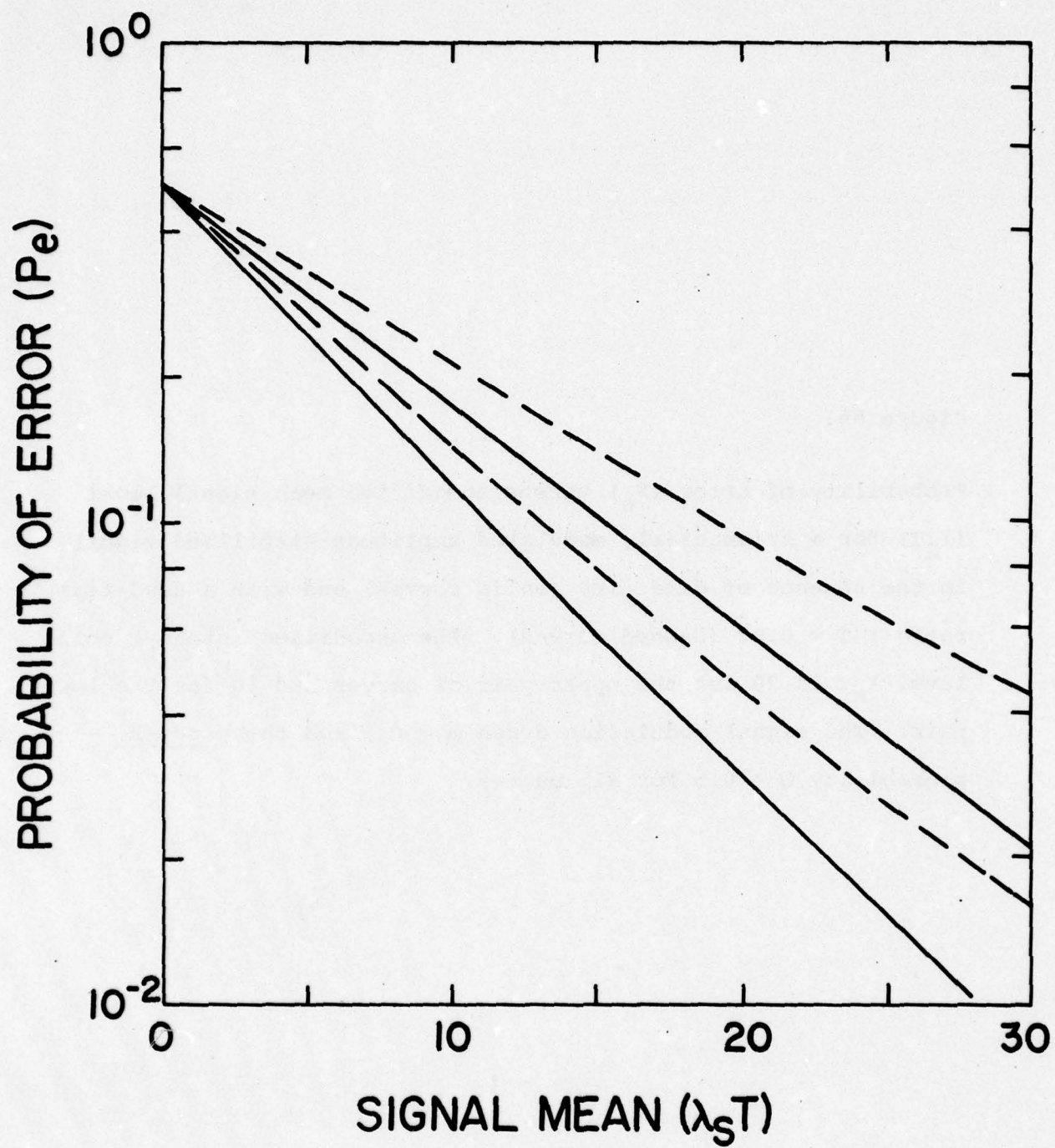


Figure 66

in all cases. The modulation depth m is 0.5 and the unmodified noise level $\lambda_H T$ is 20 for the upper pair of curves and 10 for the lower pair.

Whereas the probability of error and the ROC specify receiver performance, the rate of information transmission is governed by average mutual information and the channel capacity. (42-44)

In Fig. 67 we present the mutual information $I(U;V)$ as a function of the a priori signal probability Q . The solid curves refer to the simple counting receiver without the likelihood-ratio test, whereas the dashed curves represent the likelihood-ratio counting receiver (see Fig. 64). The dead-time ratio takes on several values as shown, viz., $\tau/T = 0, 0.05$, and 0.1 . The source is an amplitude-stabilized unmodulated signal ($m=0$) with unmodified signal mean $\lambda_S T = 15$, and the unmodified noise mean is $\lambda_H T = 10$. We have ascertained that the channel capacity decreases with decreasing signal mean, increasing modulation depth, and increasing dead time (see Fig. 67). Note that the peak mutual information occurs at or near $Q = 0.5$ in all cases.

An obvious distinction between the two types of receiver is that the likelihood-ratio receiver exhibits discontinuities in the $I(U;V)$ vs Q curves. This is because of the discrete nature of the decision threshold which jumps from one integer to the next at certain values of Q , as Q varies. The likelihood-ratio receiver yields a lower capacity than the simple counting receiver in all cases. Since both the input and output take on the values of 0 and 1 only with the binary counting likelihood-ratio receiver,

Figure 67:

Average mutual information $I(U;V)$ versus a priori signal probability Q for a simple counting receiver (solid curves) and for a maximum-likelihood counting receiver (dashed curves) with the dead-time ratio τ/T as a parameter. $\lambda_S T = 15$, $\lambda_H T = 10$, and $m = 0$ for all cases. Curves are shown for $\tau/T = 0, 0.05$, and 0.1 as indicated. The peak of each curve represents the channel capacity.

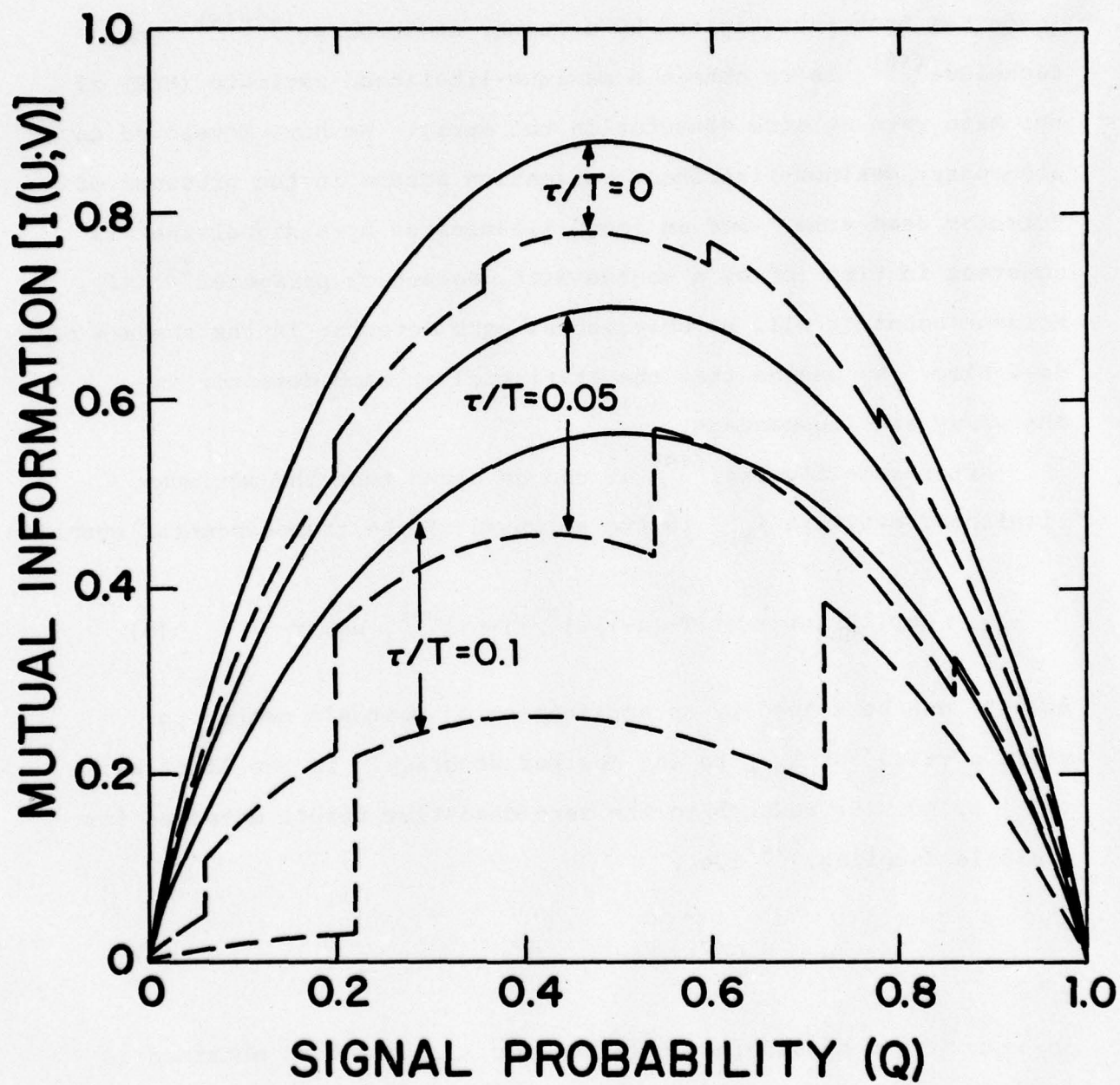


Figure 67

it may be considered as an asymmetrical binary channel with varying error transition probability. Thus it is expected that the channel capacity will not exceed 1.

The use of an unperturbed counting array to detect a received image has been investigated by a number of authors.⁽⁴⁵⁻⁴⁸⁾ One technique⁽⁴⁶⁾ is to obtain a maximum-likelihood estimate (MLE) of the mean rate at each detector in the array. We have developed an elementary maximum-likelihood estimation scheme in the presence of detector dead time. For an image illuminated by a signal that is constant in time (or by a source with degeneracy parameter⁽³⁾ $\ll 1$), Poisson counting will be observed at each detector in the absence of dead time. We assume that the statistics at each detector in the array are independent.

After some algebra,⁽⁴⁹⁾ it can be shown that the maximum-likelihood estimate λ_{MLE} is the solution of the transcendental equation

$$\lambda_{MLE} \tau \exp(\lambda_{MLE} \tau) = n \tau [T - (n-1)\tau]^n / [T - n\tau]^{n+1}, \quad n < T/\tau. \quad (5)$$

Eq. (5) can be solved by an application of Newton's method to yield a value for λ_{MLE} to any desired accuracy. In the limit as $\tau/T \rightarrow 0$, Eq. (5) reduces to the zero-dead-time result obtained for a single sampling,⁽⁴⁶⁾ i.e.,

$$\lambda_{MLE} = n/T. \quad (6)$$

An approximate closed form solution for λ_{MLE} has been obtained in

the two limiting cases $\lambda_{MLE}\tau \ll 1$ and $\lambda_{MLE}\tau \gg \ln \lambda_{MLE}\tau$. For $\lambda_{MLE}\tau \ll 1$, $\exp(\lambda_{MLE}\tau) \approx 1 + \lambda_{MLE}\tau$, and λ_{MLE} can be obtained as the solution to the quadratic equation

$$\lambda_{MLE}\tau(1 + \lambda_{MLE}\tau) = n\tau[T - (n-1)\tau]^n / [T - n\tau]^{n+1}. \quad (7)$$

For the opposite limiting case, we take the natural logarithm of Eq. (5) yielding

$$\ln \lambda_{MLE}\tau + \lambda_{MLE}\tau = \ln\{n\tau[T - (n-1)\tau]^n / [T - n\tau]^{n+1}\}; \quad (8)$$

for $\lambda_{MLE}\tau \gg \ln \lambda_{MLE}\tau$ (which is valid for $\lambda_{MLE}\tau \gtrsim 30$), the solution is

$$\lambda_{MLE} \approx \tau^{-1} \ln\{n\tau[T - (n-1)\tau]^n / [T - n\tau]^{n+1}\}. \quad (9)$$

We have also obtained the statistical confidence level of the maximum likelihood estimate.

With our confidence inspired by the experimental results reported in the two preceding subsections, we have been able to carry out a rather complete theoretical investigation of dead-time-perturbed information transmission, error, and imaging in this reporting period. A manuscript has been prepared and submitted for publication.⁽⁴⁹⁾ It appears that, at least in some ways, the deleterious effects of detector dead time on system performance may not be as severe as anticipated. In the next interval we expect to evaluate some of these effects more carefully for a simple but practical system: Poisson signal in Poisson noise.

* This research was also supported by the National Science Foundation under Grant NSF-ENG75-09325.

- (1) M. Greenwood and G. U. Yule, J. Royal Stat. Soc., Ser. A, 83, 255 (1920).
- (2) E. M. Purcell, Nature 178, 1449 (1956).
- (3) L. Mandel, Proc. Phys. Soc. 74, 233 (1959).
- (4) W. J. McGill, J. Math. Psychol. 4, 351 (1967).
- (5) M. C. Teich and W. J. McGill, Phys. Rev. Lett. 36, 754; 1473 (1976).
- (6) J. Peřina, Phys. Lett. 24A, 333 (1967); Acta Universitatis Palackianae Olomucensis Facultas Rerum Naturalium(Olomouc) 27, 227 (1968).
- (7) J. Peřina, Coherence of Light (Van Nostrand-Reinhold, London, 1972).
- (8) E. Parzen, Stochastic Processes (Holden-Day, San Francisco, 1962), pp. 117-186.
- (9) C. Palm, Ericsson Technics (Stockholm) 44, 1 (1943).
- (10) D. R. Cox and W. L. Smith, Biometrika 40, 1 (1953); 41, 91 (1954).
- (11) E. Çinlar, "Superposition of point processes," in Stochastic Point Processes: Statistical Analysis, Theory, and Applications, edited by P. A. W. Lewis (Wiley-Interscience, New York, 1972), pp. 549-606, and references contained therein.
- (12) R. J. Glauber, Phys. Rev. 130, 2529 (1963); 131, 2766 (1963).
- (13) P. L. Kelley and W. H. Kleiner, Phys. Rev. 136, A316 (1964).
- (14) D. Stoler, Phys. Rev. Lett. 33, 1397 (1974).
- (15) M. C. Teich and P. Diament, Phys. Lett. 30A, 93 (1969).
- (16) M. C. Teich and P. Diament, J. Appl. Phys. 41, 415 (1970).
- (17) P. Diament and M. C. Teich, J. Opt. Soc. Am. 60, 682 (1970).
- (18) P. Diament and M. C. Teich, J. Opt. Soc. Am. 60, 1489 (1970).
- (19) M. C. Teich and S. Rosenberg, J. Opto-Electron. 3, 63 (1971).

- (20) M. C. Teich and G. Vannucci, "Observation of dead-time-modified photocounting distributions for modulated laser radiation," submitted for publication.
- (21) D. L. Snyder, Random Point Processes (Wiley, New York, 1975).
- (22) B. Reiffen and H. Sherman, Proc. IEEE 51, 1316 (1963).
- (23) G. W. Flint, IEEE Trans. on Military Electron. MIL-8, 22 (1964).
- (24) C. W. Helstrom, IEEE Trans. Inform. Theory IT-10, 275 (1964).
- (25) M. C. Teich, P. R. Prucnal, and G. Vannucci, Opt. Lett. 1, 208 (1977).
- (26) H. L. Van Trees, Detection, Estimation, and Modulation Theory (Wiley, New York, 1968), Part 1.
- (27) W. K. Pratt, Laser Communication Systems (Wiley, New York, 1969).
- (28) M. Gagliardi and S. Karp, Optical Communications (Wiley, New York, 1976).
- (29) C. W. Helstrom, Quantum Detection and Estimation Theory (Academic, New York, 1976).
- (30) D. M. Green and J. A. Swets, Signal Detection Theory and Psychophysics (Wiley, New York, 1966) [reprinted by Robert E. Krieger Publishing Co., Huntington, New York, 1974].
- (31) J. P. Egan, Signal Detection Theory and ROC Analysis (Academic, New York, 1975).
- (32) C. E. Shannon, Bell Syst. Tech. J. 27, 379, 623 (1948).
- (33) T. E. Stern, IRE Trans. Inform. Theory IT-6, 435 (1960); IRE Int. Conv. Rec., pt. 4, 182 (1960).
- (34) J. P. Gordon, Proc. IRE 50, 1898 (1962).
- (35) G. L. Fillmore, IEEE Trans. Inform. Theory IT-15, 465 (1969).
- (36) F. T. S. Yu, Optics and Information Theory (Wiley, New York, 1976).
- (37) B. I. Cantor and M. C. Teich, J. Opt. Soc. Am. 65, 786 (1975).
- (38) I. DeLotto, P. F. Manfredi, and P. Principi, Energia Nucleare 11, 557 (1964).

- (39) J. W. Müller, Nucl. Instr. Meth. 112, 47 (1973); Nucl. Instr. Meth. 117, 401 (1974).
- (40) L. M. Ricciardi and F. Esposito, Kybernetik 3, 148 (1966).
- (41) M. C. Teich, L. Martin, and B. I. Cantor, J. Opt. Soc. Am. 68, 386 (1978).
- (42) R. G. Gallager, Information Theory and Reliable Communication (Wiley, New York, 1968), p. 18.
- (43) R. B. Ash, Information Theory (Wiley-Interscience, New York, 1965), pp. 1-26, 46-50.
- (44) C. W. McMullen, Communication Theory Principles (Macmillan, New York, 1968), p. 268.
- (45) C. W. Helstrom, J. Opt. Soc. Am. 59, 164 (1969).
- (46) J. Amoss and F. Davidson, Appl. Opt. 11, 1793 (1972).
- (47) F. Davidson and J. Amoss, J. Opt. Soc. Am. 63, 30 (1973).
- (48) F. Davidson and R. S. Iyer, Appl. Opt. 13, 2171 (1974).
- (49) M. C. Teich and B. I. Cantor, "Information, error, and imaging in dead-time-perturbed doubly-stochastic Poisson counting systems," submitted for publication.

5. Photocounting Distributions for Exponentially Decaying Sources
(M. C. Teich, H. C. Card)

Photocounting distributions have been calculated for an exponentially decaying pulse of light with a uniformly distributed starting time for the sampling interval (in the absence of dead time). The probability of registering n counts in the fixed sampling interval T is expressible in terms of the incomplete gamma function for count numbers $n \geq 1$ and in terms of the exponential integral for $n=0$. The results may be expected to find use in experiments concerned with spontaneous emission and with radioactive decay. This work is essentially complete and a manuscript detailing the theoretical calculations is in preparation.

PRECEDING PAGE BLANK - NOT FILMED

IV. PHYSICAL EFFECTS OF ELECTRONIC MATERIALS

A. CARRIER TRANSPORT ACROSS SEMICONDUCTOR INTERFACES

1. MIS-Schottky Barrier Quantum Detectors*

(H. C. Card, K. K. Ng, M. C. Teich, E. S. Yang)

This project (as well as those described in parts 1 and 2) was initiated in April 1977, and we report here the progress during the first interval. The purpose of this work is to understand the basic electronic and optical mechanisms of Schottky barrier or MIS-Schottky barrier quantum detectors operating over the infrared and visible spectrum. We are also developing some new detection modes which extend either the sensitivity or the useful wavelength range of MIS detectors made with a given semiconductor material. The carrier transport in these device structures is tunneling of majority or minority carriers. The principal applications of the present work is to optical communications, primarily by guided fiber optic channel. This work is described in the following subsections: a. Properties of Ultra-Thin Oxide Layers, b. Photocurrent Suppression and Interface State Recombination, and c. Low-Voltage Photomultiplication.

a. Properties of Ultra-Thin Oxide Layers

In order to characterize the MIS-Schottky barrier detectors used in this work, we have initiated a program to develop a reliable technology of ultra-thin oxide layers and to

study the electrical and optical properties of these layers in a completed device. We have recently obtained ellipsometry facilities which enable us to measure precisely oxide thickness, and their variation across a sample, with $< 1\%$ error for thickness range of interest ($0 \sim 50 \text{ \AA}$) in tunneling-dominated devices. (Thickness and optical constants of considerably thicker dielectric layers can also be measured with these facilities, which determine the change in the state of polarization of laser light due to reflection from an oxide-covered silicon surface). We are presently examining several methods of oxide growth in an effort to determine reliability and reproducibility of oxide parameters.

Beginning with a technology developed in earlier work⁽¹⁻³⁾ for ultra-thin oxides we have also, during this interval, conducted experimental investigations of the characteristics of completed MIS-Schottky barrier detectors. These devices are as shown in Fig. 68. The structure is a Au-SiO₂-Si sandwich with a Au thickness of $\approx 80\text{-}100 \text{ \AA}$ chosen to optimize the optical transparency and electrical resistance of the contact. The oxides were grown by the thermal oxidation of silicon in dry O₂ at a temperature of 700-800°C (see Fig. 69).

A parameter of central importance in detectors of this nature is the Schottky barrier height ϕ_{bn} shown in Fig. 68, and the dependence of this parameter on the oxide thickness is given in Fig. 70 for the Au-SiO₂-Si system. The decrease in ϕ_{bn} with oxide thickness δ is due primarily to the buildup

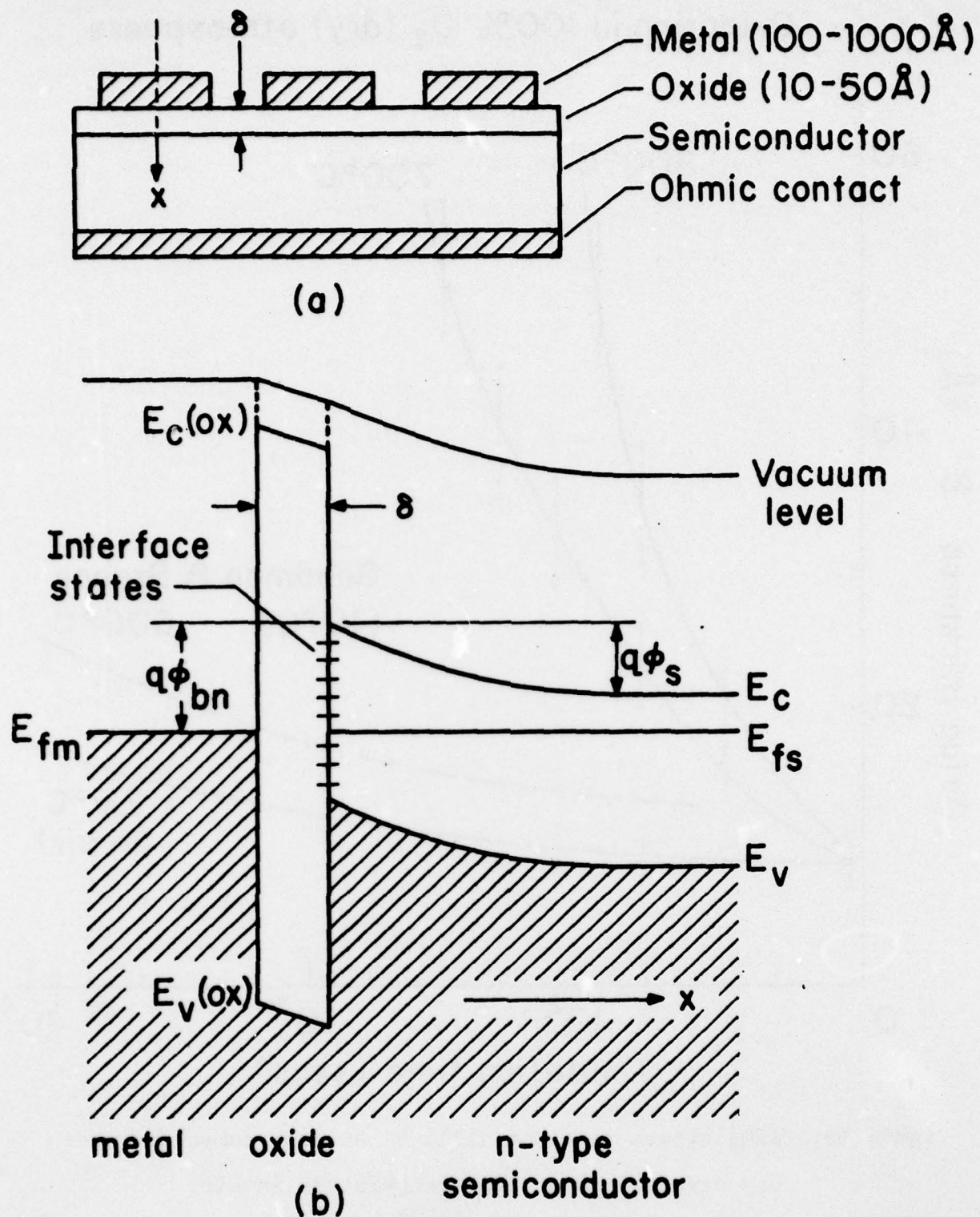


Figure 68

Schematic structure of the MIS-Schottky barrier (a) and the energy band diagram under thermal equilibrium (b).

Oxidation in 100% O₂ (dry) atmosphere

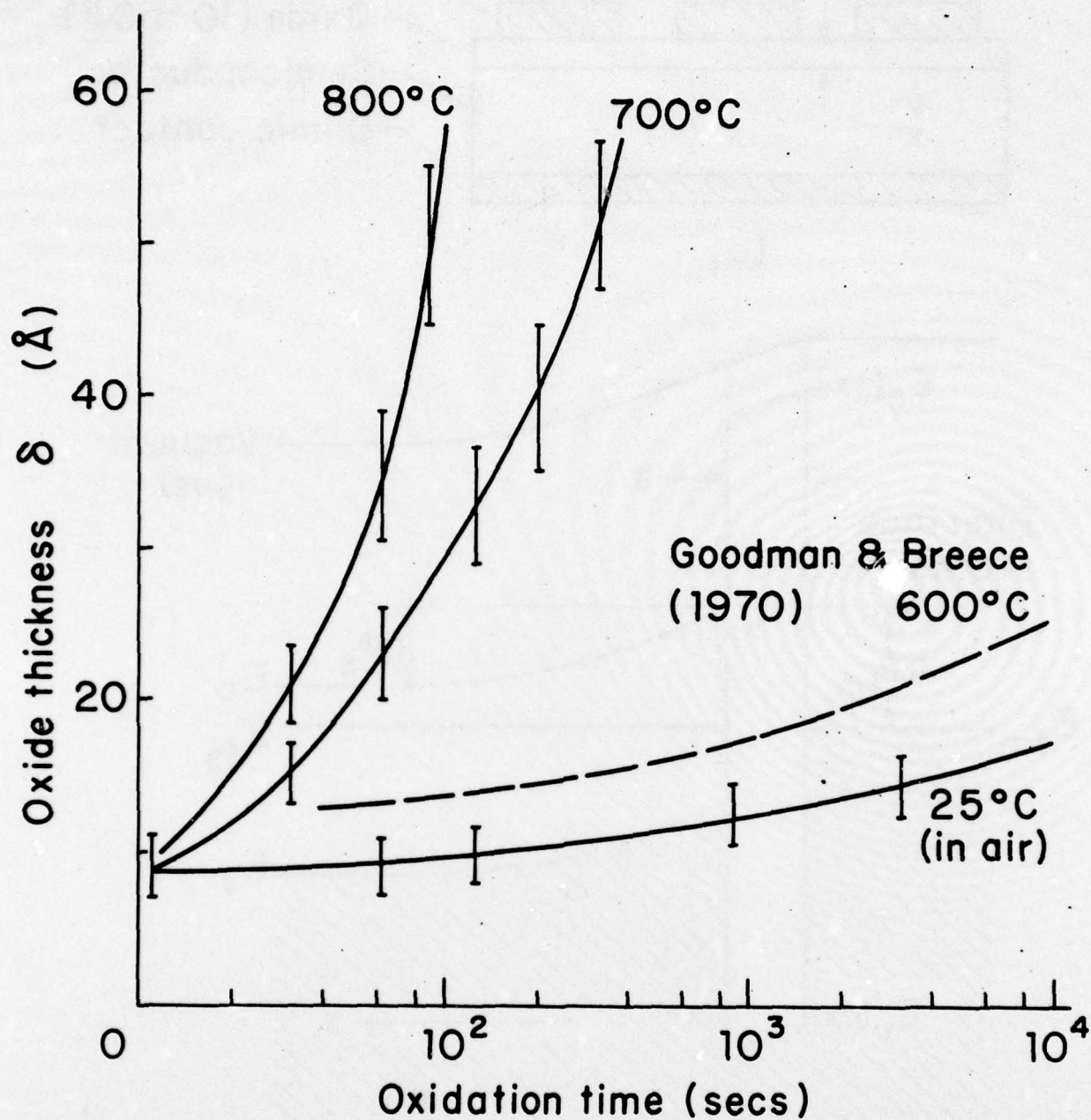


Figure 69: SiO₂ growth rates on (111) Si at high temperatures in dry oxygen, and at room temperature in air.

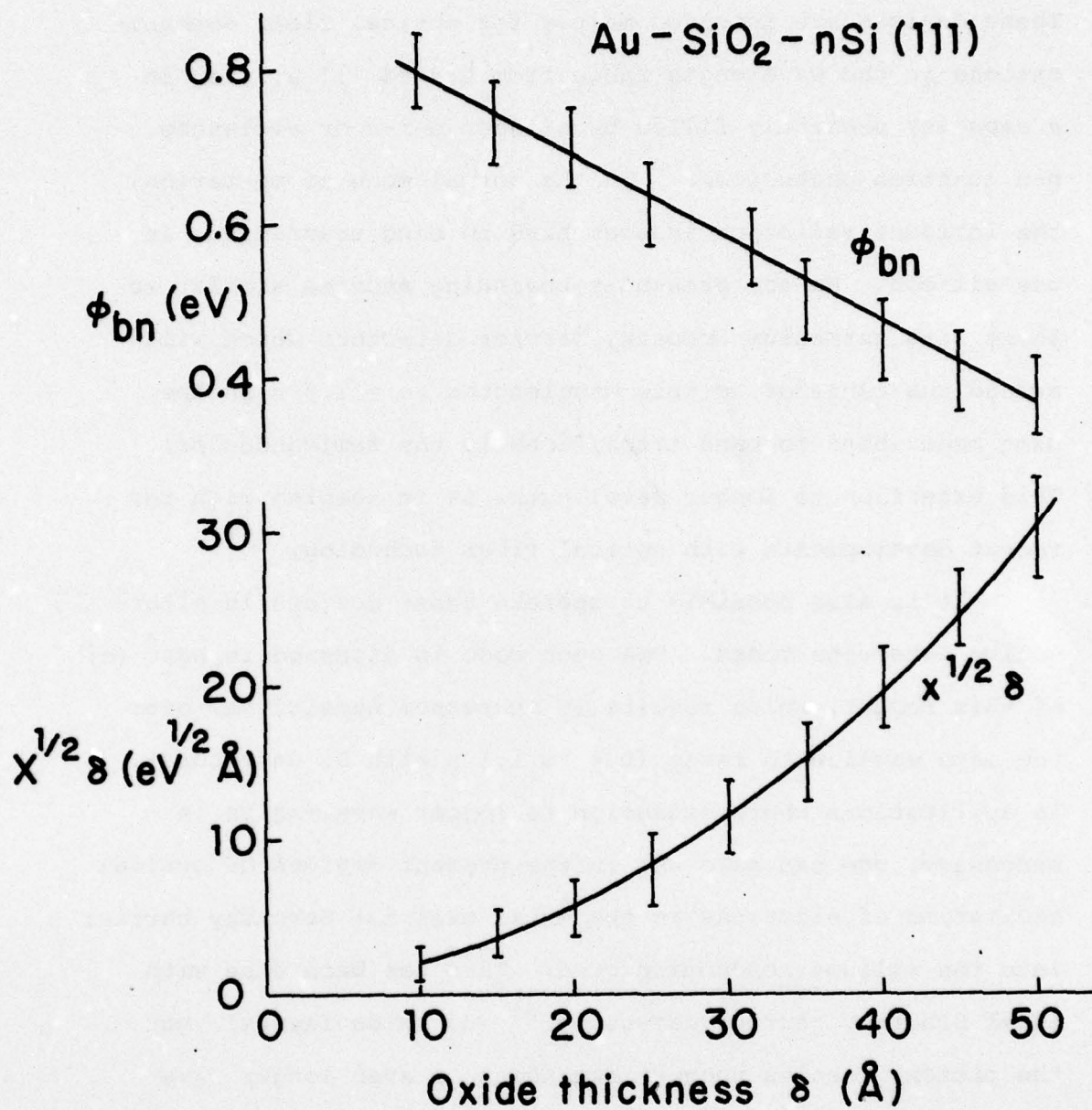


Figure 70: Tunnel exponent $x^{1/2} \delta$ and barrier height ϕ_{bn} vs. oxide thickness, showing spread between a group of devices.

of positive charge in the oxide, and this charge is expected to be strongly influenced by the oxide growth technology.⁽⁴⁾ These devices are intended mainly for optical fiber communications in the wavelength range from 0.4 to 1.1 μ , i.e. in a capacity presently filled by silicon p-i-n or avalanche p-n junction photodiodes. In the normal mode of operation, the incident radiation induces band to band transitions in the silicon. We are presently beginning studies similar to these with germanium Schottky barrier detectors which will extend the range of useable wavelengths to $\approx 1.5 \mu$ in the same mode (band to band transitions in the semiconductor). This extension to longer wavelengths is in keeping with the recent developments with optical fiber technology.⁽⁵⁾

It is also possible to operate these devices in alternative detection modes. One such mode is discussed in part (c) of this report, which results in increased sensitivity over the same wavelength range (0.4 to 1.1 μ with Si detectors). In applications where extension to longer wavelengths is necessary, one can make use in the present devices of optical excitation of electrons in the metal over the Schottky barrier into the silicon conduction band. This has been done with ideal Schottky barrier detectors⁽⁶⁾ (no oxide layers), but the present results suggest extension to even longer wavelengths due to the reduction in Fig. 70 of ϕ_{bn} with δ . In particular, for $\delta \approx 25 \text{ \AA}$, $\phi_{bn} \approx 0.5 \text{ eV}$ for Au-SiO₂-Si devices so that operation in this mode can extend the region of use-

able wavelengths to more than 2μ . The metal thickness for devices operating in this mode must be considerably greater than in the above case, so that the bulk of the optical radiation is absorbed in the metal. It must be thin enough that the photo-excited electrons in the metal are able to reach the junction without being scattered, the optimum thickness being $\approx 200 - 300 \text{ \AA}$.

In the MIS-Schottky barrier the probability of electron tunneling between the metal and semiconductor is proportional to $\exp(-x^{\frac{1}{2}}\delta)$ where x is the averaged potential barrier of the oxide to electrons with energy equal to the conduction band edge at the semiconductor surface. Experimental values of $x^{\frac{1}{2}}\delta$ vs. δ are shown in Fig. 70. The dark current for the MIS-Schottky barriers studied here is a majority-carrier current given by⁽¹⁾

$$J = AT^2 \exp\left(-\frac{q\phi_{bn}}{kT}\right) \exp(-x^{\frac{1}{2}}\delta) \left[\exp\left(\frac{qV}{nkT}\right) - 1\right] \quad (1)$$

where A is the Richardson constant, T is the absolute temperature in $^{\circ}\text{K}$, and V is the applied voltage.

Note that while $x^{\frac{1}{2}}\delta$ increases with oxide thickness δ , the dark saturation current in reverse bias may still increase with δ due to the decrease in ϕ_{bn} . This would result in a larger shot noise, with an accompanying increase in the noise equivalent power of the detector. Contributions to the noise from recombination-generation processes in inter-

face states have yet to be determined for the present detectors, but are expected to be restricted to low frequencies.⁽⁷⁾ The results of Figs. 69 and 70 pertain to dry oxides grown at 700°C, and the magnitude and variability ($\pm 20\%$) of ϕ_{bn} , n and $x^{1/2}\delta$ for a given δ are expected to vary greatly with the ultra-thin oxide technology. This is under present study in our laboratory. Some of the results presented in this section have been published by one of us during this interval.⁽⁸⁾

b. Photocurrent Suppression and Interface State Recombination

For a Schottky-barrier quantum detector operating in reverse bias, the usual mode is that in which photogenerated minority carriers are collected by the metal. Ideally, these carriers should be generated in the depletion region where due to the large electric fields ($10^4 - 10^5 \text{ V cm}^{-1}$) the carrier transit times are short (10^{-12} to 10^{-11} sec). For incident radiation with $h\nu \gg E_g$, the absorption coefficient is sufficiently large that all of the photogeneration occurs in the depletion region and the photocurrent is independent of reverse bias.

In the MIS-Schottky barrier, however, the photocurrent is in general a function of the reverse bias voltage due to a suppression at low voltages of this current by the potential barrier of the oxide, and by recombination of majority and minority carriers in localized states at the oxide-semiconductor interface. We describe in this section the experimental findings for silicon MIS-Schottky barriers, in which

photocurrent suppression is found to be important for oxide thicknesses $\geq 20 \text{ \AA}$. The critical voltage for complete collection of the photogenerated carriers (100% internal quantum efficiency) is also determined for devices with oxide thicknesses of $\leq 50 \text{ \AA}$.

The quantum detectors to be described here have the structure of Fig. 68, and the dark characteristics are described in the previous section. The current-voltage (J-V) characteristics in reverse bias (negative voltage on metal) are shown in Figs. 71 and 72 as a function of illumination intensity with light of greater than bandgap energy. White light was used for simplicity, but monochromatic radiation will be necessary in evaluating the frequency response. Fig. 71 pertains to a near-ideal MIS-Schottky barrier detector with no intentional oxide layer, whereas Fig. 72 refers to a device with an oxide thickness of 35 \AA . These results show that the photocurrent for zero reverse bias (short-circuit conditions) is not suppressed by the (unavoidable) $\approx 10 \text{ \AA}$ oxide grown before evaporation of the metal electrode. On the other hand, for an MIS diode with $d \approx 35 \text{ \AA}$ (Fig. 72), photocurrent suppression is pronounced for small reverse voltages. We note that for sufficient reverse bias V_R the photocurrent suppression effects are removed, such that for the same illumination level, the collected photocurrent J_{ph} is the same for all our oxide thicknesses and equal to that of the near-ideal diode of Fig. 71. The magnitude of the

AD-A056 767

COLUMBIA RADIATION LAB NEW YORK

RESEARCH INVESTIGATION DIRECTED TOWARD EXTENDING THE USEFUL RANGE--ETC(U)

MAR 78 W HAPPER

F/G 7/4

DAAG29-77-C-0019

NL

UNCLASSIFIED

4 OF 44
AD
A056 767



END
DATE
FILMED
9-78

DDC

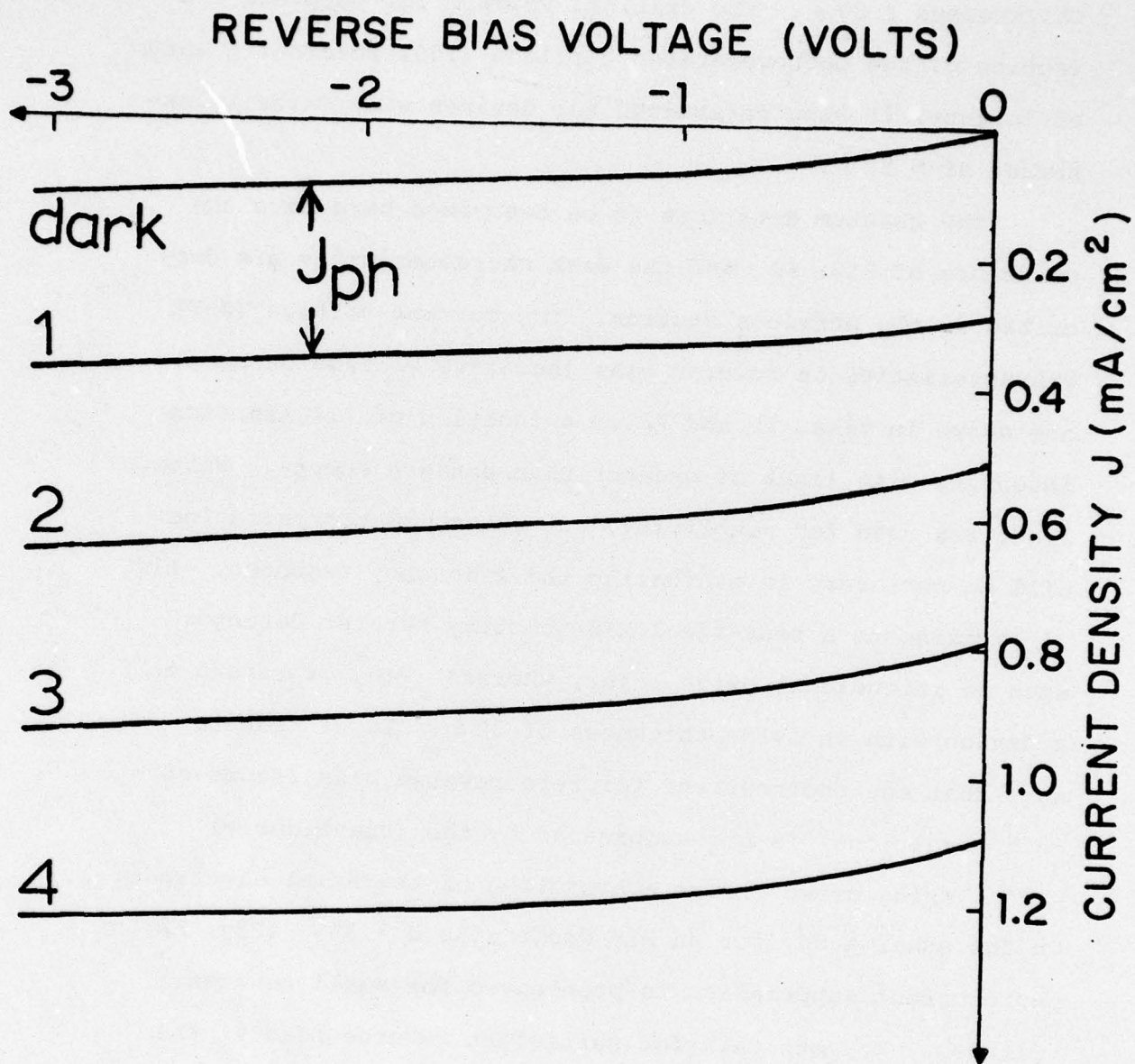


Figure 71

Reverse I-V characteristics of a near-ideal Schottky barrier.
1-4 represent progressively increasing illumination levels.

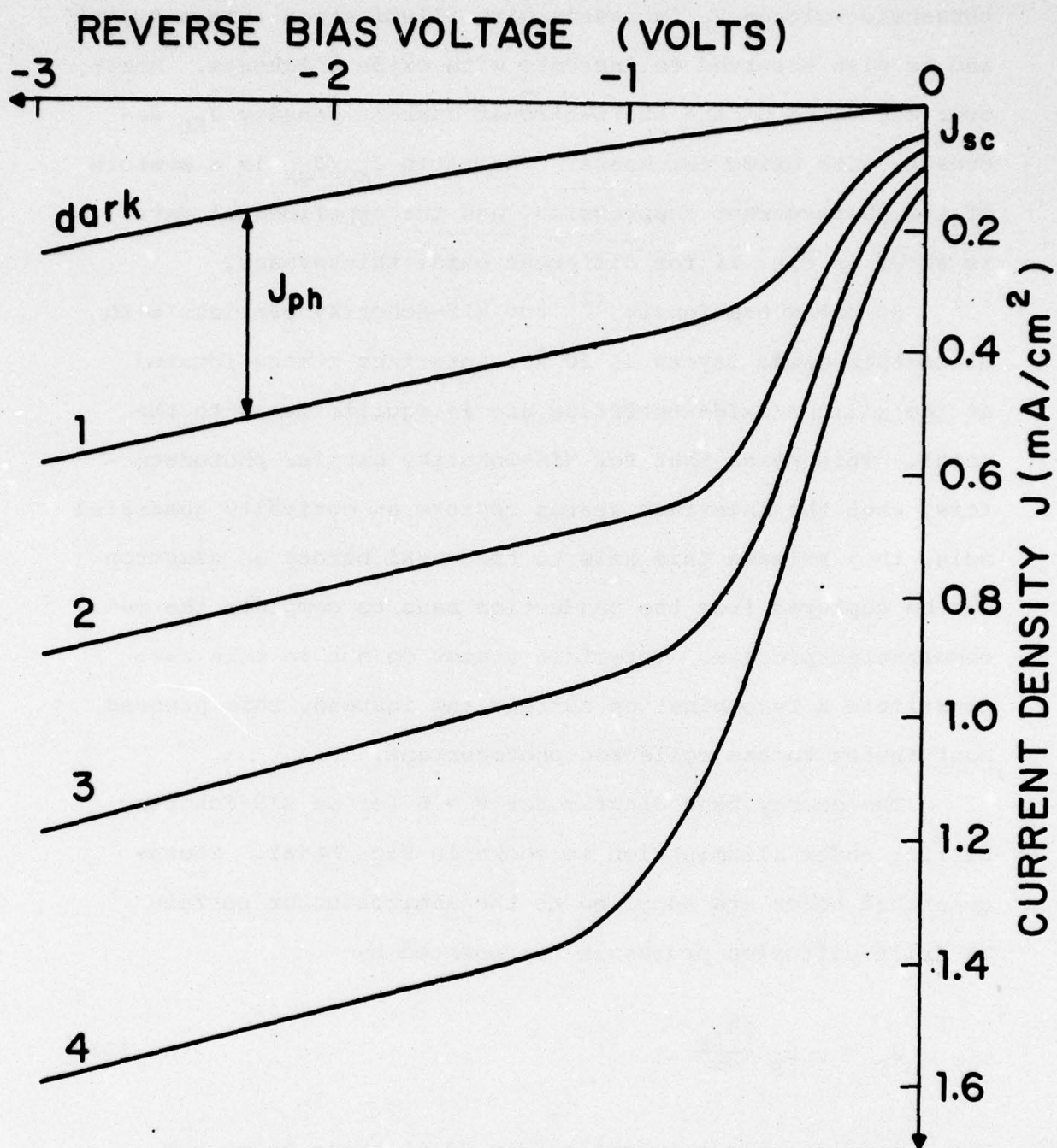


Figure 72

Reverse I-V characteristics of an MIS-Schottky barrier ($d \approx 35 \text{ \AA}$). 1-4 represent progressively increasing illumination levels; these are not the same as in Fig. 71.

threshold voltage V_R increases with illumination intensity, and is also observed to increase with oxide thickness. Moreover the value of the short-circuit current density J_{SC} decreases with oxide thickness. The ratio J_{SC}/J_{ph} is a measure of the photocurrent suppression, and the experimental data is shown in Fig. 73 for different oxide thicknesses.

As noted previously,⁽²⁾ for MIS-Schottky barriers with ultra-thin oxide layers ($\leq 20 \text{ \AA}$), interface states located at the silicon/oxide interface are in equilibrium with the metal. This means that for MIS-Schottky barrier photodetectors, when the interface states capture an optically generated hole, they release this hole to the metal before an electron can be captured from the conduction band to complete the recombination process. Interface states do not in this case constitute a recombination current and instead, this process contributes to the collected photocurrent.

The energy band diagram for $V = 0$ for an MIS-Schottky barrier under illumination is shown in Fig. 74 (a). Photo-generated holes are supplied to the semiconductor surface by drift-diffusion processes represented by

$$J_p = p \mu_p \frac{dE_{fp}}{dx} \quad (2)$$

For a sufficiently thin oxide ($d \leq 20 \text{ \AA}$) these holes are readily removed by tunneling into the metal. Under these conditions the photocurrent collected obtains its maximum

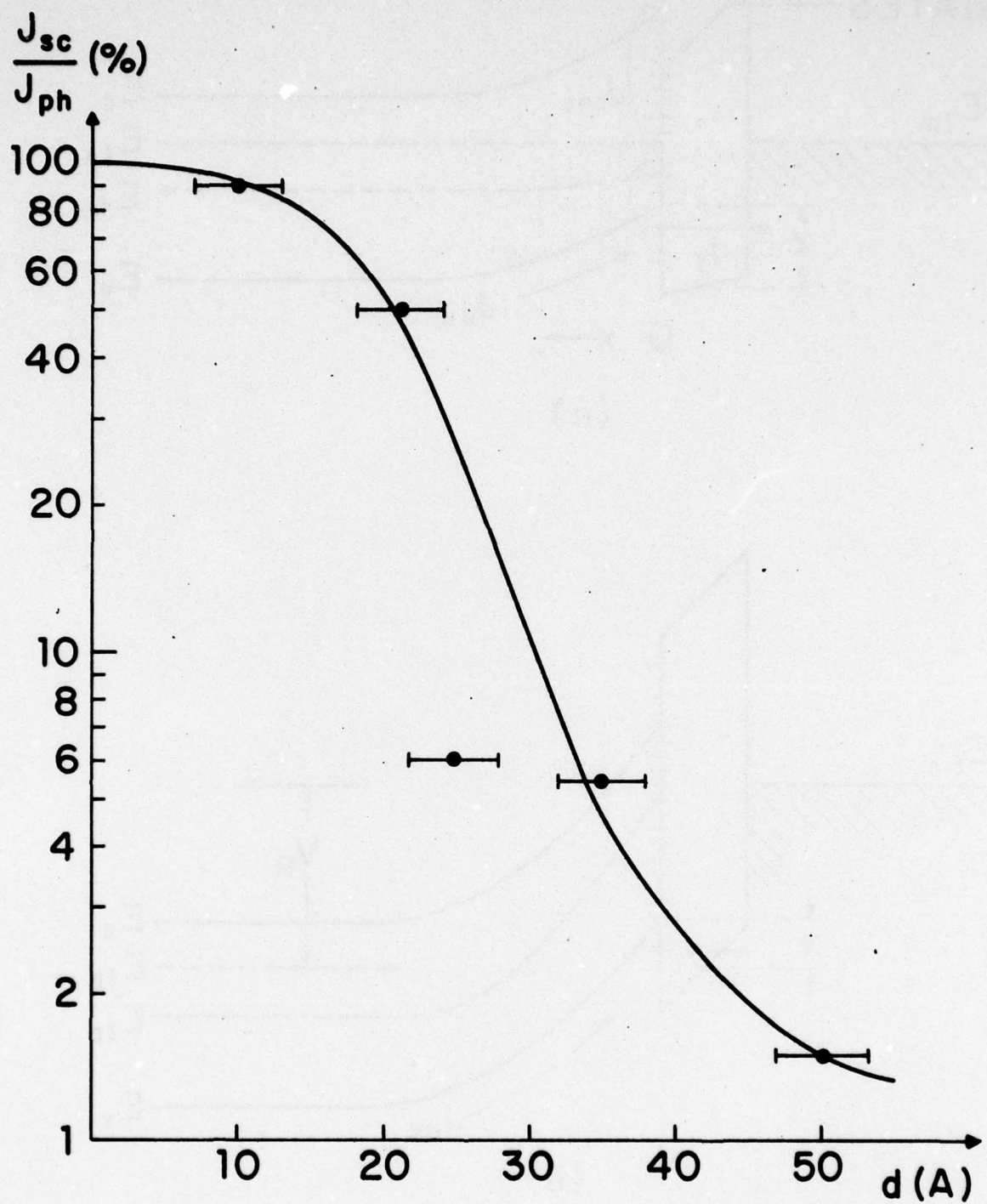


Figure 73: Percentage of photocurrent collected as short-circuit current vs. MIS oxide thickness under the same illumination intensity.

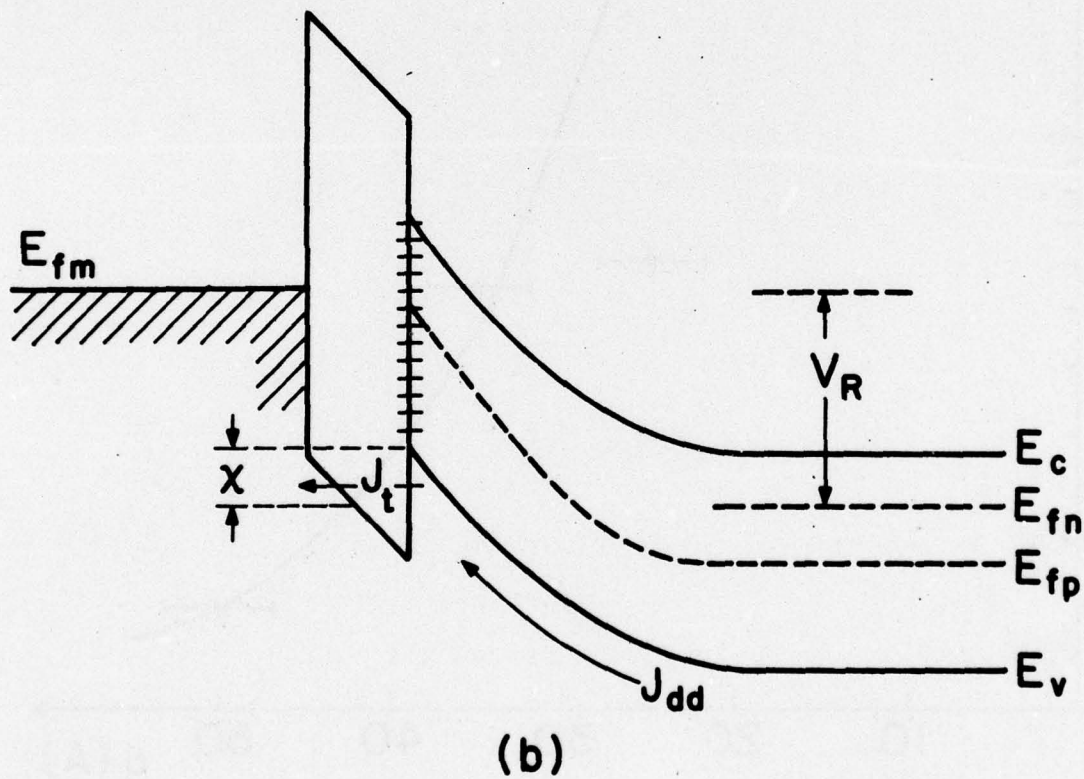
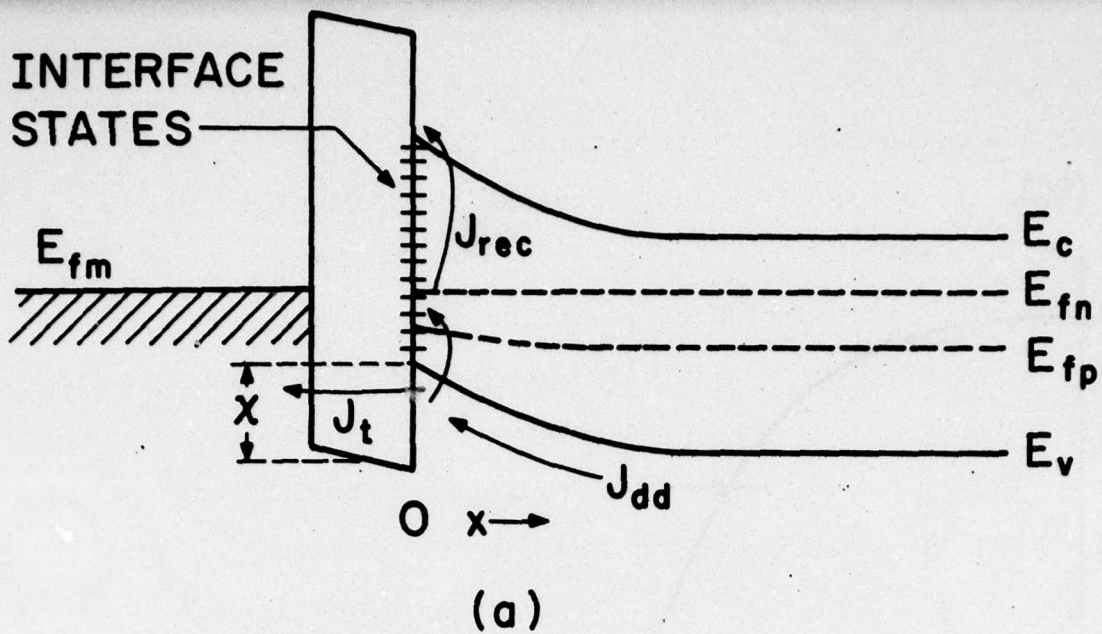


Figure 74:
Energy band diagram of an MIS-Schottky barrier under illumination in short-circuit condition (a) and under reverse bias until suppression is eliminated (b).

value, determined by the illumination level.

As the oxide thickness increases, the tunneling probability is diminished by the factor $\exp(-\chi^{1/2}d)$ where χ is the average potential barrier of the oxide for holes tunneling into the metal. For $d \geq 20 \text{ \AA}$ (in the Au-SiO₂-nSi system) we have observed that the oxide begins to limit the collected photocurrent. The concentration of holes at the silicon surface increases and this reduces the net current supplied from the neutral region by increasing the diffusion of holes in the opposite direction. The quasi-Fermi level for holes becomes relatively flat in the depletion region ($d E_{fp}/dx$ is small in Eq. (2)) and moves closer to E_v at the surface.

At the same time the tunnel current of holes into the metal, given by⁽¹⁾

$$J_t \approx \frac{4\pi m_{th} q (KT)^2}{h^3 N_v} p(o) \exp(-\chi^{1/2}d) \quad (3)$$

increases due to the increase in $p(o)$, the hole concentration at the surface. A balance is struck for which, in the absence of significant recombination in interface states, $J_p = J_t$ and this occurs for a smaller current than was observed for thinner oxides, where the current was not tunnel-limited. We see therefore that suppression of the photocurrent collected at zero bias occurs for $d \geq 20 \text{ \AA}$ even in the absence of interface states.

Let us now consider further the case of $d \geq 20 \text{ \AA}$ and

include the effects of interface state recombination. Under normal operating conditions, the hole concentration $p(o)$ at the surface is much greater than the electron concentration $n(o)$. This means that recombination in interface states (capture by these states of a hole followed by capture of an electron) is limited by the capture rate of electrons, which for states below the electron Fermi level E_{fn} , is described by⁽⁹⁾

$$J_{rec} = qN\sigma v[(1-f)n(o)] \quad (4)$$

where N , σ are the density and electron capture cross-section of interface states, v is the thermal velocity of electrons, f is the occupancy function of interface states and $n(o)$ is the surface concentration of electrons. For typical values $N \approx 10^{12}$ states cm^{-2} , $\sigma \approx 10^{-15}$ cm^2 and $n(o) \approx 10^5$ cm^{-3} (determined by a Schottky barrier height ϕ_{bn} of 0.8 eV for the Au-nSi device), $J_{rec} \approx 10^{-10}$ A cm^{-2} . This may greatly underestimate J_{rec} for oxides with positive charges in which case ϕ_{bn} will be reduced from 0.8 eV and $n(o)$ will increase considerably. Large values of σ have also been observed for interface states in these devices⁽¹⁰⁾ under certain conditions (choice of metal, oxide thickness and sample annealing). Provided $J_{rec} \ll J_{sc}$, interface state recombination does not further suppress the photocurrent beyond that suppression due to the oxide layer alone. At low illumination levels, and

for lower Schottky barrier height ϕ_{bn} , interface recombination will have a major effect on photocurrent suppression for oxides $\geq 20\text{\AA}$.

If the MIS-Schottky barrier photodetector is placed under a substantial reverse bias, part of the voltage will be developed across the oxide and this in turn reduces the effective barrier χ . A larger tunneling probability will allow an increased J_t and the hole concentration at the silicon surface will be depleted. This increases the net hole drift-diffusion current, J_p , towards the surface and E_{fp} rises towards the metal Fermi level (Fig. 74(b)). For sufficient reverse bias, the short-circuit current is again limited by the photogeneration rate, as in the oxide-free case. It is also clear qualitatively that for an MIS diode, the threshold reverse bias (V_R) for elimination of suppression increases with intensity since more tunnel current must be passed and for a fixed intensity, V_R should increase with the oxide thickness. This is in accordance with experimental data shown in Fig. 75 for 3 different oxide thicknesses.

Further investigation is under way regarding the dependence of photocurrent suppression on oxide thickness and interface state parameters. We believe that the threshold V_R for the complete collection of photocurrent and the shape of the photocurrent-voltage curves will help to a basic understanding of interface state processes.

In summary, the MIS-Schottky barrier quantum detector

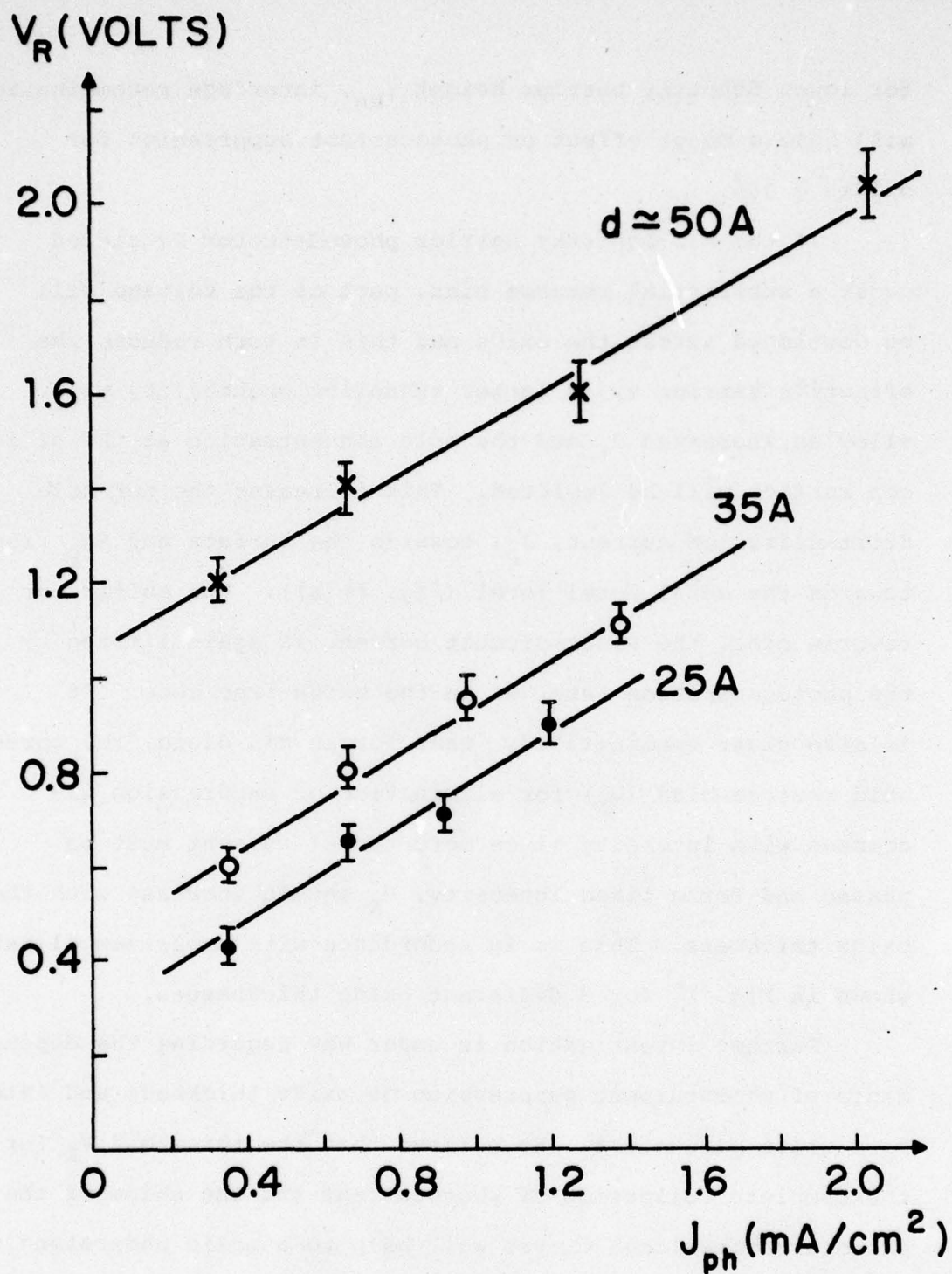


Figure 75: Threshold reverse bias for no suppression vs. photocurrent density for 3 different MIS oxide thicknesses.

behaves as an ideal Schottky barrier detector for oxide thicknesses $\leq 20 \text{ \AA}$. For greater oxide thicknesses, a minimum reverse bias voltage must be applied (V_R) for the complete collection of the photogenerated carriers. These results have been reported by us recently.⁽¹¹⁾ We are concerned with the thicker oxide devices ($> 20 \text{ \AA}$) because they are able to show, under the appropriate experimental conditions, other detection modes such as low-voltage photomultiplication. This is the subject of the next section.

c. Low-Voltage Photomultiplication

The results presented in this section are of a preliminary nature, and have not yet been reproducibly controlled. It has been observed that, under certain experimental conditions of oxide thickness and illumination level, the Au-SiO₂-Si detectors in this study exhibit a photomultiplication mechanism (internal quantum efficiency $\gg 100\%$). The multiplication occurs at very low voltages (as low as -2V) and is not related to avalanche multiplication observed at much larger voltages. Multiplication ratios (M) as large as 20 have been found for oxide thicknesses in the range 20-30 \AA , but more typical results are shown in Fig. 76. This ratio M refers to the number of electrons which flow in the external circuit for each absorbed photon.

The experimental technique is to fabricate MIS-Schottky detectors together with ideal Schottky barrier detectors

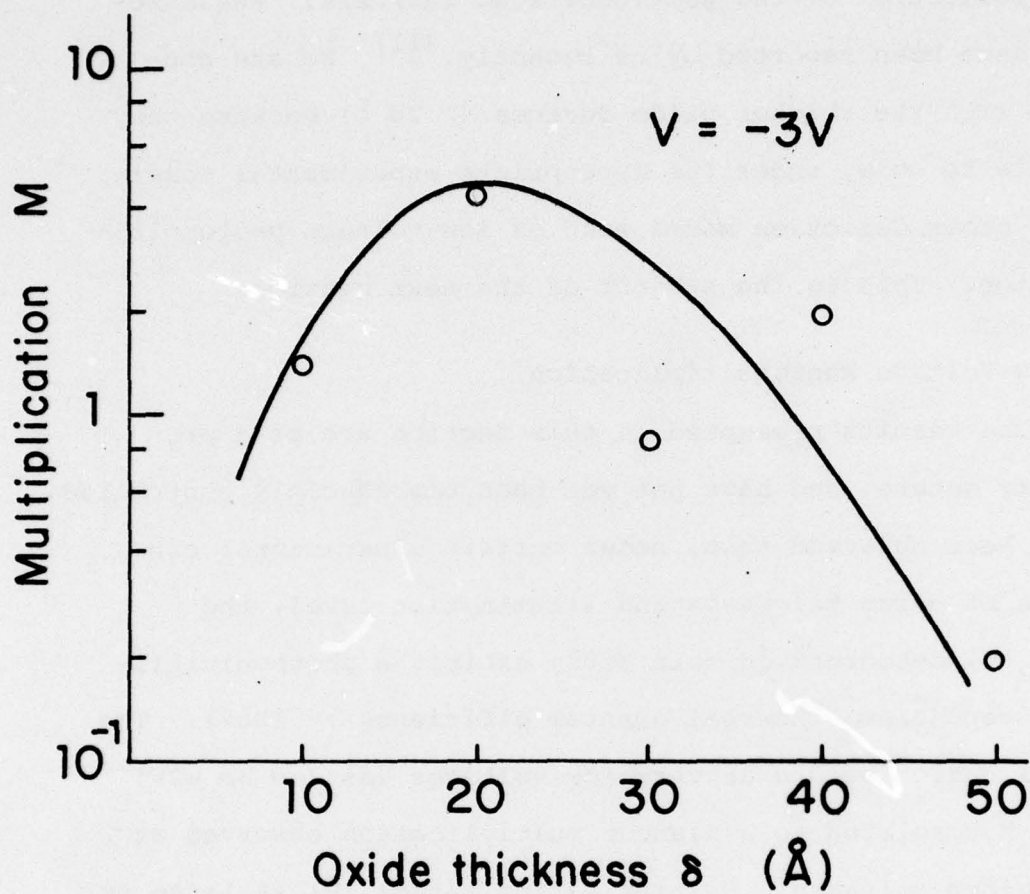


Figure 76: Photomultiplication ratio for Au-SiO₂-Si detectors.

$$M = \frac{J_{ph}}{J_{pho}} \text{ where } J_{pho} = J_{sco} \text{ is the photocurrent for } \delta \approx 0.$$

having no intentional oxide layer. The metal electrodes are evaporated simultaneously so that the optical constants are the same for both ideal and MIS detectors. Finally the photocurrent in reverse bias is compared under identical illumination conditions and the ratio of these photocurrents is simply M .

The mechanism for the low-voltage photomultiplication had been suggested earlier.⁽¹²⁾ Electron-hole pairs are produced in the semiconductor depletion region and the holes are drawn to the semiconductor surface by the electric field in the depletion region. An inversion layer of holes builds up at the surface until $p(o)$ in Eq. (3) is large enough to remove all of the photogenerated holes into the metal. Due to the increase in $p(o)$ with its accompanying positive charge, the electric field in the oxide increases (in reverse bias the voltage on the metal is negative) and the metal Fermi level E_{fm} rises towards the semiconductor conduction band edge at the surface. The electron tunnel current from the metal to semiconductor conduction band thus increases rapidly, greatly outweighing the hole tunnel current itself. In other words, the holes are employed primarily for their electrostatic effect on the potential distribution which has a multiplied effect on the overall reverse current of the contact.

Our present results show considerable variation of the multiplication ratio for oxides of nominally the same thickness (M varies from unity to 20 in some cases). We are pre-

sently attempting to obtain better technological control over this mechanism, and are expecting further improvements in the next interval.

* This research was partially supported by the National Science Foundation under grant NSFENG76-15063.

- (1) H. C. Card and E. H. Rhoderick, J. Phys. D; Appl. Phys. 4, 1589 (1971).
- (2) H. C. Card and E. H. Rhoderick, Solid St. Electron. 15, 993 (1972).
- (3) H. C. Card, Solid St. Commun. 14, 1011 (1974).
- (4) S. M. Sze, Physics of Semiconductor Devices, Wiley, New York (1969).
- (5) H. Melchior, Physics Today 30, 32-39 (November, 1977).
- (6) F. D. Shepherd, Jr., A. C. Yang, and R. W. Taylor, Proc. IEEE (Lett.) 58, 1160-2 (July 1970).
- (7) V. Kumar and W. E. Dahlke, IEEE Trans. ED-24, 146 (1977).
- (8) H. C. Card, Solid St. Electron. 20, 971 (1977).
- (9) W. Shockley and W. T. Read, Phys. Rev. 87, 835 (1952); R. N. Hall, Phys. Rev. 87, 387 (1952).
- (10) S. Kar and W. E. Dahlke, Solid St. Electron. 15, 221 (1972).
- (11) K. K. Ng and H. C. Card, IEEE-IEDM Digest of Tech. Papers, 57-61 (1977).
- (12) M. A. Green and J. Shewchun, Solid St. Electron. 17, 349 (1974).

2. Carrier Transport Across Heterojunction Interfaces*

(E. S. Yang, C. M. Wu, H. C. Card)

The purpose of this project is to study the physics of carrier transport across semiconductor heterojunctions. The initial work is concerned with carrier confinement in double heterostructure (DH) injection lasers in which the carrier leakage is analyzed using both the diffusion and thermionic emission models.

An important consideration in the CW operation of a DH AlGaAs/GaAs injection laser is the aluminum concentration in both the active and confining (passive) layers. Very low threshold current densities ($< 1000 \text{ A/cm}^2$) have been achieved by combining a thin active layer with high Al concentration differences at the heterojunctions.⁽¹⁾ These lasers also exhibit low J_{th} temperature dependence⁽²⁾ which is desirable for CW operation at and above room temperature. In addition, appropriate selection of the aluminum concentration difference leads to lasers with low degradation rate.⁽³⁾ A detailed analysis of the optimum Al concentration was first published by Rode⁽⁴⁾ who showed that carrier confinement in the active layer is not perfect because of leakage through the confining layers. He assumed a constant thermal velocity for carriers leaking out and his theoretical prediction of the excess leakage current is found to be 10 times his experimental data. Following Rode's work, Goodwin and co-workers⁽⁵⁾ assumed that the carrier leakage is controlled by the diffusion of carriers

in the confinement layer and they obtained good correlation between their model and experimental results.

In considering the electron transport in the conduction band in Fig. 77, we find that electrons injected from the N-AlGaAs layer into the p-GaAs active layer must first overcome the potential barrier $q\phi_{Bn}$ in order to reach the P-AlGaAs confining layer. Subsequently, the electrons diffuse away from the p-P heterojunction into the P-AlGaAs layer. As a result, either the thermionic emission over the barrier or the carrier diffusion in the confining layer may dominate the leakage current in a DH injection laser. The energy band diagram of the p-P heterojunction is similar to that of a Schottky barrier⁽⁶⁾ where the thermionic emission is found to control the carrier transport. Since the barrier height in the p-P heterojunction is much lower than the usual Schottky barrier, the diffusion current should be considered. In this report, both the diffusion and thermionic emission are included. It should be pointed out that the present model is applicable to AlGaAs/GaAs lasers and other structures using high mobility materials such as InAs and InSb compounds. In the case where experimental data are available, the model is in agreement with Goodwin's results.

The Thermionic Emission Model

Biased at the threshold current in a laser diode, the depletion regions of the heterojunction interfaces become very narrow, especially with heavily-doped passive layers. The majority carriers will tunnel through the barriers similar

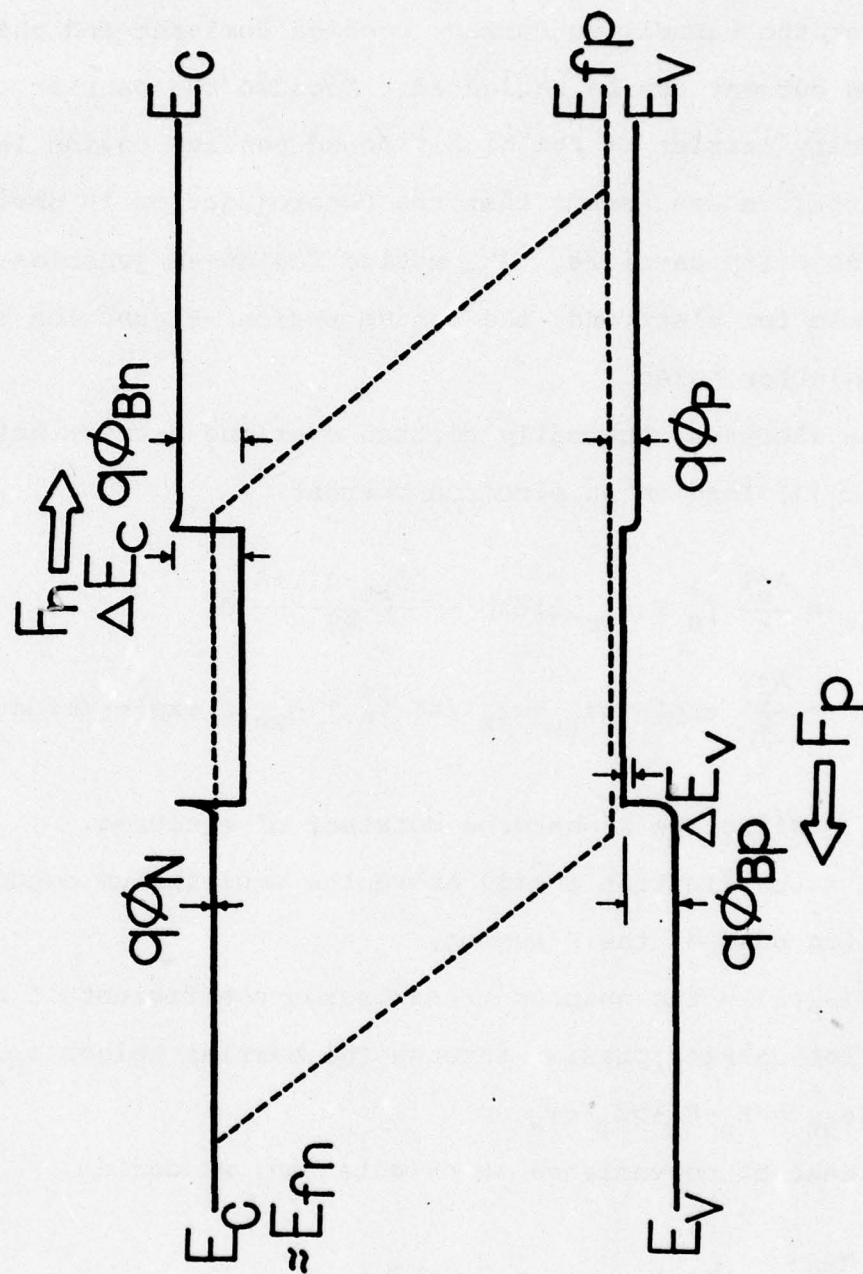


Figure 77: The energy-band diagram of the DH heterojunction under lasing condition.

to the case of Schottky diode emission.⁽⁷⁾ According to the work of Chang and Sze⁽⁸⁾ for Schottky diodes on heavily-doped substrates, the tunnelling current becomes dominant and the diffusion current can be neglected. Because the barrier of the majority carrier of the highly doped passive region is very narrow, we can assume that the heterojunction is ohmic for the majority carriers. The active region -N junction becomes ohmic for electrons, the active region -P junction becomes ohmic for holes.

The electrons thermally emitted over the barrier height ϕ_{Bn} (Fig. 77) lead to an electron current

$$\begin{aligned} J_{nt} &= \frac{A_n^* T}{k} \int_0^\infty T(\phi_{Bn}, \xi) \exp\left[-\frac{q\phi_{Bn} - q\phi_n + \xi}{kT}\right] d\xi \\ &= \frac{A_n^* T}{k} \exp[-(q\phi_{Bn} - q\phi_n)/kT] \int_0^\infty T(\phi_{Bn}, \xi) \exp[-\xi/kT] d\xi \quad (1) \end{aligned}$$

where A_n^* = Effective Richardson constant of electron,

ξ = the electron energy above the equilibrium conduction band of the P-region,

$T(\phi_B, \xi)$ = the quantum transmission coefficient of a free carrier passing through the barrier height ϕ_B ,

$$q\phi_{Bn} = E_p - E_A + q\phi_p - q\phi_n.$$

For the sake of convenience in calculation, we define

$$\eta\left(\frac{q\phi_B}{kT}\right) = \frac{1}{kT} \int_0^\infty T(q\phi_B, \xi) \exp[-\xi/kT] d\xi. \quad (2)$$

According to Rode's calculation⁽⁴⁾, the electrons are

mostly in the Γ -band if the aluminum concentration (x) of the active region does not exceed 0.15. In other words, we can assume the electron leakage through the X-band as negligible. By using Rode's parameters (i.e. the effective mass and energy band gaps in the X, L and valence bands) and setting $n_{th} = 2 \times 10^{18} \text{ cm}^{-3}$, the electron leakage current can be calculated:

$$J_{nt} = A_n^* T^2 \exp\left(\frac{q\phi_{Bn}}{kT}\right) \exp[-q(\phi_{Bn} - \phi_n)/kT] \quad (3)$$

Similarly, the hole leakage current is:

$$J_{pt} = A_p^* T^2 \exp\left(\frac{q\phi_{Bp}}{kT}\right) \exp[-q(\phi_{Bp} - \phi_p)/kT] \quad (4)$$

where $A_n^*/A = m_{eA}^*/m_0$, $A_p^*/A = m_{pA}^*/m_0$ and $A = 120 \text{ Amp/cm}^2/\text{°K}^2$, and $q\phi_{Bp} = E_n - E_A + q\phi_N - q\phi_\eta$. The sum of these currents is

$$J_t = J_{nt} + J_{pt} \quad (5)$$

The foregoing equations are used to calculate the magnitude of the thermionic emission current. Notice that the current is controlled by the effective Richardson's constant (which is determined by the effective masses) and the barrier heights ϕ_{Bn} and ϕ_{Bp} . The significance of these parameters will be discussed later.

The Diffusion Model

Let us consider the diffusion of electrons in the P-layer. We assume that the minority quasi-Fermi potential of the passive region is flat across the depletion region. Then the excess minority carrier concentration is given by

$$n_p(0) - n_{p0} \cong N_{cp} \exp \frac{[E_{fn} - E_{cp}]}{kT} \quad (6)$$

where $n_p(0)$ = the electron concentration in the P-region,

n_{p0} = the equilibrium electron concentration in the P-region,

N_{cp} = the effective density of states in the P-region,

E_{cp} = the conduction band energy of the P-region.

Therefore, the diffusion current is

$$J_{nd} = q(n_p(0) - n_{p0}) D_{nP} / L_{nP} \quad (7)$$

When the width of the passive region W_p is less than the minority diffusion length L_{nP} , the minority carrier distribution will have a slope limited by W_p . The worst case is given by

$$J_{nd} = q(n_p(0) - n_{p0}) \frac{D_{nP}}{L_{nP}} \coth\left(\frac{L_{nP}}{W_p}\right) \quad (8)$$

where the surface recombination velocity at W_p is assumed to be infinity which is similar to the diffusion current in the narrow base region of a bipolar transistor. When $W_p \ll L_{nP}$, Eq. (8) can be simplified as

$$J_{nd} = q(n_p(0) - n_{p0}) \frac{D_{np}}{W_p} \quad (9)$$

Similarly, we can obtain the hole diffusion current in the N-region,

$$J_{pd} = q(P_N(0) - P_{No}) \frac{D_{PN}}{W_N} \quad \text{if } L_{PN} \gg W_N \quad (10)$$

Therefore, the total diffusion current is

$$J_d = J_{nd} + J_{pd} + J_{xd} \quad (11)$$

where J_{xd} is the electron diffusion current expressed in terms of the X-band diffusion constant and diffusion length.

Discussion

We use the dimension of Rode's devices, and the GaAs mobility⁽⁹⁾ and life time data calculated from Stern's work.⁽¹⁰⁾ The leakage currents due to both mechanisms are calculated and shown in Figs. 78 and 79. It is found that the thermionic current is about seven times the diffusion current, and the leakage current should be dominated by the smaller one of two series transport mechanisms. Considering separately the single mechanism only, the threshold current of Rode's devices is shown in Fig. 80, it is seen that the leakage current due to minority diffusion in the passive region agrees well with Rode's experimental data. Physically, the ratio of two currents due to different mechanisms is

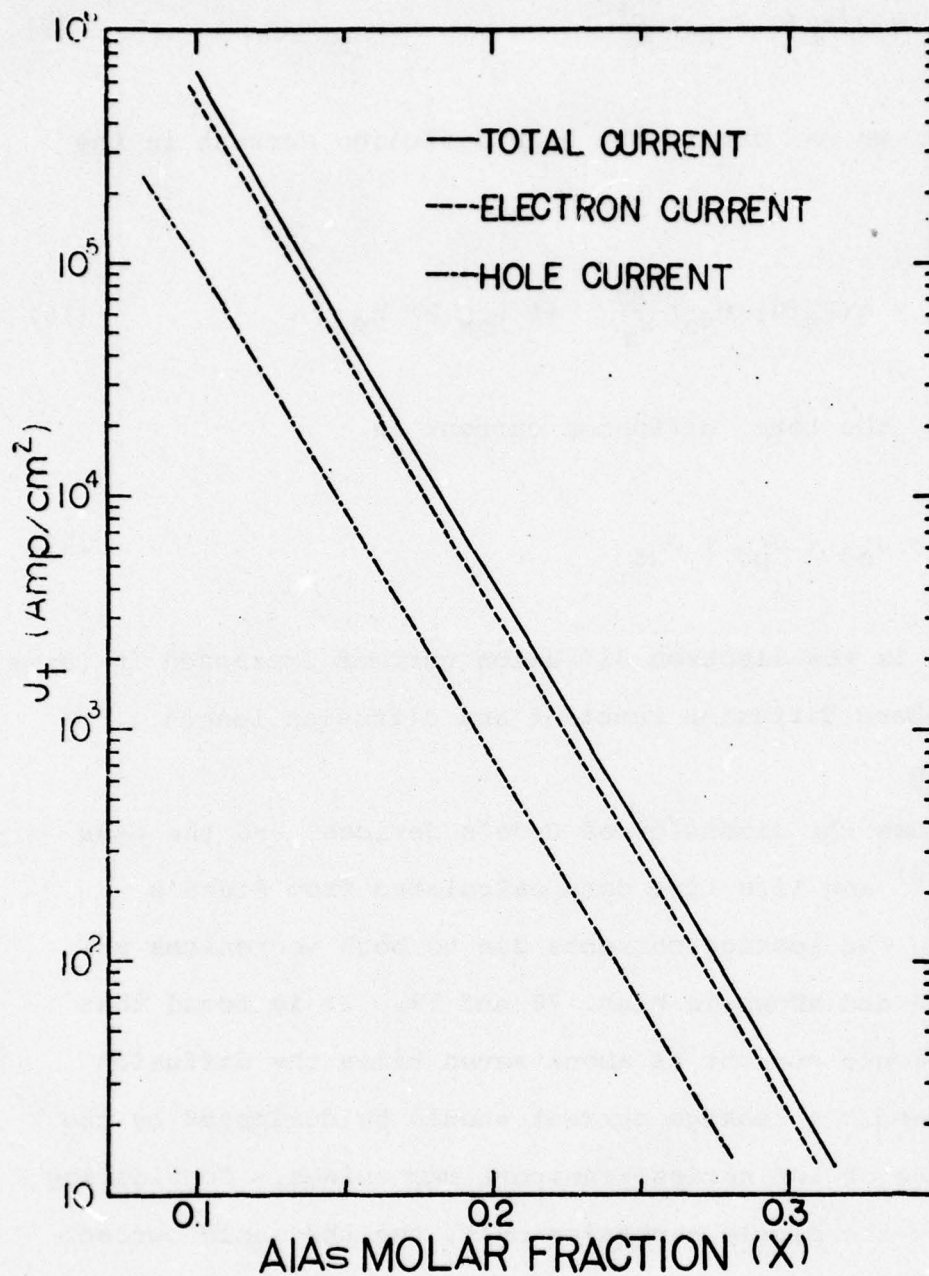


Figure 78:

The leakage currents of the thermionic emission mechanism. Device dimensions and doping concentrations are taken from Rode's work in Reference 4.

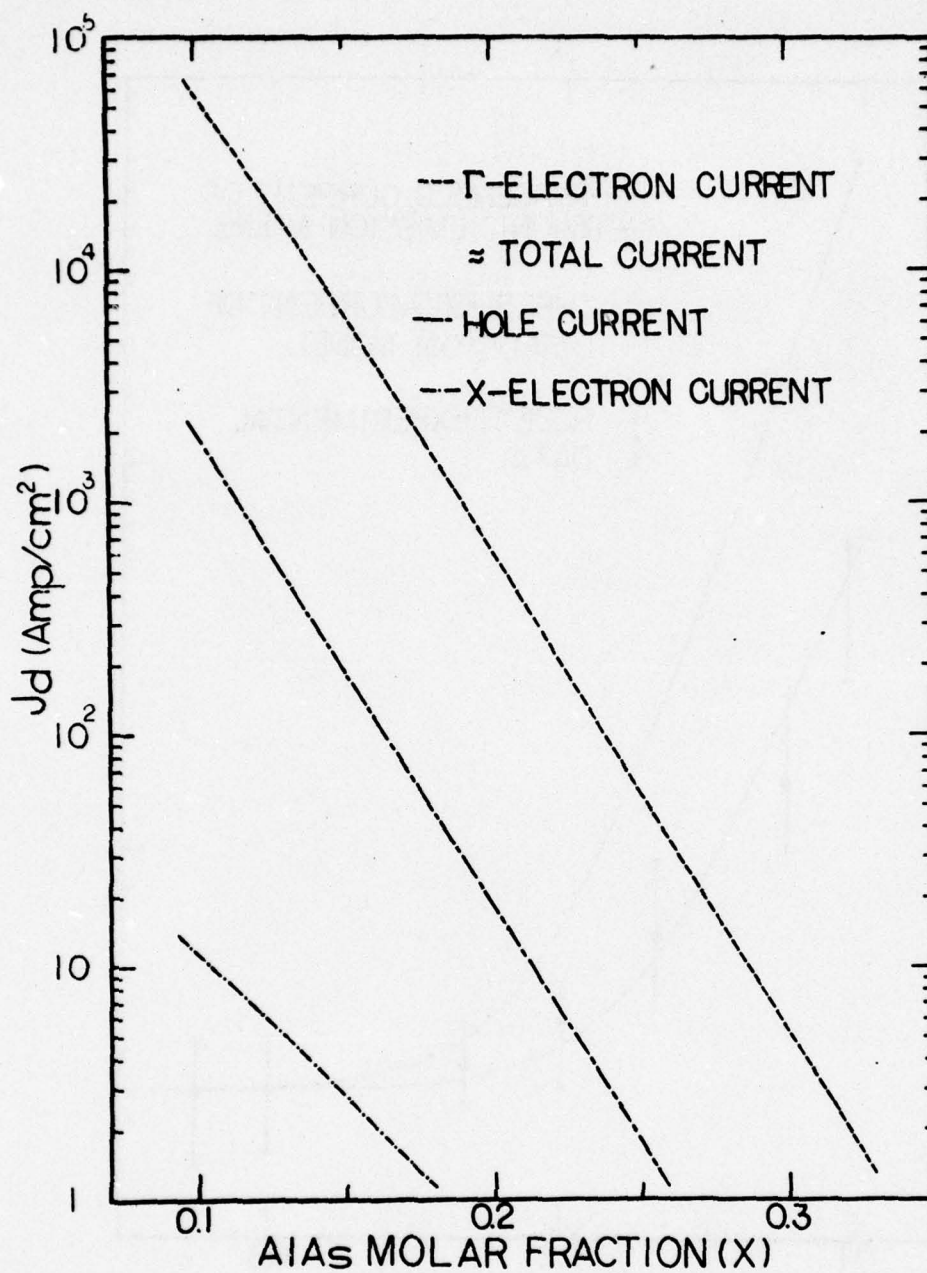


Figure 79:

The leakage currents of the diffusion mechanism. Device dimensions and doping concentrations are taken from Rode's work in Reference 4.

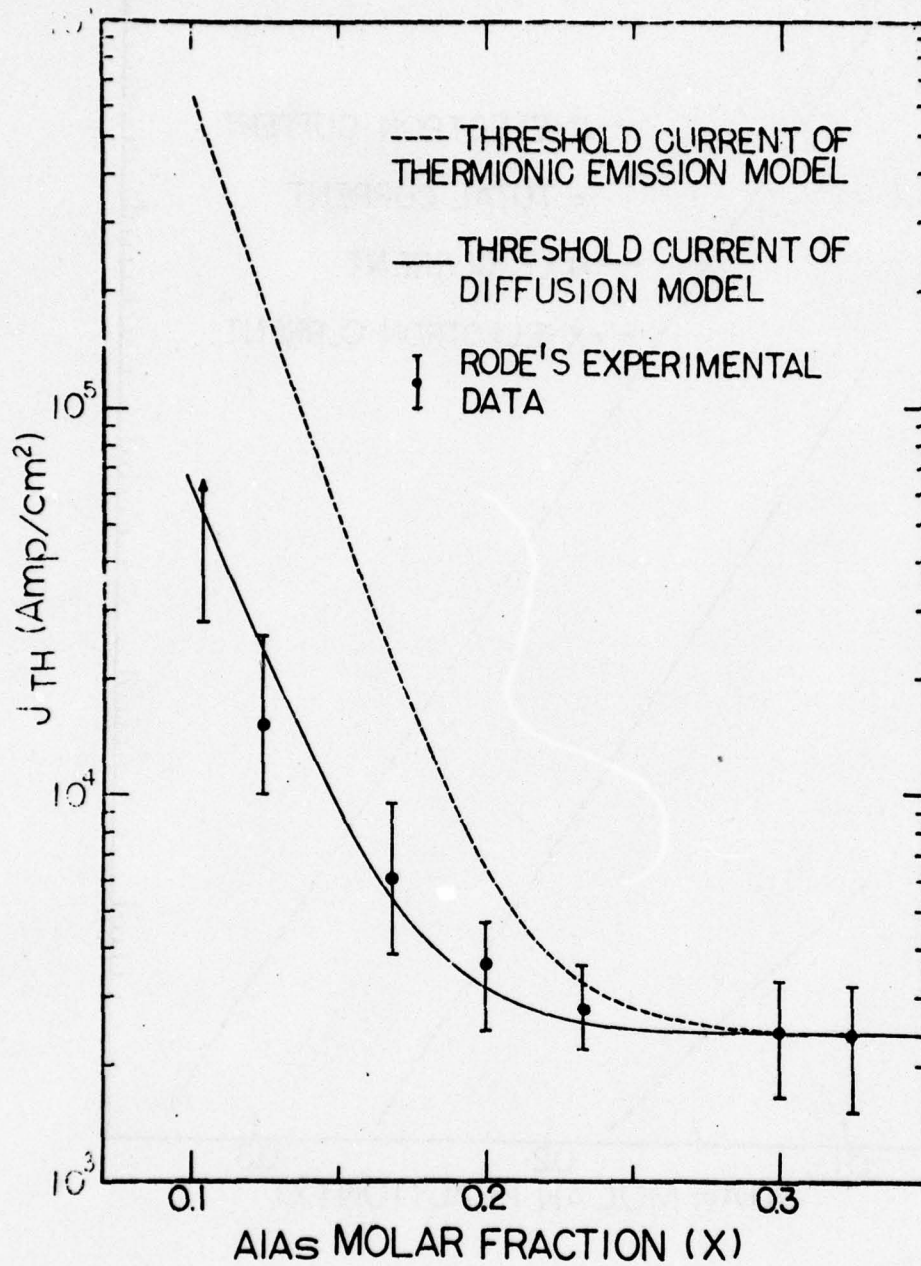


Figure 80:

The threshold current of two leakage models and comparison with Rode's data.

$$\begin{aligned}
\frac{J_{nt}}{J_{nd}} &= \frac{A_n^* T^2 \eta}{q N_{cP} D_{nP} / L_{nP}} \\
&= \eta \left(\frac{m_{eA}^*}{m_{eP}^*} \right) \left(\frac{1}{2\pi} \frac{q \tau_{nP}}{m_{eP}^* \eta_{nP}} \right)^{1/2} \\
&\approx \frac{2}{5} \eta \left(\frac{m_{eA}^*}{m_{eP}^*} \right) \left(\frac{\tau_{nP}}{\tau_{cP}} \right)^{1/2} \quad (12)
\end{aligned}$$

where τ_{cP} is the electron collision time in the passive region. Therefore, the diffusion current will dominate except when the carrier confinement barrier or the mobility is very high, i.e.

$$\eta \left(\frac{\tau_{nP}}{\tau_{cP}} \right)^{1/2} \approx 1.$$

When the width of the passive region is designed thicker, the diffusion current will be reduced. The minimum diffusion current is calculated and shown in Fig. 81. It is observed that the width of the passive region should be as large as the minority diffusion length to lower the leakage current. The doping-dependent diffusion current is also considered and shown in Fig. 82. We find that a highly-doped passive region will have a better carrier confinement. Usually, the active region contains 10% AlAs.⁽⁵⁾ The diffusion current versus the difference of the molar fractions of the passive and active regions is also shown in Fig. 82. We find the leakage current is reduced 20% for the same molar fraction difference Δx between the passive and active layers.

The diffusion current is also dependent upon the tem-

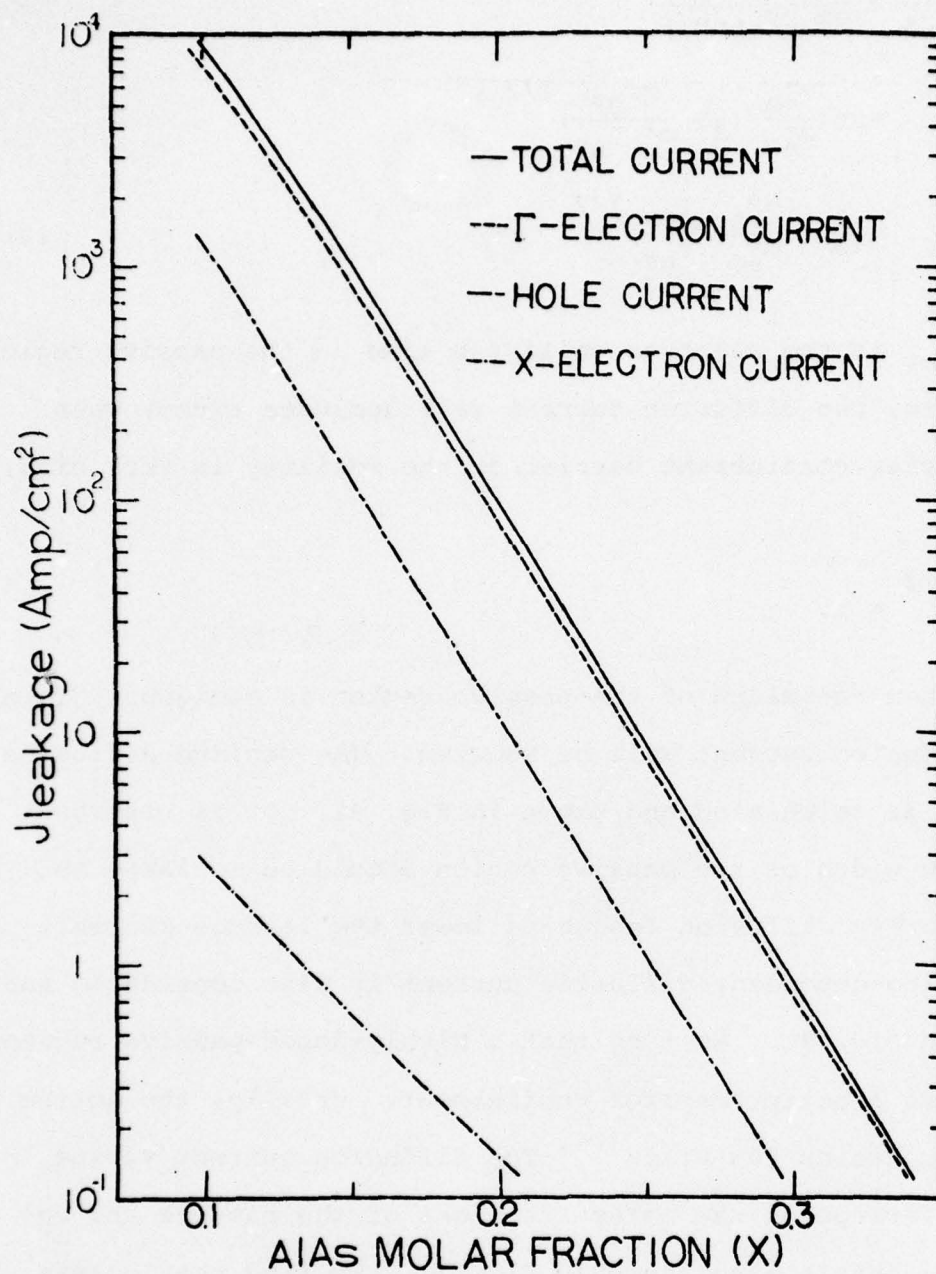


Figure 81:

Ideal leakage current with thick passive layer.

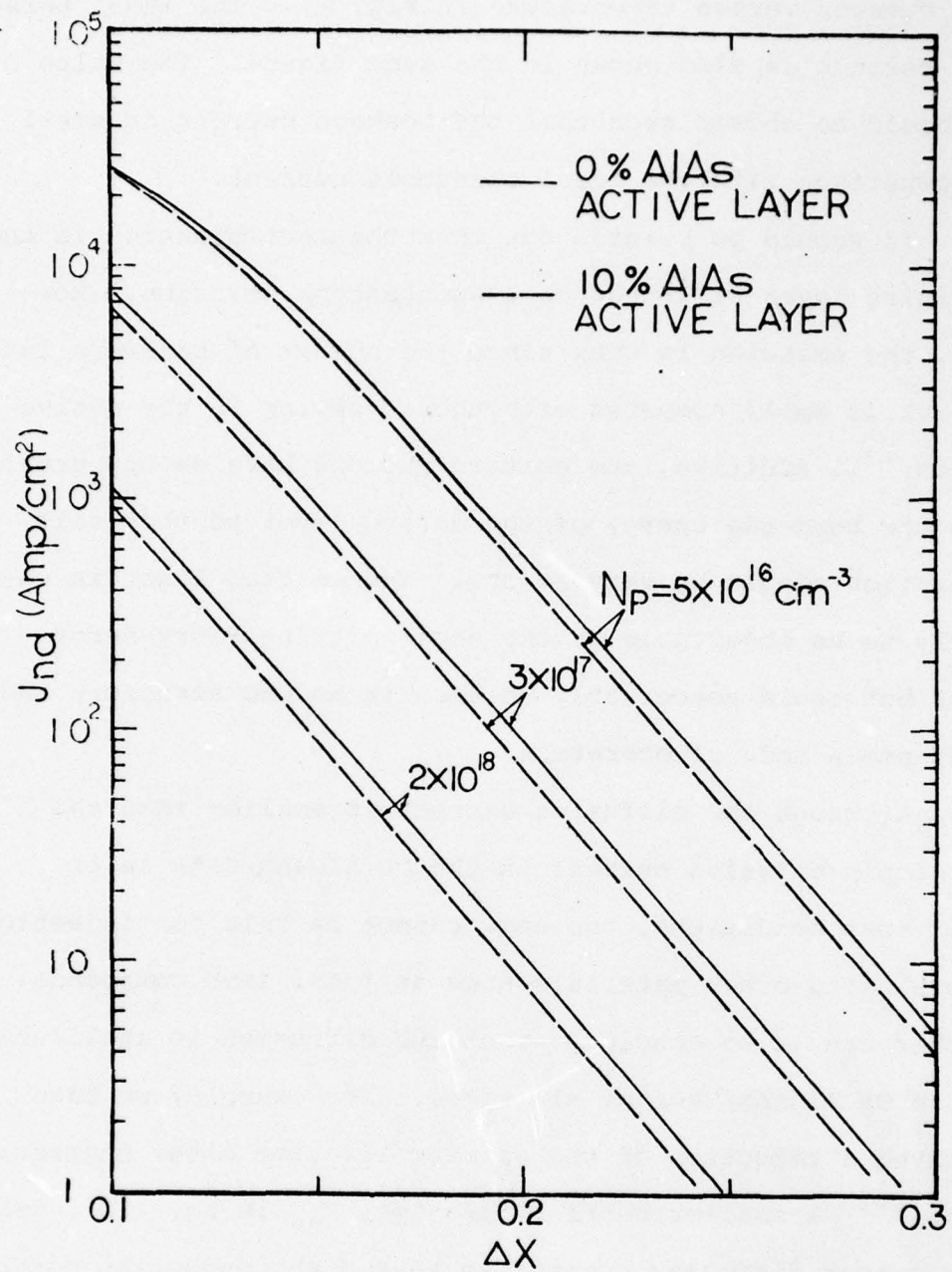


Figure 82:

Electron diffusion current versus the difference of mole fractions ΔX .

perature. We use Stern's calculation⁽¹⁰⁾ and show the diffusion current versus temperature in Fig. 83. The ideal threshold current is also shown in the same figure. The value of Δx should be chosen such that the leakage current is small in comparison with the ideal threshold current.

It should be pointed out that the recombination in the confining layer will produce a spontaneous emission. However, the emission is weak since the number of carriers leaking out is small compared with those staying in the active region. In addition, the emitted photons have energy greater than the band-gap energy of the active layer so that self absorption should be very strong. The emitted light is unlikely to be observable in the edge-emitting Fabry-Perot laser but could conceivably be seen in an LED structure under spontaneous mode of operation.

Although the diffusion current is smaller than the thermionic emission current in the DH AlGaAs/GaAs laser under most conditions, the same cannot be said for injection lasers using other materials such as InAs, InSb compounds. Neither can it be concluded that the diffusion is applicable to the DH AlGaAs/GaAs at all times. For example, we have observed a reduction of the carrier lifetime after degradation.⁽¹¹⁾ A smaller carrier lifetime, τ_{np} in Eq. (12), leads to a larger diffusion current so that both conduction mechanisms may become equally important.

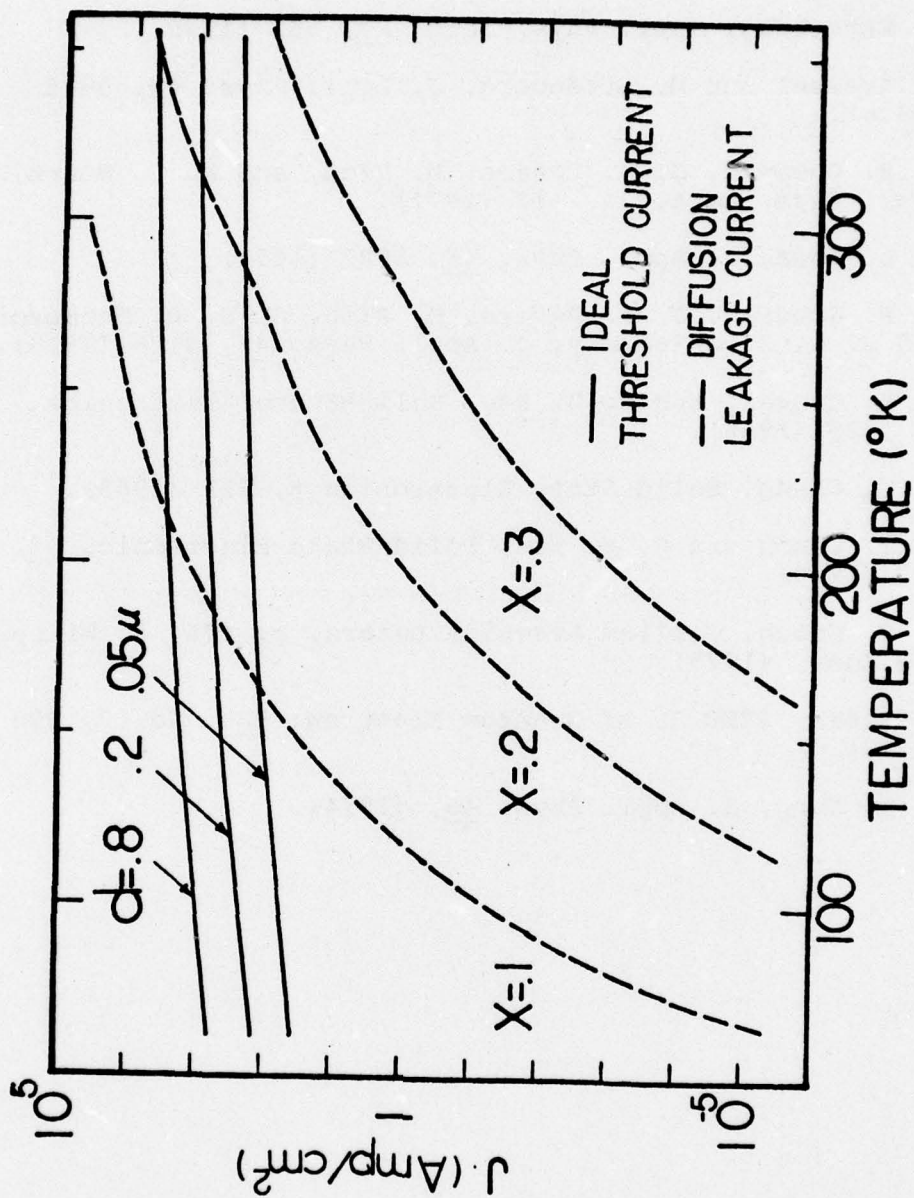


Figure 83: The leakage current versus temperature. (The ideal threshold current is drawn according to Stern's calculation in Reference 10.)

* This research was partially supported by the National Science Foundation under Grant NSFENG-76-18074.

- (1) M. Ettenberg, Appl. Phys. Lett. 27, 652 (1975).
- (2) H. Kressel and M. Ettenberg, J. Appl. Phys. 47, 3533 (1976).
- (3) A. R. Goodwin, J. R. Peters, M. Pion, and W. O. Bourn, Appl. Phys. Lett. 30, 110 (1977).
- (4) D. L. Rode, J. Appl. Phys. 45, 3887 (1974).
- (5) A. R. Goodwin, J. R. Peters, M. Pion, G. H. B. Thompson and J. E. A. Whiteaway, J. Appl. Phys. 46, 3126 (1975).
- (6) C. R. Crowell and S. M. Sze, Solid-State Electronics 9, 1035 (1966).
- (7) L. L. Chang, Solid-State Electronics 8, 721 (1965).
- (8) C. Y. Chang and S. M. Sze, Solid-State Electronics 13, 727 (1970).
- (9) C. H. Gooch, Gallium Arsenide Lasers, p. 178, J. Wiley and Sons, (1975).
- (10) F. Stern, IEEE J. of Quantum Electron. QE9, No. 2, 290 (1973).
- (11) E. S. Yang, J. Appl. Phys. 45, (1974).

3. Schottky Barrier Classical Detectors for Submillimeter Radiation*

(H. C. Card, E. S. Yang, E. Y. Chan, A. R. Kerr,
P. Thaddeus)

Schottky barrier diodes have inherently high frequency response by virtue of their majority-carrier behavior. These devices have long been used in the microwave region as mixers or detectors, and their operation has recently been extended into the submillimeter region. Unlike in section 1, where we discussed the operation of Schottky barriers as quantum detectors with photon absorption in the semiconductor, in the present section we deal with classical modes of detection. In these classical modes, the incident radiation is absorbed in a metal whisker which probes the device, and acts as a microwave or submillimeter antenna. The Schottky barrier itself simply serves to rectify the received signal and the transport mechanisms are those of the dark characteristics. In order to achieve the maximum frequency of operation, the device geometry is made as small as possible, and the present study investigates the transport in small-geometry devices, and the way in which this differs from large-geometry Schottky barriers.

In the following, we describe the experimental findings during this interval, and show experimentally that the minority carrier injection ratio decreases with increasing forward bias voltage in the small area devices (2 μm diameter), in contrast to devices of large area.

The device structure is shown in Fig. 84 . The epitaxial layer (thickness $0.5\text{ }\mu\text{m}$) has an impurity concentration of $N_d = 3 \times 10^{17}\text{ cm}^{-3}$. Phosphor bronze wire of diameter $12\text{ }\mu\text{m}$ was electrolytically etched in NaOH to the proper dimension for whisker contacts to the evaporated Au-Pt contacts.

The principle of the electrical measurements is as follows. When a particular diode is forward biased, the current is composed of a majority carrier current (due to conduction electrons being removed from the semiconductor) and a minority carrier injection current (due to holes being injected from the metal, corresponding to valence electrons being removed from the semiconductor). The minority-carriers recombine with majority-carriers either in the space charge region (space charge recombination current) or in the neutral region (minority-carrier injection current, I_p , sometimes called diffusion current). This forward-biased diode can be viewed as the emitter junction of a transistor. The majority-carrier current flows into the N^+ substrate and out the back (ohmic) contact; this corresponds to the base current of the transistor. Any minority-carriers (holes) injected at the emitter and contributing to I_p may be collected at neighboring Schottky barriers which are contacted so as to maintain them at ground potential; the current collected at these contacts is the collector current of the transistor. If none of the neighboring devices are contacted, the injected holes simply recombine in the epitaxial layer.

By means of 3-dimensional differential translational

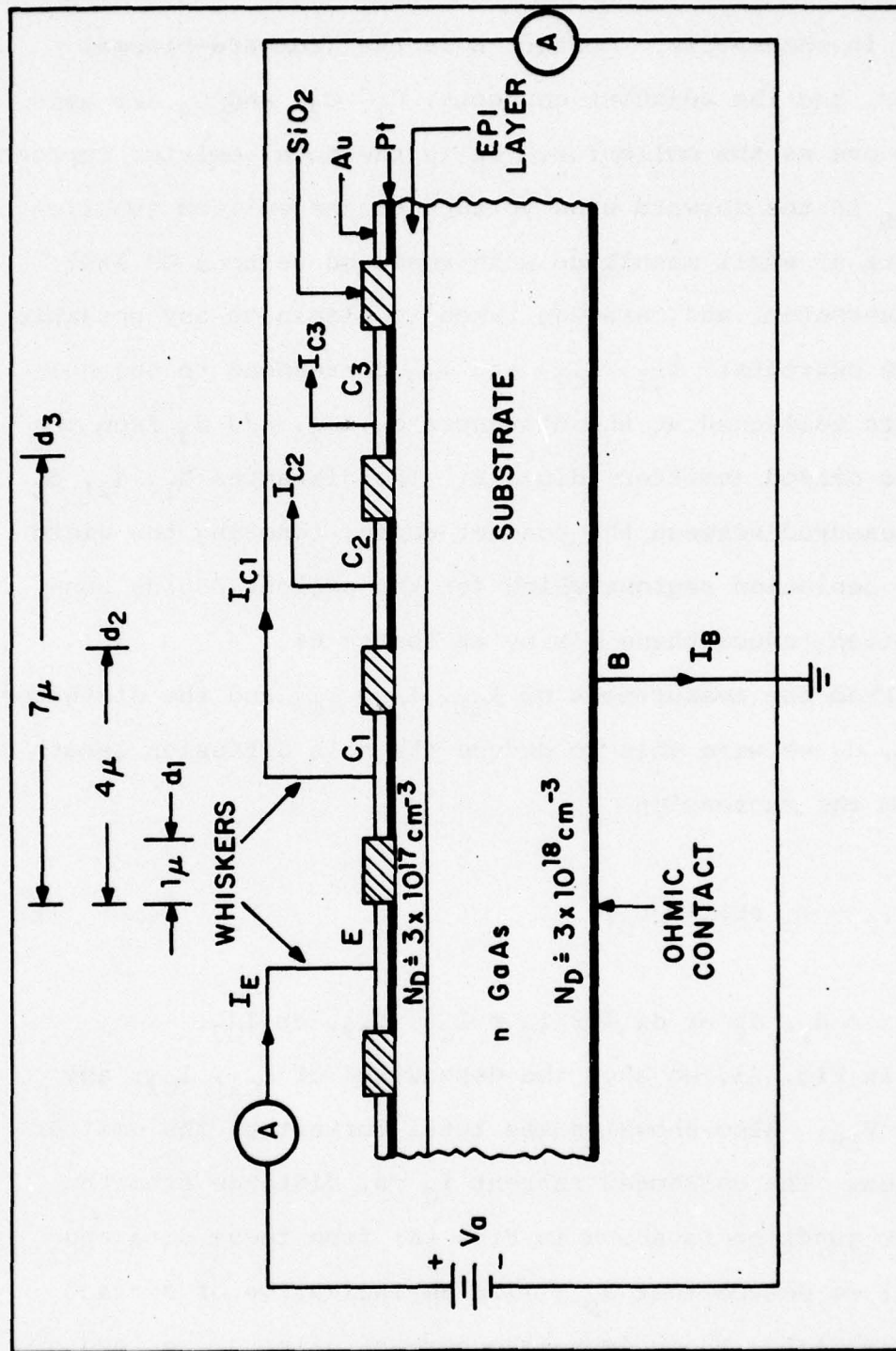


Figure 84: Schematic diagram of device structure and the circuit for transistor measurements.

stages, two whiskers were made to contact two neighboring diodes in the matrix. Contact E is the (forward-biased) emitter, and the adjacent contacts, C_1 , C_2 , and C_3 are used one by one as the collector. I_E is the total emitter current and V_{EB} is the forward bias voltage of the emitter junction. Currents of small magnitude were measured using a GR 1807 D.C. nanometer, and care was taken to eliminate any possible leakage currents. I_{C1} , I_{C2} , and I_{C3} correspond to the hole currents collected at the distances d_1 , d_2 , and d_3 from the forward biased (emitter) diode E. The distances d_1 , d_2 , d_3 were measured between the contact edges, ignoring the width of the depletion regions which for the present doping concentration reduce these d 's by at most $\approx 6\%$.

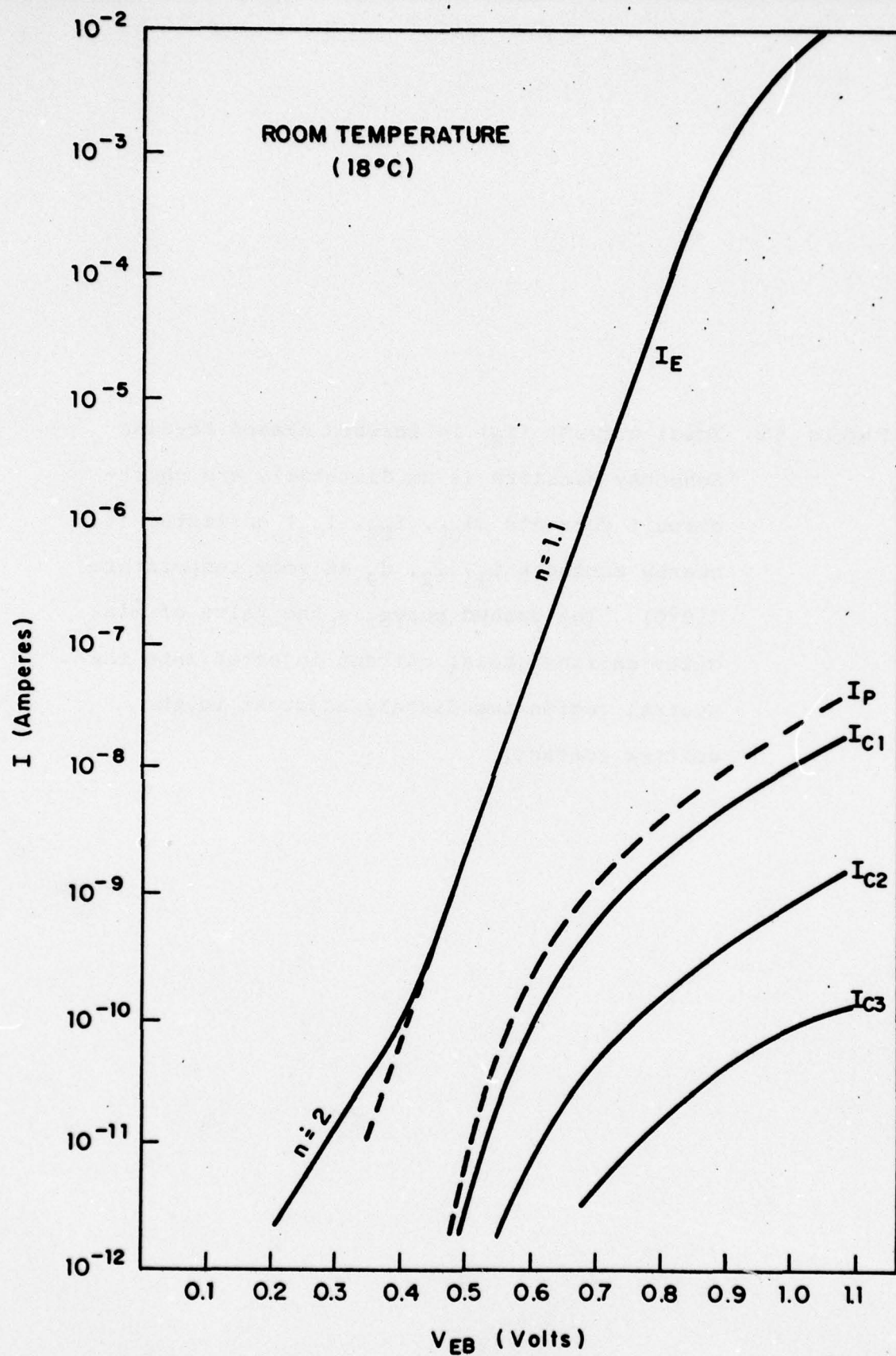
From the measurement of I_{C1} , I_{C2} , I_{C3} and the distances d_1 , d_2 , d_3 we were able to deduce the hole diffusion length L_p from the expression

$$I_C = I_p \exp(-x/L_p) \quad (1)$$

where $x = d_1$, d_2 or d_3 for $I_C = I_{C1}$, I_{C2} , or I_{C3} .

In Fig. 85, we show the dependence of I_{C1} , I_{C2} , and I_{C3} on V_{EB} . Also shown is the total current at the emitter junction. The collected current I_C vs. distance from the emitter junction is shown in Fig. 86; from these data and Eq. (1) we deduce that $L_p \approx 1.26 \mu\text{m}$ indicative of surface recombination. The common base current gains α_1 , α_2 and α_3

Figure 85: Total current (I_E) in forward biased Pt-GaAs Schottky barriers (2 μm diameter), and short-circuit currents (I_{C1} , I_{C2} , I_{C3}) collected at nearby contacts C_1 , C_2 , C_3 at room temperature (18°C). The dashed curve is the value of minority carrier (hole) current injected into the neutral region immediately adjacent to the emitter contact.



V_{EB} (Volts)

Figure 85

300

Figure 86: Collector current (I_c) vs. distance from the emitter (x) taken at three different forward bias voltages. O's show experimental data which are fit by the three approximately parallel straight lines. L_p is the diffusion length derived from the slope.

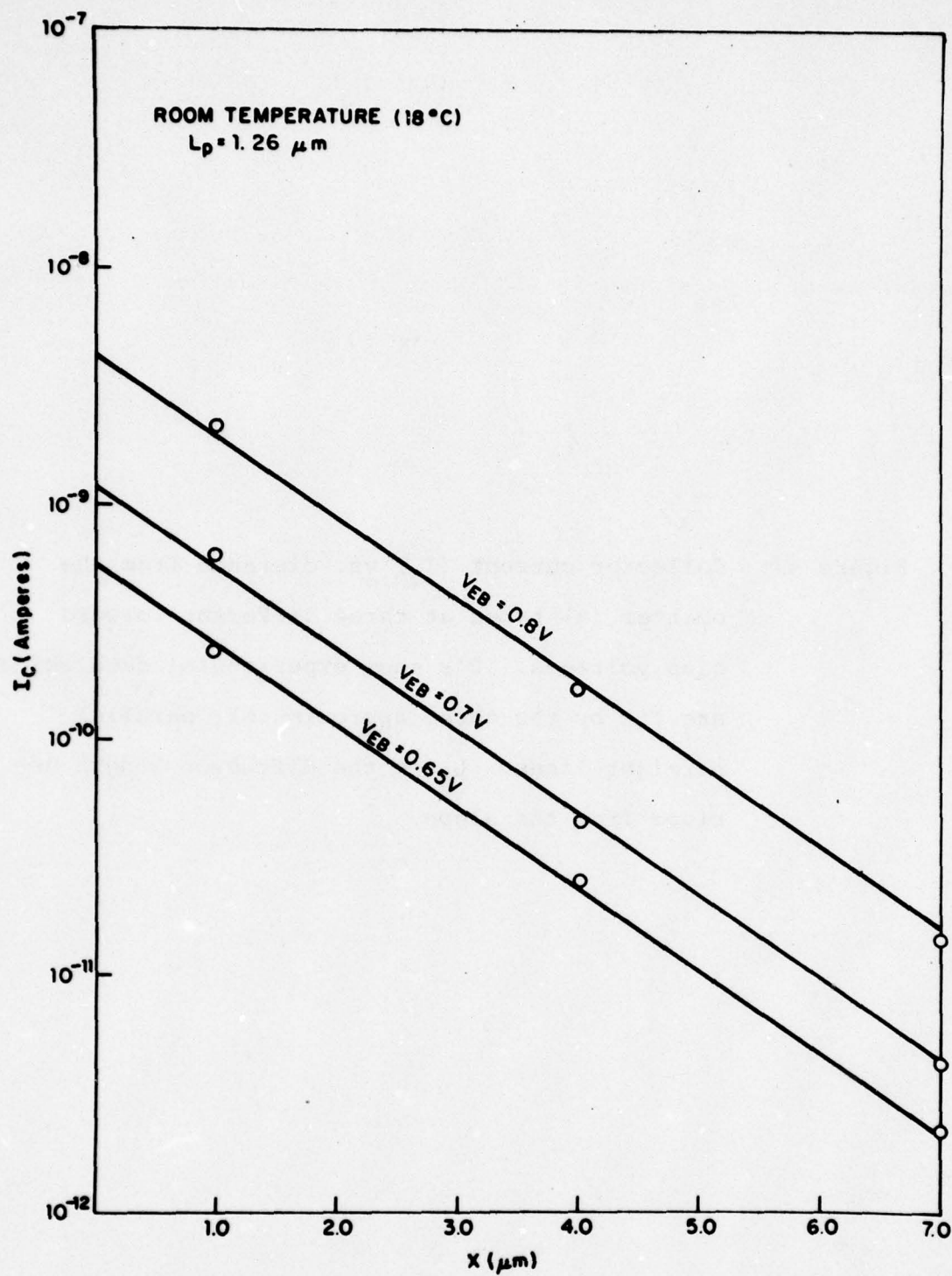


Figure 86

and the minority-carrier injection ratio γ are shown in Fig. 87.

Several features of Fig. 85 and Fig. 87 are of interest. For $V \geq 0.4$ V, the small area Pt-GaAs diodes behave as near-ideal Schottky barriers, with a current-voltage relation which agrees with the thermionic emission expression

$$I_R \approx A^* T^2 \exp\left(-\frac{q\phi_b}{kT}\right) \exp\left(\frac{qV}{nkT}\right) \quad (2)$$

where A^* is the modified Richardson constant $\approx 4.4 \text{ A cm}^{-2} \text{ K}^{-2}$ for (111) GaAs.⁽¹⁾ ϕ_b is the barrier height (determined from the extrapolation of the characteristic for $V \geq 0.4$ V to the $V = 0$ axis) which is found from Fig. 85 to be $\phi_b \approx 0.86$ eV. The 'n value' or ideality factor (for $V_{EB} \geq 0.4$ V) is ≈ 1.1 to 1.2 . For $V_{EB} \leq 0.4$ V, the forward current of Pt-GaAs diodes is dominated by recombination in the space charge region. The n-value in this region is $\approx 1.95 \pm 0.05$, very close to $n = 2$ expected for this mechanism.

The dependence of γ on V_{EB} shown in Fig. 87 is in qualitative agreement with the theoretical description of small-area Schottky barriers of Clarke et al.⁽²⁾ These authors also predict that $\gamma \approx 1$ for low forward voltages decreasing to negligible values at higher voltages. It should be noted that this behavior is the opposite of that for large Schottky barriers; for large area devices γ is very small at low V_{EB} , increasing at higher forward voltages and

Figure 87: Minority carrier injection ratio (γ) and ratio of collected currents at C_1 , C_2 , C_3 as a function of the forward bias voltage on the Schottky barrier emitter contact E.

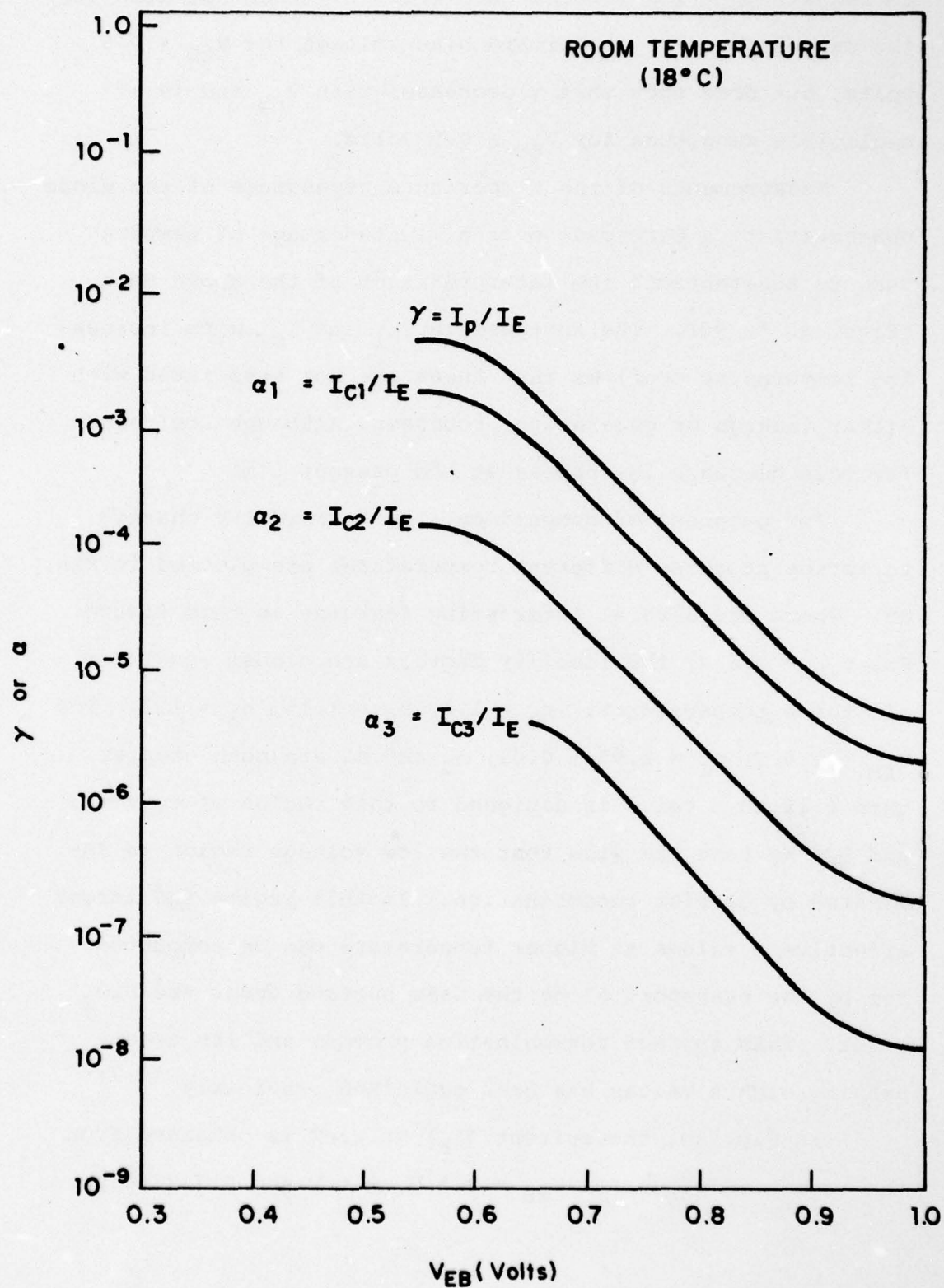


Figure 87

currents. (3-5) The present data (Fig. 87) does not describe the dependence of γ on forward bias voltage for $V_{EB} \leq 0.5$ volts, but does show that γ decreases with V_{EB} and is of negligible magnitude for $V_{EB} \geq 0.5$ volts.

Measurements of the temperature dependence of the diode characteristics were made over a limited range of temperature to substantiate the interpretation of the above data (Figs. 88 to 90). The decrease in I_{C1} and I_{C2} with increasing temperature confirms that these are not associated with either leakage or generation processes, although the reason for this decrease is unclear at the present time.

For purposes of comparison, the forward I-V characteristics at three different temperatures are plotted in Fig. 89. There are several interesting features in this figure. For $V_{EB} > 0.4$ V, the ideality factors are almost equal for all three temperatures: $n_1 = 1.1$, $n_2 = 1.15$, $n_3 = 1.2$. For $V_{EB} < 0.4$ V, $n_1 = 1.95 \pm 0.05$, n_2 and n_3 are both greater than 4 if an n value is assigned to this region of curves 2 and 3. We take the view that the low voltage region is dominated by carrier recombination. In this region the larger effective n values at higher temperature can be accounted for by the transport along the GaAs surface under the SiO_2 layer. This surface recombination process and its accompanying high n values has been explained previously. (6,7)

In Fig. 90, the current (I_E) vs. $1/T$ is obtained from the data of Fig. 89 for $V_{EB} = 0.5$ V, 0.6 V and 0.7 V respec-

Figure 88: Similar transistor measurements performed at 40°C. I_{C1} and I_{C2} are the collector currents detected at this temperature, I_{C3} is too small to be measured. I_{C1} and I_{C2} in this figure are smaller than those in Fig. 85.

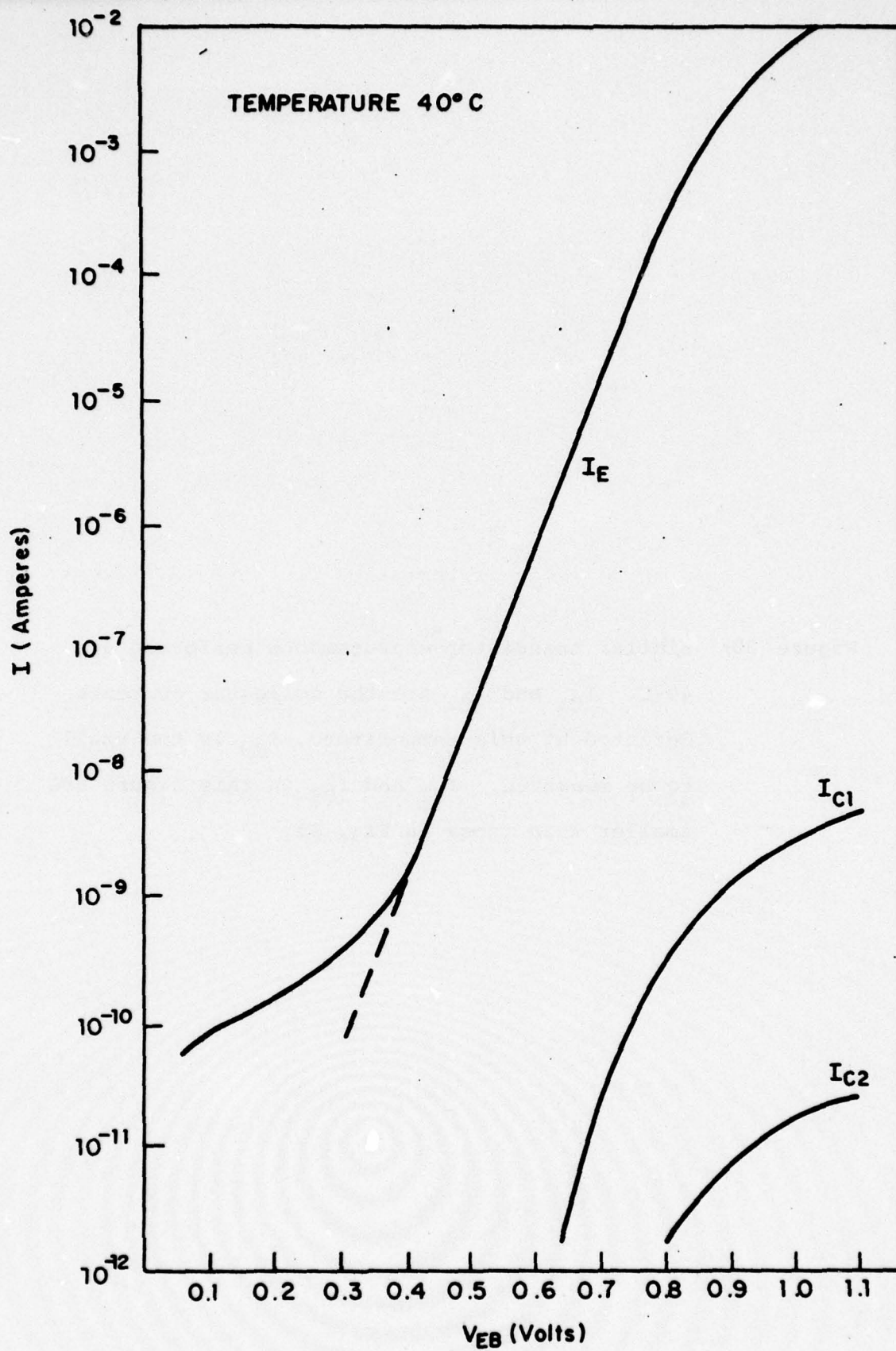


Figure 88

Figure 89: Forward I-V characteristics for three different temperatures; for $V_{EB} \geq 0.4$ V, $n_1 = 1.1$, $n_2 = 1.15$, $n_3 = 1.20$; for $V_{EB} < 0.4$ V, $n_1 = 1.95 \pm 0.05$, n_2 and n_3 are both greater than 4. Barrier height calculated by extrapolation of the room temperature I-V characteristic is $\phi_B = 0.86$ V.

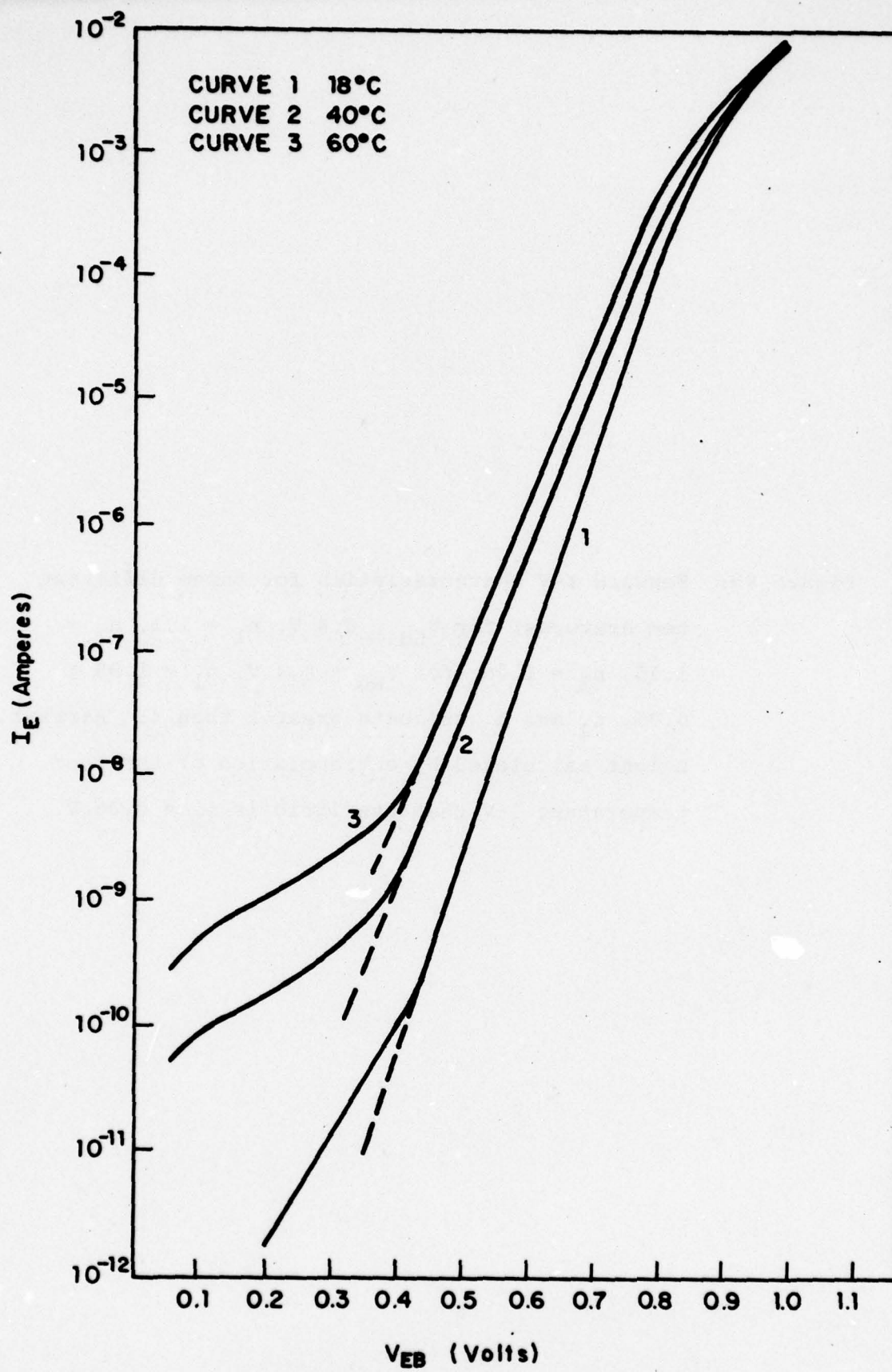


Figure 89
310

Figure 90: Total current I_E vs. reciprocal of temperature ($1/T$), 0's show the experimental data, ϕ_b 's are barrier heights calculated from the slope of the three straight lines with an assumed $n = 1.15$. Curves 1, 2, 3 refer to three values of forward bias voltage.

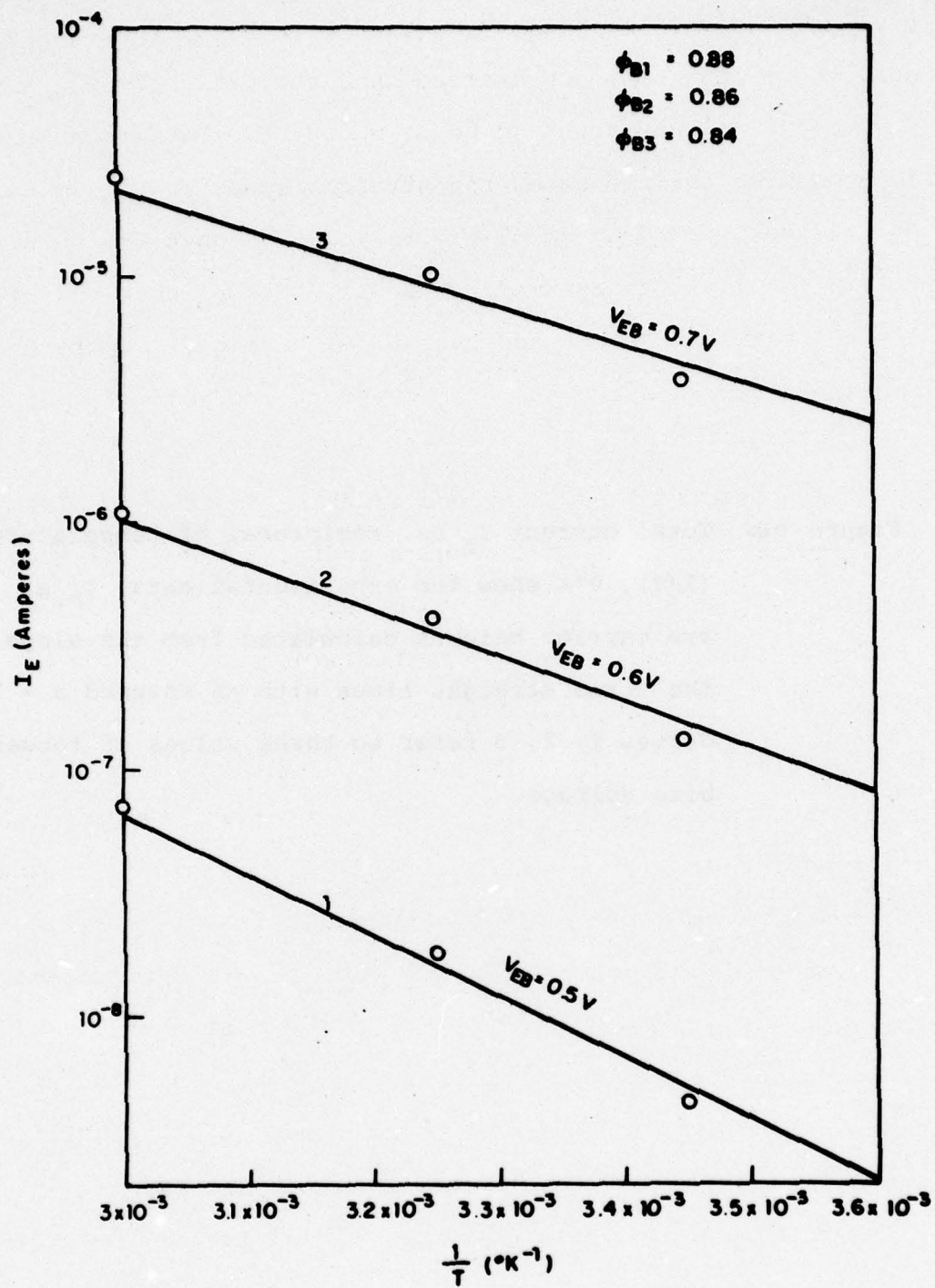


Figure 90

tively. The barrier height measured from Fig. 89 by extrapolation of the room temperature characteristic for $V_{EB} > 0.4$ to $V_{EB} = 0$ was found to be $\phi_b = 0.86$ V. Barrier heights deduced from the slopes of the straight lines in Fig. 90 using Eq. (2) were found to be $\phi_b = 0.86 \pm 0.02$ V when an average n value of 1.15 was assumed. The values of ϕ_b obtained by the two methods (saturation current at a single temperature, and temperature dependence of current at a given voltage) are therefore in close agreement.

For practical applications of these devices as classical detectors, the present results indicate that operation at forward biases of ≤ 0.4 V would reduce the sensitivity of these detectors, which is inversely proportional to the ' n ' value. Excess noise is also associated with the recombination current at lower voltages.

The implications of the present measurements for millimeter wave detectors and mixers may be summarized as follows. Provided the small-area ($2 \mu\text{m}$) Pt-GaAs diodes are operated at forward bias voltages greater than ≈ 0.4 V, the current transport is dominated by the majority-carrier thermionic-emission current with ' n ' values near unity. In this region, the best performance is expected with high frequency response and low noise. The contributions from minority-carrier injection to total current are < 1 percent decreasing to negligible values as the forward voltage increases above 0.4 V (Fig. 87). This means that diffusion capaci-

tance resulting from the storage of minority-carrier charges is not problematic for these devices.

* This work is presently being prepared for publication.

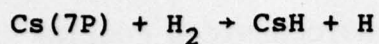
- (1) C. R. Crowell and S. M. Sze, Solid-State Electron. 9, 1035 (1966).
- (2) R. A. Clarke, M. A. Green, and J. Shewchun, J. Appl. Phys. 45, 1442 (1974).
- (3) D. L. Scharfetter, Solid-State Electron. 8, 299 (1965).
- (4) A. Y. C. Yu and E. H. Snow, Solid-State Electron. 12, 155 (1969).
- (5) H. C. Card and E. H. Rhoderick, Solid-State Electron. 16, 365 (1973).
- (6) C. T. Sah, IRE Trans. ED-9, 94 (1962).
- (7) C. T. Sah, Proc. IRE 49, 1623 (1961).

B. THERMODYNAMICS OF LASER SNOW—PHOTOCHEMICAL COOLING

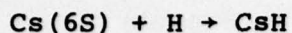
(T. Yabuzaki, S. Curry, J. Camparo, W. Happer)

Photochemically produced alkali hydride particles were discovered in 1976 in our laboratory,⁽¹⁾ and were named "laser snow" because they are white crystals and they fall down under the influence of gravity. Furthermore, the particles are expected to be cold like ordinary snow after they fall out of the laser beam. This laser snow is quite unique, compared with the other light-induced particle formation because the alkali hydride snow decomposes to hydrogen gas and alkali metal when the light is removed, while other light-induced particles which have been reported so far are thermodynamically more stable than the original gaseous phase, and they show no tendency to decompose to a gas again once the light is removed.

We would like to investigate the thermodynamical properties of laser snow more thoroughly, especially the cooling of laser snow. This cooling mechanism is also quite unique compared with other recently studied cooling mechanisms induced by light in the gaseous or solid state, since the cooling of laser snow involves a phase transition between solid and gaseous phases. This is closely analogous to the operation of mechanical refrigerators. Consider, as an example, cesium vapor mixed with hydrogen gas, to which we apply a laser beam with a wavelength suitable for excitation of the Cs atoms from the ground state (6S) to the second excited states (7P). The excited Cs atoms produce CsH molecules by the following probable reactions:



(1)



When the pressure of CsH exceeds the saturation pressure, crystalline CsH particles are created and grow in the laser beam by the condensation of CsH diatomic molecules. Consequently, the laser beam plays the role of a compressor in a mechanical refrigerator. When the crystals fall out of the beam, they decompose into Cs vapor and hydrogen gas with the absorption of a substantial amount of latent heat, and the surrounding gas is therefore cooled. This is quite analogous to the cooling in the cold side of a mechanical refrigerator. Here, we would like to report some of our preliminary results on this unique cooling cycle of laser snow, and we will discuss our future plans.

1. Theoretical Estimate of Laser Snow Temperature:

The cooling mechanism of the laser snow is quite similar to that of a cooling tower for cooling hot water, or to the cooling of a wet bulb of a thermometer to measure the humidity of air. We have constructed psychrometric charts to estimate the cooling of the snow and of the surrounding buffer gas. As an example, consider the CsH system in a He buffer gas. The enthalpy for a helium atom, $h(\text{He})$, is given by $5/2 kT$, while that of hydrogen gas per H_2 molecule is obtained from Table XIII, which shows the thermodynamic properties of the cesium hydrogen system.⁽²⁾ Then, the total gas-phase enthalpy per helium atoms is given by

$$h_o = h(\text{He}) + fh(\text{H}_2) = 2.17 \times 10^{-4}T + f[1.135 + 1.33 \times 10^{-4}T] \quad (2)$$

TABLE XIII

T (°K)	ΔG° (kcal mole ⁻¹)	ΔH° (kcal mole ⁻¹)	ΔS° (cal mole ⁻¹ deg ⁻¹)
0	-26.2	-	-
302	-14.8	-26.2	-37.7
661	0.0	-27.3	-41.2

where T is in $^{\circ}\text{C}$, and f is the number of hydrogen molecules per helium atom in the gaseous phase, i.e.

$$f = \frac{[\text{H}_2]}{[\text{He}]} \quad (3)$$

Because of the low heat capacity of condensed CsH crystals compared with the latent heat of decomposition of the crystal, h_0 in Eq. (2) remains very nearly constant during the decomposition, so that h_0 may be given by the enthalpy of the dry gas before the crystals have decomposed. The psychrometric chart for the CsH system in a He buffer gas at a density of one amagat is shown in Figure 91, where the nearly straight lines show the fraction f as a function of temperature T , given by Eq. (2). On the other hand, the saturated hydrogen pressure in Figure 91 is given by

$$P(\text{H}_2) = \exp \frac{-\Delta G^{\circ}}{RT} \quad (4)$$

where empirical values for ΔG° are shown in Table XIII.

Consider, as an example, a cesium cell containing hydrogen gas of about 1 torr and helium buffer gas of 760 torr at room temperature, values quite representative of the experiments described below. The fraction f is 1.3 parts per thousand in this case. Suppose that the cell is maintained at 300°C where, according to Figure 91, the relative saturation is about 5%. When the laser snow CsH begins to evaporate into surrounding buffer gas, the temperature decreases along the lines

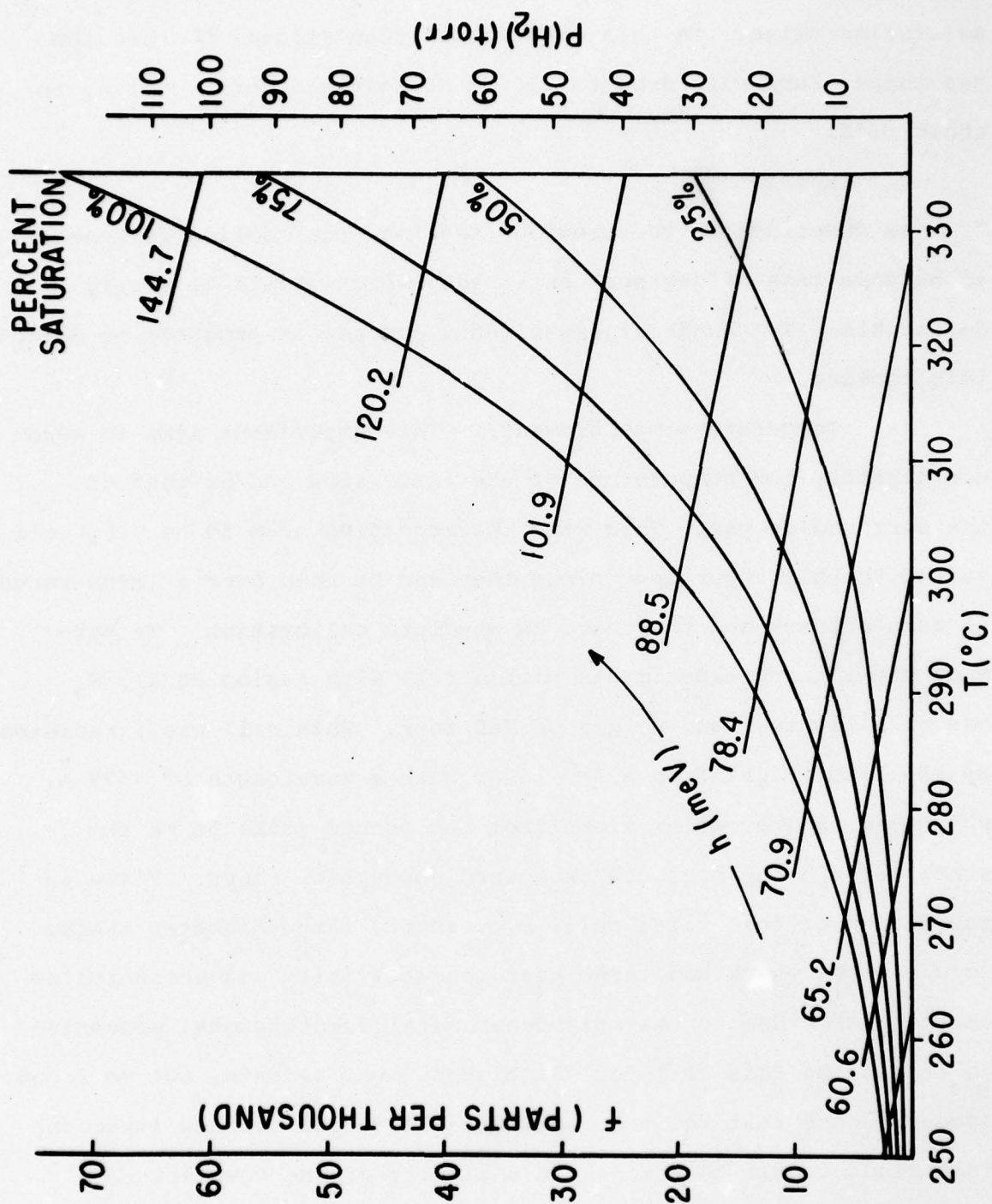


Figure 91

of constant gas-phase enthalpy until the H_2 pressure reaches its saturation value. In this case we see from Figure 91 that the gas temperature will drop to 270°C , so that the total cooling is about 30°C .

2. Experiments:

As described in the previous section, the cooling is expected to be some tens of degrees centigrade, which should be easily detectable. Two kinds of experiments are now in progress to detect this cooling.

(a) Temperature Measurement: This experiment aims to measure directly the temperature of the laser snow and/or that of the surrounding gas. Thin wire thermocouples seem to be very well suited to this experiment since they can be used over a large range of temperatures and they have an absolute calibration. We have made preliminary experiments with a cell with cesium metal, H_2 gas of a few torr and He gas of 760 torr. This cell was irradiated by the laser light from a Ar^+ laser with a wavelength of 4579 \AA , which can excite cesium atoms from the ground state 6S to the 7P state through the pressure broadened absorption lines. Flaws in the design of this first cell, e.g. short, large-diameter thermocouple wires which had large heat conductivities and uncontrolled thermal EMF's due to the molybdenum metal feedthroughs, prevented us from using this cell for unambiguous measurements, but we found some evidence that the snow is indeed cold. We are now improving this kind of cell to remove the ambiguity of the temperature measurements.

(b) Velocity Measurement of Falling Snow: As described above, the laser snow grown in the laser beam falls down slowly within a buffer gas of relatively high pressure. If we measure the falling velocity just below the laser beam, we can measure the size of the laser snow. Furthermore, by measuring the change in the velocity during its falling, we may determine whether or not the snow is really cold.

The "viscous" velocity v_v of the snow with respect to the surrounding gas is obtained by equating the force of gravity to the viscous retarding force of the gas

$$v_v = \frac{2}{9} \left(\frac{\rho g}{\eta} \right) r^2 \quad (5)$$

where ρ is the mass density of the crystal, g is the acceleration of gravity, η is the viscosity of the gas and r is the effective radius of the crystals. For simplicity the crystal is assumed to have a spherical shape. Denote the convective velocity of the gas by v_c . Then the apparent velocity of the falling crystals is

$$v = v_v + v_c = \frac{2}{9} \left(\frac{\rho g}{\eta} \right) r^2 + v_c \quad (6)$$

Both v_v and v_c are considered positive in the downward direction.

There is no doubt that the falling crystals diminish in size due to evaporation so that the crystal radius r decreases with time. Thus if the convective gas velocity v_c were zero the falling

velocity of the crystals would decrease with time. Because the experimental cells are operated with a variable temperature which increases from the bottom to the top, the gas is normally stratified and is stable against convection. However if the gas is heated or cooled substantially the gas will rise or fall due to convection. Consequently, if there is evaporative cooling of the gas by the falling snow, we expect that a downward convective velocity v_c will develop, and the overall downward velocity v of Eq. (6) will increase if the increase in convective velocity exceeds the decrease in the viscous velocity.

We have made a preliminary experiment with a cesium cell containing 1 torr hydrogen and 760 torr helium, which is irradiated by a Ar laser beam of 4579 Å. A second light beam (the 6328 Å line from a He-Ne laser in this experiment, is applied as a probe beam, which is placed under the first excitation beam. A sharp increase of scattered light intensity of the probe light can be observed with a time delay t after the Ar laser is on. By changing the distance between two laser beams and measuring the time of flight, we can precisely measure the velocity of the falling laser snow. Typical results of the present experiment are shown in Fig. 92, where the falling velocity is plotted as a function of the time of flight t , for several values of Ar laser power. From the initial velocities in Fig. 92, we see that the size of snow increases with the increase of laser power (using Eq. (5) the radius of snow is calculated to be 1.13 μm for the Ar laser power of 24 mW and 1.59 μm for 120 mW). As

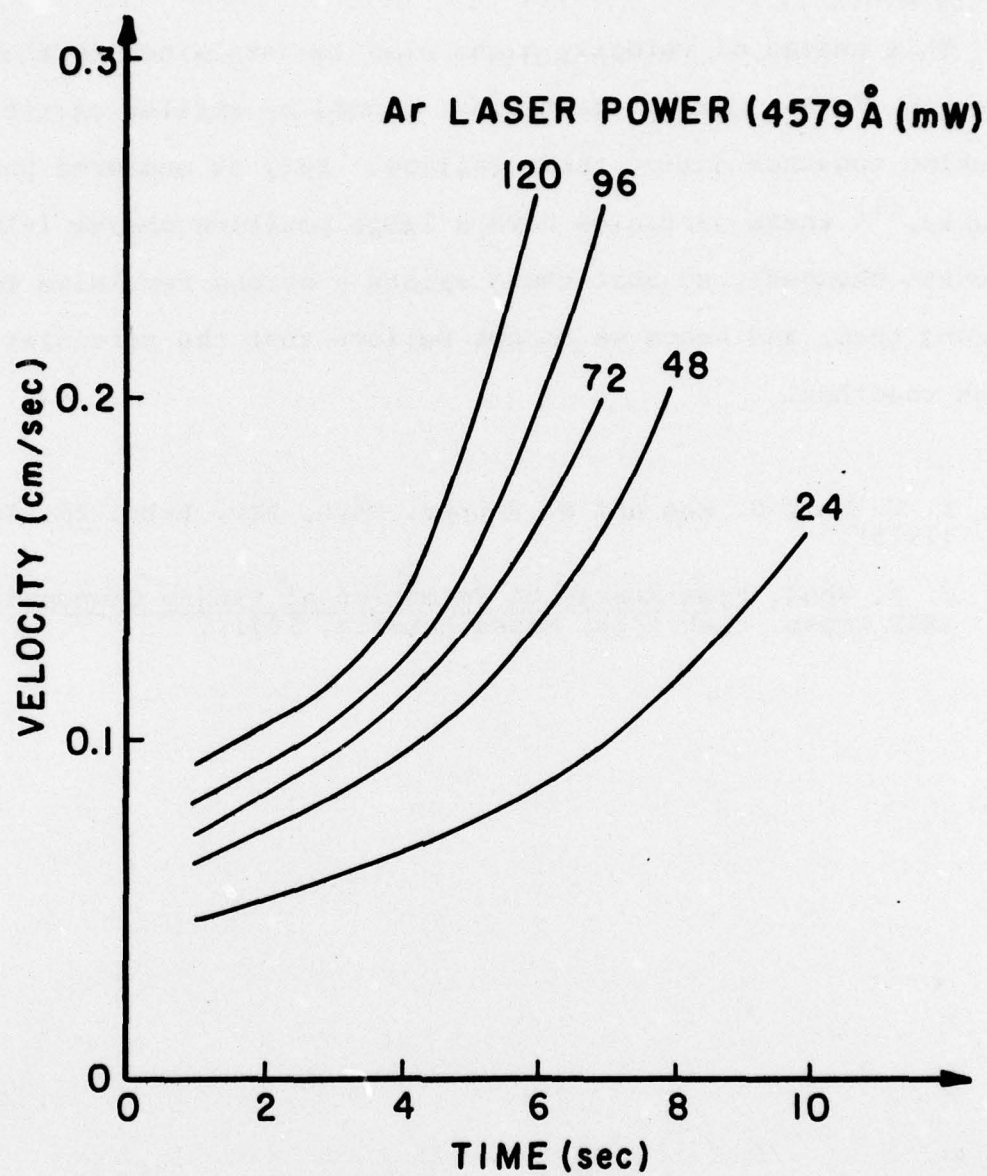


Figure 92

seen in Fig. 92, the falling velocity increases clearly with the increase of t . These results suggest that the velocity of the snow increases by falling together with a cooled surrounding buffer gas.

This change of velocity might also be explained by the increase of the size of particles, caused by smaller particles sticking together during their falling. But, as measured previously, ⁽¹⁾ these particles have a large positive charge ($\sim 10^4$ electron charges), so that there exists a strong repulsive force between them, and hence we do not believe that the particles stick together.

- (1) A. C. Tam, G. Moe and W. Happer, Phys. Rev. Lett. 35, 1630 (1975).
- (2) T. B. Read, Free Energy of Formation of Binary Compound, (MIT Press, Cambridge, Massachusetts, 1971).

PERSONNEL

Faculty

H. C. Card, Associate Professor of Electrical Engineering
S. M. Curry, Visiting Assistant Professor of Physics
A. Flusberg, Assistant Professor of Physics
G. W. Flynn, Professor of Chemistry
R. Gupta, Assistant Professor of Physics
W. Happer, Professor of Physics, Director
S. R. Hartmann, Professor of Physics
J. M. Luttinger, Professor of Physics
I. I. Rabi, University Professor Emeritus
A. M. Sachs, Professor of Physics
M. C. Teich, Professor of Engineering Science
P. Thaddeus, Adjunct Professor of Physics
C. S. Wu, Pupin Professor of Physics
T. Yabuzaki, Visiting Assistant Professor of Physics
E. Yang, Professor of Electrical Engineering

Research Associates and Physicists

Dr. N. Bhaskar	Dr. J. McVey
Dr. K. Casleton	Dr. G. Moe
Dr. Y. Chen	Dr. Y. Taur
Dr. G. Hill	Dr. G. Tomasevich

Graduate Research Assistants

J. Camparo	K. Leung	R. Sheorey
K. Chiang	R. Meyers	P. Siegel
P. Fu	T. Mossberg	C. Wu
M. Hou	K. Ng	G. Vannucci
M. Isack	P. Prucnal	E. Zouboulis
R. Kachru	I. Shamah	

Technical Research Assistants

Mr. I. Beller
Mr. E. Deery

Physics Department Electronics Engineering and Construction Shop*

Mr. J. Packer

Physics Department Machine Shop*

Mr. E. Jauch

Administration

Ms. T. Brasfield
Ms. I. Moon
Ms. P. Pohlman

*The Machine Shop and Electronics Shop facilities are available for the Columbia Radiation Laboratory.

JSEP REPORTS DISTRIBUTION LIST

DEPARTMENT OF DEFENSE

Director
National Security Agency
ATTN: Dr. T. J. Beahn
Fort George G. Meade, MD 20755

Defense Documentation Center
(12 copies)
ATTN: DDC-TCA
(Mrs. V. Caponio)
Cameron Station
Alexandria, VA 22314

Asst. Dir. Electronics &
Computer Sciences
Office of Dir. of Defense
Research & Engineering
The Pentagon
Washington, DC 20315

Defense Advanced Research
Projects Agency
ATTN: (Dr. R. Reynolds)
1400 Wilson Boulevard
Arlington, VA 22209

DEPARTMENT OF THE ARMY

Commandant
US Army Air Defense School
ATTN: ATSAD-T-CSM
Fort Bliss, TX 79916

Commander
US Army Armament R&D Command
ATTN: DRSAR-RD
Dover, NJ 07801

Commander
US Army Ballistics Research
Laboratory
ATTN: DRXRD-BAD
Aberdeen Proving Ground
Aberdeen, MD 21005

Commandant
US Army Command and General Staff
College
ATTN: Acquisitions, Lib. Div.
Fort Leavenworth, KS 66027

Commander
US Army Communication Command
ATTN: CC-OPS-PD
Fort Huachuca, AZ 85613

Commander
US Army Materials and Mechanics
Research Center
ATTN: Chief, Materials Sciences
Division
Watertown, MA 02172

Commander
US Army Material Development
and Readiness Command
ATTN: Technical Library, Rm. 7S 35
5001 Eisenhower Avenue
Alexandria, VA 22333

Commander
US Army Missile R&D Command
ATTN: Chief, Document Section
Redstone Arsenal, AL 35809

Commander
US Army Satellite Communications
Agency
Fort Monmouth, NJ 07703

Commander
US Army Security Agency
ATTN: IARD-T
Arlington Hall Station
Arlington, VA 22212

Project Manager
ARTADS
EAI Building
West Long Branch, NJ 07764

Commander/Director
Atomospheric Sciences Lab. (ECOM)
ATTN: DRSEL-BL-DD
White Sands Missile Range, NM
88002

Commander
US Army Electronics Command
ATTN: DRSEL-NL-O
(Dr. H. S. Bennett)
Fort Monmouth, NJ 07703

Director
TRI-TAC
ATTN: TT-AD (Mrs. Briller)
Fort Monmouth, NJ 07703

Commander
US Army Electronics Command
ATTN: DRSEL-CT-L (Dr. R. Buser)
Fort Monmouth, NJ 07703

Director
Electronic Warfare Lab. (ECOM)
ATTN: DRSEL-WL-MY
White Sands Missile Range, NM
88002

Executive Secretary, TAC/JSEP
US Army Research Office
P. O. Box 12211
Research Triangle Park, NC
27709

Commander
Frankford Arsenal
Deputy Director, Pitman-Dunn
Laboratory
Philadelphia, PA 19137

Project Manager
Ballistic Missile Defense
Program Office
ATTN: DACS-DMP (Mrs. A. Gold)
1300 Wilson Blvd.
Arlington, VA 22209

Commander
Harry Diamond Laboratories
ATTN: Mr. John E. Rosenberg
2800 Powder Mill Road
Adelphi, MD 20783

HQDA (DAMA-ARZ-A)
Washington, DC 20310

Commander
US Army Electronics Command
ATTN: DRSEL-TL-E (Dr. J. A. Kohn)
Fort Monmouth, NJ 07703

Commander
US Army Electronics Command
ATTN: DRSEL-TL-EN
(Dr. S. Kroenenberg)
Fort Monmouth, NJ 07703

Commander
US Army Electronics Command
ATTN: DRSEL-NL-T (Mr. R. Kulinyi)
Fort Monmouth, NJ 07703

Commander
US Army Electronics Command
ATTN: DRSEL-NL-B (Dr. E. Lieblein)
Fort Monmouth, NJ 07703

Commander
US Army Electronics Command
ATTN: DRSEL-TL-MM (Mr. N. Lipetz)
Fort Monmouth, NJ 07703

Commander
US Army Electronics Command
ATTN: DRSEL-RD-O
(Dr. W. S. McAfee)
Fort Monmouth, NJ 07703

Director
Night Vision Laboratory
ATTN: DRSEL-NV-D
Fort Belvoir, VA 22060

COL Robert Noce
Senior Standardization Rep.
US Army Standardization Group,
Canada
Canadian Force Headquarters
Ottawa, Ontario, Canada KIA)K2

Commander
US Army Electronics Command
ATTN: DRSEL-NL-B
(Dr. D. C. Pearce)
Fort Monmouth, NJ 07703

Commander
Picatinny Arsenal
ATTN: SMUPA-TS-T-S
Dover, NJ 07801

Dr. Sidney Ross
Technical Director
SARFA-TD
Frankford Arsenal
Philadelphia, PA 19137

Commander
US Army Electronics Command
ATTN: DRSEL-NL-RH-1
(Dr. F. Schwering)
Fort Monmouth, NJ 07703

Commander
US Army Electronics Command
ATTN: DRSEL-TL-I
(Dr. C. G. Thornton)
Fort Monmouth, NJ 07703

US Army Research Office
(3 copies)
ATTN: Library
P. O. Box 12211
Research Triangle Park, NC
27709

Director
Division of Neuropsychiatry
Walter Reed Army Institute of
Research
Washington, DC 20012

Commander
White Sands Missile Range
ATTN: STEWS-ID-R
White Sands Missile Range, NM
88002

DEPARTMENT OF THE AIR FORCE

Mr. Robert Barrett
RADDC/ETS
Hanscom AFB, MA 01731

Dr. Carl E. Baum
AFWL (ES)
Kirtland AFB, NM 87117

Dr. E. Champagne
AFAL/DH
Wright-Patterson AFB, OH 45433

Dr. R. P. Dolan
RADDC/ETSE
Hanscom AFB, MA 01731

Mr. W. Edwards
AFAL/TE
Wright-Patterson AFB, OH 45433

Professor R. E. Fontana
Head Dept. of Electrical Eng.
AFIT/ENE
Wright-Patterson AFB, OH 45433

Dr. Alan Garscadden
AFAPL/POD
Wright-Patterson AFB, OH 45433

USAF European Office of Aerospace
Research
ATTN: Major J. Gorrell
Box 14, FPO, New York 09510

LTC Richard J. Gowen
Department of Electrical Eng.
USAF Academy, CO 80840

Mr. Murray Kesselman (ISCA)
Rome Air Development Center
Griffiss AFB, NY 13441

Dr. G. Knausenberger
Air Force Member, TAC
Air Force Office of Scientific
Research (AFSC) AFSOR/NE
Bolling Air Force Base, DC
20332

Dr. L. Kravitz
Air Force Member, TAC
Air Force Office of Scientific
Research
(AFSC) AFSOR/NE
Bolling Air Force Base, DC 20332

Mr. R. D. Larson
AFAL/DHR
Wright-Patterson AFB, OH 45433

Dr. Richard B. Mack
RADC/EATER
Hanscom AFB, MA 01731

Mr. John Mottsmith (MCIT)
HQ ESD (AFSC)
Hanscom AFB, MA 01731

Dr. Richard Picard
RADC/ETSL
Hanscom AFB, MA 01731

Dr. J. Ryles
Chief Scientist
AFAL/CA
Wright-Patterson AFB, OH 45433

Dr. Allan Schell
RADC/ETE
Hanscom AFB, MA 01731

Mr. H. E. Webb, Jr. (ISCP)
Rome Air Development Center
Griffiss AFB, NY 13441

LTC G. Wepfer
Air Force Office of Scientific
Research
(AFSC) AFOSR/NP
Bolling Air Force Base, DC 20332

LTC G. McKemie
Air Force Office of Scientific
Research
(AFSC) AFOSR/NM
Bolling Air Force Base, DC 20332

Dr. R. S. Allgaier
Naval Surface Weapons Center
Code WR-303
White Oak
Silver Spring, MD 20910

Naval Weapons Center
ATTN: Code 5515 - H. F. Blazek
China Lake, CA 93555

Dr. H. L. Blood
Technical Director
Naval Undersea Center
San Diego, CA 95152

Naval Research Laboratory
ATTN: Code 5200 - A. Brodzinsky
4555 Overlook Avenue, SW
Washington, DC 20375

Naval Research Laboratory
ATTN: Code 7701 - J. D. Brown
4555 Overlook Avenue, SW
Washington, DC 20375

Naval Research Laboratory
ATTN: Code 5210 - J. E. Davey
4555 Overlook Avenue, SW
Washington, DC 20375

Naval Research Laboratory
ATTN: Code 5460/5410 - J. R. Davis
4555 Overlook Avenue, SW
Washington, DC 20375

Naval Ocean Systems Center
ATTN: Code 75 - W. J. Dejka
271 Catalina Boulevard
San Diego, CA 92152

Naval Weapons Center
ATTN: Code 601 - F. C. Essig
China Lake, CA 93555

Naval Research Laboratory
ATTN: Code 5510 - W. L. Faust
4555 Overlook Avenue, SW
Washington, DC 20375

Naval Research Laboratory
ATTN: Code 2627 - Mrs. D. Folen
4555 Overlook Avenue, SW
Washington, DC 20375

Dr. Robert R. Fossum
Dean of Research
Naval Postgraduate School
Monterey, CA 93940

Dr. G. G. Gould
Technical Director
Naval Coastal System Laboratory
Panama City, FL 32401

Naval Ocean Systems Center
ATTN: Code 7203 -
V. E. Hildebrand
271 Catalina Boulevard
San Diego, CA 92152

Naval Ocean Systems Center
ATTN: Code 753 - P. H. Johnson
271 Catalina Boulevard
San Diego, CA 92152

Donald E. Kirk
Professor and Chairman
Electronic Engineer, SP-304
Naval Postgraduate School
Monterey, CA 93940

Naval Air Development Center
ATTN: Code 01 - Dr. R. K. Lobb
Johnsville
Warminster, PA 18974

Naval Research Laboratory
ATTN: Code 5270 - B. D. McCombe
4555 Overlook Avenue, SW
Washington, DC 20375

Capt. R. B. Meeks
Naval Sea Systems Command
NC #3
2531 Jefferson Davis Hwy
Arlington, VA 20362

Dr. H. J. Mueller
Naval Air Systems Command
Code 310
JP #1
1411 Jefferson Davis Hwy
Arlington, VA 20360

Dr. J. H. Mills, Jr.
Naval Surface Weapons Center
Electronics Systems Dept.
Code DF
Dahlgren, VA 22448

Naval Ocean Systems Center
ATTN: Code 702 - H. T. Mortimer
271 Catalina Boulevard
San Diego, CA 92152

Naval Air Development Center
ATTN: Technical Library
Johnsville
Warminster, PA 18974

Naval Ocean Systems Center
ATTN: Technical Library
271 Catalina Boulevard
San Diego, CA 92152

Naval Research Laboratory
Underwater Sound Reference Divi.
Technical Library
P. O. Box 8337
Orlando, FL 32806

Naval Surface Weapons Center
ATTN: Technical Library
Code DX-21
Dahlgren, VA 22448

Naval Surface Weapons Center
ATTN: Technical Library
Building 1-330, Code WX-40
White Oak
Silver Spring, MD 20910

Naval Training Equipment Center
ATTN: Technical Library
Orlando, FL 32813

Naval Undersea Center
ATTN: Technical Library
San Diego, CA 92152

Naval Underwater Systems Center
ATTN: Technical Library
Newport, RI 02840

Office of Naval Research
Electronic & Solid State
Sciences Program (Code 427)
800 North Quincy Street
Arlington, VA 22217

Office of Naval Research
Mathematics Program (Code 432)
800 North Quincy Street
Arlington, VA 22217

Office of Naval Research
Naval Systems Division
Code 220/221
800 North Quincy Street
Arlington, VA 22217

Director
Office of Naval Research
New York Area Office
715 Broadway, 5th Floor
New York, NY 10003

Office of Naval Research
San Francisco Area Office
760 Market Street, Room 447
San Francisco, CA 94102

Director
Office of Naval Research
Branch Office
495 Summer Street
Boston, MA 02210

Director
Office of Naval Research
Branch Office
536 South Clark Street
Chicago, IL 60605

Director
Office of Naval Research
Branch Office
1030 East Green Street
Pasadena, CA 91101

Mr. H. R. Riedl
Naval Surface Weapons Center
Code WR-34
White Oak Laboratory
Silver Spring, MD 20910

Naval Air Development Center
ATTN: Code 202 - T. J. Shopple
Johnsville
Warminster, PA 18974

Naval Research Laboratory
ATTN: Code 5403 - J. E. Shore
4555 Overlook Avenue, SW
Washington, DC 20375

A. L. Slafkovsky
Scientific Advisor
Headquarters Marine Corps
MC-RD-1
Arlington Annex
Washington, DC 20380

Harris B. Stone
Office of Research, Development,
Test and Evaluation
NOP-987
The Pentagon, Room 5D760
Washington, DC 20350

Mr. L. Sumney
Naval Electronics Systems Command
Code 3042, NC #1
2511 Jefferson Davis Hwy
Arlington, VA 20360

David W. Taylor
Naval Ship Research & Development
Center
Code 522.1
Bethesda, MD 20084

Naval Research Laboratory
ATTN: Code 4105 - Dr. S. Teitler
4555 Overlook Avenue, SW
Washington, DC 20375

Lt. Cdr. John Turner
NAVMAT 0343
CP #5, Room 1044
2211 Jefferson Davis Hwy.
Arlington, VA 20360

Naval Ocean Systems Center
ATTN: Code 746 - H. H. Wieder
271 Catalina Boulevard
San Diego, CA 92152

Dr. W. A. Von Winkle
Associate Technical Director
for Technology
Naval Underwater Systems Center
New London, CT 06320

Dr. Gernot M. R. Winkler
Director, Time Service
US Naval Observatory
Massachusetts Avenue at 34th
Street, NW
Washington, DC 20390

OTHER GOVERNMENT AGENCIES

Dr. Howard W. Etzel
Deputy Director
Division of Materials Research
National Science Foundation
1800 G Street
Washington, DC 20550

Mr. J. C. French
National Bureau of Standards
Electronics Technology Division
Washington, DC 20234

Dr. Jay Harris
Program Director
Devices and Waves Program
National Science Foundation
1800 G Street
Washington, DC 20550

Los Alamos Scientific Lab.
ATTN: Reports Library
P. O. Box 1663
Los Alamos, NM 87544

Dr. Dean Mitchell
Program Director, Solid-State
Physics
Division of Materials Research
National Science Foundation
1800 G Street
Washington, DC 20550

Mr. F. C. Schwenk, RD-T
National Aeronautics & Space
Administration
Washington, DC 20546

M. Zane Thornton
Deputy Director Institute for
Computer Sciences and Technology
National Bureau of Standards
Washington, DC 20234

NON-GOVERNMENT AGENCIES

Director
Columbia Radiation Laboratory
Columbia University
538 West 120th Street
New York, NY 10027

Director
Coordinated Science Laboratory
University of Illinois
Urbana, IL 61801

Director of Laboratories
Division of Engineering and
Applied Physics
Harvard University
Pierce Hall
Cambridge, MA 02138

Director
Electronics Research Center
The University of Texas
Engineering-Science Bldg. 112
Austin, TX 78712

Director
Electronics Research Laboratory
University of California
Berkeley, CA 94720

Director
Electronics Sciences Laboratory
University of Southern California
Los Angeles, CA 90007

Director
Microwave Research Institute
Polytechnic Institute of
New York
333 Jay Street
Brooklyn, NY 11201

Director
Research Laboratory of Electronics
Massachusetts Institute of
Technology
Cambridge, MA 02139

Director
Stanford Electronics Laboratory
Stanford University
Stanford, CA 94305

Stanford Ginzton Laboratory
Stanford University
Stanford, CA 94305